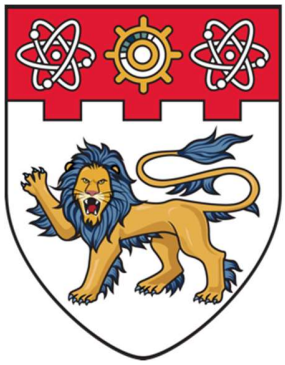

NANYANG TECHNOLOGICAL UNIVERSITY
SINGAPORE

# MODULATION OF NON-RADIATIVE RECOMBINATION IN ORGANIC-INORGANIC HALIDE PEROVSKITES FOR LIGHT EMISSION

**NUR FADILAH BINTE JAMALUDIN**

**Interdisciplinary Graduate School**
**Energy Research Institute @ NTU**

**2019**

# MODULATION OF NON-RADIATIVE RECOMBINATION IN ORGANIC-INORGANIC HALIDE PEROVSKITES FOR LIGHT EMISSION

**NUR FADILAH BINTE JAMALUDIN**

INTERDISCIPLINARY GRADUATE SCHOOL

A thesis submitted to the Nanyang Technological University
in partial fulfilment of the requirement for the degree of
Doctor of Philosophy

**2019**

## Statement of Originality

I hereby certify that the work embodied in this thesis is the result of original research, is free of plagiarised materials, and has not been submitted for a higher degree to any other University or Institution.

19 August 2019

. . . . . .
Date

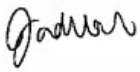

. . . . . .
Nur Fadilah Jamaludin

## Supervisor Declaration Statement

I have reviewed the content and presentation style of this thesis and declare it is free of plagiarism and of sufficient grammatical clarity to be examined. To the best of my knowledge, the research and writing are those of the candidate except as acknowledged in the Author Attribution Statement. I confirm that the investigations were conducted in accord with the ethics policies and integrity standards of Nanyang Technological University and that the research data are presented honestly and without prejudice.

19 August 2019

. . . . . .
Date

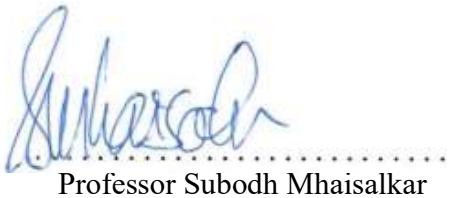

Professor Subodh Mhaisalkar

# Authorship Attribution Statement

This thesis contains material from 2 papers published in the following peer-reviewed journals where I was the first author.

Chapter 4 is published as Nur Fadilah Jamaludin, Natalia Yantara, Yan Fong Ng, Mingjie Li, Teck Wee Goh, Krishnamoorthy Thirumal, Tze Chien Sum, Nripan Mathews, Cesare Soci, and Subodh Mhaisalkar, Grain Size Modulation and Interfacial Engineering of $CH_3NH_3PbBr_3$ Emitter Films through Incorporation of Tetraethylammonium Bromide. *ChemPhysChem* **2018**, 19, 1075 – 1080. DOI: 10.1002/cphc.201701380.

The contributions of the co-authors are as follows:

- Prof Subodh Mhaisalkar and Assoc Prof Nripan Mathews provided the direction for the experiment.
- I co-designed and carried out the experiments with Dr Natalia Yantara.
- Dr Mingjie Li and Dr Teck Wee Goh designed and executed the PLQY, TRPL and XPS spectroscopic measurements.
- Mr Krishnamoorthy Thirumal assisted in the PESA measurement and analysis.
- Mr Yan Fong Ng assisted in the PeLED device fabrication process
- Prof Tze Chien Sum and Assoc Prof Cesare Soci assisted in the data collection and data analysis.
- I wrote the manuscript which was vetted by Dr Natalia Yantara.

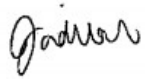

Chapter 5 is published as Nur Fadilah Jamaludin, Natalia Yantara, Yan Fong Ng, Annalisa Bruno, Bevita K. Chandran, Xin Yu Chin, Krishnamoorthy Thirumal, Nripan Mathews, Cesare Soci and Subodh Mhaisalkar, Perovskite templating via a bathophenanthroline additive for efficient light-emitting devices. *J. Mater. Chem. C*, **2018**, 6, 2295 –2302. DOI: 10.1039/C7TC05643E.

The contributions of the co-authors are as follows:

- Prof Subodh Mhaisalkar and Assoc Prof Nripan Mathews provided the direction for the experiment.
- Dr Natalia Yantara and I co-designed and executed the experiments.
- Dr Annalisa Bruno, Dr Xin Yu Chin and Assoc Prof Cesare Soci carried out the TRPL and FTIR measurements and analysis.
- Mr Krishnamoorthy Thirumal assisted in the PESA measurement and analysis
- Dr Bevita K. Chandran ran the thin film XRD experiment and analysis.
- Mr Yan Fong Ng assisted in the PeLED device fabrication and data analysis.
- I wrote the manuscript which was vetted by Dr Natalia Yantara.

19 August 2019
. . . . . . . . . . . . . . . . .
Date

. . . . . . . . . . . . . . . . . . . . . . . . . . . .
Nur Fadilah Jamaludin

# Abstract

Metal halide perovskites (MHPs) have garnered extensive attention from the scientific community since its inception as a light harvester in 2009. With a general formula of $ABX_3$, where the monovalent A-site cation is surrounded by four corner-sharing $BX_6$ metal halide octahedra, solar cells based on this material (PSCs) have shown remarkable efficiencies owing to their superior optoelectronic properties. Research on MHP-based LEDs (PeLEDs) has made tremendous progress following early reports on light emission in 2014, with current state-of-the-art devices exhibiting external quantum efficiencies exceeding 20%. However, industrialization of PeLED is not without challenges, with performance, reliability, and scalability; all contingent towards advancing the fundamental understanding of these materials and their light-emitting characteristics.

Ideally, for effective light emission, high radiative recombination rate is required and can be achieved through either (a) suppression of non-radiative recombination or (b) improvements to radiative recombination via charge carrier confinement. The tendency for non-radiative recombination to precede radiative recombination leads to the mediocre efficiencies seen at low driving voltages, underscoring the importance of remedying defects. Radiative recombination can be enhanced through employment of an energetic landscape, where structural modulation of the emitter facilitates efficient light generation via a process termed as energy cascade. Such a landscape is obtained through the templated formation of quasi-2D MHPs, where on injection of charge carriers into higher band gap domains, the charge transfer to the energetically favoured lowest band gap domains ensures increased charge carrier concentration and efficient emission.

This thesis is focused on enhancing radiative recombination through materials processing techniques for defect alleviation as well as via engineering an energetic landscape for mitigation of non-radiative losses and efficient bimolecular radiative recombination through charge carrier localization. Though necessary for solvent removal, annealing also accelerates film degradation due to the formation of under-coordinated surface atoms; and a post-deposition treatment that results in an enhancement to the device performance, was

developed. Reduced grain size is an effective way to increase spatial confinement of charge carriers and boost radiative recombination; however, the accompanying effect of increasing grain boundary density needs to be contained. An additive engineering technique that introduces a small organic molecule during processing, forming small passivated grains thus promoting radiative recombination, was effectively devised.

Efforts to improve efficiency of PeLEDs have been hampered by low exciton binding energies, moisture instability and tendency for light degradation. Layered (2D) MHPs, offering superior ambient stability and high exciton binding energies were introduced to form mixed-dimensional MHPs. The notable increase in performance of these MHPs stem from the formation of multiple domains of varying band gaps, creating an energetic landscape, whereby charge carriers undergo an energy cascade from larger band gap domains to the energetically favoured lower band gap domains. The rapid energy transfer process circumvents non-radiative recombination in the larger band gap domains, resulting in confinement of charge carriers in the lowest band gap domains which not only overwhelm the defect states, but also facilitate highly efficient photon generation. Translating these design principles into practice necessitates the implementation of new processes and rational selection of molecular moieties that engineer mixed-dimensionality in the MHPs. While the energy cascade phenomenon has been demonstrated for red and green emissions, this challenge is accentuated for blue emission, where charge carrier funneling to the smallest band gap domains needs to be countered. A protocol to influence the crystallization kinetics and to regulate the formation of pure 2D domains was developed to yield record efficiencies and spectrally stable blue emission.

To summarize, the work presented in this thesis is centered on managing defects and designing an energetic landscape that favours radiative recombination. A combination of prudent molecular additive selection, process design, and fine tuning of a mono-halide material system enable both defect passivation and effective energy cascade to be achieved. This mitigation of non-radiative recombination process and improved photon generation due to charge carrier localization boosted emission; highlight the importance of defect management and process design for high performance PeLEDs.

# Lay Summary

The world energy consumption continues to rise, driven by the need for increasing growth and standards of living, fueling the demand for energy. Of the numerous electricity end users, artificial lighting is singularly one of the highest; accounting for a fifth of the world's total energy output. The reason for this lies in the significant wastage of energy for lighting purposes, which highlights the need for development of more efficient illumination technologies such as OLEDs. However, despite the high energy savings and wide-ranging applications offered, the high manufacturing cost of OLEDs renders it impractical for large scale production. This creates opportunities for the development of newer lighting concepts capable of providing higher efficiencies at lower production cost. Metal halide perovskites (MHPs) have garnered extensive attention from the scientific community since it was first reported as a solar cell absorber material in 2009. Over the past decade, with efficiencies reaching 25.2%, perovskite solar cells (PSCs) have now established themselves as a strong contender for industrialization, with efficiencies in the range of multi-crystalline silicon solar cells. Subsequently, research on perovskite LEDs (PeLEDs) has made tremendous progress with best-in-class devices exhibiting efficiencies exceeding 20%, putting them on par with current state-of-the-art OLEDs. However, commercialization of PeLED is not without its challenges, with fundamental understanding of the correlation between the materials' processing and desired properties still required for efficiency to improve further. For effective light generation, defect suppression and enhanced probability of light generating process termed as radiative recombination, are needed. The tendency for defect filling to precede radiative recombination leads to the mediocre efficiencies seen at low voltages. Radiative recombination can be enhanced through structural modulation of the MHP phases that funnels charge carriers to facilitate efficient light generation via a process termed as energy cascade. This thesis is thus focused on defect management in PeLEDs through materials processing techniques such as post-deposition treatment and additive engineering for defect alleviation as well as via process engineering to control the MHP structural diversity so as to facilitate enhanced light emission.

# Acknowledgements

The author would like to first and foremost extend her deepest appreciation to her supervisor, Professor Subodh Mhaisalkar, for providing her not just with the opportunity to pursue this journey but also for never denying her chemical purchase request regardless of the cost. The author feels blessed to be under the tutelage of a forward-thinking supervisor, whose drive for innovative, cutting-edge research has never failed to inspire her. Moreover, the unlimited access to state-of-the-art research facilities in ERI@N and opportunities for collaborative interactions with world renowned research groups, have contributed immensely towards her research journey.

The author cannot begin to express her appreciation to Associate Professor Nripan for his guidance and feedback on her research, not to mention the different perspectives he provides to towards data analysis, encouraging the author to think critically of her work. The author would also like to portray her gratitude to her co-supervisor, Associate Professor Cesare Soci, for the meaningful discussions held over the author's research.

To Dr Natalia Yantara, the author extends her heartfelt gratitude for her patience and selflessness in imparting skills and knowledge. The author is especially touched by her 'mothering' and sincerely hopes that every PhD student is as fortunate as she is to have someone to run to for guidance and assistance (read: HELP!) when trouble strikes. Needless to say, the author is beyond honoured to be mentored by a knowledgeable and dedicated researcher, whom the author strongly believes is one of the best that the institute has to offer.

The author would like to express her thanks to Dr Chin Xin Yu for his significant efforts in streamlining the experimental processes – be it in terms of device fabrication or data analysis. Not to mention, the wide-ranging topics discussed which have left an indelible impression on the author.

The author would also like to thank members of the perovskite LED team, many of whom have come and gone since the author started her PhD ): Despite the countless confusing graphs and results the author presented during the weekly meetings, the author is humbled that the group members have always offered constructive feedback which not only enabled the author to further improve on her research direction, but also on her communication skills.

The author wishes to express her thanks to Dr Annalisa Bruno for her constant guidance and advice pertaining to photophysical characterization. Dr Annalisa Bruno's dedication to research and her curiosity towards the unknown have not only enabled the design of intriguing experiments of which the author is fortunate enough to partake in but also facilitated the author's fundamental understanding of perovskite.

The author's soundboard and cheerleader when the going gets tough, fellow luminescent comrade Yan Fong, what will the author do without you? Thank you for being the light at the end of the tunnel – bright and unwavering, a beacon of hope for the lost soul (read: the author).

To fellow PhD students who matriculated together with the author; Yan Fong, Xintong, Benny, Mohit, Naveen, Ankit and Harikesh, the author would like to say – thank you for the support throughout this journey. We did it!

The author would also like to express her sincere gratitude to the ERI@N and IGS staff who have assisted in ensuring the smooth progress of the author's journey. The author acknowledges the financial support provided by NTU, IGS, ERI@N and the NRF. Last but not least, the author would like to dedicate her thesis to her parents and siblings, to thank them for their boundless love, encouragement and support, without which the author would (confirm plus chop) not be able to attend weekly 8.30 am meetings nor complete her thesis with her sanity still intact.

# Table of Contents

**Abstract** i

**Lay Summary** iii

**Acknowledgements** v

**Table of Contents** vii

**Table Captions** xiii

**Figure Captions** xv

**Abbreviations** xxiii

**Chapter 1** 1

**Introduction** 1

**1.1 Background and Motivation** ..... **2**

**1.2 Challenges for High Performance PeLEDs and Gap Analysis** ..... **5**

**1.3 Objective and Scope** ..... **6**

1.3.1 Passivation of surface defects in MHPs 7

1.3.2 Investigations into energy cascade process and design of organic spacer molecules (2D cations) for mitigation of non-radiative recombination losses 8

1.3.3 Effect of organic spacer molecules and A-site cations for efficient and spectrally stable blue emission 8

**1.4 Dissertation Overview** ..... **9**

**1.5 Findings and Outcomes/Originality** ..... **10**

1.5.1 Establishing the importance of defect passivation during film processing for PeLEDs 10

1.5.2 Demonstrating the effect of molecular design on the effectiveness of 2D cation in engineering the formation of an efficient energetic landscape for mixed-dimensional MHP emitters 11

1.5.3 Validating the need for control over the distribution of mixed-dimensional domains in an energetically engineered landscape for spectrally stable blue emission 12

**References** 13

**Chapter 2** 17

**Literature Review** 17

**2.1 Organic Light Emitting Diodes** ..... **18**
2.1.1 Device architecture 18
2.1.2 Working principle 21
2.1.3 Performance metrics for OLEDs 22
2.1.4 Disadvantages of OLEDs 25

**2.2 Metal Halide Perovskites for Light Emission** ..... **25**
2.2.1 Three-dimensional metal halide perovskites 25
2.2.2 Lower dimensional metal halide perovskites 29
2.2.3 Colour tunability 31

**2.3 Perovskite-based Light Emitting Diodes (PeLEDs)** ..... **33**
2.3.1 Device architecture 33
2.3.2 Optical and electrical losses in PeLEDs 34

**2.4 Defects in Halide Perovskites** ..... **35**
2.4.1 Effect of defects on PeLED characteristics 36
2.4.2 Influence of defects on stability of MHPs and PeLEDs 37

**2.5 Managing Defects in MHPs** ..... **38**
2.5.1 Passivation of defects 39
2.5.2 Energy cascade for mitigation of non-radiative recombination losses 39

**2.6 Challenges** ..... **40**

**References** 42

**Chapter 3** 53

**Experimental Methodology** 53

**3.1 Material Synthesis** ..... **54**
3.1.1 Molecular design of two-dimensional perovskite cation for energy cascade 54

**3.2 Film Fabrication** ..... **55**
3.2.1 Passivation of surface defects through post-deposition treatment 55
3.2.2 Additive engineering for suppression of grain size modulated defects 55
3.2.3 Molecular design of two-dimensional perovskite cation for energy cascade 55
3.2.4 Tailoring the distribution and spread of m domains for stable blue emission 56

**3.3 Device Fabrication** ..... **56**

**3.4 Physical Characterization Techniques** ..... **57**
3.4.1 Field emission scanning electron microscopy (FESEM) 57
3.4.2 X-ray diffraction (XRD) 58
3.4.3 Ultraviolet-visible (UV-Vis) spectroscopy 61

3.4.4 Nuclear Magnetic Resonance (NMR) spectroscopy 64
3.4.5 Photoluminescence (PL) spectroscopy 66
3.4.6 Transient PL spectroscopy 67
3.4.7 Transient Absorption (TA) spectroscopy 69
3.4.8 PL Quantum Yield (PLQY) 71

**3.5 Electrical Characterization Technique ..... 72**

**References 74**

**Chapter 4 77**

**Passivation of surface defects through post-deposition treatment 77**

**4.1 Introduction ..... 78**

**4.2 Results and Discussion ..... 80**
4.2.1 Crystal structure and phase analysis 80
4.2.2 Photophysical properties 83
4.2.3 Morphological analysis 89
4.2.4 Phase distribution analysis 92
4.2.5 Eliminating solvent effect on film properties 93
4.2.6 Correlating film properties with PeLED performance 93
4.2.7 Eliminating influence of film thickness on PeLED performance 95

**4.3 Conclusion ..... 96**

**References 97**

**Chapter 5 101**

**Additive engineering for suppression of grain size modulated defects 101**

**5.1 Introduction ..... 102**

**5.2 Results and Discussion ..... 102**
5.2.1 Phase and crystal structure analysis 103
5.2.2 Photophysical properties 104
5.2.3 Morphological analysis of Bphen-incorporated films 109
5.2.4 Electrical characterization of additive incorporated films 114
5.2.5 Effect of type of additive used 118
5.2.6 Effect of electron transporting material selection on PeLED performance 120

**5.3 Conclusion ..... 122**

**References 123**

**Chapter 6** 127

**Molecular design of two-dimensional perovskite cation for energy cascade** 127

**6.1 Introduction** ..... **128**

**6.2 Results and Discussion** ..... **129**
6.2.1 Crystal structure and phase analysis of pure 2D perovskite single crystals 129
6.2.2 Crystal structure and phase analysis of pure 2D perovskite thin films 132
6.2.3 Photophysical characteristics of pure 2D perovskite thin films 133
6.2.4 Crystal structure and phase analysis of mixed-dimensional perovskites 134
6.2.5 Photophysical characteristics of mixed-dimensional perovskites 135
6.2.6 Electrical characteristics of mixed-dimensional perovskites 140
6.2.7 Morphological analysis of mixed-dimensional perovskites 142

**6.3 Conclusion** ..... **143**

**References** 145

**Chapter 7** 149

**Tailoring the distribution and spread of m domains for stable blue emission** 149

**7.1 Introduction** ..... **150**

**7.2 Results and Discussion** ..... **151**
7.2.1 Proposed growth mechanism of intermediate mixed-dimensional perovskite domains 153
7.2.2 Crystal structure and phase analysis of mixed-dimensional MHP films 154
7.2.3 Photophysical characteristics of mixed-dimensional perovskite films 155
7.2.4 Influence of A-site cation substitution on morphology 159
7.2.5 Electrical characterization of RP PeLEDs based on different A-site cations 161
7.2.6 Influence of A-site, B-site and L-cations ratios on RP film properties 164
7.2.7 Electrical characterization of RP-Cs-based PeLEDs with varying precursor stoichiometry 166
7.2.8 Device and film stability 170

**7.3 Conclusion** ..... **173**

**References** 174

**Chapter 8** 177

**Conclusion and Future Work** 177

**8.1 Contribution and Summary of Work** ..... **178**
8.1.1 Passivation of surface defects through post-deposition treatment 178
8.1.2 Additive engineering for suppression of grain size modulated defects 179
8.1.3 Molecular design of two-dimensional perovskite cation for energy cascade 179

8.1.4 Tailoring the distribution and spread of m domains for stable blue emission 180

**8.2 Overall Conclusion....181**

**8.3 Future Work and Possible Directions ....184**
8.3.1 Merging defect passivation with energy cascade 184
8.3.2 Graded emitter for high efficiency PeLEDs 187
8.3.3 White light emission for lighting applications 188

**References 190**

**List of Publications 191**

# Table Captions

**Table 1.1 Comparison of performance metric across various lighting technologies[6]. 2**

**Table 4.1 PLQY values of reference and TEABr treated films ..... 84**

**Table 4.2 Summary of transient PL decay lifetime for reference and TEABr treated films ..... 89**

**Table 5.1 Exciton binding energy and optical band gap energy of reference and BPhen-incorporated films obtained by Elliot's fitting of the absorbance spectra .. 107**

**Table 5.2 Summary of the PL decay lifetimes of reference and BPhen-incorporated films ..... 109**

**Table 5.3 Summary of electron mobility values for the various electron transporting materials used ..... 122**

**Table 6.1 Summary of $\Delta d$, $\lambda_{oct}$ and $\sigma_{oct}^2$ of pure 2D $(PEA)_2PbBr_4$, (PyrEA)$PbBr_4$ and (ImEA)$PbBr_4$ obtained from single crystal analysis ..... 131**

**Table 7.1 Comparison of fabricated device performance with state-of-the-art blue PeLEDs..... 172**

# Figure Captions

**Figure 1.1 (a) The crystal structure of $ABX_3$ perovskite[13]. Working mechanisms of a (b) PSC[14] and (c) PeLED[15]. (d) The wide-ranging emission spectrum achievable through halide composition variation[16]. (e) Examples of device architectures typically adopted for PeLEDs[17]..... 4**

**Figure 1.2 (a) Schematic on trap and band-state filling processes[27]. (b) Examples of commonly used 2D organic spacer molecules. Schematic of (c) dimensionality tuning[28] and (d) energy transfer from high band gap to low band gap domains[23]. (e) Typical performance metric for PeLED[29]..... 5**

**Figure 2.1 Examples of applications of the OLED technology[2-5]..... 18**

**Figure 2.2 Evolution of OLED architecture over the years to improve device efficiency and stability[7] ..... 19**

**Figure 2.3 OLED device architecture[8] ..... 20**

**Figure 2.4 Schematic of electroluminescence process occurring in an OLED device[6] ..... 22**

**Figure 2.5 Human eye response function as a function of wavelength[11] ..... 24**

**Figure 2.6 Crystal structure of a typical oxide perovskite[13] ..... 25**

**Figure 2.7 (a) Planar view (001) of metal halide perovskite. (b) Tolerance and octahedral factor variation on substitution of A-site and B-site cation respectively for chloride-, bromide- and iodide-based perovskites[18] ..... 27**

**Figure 2.8 Possible doping elements for the A-, B- and X-sites of the perovskite structure and their influence on material properties[18] ..... 28**

**Figure 2.9 Proposed routes for increasing exciton confinement to promote radiative recombination[29]. ..... 29**

**Figure 2.10 Schematic of mixed-dimensional perovskites where incorporation of organic spacer molecules results in the destruction of the 3D metal-halide network and the formation of characteristic 2D layered structure[38] ..... 31**

**Figure 2.11 Tuning of PL emission through halide-mixing[46] ..... 32**

**Figure 2.12 Evolution of (left) EQE and (right) luminance of PeLEDs over the years as compared to OLEDs and quantum dot LEDs (QLEDs)[50] ..... 33**

**Figure 2.13 Schematic of a PeLED device architecture ..... 34**

**Figure 2.14 Schematic of electrical loss mechanisms in PeLED devices[64] ..... 35**

**Figure 2.15 Schematic of deep traps and shallow traps present in defect intolerant and defect tolerant systems respectively[67] ..... 36**

**Figure 2.16 Schematic of the electron-hole recombination processes occurring within MHPs at different carrier density regimes[29] ..... 37**

**Figure 3.1 Components of Field Emission Scanning Electron Microscope[3] ..... 57**

**Figure 3.2 Types of signal obtained from electron-sample interaction[2] ..... 58**

**Figure 3.3 Schematic of X-ray interaction with crystal planes to produce diffraction pattern[4] ..... 59**

**Figure 3.4 Bragg-Brentano geometry of diffractometer[4] ..... 60**

**Figure 3.5 An example of XRD pattern obtained from a polycrystalline powder sample[4] ..... 60**

**Figure 3.6 Components of UV-Vis spectrophotometer[6] ..... 62**

**Figure 3.7 An example of a typical absorbance spectrum[5] ..... 63**

**Figure 3.8 Effect on nucleus on application of external magnetic field[7] ..... 64**

**Figure 3.9 Spin coupling effect on interacting with other nuclei in the vicinity of nucleus of interest[7] ..... 65**

**Figure 3.10 Jablonski energy diagram showcasing the various electron transition on light absorption[8] ..... 66**

**Figure 3.11 Components in a photoluminescence spectrometer[10] ..... 67**

**Figure 3.12 Components in a streak camera[12] ..... 68**

**Figure 3.13 Schematic diagram of the experimental set up for TRPL spectroscopy[13] ..... 69**

**Figure 3.14 Schematic of a transient absorption measurement set up[14] ..... 70**

**Figure 3.15 Schematic of photon collection during PLQY measurement[16] ..... 71**

**Figure 3.16 Schematic of PeLED electrical measurement set up[17] ..... 72**

**Figure 4.1 Schematic of the post-deposition treatment process of $MAPbBr_3$ with TEABr ..... 78**

**Figure 4.2 XRD patterns of the reference and TEABr-treated films ..... 80**

**Figure 4.3 NMR spectra of reference (top) and 10mg $ml^{-1}$ TEABr-treated (bottom) films. Characteristic peaks corresponding to TEABr are indicated in red in the bottom figure. ..... 82**

**Figure 4.4 (a) Absorbance, normalized PL and (b) excitation spectra of reference and TEABr treated films ..... 84**

**Figure 4.5 (a) XPS spectra for reference and 20 mg $ml^{-1}$, and the analysis at (b) Pb 4f, (c) Br 3d, (d) C 1s, and (e) N 1s positions ..... 85**

**Figure 4.6 Valence band and band gap determination for (a) reference, (b) 10, (c) 15 and (d) 20 mg $mL^{-1}$ TEABr treated films. (f) Schematic of the conduction and valence band energy levels ..... 87**

**Figure 4.7 Transient PL decay for reference and TEABr treated films ..... 88**

**Figure 4.8 Top and cross-sectional view of the reference and TEABr treated samples ..... 90**

**Figure 4.9 Grain thickness and PLQY as a function of TEABr concentration ..... 91**

**Figure 4.10 Backscattered electron image of the reference and TEABr treated films ..... 92**

**Figure 4.11 Surface morphology of films (a) untreated and (b) IPA-treated films .. 93**

**Figure 4.12 (a) Architecture of fabricated device. (b) Current density and luminance against voltage, (c) current efficiency and external quantum efficiency against**

**voltage and (d) electroluminescence spectra of the reference and TEABr treated films ..... 94**

**Figure 4.13 (a) Current density and luminance against voltage and (b) current efficiency against voltage for 1 M (reference) and 1.2 M films ..... 95**

**Figure 5.1 XRD pattern of films prepared with varying amounts of Bphen in the anti-solvent ..... 103**

**Figure 5.2 FTIR spectra of reference and BPhen-incorporated films ..... 104**

**Figure 5.3 Absorbance and PL spectra of reference and BPhen-incorporated films ..... 105**

**Figure 5.4 PL peak fitting of reference and BPhen-incorporated films ..... 105**

**Figure 5.5 Elliot fitting of reference and BPhen-incorporated films to derive band gap and exciton binding energy values ..... 106**

**Figure 5.6 Schematic diagram on the change in emitter valence and conduction band levels of reference and BPhen-incorporated films ..... 107**

**Figure 5.7 PL decay lifetimes of reference and BPhen-incorporated films ..... 108**

**Figure 5.8 Top and cross-sectional image of reference and BPhen-incorporated films ..... 110**

**Figure 5.9 Surface roughness analysis of reference and BPhen-incorporated films ..... 112**

**Figure 5.10 Graph of surface roughness as a function of Bphen concentration ..... 113**

**Figure 5.11 (a) Current density and luminance against voltage, (b) current efficiency against current density and (c) EQE against luminance curves. (d) EL spectra of devices prepared from reference and BPhen-incorporated films ..... 114**

**Figure 5.12 Statistical representation of the performance metric of 50 devices ..... 116**

**Figure 5.13 Current density against voltage of hole-only devices of reference and BPhen-incorporated films ..... 117**

**Figure 5.14 Comparison of PL emission spectra of films incorporated with different molecules ..... 118**

**Figure 5.15 (a) Current density and luminance against voltage as well as (b) current efficiency against current density of Bphen, TPBi and PBD incorporated devices 119**

**Figure 5.16 Molecular structures of Bphen, TPBi and PBD ..... 119**

**Figure 5.17 Energy diagram of Bphen incorporated emitter and the various alternative electron transporting material used ..... 120**

**Figure 5.18 PeLED performance on substitution on electron transporting material. (a) Current density and luminance against voltage as well as (b) current efficiency against current density for 0.500 mg ml$^{-1}$ Bphen. ..... 121**

**Figure 6.1 Molecular structure of (a) $PEA^+$, (b) $PyrEA^{2+}$ and (c) $ImEA^{2+}$ cations. 129**

**Figure 6.2 Crystal structure of pure (a) $(PEA)_2PbBr_4$, (b) $(PyrEA)PbBr_4$ and (c) $(ImEA)PbBr_4$ ..... 130**

**Figure 6.3 Simulated and thin film XRD patterns of pure 2D (a) $(PEA)_2PbBr_4$, (b) $(PyrEA)PbBr_4$ and (c) $(ImEA)PbBr_4$ ..... 132**

**Figure 6.4 (a) Absorbance and steady state photoluminescence of pure $(PEA)_2PbBr_4$ thin films as well as $(PyrEA)PbBr_4$ and $(ImEA)PbBr_4$ single crystals. (b) Transient photoluminescence decay of $(PEA)_2PbBr_4$ and $(PyrEA)PbBr_4$ films. ..... 133**

**Figure 6.5 XRD patterns of 2D3D (a) PEA, (b) PyrEA and (c) ImEA as compared to pure 3D FA and their respective 2D perovskites as well as (d) relative to each other. ..... 134**

**Figure 6.6 (a) Absorbance and normalized photoluminescence spectra and (b) static photoluminescence spectra in logarithmic scale for 2D3D PEA, PyrEA and ImEA ..... 135**

**Figure 6.7 Photoluminescence excitation spectra of 2D3D PEA, PyrEA and ImEA ..... 137**

**Figure 6.8 Transient photoluminescence decay lifetimes ($\lambda_{exc}$ = 405 nm) of 2D3D PEA, PyrEA and ImEA ..... 138**

**Figure 6.9 Photoluminescence intensity as a function of pump fluence of 2D3D PEA, PyrEA and ImEA ..... 139**

**Figure 6.10 (a) Current density and luminance against voltage curves, (b) EQE against luminance, (c) normalized EL spectra at peak luminance, (d) normalized EL spectra at various voltage application for 2D3D PEA, 2D3D PyrEA and 2D3D ImEA. ..... 140**

**Figure 6.11 Top and cross-sectional SEM images of 2D3D PEA, PyrEA and ImEA spin coated on PEDOT: PSS coated ITO, with inset showcasing top view of samples prepared on glass. ..... 142**

**Figure 7.1 (a) Variation in distribution of intermediate mixed-dimensional MHP domains on introduction of low solubility A-site cation and excess of organic spacer molecule and (b) the schematic of the anti-solvent treatment process, enabling narrow intermediate mixed-dimensional MHP distribution to be attained. ..... 152**

**Figure 7.2 Schematic of film growth process on introduction of A-site cations of varying bulk solubility ..... 153**

**Figure 7.3 XRD patterns of pure $PBA_2PbBr_4$, RP-FA, RP-MA and RP-Cs. ..... 154**

**Figure 7.4 Absorbance and PL of RP-FA, RP-MA and RP-Cs films which are prepared (a) with and (b) without the anti-solvent process ..... 155**

**Figure 7.5 Absorbance and PL spectra of RP-Cs (PEABr) prepared with and without anti-solvent process ..... 157**

**Figure 7.6 Transient absorption spectra of (a) RP-FA, (b) RP-MA and (c) RP-Cs. (d) The kinetics of photo-bleaching in RP-Cs. ..... 158**

**Figure 7.7 Transient photoluminescence decay of RP-Cs. (a) PL decay profile of RP-Cs and (b) rise time comparison at probed wavelengths of 465 nm, 475 nm and 485 nm. ..... 159**

**Figure 7.8 Topological mapping of (a) RP-FA, (b) RP-MA and (c) RP-Cs for roughness analysis (left column), surface morphology (middle column) and thickness verification (right column). ..... 160**

**Figure 7.9 Energy band alignments of the various layers in a PeLED device..... 161**

**Figure 7.10 (a) Current density-luminance against voltage curves, (b) EQE against luminance and (c) electroluminescence spectra taken at various voltages for RP-FA, RP-MA and RP-Cs. ..... 162**

**Figure 7.11 Normalized (a) PL spectra of RP-Cs prepared with and without anti-solvent process and (b) EL spectra for RP-Cs prepared without anti-solvent process ..... 163**

**Figure 7.12 (a) Absorbance and (b) normalized PL spectra on varying PBA/Pb and PBA/Cs ratios in the precursor solution. ..... 164**

**Figure 7.13 The corresponding positions of the PL with varying PBA/Pb and PBA/Cs on the CIE chart ..... 165**

**Figure 7.14 (a) Current density – luminance against voltage curves, (b) EQE as a function of luminance curves, (c) normalized EL spectra and (d) photos of device under operation for PBA/Pb (PBA/Cs) ratios of 1.67 (5.0), 1.67 (3.3), 1.50 (2.5) and 1.33 (2.0) respectively. ..... 166**

**Figure 7.15 Current density – luminance against voltage for PBA/Pb ratios of (a) 1.7, (c) 1.5 and (e) 1.3. EQE as a function of luminance for PBA/Pb ratios of (b) 1.7, (d) 1.5 and (f) 1.3. ..... 168**

**Figure 7.16 EL stability of various PBA/Pb and PBA/Cs ratios at different voltages ..... 169**

**Figure 7.17 (a) Normalized luminance as a function of time and (b) the spectral stability of device 6, corresponding to PBA/Pb and PBA/Cs ratios of 1.50 and 2.5 respectively..... 170**

**Figure 7.18 Film stability on exposure to continuous light illumination for 30 min171**

**Figure 8.1 Device performance of mixed-dimensional perovskite based on FA-PEA with post deposition treatment of trioctylphosphine oxide.[3] (a) Device architecture, (b) summary of device data and (c) luminance and current efficiency against voltage plots. ..... 186**

**Figure 8.2 An example of a graded emitter structure in an inorganic LED.[5] ..... 188**

**Figure 8.3 CIE spectrum showcasing the emission combination allowing for white light emission[6] ..... 189**

# Abbreviations

| | |
|---|---|
| CIE | Commission Internationale de l'Eclairage |
| EL | Electroluminescence |
| EQE | External Quantum Efficiency |
| LED | Light Emitting Diodes |
| MHP | Metal Halide Perovskites |
| PeLED | Perovskite-based Light Emitting Diode |
| PL | Photoluminescence |
| PLQY | Photoluminescence Quantum Yield |
| 3D | Three-dimensional |
| 2D | Two-dimensional |
| SEM | Scanning Electron Microscopy |
| XRD | X-ray Diffraction |

# Chapter 1

# Introduction

*The introduction provides the background and motivation of research into new illumination concepts beyond antecedent lighting technologies such as LEDs and OLEDs. The objective of the thesis is on the management of bulk and surface defects in perovskite-based light emitting devices, which will be explored through processing-induced defect modulation techniques and mitigation of non-radiative losses via the engineering of an energetic landscape aimed towards enhancing bimolecular recombination process for efficient photon generation. The thesis organization is detailed in the dissertation overview and this section concludes with the major findings from this research work.*

## 1.1 Background and Motivation

The world's energy consumption is on a continuous rise, driven by the growing demand for energy. In the year ending 2018, primary energy consumption grew by 2.9% despite increasing societal awareness and demands for immediate action on climate change. Of the numerous electricity end users, artificial lighting is singularly one of the highest; accounting for a fifth of the world's total energy output.[1] However, not all is utilized for light emission. In a finding by the International Energy Agency, the potential electricity savings from indoor lighting by 2030 could be equivalent to Africa's total electricity consumption in 2013.[2] The significant wastage of energy for lighting purposes highlights the need for development of more efficient illumination technologies. The advent of light-emitting diodes (LEDs), both inorganic and organic, has brought great progress to the lighting industry since the invention of the lightbulb.[3] Light emission in LEDs occurs when injected electrons and holes, recombine radiatively in a process known as electroluminescence.[4] Fundamentally different from existing illumination technologies, it boasts excellent performance in various aspects such as luminous efficiency, lifetimes and reliability,[5] proving to be a good substitute for traditional light sources. Table 1.1 is a comparison of performance metric across the various lighting technologies.

**Table 1.1** Comparison of performance metric across various lighting technologies[6]

| BC hydro powersmart | | TRADITIONAL TECHNOLOGY | COMPARING TODAY'S AVAILABLE LIGHTING TECHNOLOGIES | | |
|---|---|---|---|---|---|
| | | Incandescent | Halogen | Compact Fluorescent (CFL) | Light Emitting Diode (LED) |
| | |  |  |  |  |
| FEATURES | ENERGY EFFICIENCY | Very Low | Low | High | Very high |
| | LIGHT COLOR OR "TEMPERATURE" | Warm | Warm | Options range from Warm to Cool | Options range from Warm to Cool |
| | DIMMABILITY | Full Range | Full Range | Partial Range (special dimming CFLs available) | Partial Range (special dimming LEDs available) |
| LIGHT OUTPUT * (IN LUMENS) | 400-500 | 40W | 28-29W | 9W-11W | 9W |
| | 800-1000 | 60W | 41-43W | 13W-16W | 12.5W |
| | 1100-1300 | 75W | 51-53W | 18W-20W | Currently unavailable |
| | 1600-1800 | 100W | 70-72W | 23W-27W | |
| ESTIMATED OPERATING COST PER LAMP (BULB) | LIFE SPAN ** | 1,000 hours (Approx. one year) | 3,000 hours (Approx. three years) | 8,000 hours (Approx. 8 years) | 25,000 hours (Approx. 25 years) |
| | ANNUAL ENERGY COST *** | Approx. $5.75 | Approx. $4.25 | Approx. $1.50 | Approx. $1.25 |

Despite the high energy savings and wide-ranging applications offered by LED technology such as in the field of lighting and displays, the high manufacturing cost associated with use of expensive precursor materials, need for vacuum-based processing and epitaxial film growth,[7] renders it impractical for large scale production. This creates opportunities for the development of new lighting concepts capable of providing higher efficiencies at lower production cost.

Metal halide perovskites (MHPs) have garnered extensive attention from the scientific community since its inception as a light harvester in 2009. With a general formula of $ABX_3$, where the monovalent A-site cation is surrounded by four corner-sharing $BX_6$ metal halide octahedras ($A = CH(NH_2)_2^+$, $CH_3NH_2^+$ or $Cs^+$, $B = Pb^{2+}$, $Sn^{2+}$, $Cu^{2+}$ or $Ge^{2+}$ and $X = Cl^-$, $Br^-$ or $I^-$)[8] (Figure 1.1 (a)), solar cells based on this material (PSCs) have shown remarkable efficiencies owing to their superior optoelectronic properties such as high absorption coefficients, low defect densities and long carrier diffusion lengths.[8-10] It is thus unsurprising that not only has MHP been touted as an emerging light harvesting material but has also managed to ease its way into applications beyond photovoltaics. The rapid scale of research on this wonder material has enabled several key factors for development of highly efficient PSCs to be established. These include but are not restricted to large columnar grains, low grain boundary and defect densities. However, the question as to whether the same requirements are needed for non-photovoltaic related applications, still remains.

The strong correlation between the Shockley-Queisser limit and external luminescence efficiency suggests that good light harvesters are potentially good radiators.[11-12] This catalyzes MHPs' rapid shift from being a miracle material for photovoltaics to an extraordinary semiconductor for light emission. Albeit different from the working mechanism of a solar cell where sunlight is converted to electricity (Figure 1.1 (b)), in an LED, MHP transforms electricity into light (Figure 1.1 (c)), with an energy equivalent to its band gap. The high colour purity and photoluminescence quantum yield (PLQY) afforded by MHP emitters present it as an attractive alternative to organics for lighting and display applications. The flexibility of tuning the emission wavelength through halide

variation too provides an opportunity for a wide palette of colours to be achieved (Figure 1.1 (d)).

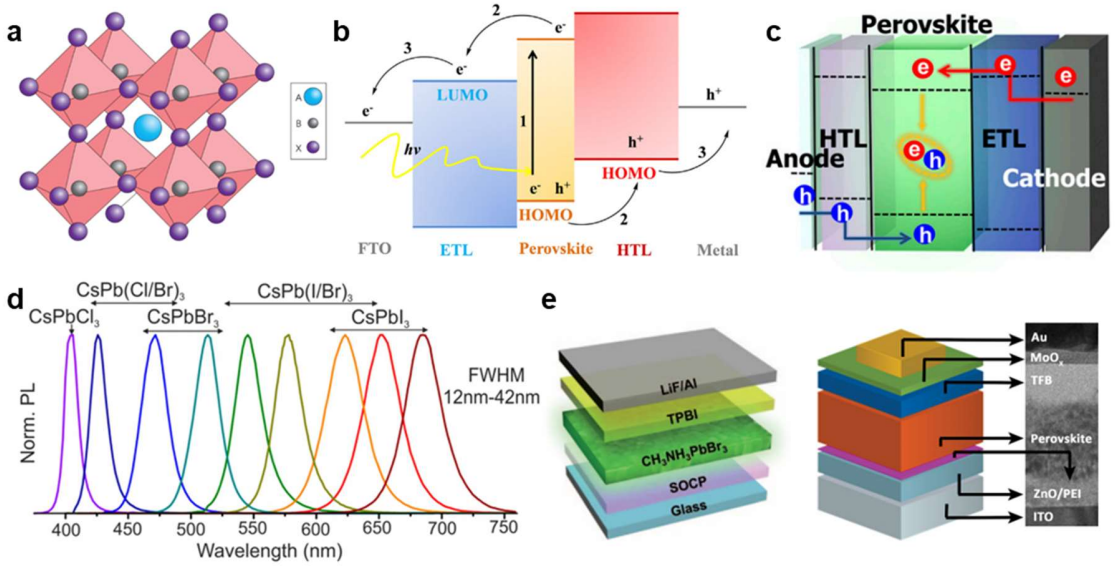


**Figure 1.1** (a) The crystal structure of $ABX_3$ perovskite[13]. Working mechanisms of a (b) PSC[14] and (c) PeLED[15]. (d) The wide-ranging emission spectrum achievable through halide composition variation[16]. (e) Examples of device architectures typically adopted for PeLEDs[17]

Research in the field of metal halide perovskite-based LEDs (PeLEDs) has made tremendous progress following the first fabricated device[18] where the MHP emitter ($CH_3NH_3PbBr_3$), sandwiched between hole transporting (PEDOT:PSS) and electron transporting (F8) layers attained a maximum luminance of 364 cd $m^{-2}$ and a current efficiency of 0.3 cd $A^{-1}$. Numerous attempts have since been made to further the device efficiency. This include modifications to the interfacial charge transport layers[19-20] to promote balanced charge injection into the emitter and engineering the energy landscape of the emitter to facilitate bimolecular radiative recombination.[21-23] The current state-of-the-art blue, green and red-emitting thin film-based PeLEDs without additional optical outcoupling structure, exhibit external quantum efficiencies (EQE) of 6.2%,[24] and 20.3%[25] and 20.1%[26] respectively. Some examples of device architecture used for PeLEDs are shown in Figure 1.1 (e).

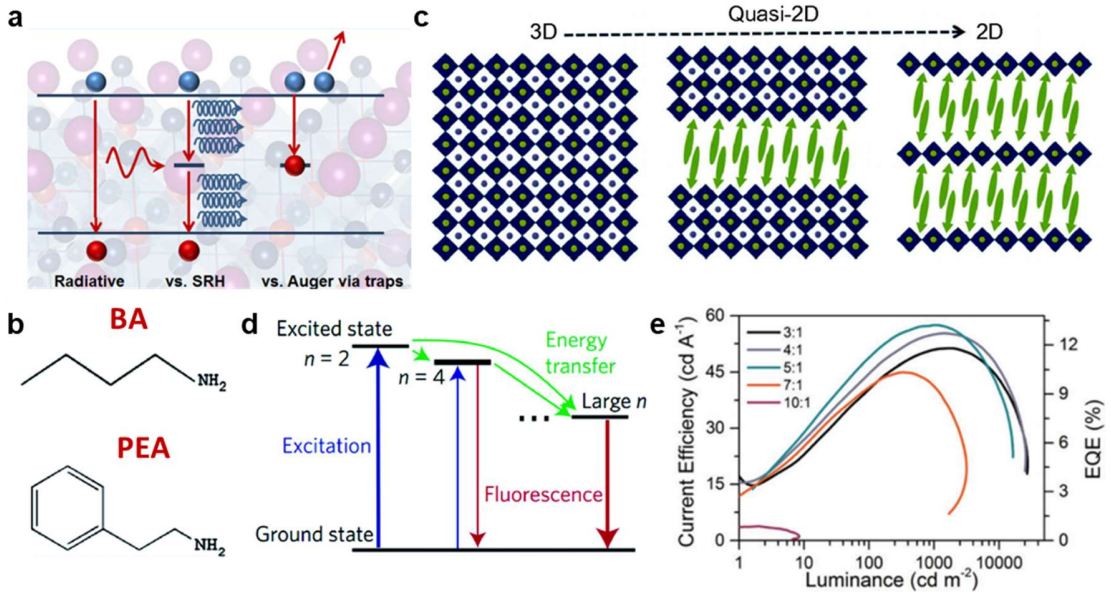


**Figure 1.2** (a) Schematic on trap and band-state filling processes[27]. (b) Examples of commonly used 2D organic spacer molecules. Schematic of (c) dimensionality tuning[28] and (d) energy transfer from high band gap to low band gap domains[23]. (e) Typical performance metric for PeLED[29].

## 1.2 Challenges for High Performance PeLEDs and Gap Analysis

However, industrialization of PeLEDs is not without its challenges. Relative to PSCs, research into PeLEDs is still in its infancy and while the progress thus far has been driven by knowledge gained from PSC research, strides further afield would require fundamental understanding of the correlation between the materials' processing and desired properties. Ideally, for effective light emission, high radiative recombination rate is required and achieved through two typical pathways, (a) suppression of non-radiative recombination and/or (b) facilitation of radiative recombination. The former relates to the presence of bulk and/or interfacial defects which are sites for non-radiative recombination.[30-32] A typical example is the defect filling process. The tendency for defect filling (Shockley Read Hall – SRH) to precede band-state filling (Figure 1.2 (a)), a radiative recombination process, leads to the mediocre efficiencies seen at low driving voltages. This underscores the importance of remedying defects in the quest for high efficiency PeLEDs. The latter, on the other hand, involves engineering the emitter to facilitate efficient light generation via a

process termed as energy cascade.[21, 29, 33] Energy cascade landscape is obtained through the introduction of two-dimensional (2D) organic spacer molecules such as butyl ammonium (BA) or phenyl ethyl ammonium (PEA) to template the formation of quasi-2D MHPs. Multiple band gap domains, akin to intrinsic quantum well structures, are formed in this mixed-dimensional film (Figure 1.2 (c)). On injection of charge carriers into higher band gap domains, the charge transfer to the energetically favoured lowest band gap domains ensures increased charge carrier concentrations in the latter (Figure 1.2 (d)). The increased number of photoexcited states and high charge carrier concentration enhances radiative recombination process and in turn translates to higher efficiency devices (Figure 1.2 (e)).

High electronic quality MHP film is just as critical for light emission as it is for light absorption. Ironically, the main advantages of employing MHPs as alternative emitters – solution processability and low defect densities, are incongruent. This is due to the propensity for defect formation during rapid crystallization that occurs amid the deposition process, thus providing the impetus for efforts toward defect management. Although current-state-of-the-art PeLEDs have shown efficiencies approaching the theoretical limit,[34] knowledge on the influence of processing and defects on light emission, is still lacking. Therefore, the intention of this thesis is to provide an in-depth investigation into the processing-induced evolution of film properties and its contribution toward defects.

## 1.3 Objective and Scope

In essence, the objective of this thesis revolves around the main theme of managing non-radiative recombination in MHPs. This is done through materials processing such as through post-deposition treatment and additive incorporation for passivation to alleviate both electronically active defects as well as grain boundary defects. Moreover, the engineering of an energetic landscape within the emitter enables non-radiative losses to be mitigated while simultaneously facilitating bimolecular radiative recombination through charge carrier localization. The scope of the research is detailed as follows:

### 1.3.1 Passivation of surface defects in MHPs

Similar to the processing of PSCs, annealing is also carried out to assist in the removal of excess solvent for PeLEDs, however, the concurrent increase in propensity for phase segregation and film degradation arising from under-coordination of surface lead atoms[35-36] during annealing, requires mitigating actions to be taken to minimize consequence to device performance. In order to circumvent this, a post-deposition treatment process employing a branched alkyl ammonium cation, is used. Although annealing is necessary for the transformation of yellow to black phase for iodide-based MHPs, the same is not required for bromide-based MHPs owing to the direct formation of desired phase on crystallization of the latter. This provides an opportunity for the adoption of alternative solvent removal steps to annealing to enable the elimination of annealing-induced defects. One such method is the vacuum drying process. While vacuum drying offers the added benefit of small grains which facilitates radiative recombination through spatial confinement of charge carriers, the simultaneous increase in grain boundary density also accompanies this process. Ideally, the former should be kept to a minimum due to its contribution towards non-radiative recombination (i.e defects and traps). A route for the formation of small passivated grains, such as through additive incorporation, is required to fully harness the advantages of spatial confinement for efficient photon generation. Due to the suppressive effect of defects on radiative recombination, it is necessary to combat them through passivation hence providing the rationale for Objective 1.3.1 which will be done through the following

- Exploring the impact of post-deposition treatment and additive incorporation in alleviating defects
- Investigating the influence of traps states on electrical loss mechanisms in PeLEDs

### 1.3.2 Investigations into energy cascade process and design of organic spacer molecules (2D cations) for mitigation of non-radiative recombination losses

Despite its impressive range of properties, low exciton binding energies, moisture instability and tendency for light degradation have hindered the development of high efficiency PeLEDs based on three-dimensional (3D) MHPs. To combat this, their 2D analogues, offering superior ambient stability and high PLQYs, are introduced to enable the harnessing of advantages from both systems. The notable increase in performance of these mixed-dimensional MHPs stem from the formation of multiple domains of varying band gaps depending on the degree of 2D cation intercalation in the 3D network. These domains result in the construction of an energetic landscape whereby charge carriers injected into the larger band gap domains get rapidly transferred to the energetically favoured lower band gap domains in a process referred to as energy cascade. The simultaneous outcompeting of non-radiative recombination process in the larger band gap domains and enhanced radiative recombination process in the lower band gap domains translate to an increase in the effectiveness of photon generation. Although the energy cascade process is hardly a new concept for PeLEDs, the knowledge on the type of 2D cation required to template the formation of an efficient energy landscape remains elusive. This provides the basis for Objective 1.3.2, where the study on the influence of aromatic core on the engineering of a mixed-dimensional landscape will be presented as follows

- Investigating 2D cations to facilitate the formation of mixed-dimensional system for enhanced radiative recombination
- Mitigation of non-radiative losses through formation of efficient energy cascade landscape

### 1.3.3 Effect of organic spacer molecules and A-site cations for efficient and spectrally stable blue emission

The PeLED efficiency for blue emission to date has been wanting, with rapid efficiency improvement to date noted primarily for green and red emissions. Although mixed-

dimensional MHPs adopting the energetic landscape concept has shown some degree of success, the tendency for charge carriers to funnel to the smallest band gap domains often results in green-emitting devices. While formation of green emitting domains can be suppressed through incorporation of excess 2D cations, the propensity for pure 2D MHPs to form due to strong van der Waals interaction inhibits charge transport in the resulting films. This translates to the need for fine control over the distribution of multi-dimensional band gap domains about the desired peak emission to enable monodispersed blue emission to be achieved without compromising on charge transport. In order to do so, it is critical to ensure that only the intermediate mixed-dimensional MHP domains crystallize whereas the formation of pure 2D domains is suppressed. The strategy to achieve Objective 1.3.3 is outlined as follows

- Validating importance of 2D cation and A-site cation relative solubilities for narrow multi band gap domain distribution
- Modulating the formation of layered MHPs to facilitate radiative recombination through efficient energy transfer

## 1.4 Dissertation Overview

*Chapter 1* highlights the crux of the thesis which is the objectives. The chapter details the purview of the research and features the key findings as well as the originality of ideas presented in this thesis.

*Chapter 2* presents a comprehensive overview of literature done in the field of MHPs and PeLEDs. Here the gaps in knowledge which will be addressed, are brought forth.

*Chapter 3* discusses the various syntheses and methodology employed in the investigation of defect passivation and the energy cascade process. The choice of characterization techniques employed will also be elaborated on.

*Chapter 4* highlights the impact of annealing as a solvent removal step on defect formation and presents post-deposition treatment process as a possible route for alleviating annealing-induced defects.

*Chapter 5* showcases the effect of additive incorporation in enabling in-situ growth of passivated nanograins which promotes increased radiative recombination for improved device performance.

*Chapter 6* presents a systematic study on the use of 2D cation to engineer the formation of an efficient energetic landscape in the emitter. The role of defects and the criteria required for design of suitable 2D cation to facilitate an efficient energy cascade process would be discussed.

*Chapter 7* encompasses the investigation into the influence of A-site cation to achieve a narrow spread of mixed-dimensional MHP distribution to achieve spectrally stable blue emission.

*Chapter 8* summarizes in its entirety the work presented from Chapters 4-7. Aside from correlating the results obtained with the defined objectives of the thesis, the possible opportunities and ramifications arising from the research work will also be duly discussed.

## 1.5 Findings and Outcomes/Originality

The work presented in this thesis has led to the following contributions towards the broader scientific community:

### 1.5.1 Establishing the importance of defect passivation during film processing for PeLEDs

The tendency for defect formation with solution-based processing necessitates remedial actions to alleviate non-radiative recombination losses in PeLEDs. Through facile

modification to the processing of MHP films, it is shown that defects can be successfully modulated as evidenced by the enhanced photoluminescence intensities and corresponding improvement to device performance. The presence of a limit to the concentrations of tetra ethyl ammonium bromide and bathophenanthroline used before PeLED performance declines suggests that excessive secondary phase in the emitter is disruptive to radiative recombination and/or charge transport. In both studies, defect passivation of the grains is also accompanied by grain size modulation and energy level realignment at the charge selective layer interfaces. Hence, although the post-deposition treatment and additive incorporation processes are intended for defect passivation, their simultaneous effect in other areas can also contribute positively or negatively (when in excess) towards device performance.

### 1.5.2 Demonstrating the effect of molecular design on the effectiveness of 2D cation in engineering the formation of an efficient energetic landscape for mixed-dimensional MHP emitters

Three 2D cations with different aromatic cores are investigated to establish their influence on engineering an efficient energetic landscape to promote the charge carrier funneling process. Although all three molecules are shown to be capable of forming 2D MHPs, their optoelectronic properties on incorporation into the 3D lead-halide network differ. Two main reasons for the disparity in performance of the three molecules are (a) the higher degree of distortion for mixed-dimensional films templated with bi-cationic molecules which contributes towards lower radiative recombination as evidenced by the lower PLQYs and shorter lifetime decays as well as (b) inefficient funneling between the higher band gap and lower band gap domains as observed from the weak photoluminescence spectra. Thus, while it is shown that mixed-dimensional MHPs provide a platform for attaining high efficiency devices, judicious selection of 2D cation is needed to enable the formation of effective mini quantum wells without detriment to charge funneling kinetics in the pursuit of PeLED efficiency.

### 1.5.3 Validating the need for control over the distribution of mixed-dimensional domains in an energetically engineered landscape for spectrally stable blue emission

Although the energy cascade process has been successful in yielding high performance green and red PeLEDs; their applicability for blue emission has been hindered by the tendency for emission to shift to the lowest band gap domains. However, by relying on a triptych of the 2D cation and A-site cation concentrations, solubility limit of the A-site cation, and nucleation kinetics; a methodology enabling the tailoring of MHP energetic landscape to deliver a narrow distribution of intermediate mixed-dimensional MHP domains allows efficient blue emission to be achieved. High concentration of the 2D cation and low solubility A-site cation are both needed to eliminate the formation of 2D and 3D MHP domains as evidenced by the absence of their characteristic emissions in the electroluminescence (EL) and photoluminescence (PL) spectra. The efficacy of the charge carrier funneling process is confirmed by the increasing rise and decay times at longer wavelengths which are indicative of suppressed non-radiative losses at intermediate mixed-dimensional MHP domains. By employing this processing strategy, record efficiencies of 2.34 and 4.8% corresponding to spectrally stable deep blue (~ 465 nm) and cyan (~ 493 nm) emissions are achieved. Issues pertaining to halide segregation are also averted with the use of a pure bromide system. This strategy is readily applicable to other material systems and would lead to significant advancements in blue emissions and offer new avenues for tunability across the *Commission Internationale de l'Eclairage* (CIE) colour gamut.

# References

1. Waide, P.; Tanishima, S., *Light's Labour's Lost: Policies for Energy-efficient Lighting*. France, 2006.

2. Agency, I. E. Energy Efficiency. http://www.iea.org/topics/energyefficiency/subtopics/lighting/ (accessed 23 September 2016).

3. N. Holonyak, S. F. B., Coherent (Visible) Light emission from Ga(As(1-x)Px) junctions. *Applied Physics Letters* **1962,** *1* (4), 82-83.

4. Brütting, W.; Frischeisen, J.; Schmidt, T. D.; Scholz, B. J.; Mayr, C., Device efficiency of organic light-emitting diodes: Progress by improved light outcoupling. *physica status solidi (a)* **2013,** *210* (1), 44-65.

5. Peralta, S.; Ruda, H., Applications for advanced solid-state lamps. *IEEE Industry Applications Magazine* **1998,** *4* (4), 31-42.

6. Klovance, R. Lighting choices: Our comparison chart should help. https://www.bchydro.com/news/unplug_this_blog/2011/lighting_comparison_chart.html (accessed 13 August 2019).

7. Thejo Kalyani, N.; Dhoble, S. J., Organic light emitting diodes: Energy saving lighting technology—A review. *Renewable and Sustainable Energy Reviews* **2012,** *16* (5), 2696-2723.

8. Boix, P. P.; Nonomura, K.; Mathews, N.; Mhaisalkar, S. G., Current progress and future perspectives for organic/inorganic perovskite solar cells. *Materials Today* **2014,** *17* (1), 16-23.

9. Xing, G.; Mathews, N.; Sun, S.; Lim, S. S.; Lam, Y. M.; Grätzel, M.; Mhaisalkar, S.; Sum, T. C., Long-Range Balanced Electron- and Hole-Transport Lengths in Organic-Inorganic CH3NH3PbI3. *Science* **2013,** *342* (6156), 344-347.

10. Jung, H. S.; Park, N.-G., Perovskite Solar Cells: From Materials to Devices. *Small* **2015,** *11* (1), 10-25.

11. O. D. Miller, E. Y., S. R. Kurtz, Strong internal and external luminescence as solar cells approach the Shockley-Queisser Limit. *Journal of Photovoltaics* **2012,** *2* (3), 303-311.

12. Veldhuis, S. A.; Boix, P. P.; Yantara, N.; Li, M.; Sum, T. C.; Mathews, N.; Mhaisalkar, S. G., Perovskite Materials for Light-Emitting Diodes and Lasers. *Advanced Materials* **2016**, n/a-n/a.

13. Green, M. A.; Ho-Baillie, A.; Snaith, H. J., The emergence of perovskite solar cells. *Nat Photon* **2014,** *8* (7), 506-514.

14. Marinova, N.; Valero, S.; Delgado, J. L., Organic and perovskite solar cells: Working principles, materials and interfaces. *Journal of Colloid and Interface Science* **2017,** *488*, 373-389.

15. Kim, Y.-H.; Cho, H.; Lee, T.-W., Metal halide perovskite light emitters. *Proceedings of the National Academy of Sciences* **2016,** *113* (42), 11694-11702.

16. Protesescu, L.; Yakunin, S.; Bodnarchuk, M. I.; Krieg, F.; Caputo, R.; Hendon, C. H.; Yang, R. X.; Walsh, A.; Kovalenko, M. V., Nanocrystals of Cesium Lead Halide Perovskites (CsPbX3, X = Cl, Br, and I): Novel Optoelectronic Materials Showing Bright Emission with Wide Color Gamut. *Nano Letters* **2015,** *15* (6), 3692-3696.

17. Veldhuis, S. A.; Boix, P. P.; Yantara, N.; Li, M.; Sum, T. C.; Mathews, N.; Mhaisalkar, S. G., Perovskite Materials for Light-Emitting Diodes and Lasers. *Advanced Materials* **2016,** *28* (32), 6804-6834.

18. Tan, Z.-K.; Moghaddam, R. S.; Lai, M. L.; Docampo, P.; Higler, R.; Deschler, F.; Price, M.; Sadhanala, A.; Pazos, L. M.; Credgington, D.; Hanusch, F.; Bein, T.; Snaith, H. J.; Friend, R. H., Bright light-emitting diodes based on organometal halide perovskite. *Nat Nano* **2014,** *9* (9), 687-692.

19. Wang, J.; Wang, N.; Jin, Y.; Si, J.; Tan, Z.-K.; Du, H.; Cheng, L.; Dai, X.; Bai, S.; He, H.; Ye, Z.; Lai, M. L.; Friend, R. H.; Huang, W., Interfacial Control Toward Efficient and Low-Voltage Perovskite Light-Emitting Diodes. *Advanced Materials* **2015,** *27* (14), 2311-2316.

20. Ling, Y.; Yuan, Z.; Tian, Y.; Wang, X.; Wang, J. C.; Xin, Y.; Hanson, K.; Ma, B.; Gao, H., Bright Light-Emitting Diodes Based on Organometal Halide Perovskite Nanoplatelets. *Advanced Materials* **2016,** *28* (2), 305-311.

21. Yuan, M.; Quan, L. N.; Comin, R.; Walters, G.; Sabatini, R.; Voznyy, O.; Hoogland, S.; Zhao, Y.; Beauregard, E. M.; Kanjanaboos, P.; Lu, Z.; Kim, D. H.; Sargent, E. H.,

Perovskite energy funnels for efficient light-emitting diodes. *Nat Nano* **2016,** *advance online publication*.

22. Silver, S.; Dai, Q.; Li, H.; Brédas, J.-L.; Kahn, A., Quantum Well Energetics of an n = 2 Ruddlesden–Popper Phase Perovskite. *Advanced Energy Materials* **2019,** *9* (25), 1901005.

23. Wang, N.; Cheng, L.; Ge, R.; Zhang, S.; Miao, Y.; Zou, W.; Yi, C.; Sun, Y.; Cao, Y.; Yang, R.; Wei, Y.; Guo, Q.; Ke, Y.; Yu, M.; Jin, Y.; Liu, Y.; Ding, Q.; Di, D.; Yang, L.; Xing, G.; Tian, H.; Jin, C.; Gao, F.; Friend, R. H.; Wang, J.; Huang, W., Perovskite light-emitting diodes based on solution-processed self-organized multiple quantum wells. *Nat Photon* **2016,** *10* (11), 699-704.

24. Vashishtha, P.; Ng, M.; Shivarudraiah, S. B.; Halpert, J. E., High Efficiency Blue and Green Light-Emitting Diodes Using Ruddlesden–Popper Inorganic Mixed Halide Perovskites with Butylammonium Interlayers. *Chemistry of Materials* **2019,** *31* (1), 83-89.

25. Lin, K.; Xing, J.; Quan, L. N.; de Arquer, F. P. G.; Gong, X.; Lu, J.; Xie, L.; Zhao, W.; Zhang, D.; Yan, C.; Li, W.; Liu, X.; Lu, Y.; Kirman, J.; Sargent, E. H.; Xiong, Q.; Wei, Z., Perovskite light-emitting diodes with external quantum efficiency exceeding 20 per cent. *Nature* **2018,** *562* (7726), 245-248.

26. Zhao, B.; Bai, S.; Kim, V.; Lamboll, R.; Shivanna, R.; Auras, F.; Richter, J. M.; Yang, L.; Dai, L.; Alsari, M.; She, X.-J.; Liang, L.; Zhang, J.; Lilliu, S.; Gao, P.; Snaith, H. J.; Wang, J.; Greenham, N. C.; Friend, R. H.; Di, D., High-efficiency perovskite–polymer bulk heterostructure light-emitting diodes. *Nature Photonics* **2018,** *12* (12), 783-789.

27. Staub, F.; Rau, U.; Kirchartz, T., Statistics of the Auger Recombination of Electrons and Holes via Defect Levels in the Band Gap—Application to Lead-Halide Perovskites. *ACS Omega* **2018,** *3* (7), 8009-8016.

28. Ma, S.; Cai, M.; Cheng, T.; Ding, X.; Shi, X.; Alsaedi, A.; Hayat, T.; Ding, Y.; Tan, Z. a.; Dai, S., Two-dimensional organic-inorganic hybrid perovskite: from material properties to device applications. *SCIENCE CHINA Materials* **2018,** *61* (2095-8226), 1257.

29. Chin, X. Y.; Perumal, A.; Bruno, A.; Yantara, N.; Veldhuis, S. A.; Martínez-Sarti, L.; Chandran, B.; Chirvony, V.; Lo, A. S.-Z.; So, J.; Soci, C.; Grätzel, M.; Bolink, H. J.; Mathews, N.; Mhaisalkar, S. G., Self-assembled hierarchical nanostructured perovskites

enable highly efficient LEDs via an energy cascade. *Energy & Environmental Science* **2018,** *11* (7), 1770-1778.

30. Abate, A.; Saliba, M.; Hollman, D. J.; Stranks, S. D.; Wojciechowski, K.; Avolio, R.; Grancini, G.; Petrozza, A.; Snaith, H. J., Supramolecular Halogen Bond Passivation of Organic–Inorganic Halide Perovskite Solar Cells. *Nano Letters* **2014,** *14* (6), 3247-3254.

31. Wei, F.; Jiao, B.; Dong, H.; Xu, J.; Lei, T.; Zhang, J.; Yu, Y.; Ma, L.; Wang, D.; Chen, J.; Hou, X.; Wu, Z., Bifunctional π-conjugated ligand assisted stable and efficient perovskite solar cell fabrication via interfacial stitching. *Journal of Materials Chemistry A* **2019,** *7* (27), 16533-16540.

32. Zhao, T.; Chueh, C.-C.; Chen, Q.; Rajagopal, A.; Jen, A. K. Y., Defect Passivation of Organic–Inorganic Hybrid Perovskites by Diammonium Iodide toward High-Performance Photovoltaic Devices. *ACS Energy Letters* **2016,** *1* (4), 757-763.

33. Quan, L. N.; Zhao, Y.; García de Arquer, F. P.; Sabatini, R.; Walters, G.; Voznyy, O.; Comin, R.; Li, Y.; Fan, J. Z.; Tan, H.; Pan, J.; Yuan, M.; Bakr, O. M.; Lu, Z.; Kim, D. H.; Sargent, E. H., Tailoring the Energy Landscape in Quasi-2D Halide Perovskites Enables Efficient Green-Light Emission. *Nano Letters* **2017,** *17* (6), 3701-3709.

34. Shi, X.-B.; Liu, Y.; Yuan, Z.; Liu, X.-K.; Miao, Y.; Wang, J.; Lenk, S.; Reineke, S.; Gao, F., Optical Energy Losses in Organic–Inorganic Hybrid Perovskite Light-Emitting Diodes. *Advanced Optical Materials* **2018,** *6* (17), 1800667.

35. Bi, D.; Li, X.; Milić, J. V.; Kubicki, D. J.; Pellet, N.; Luo, J.; LaGrange, T.; Mettraux, P.; Emsley, L.; Zakeeruddin, S. M.; Grätzel, M., Multifunctional molecular modulators for perovskite solar cells with over 20% efficiency and high operational stability. *Nature Communications* **2018,** *9* (1), 4482.

36. Kim, J.; Chung, C.-H.; Hong, K.-H., Understanding of the formation of shallow level defects from the intrinsic defects of lead tri-halide perovskites. *Physical Chemistry Chemical Physics* **2016,** *18* (39), 27143-27147.

# Chapter 2

# Literature Review

*This chapter provides a detailed description of the advantages of employing metal halide perovskites as alternative emitters in perovskite-based light emitting diodes. Important concepts pertaining to this thesis such as electroluminescence from metal halide perovskite emitters, performance metrics of perovskite-based light emitting diodes, dominant defects present in the active material as well as approaches which can be undertaken to mitigate effect of non-radiative recombination on metal halide perovskites and their resulting devices, will also be covered.*

## 2.1 Organic Light Emitting Diodes

Organic light-emitting diodes (OLEDs) are the organic counterpart of light-emitting diodes, where instead of an inorganic material functioning as the electroluminescent layer, for OLEDs, the emitting material is organic. While LEDs are point light sources, OLEDs are diffused sources of light. Not only are OLEDs thin, lightweight and flat light sources which can be made flexible, their versatility and uniform large-area light emission also present them as attractive candidates for various lighting applications[1] (Figure 2.1).

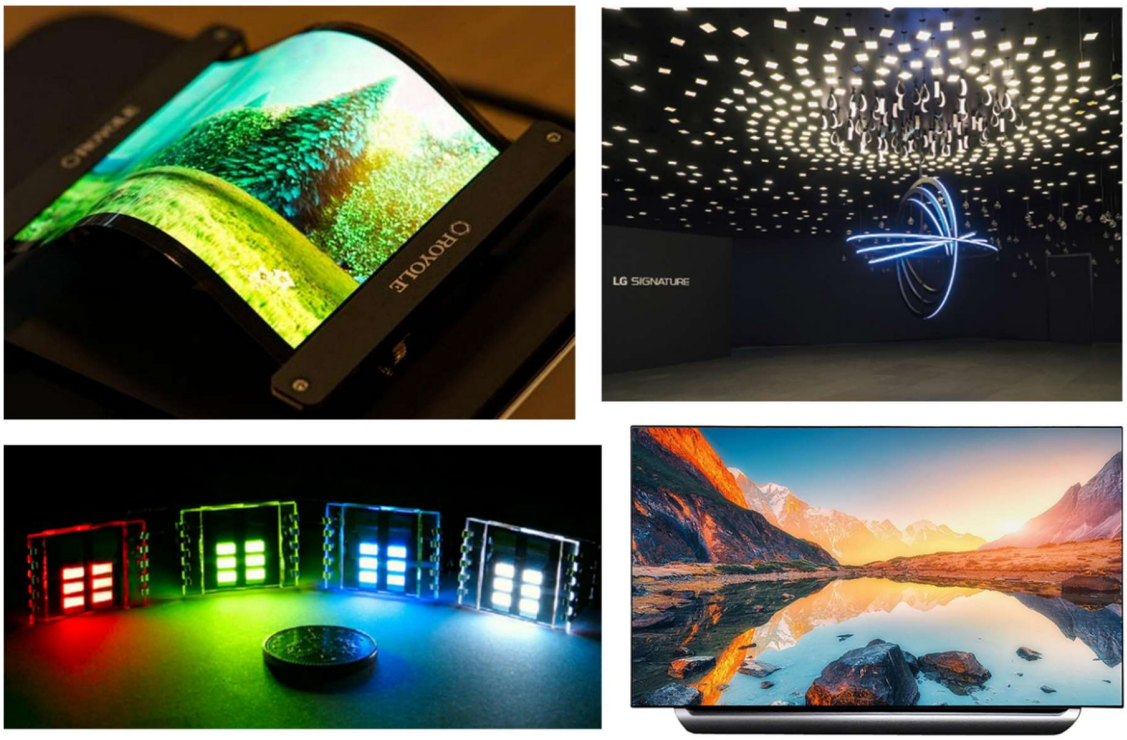


**Figure 2.1** Examples of applications of the OLED technology[2-5]

### 2.1.1 Device architecture

Light emission in OLEDs occurs through a process known as electroluminescence. Light photons are generated due to the radiative recombination of holes and electrons injected into the semiconductor materials from the electrodes. Since the early works on electroluminescence in organic semiconductors by Pope and Helfrich[1], the OLED device

architecture has evolved to become complex multi-layered systems to maximize device efficiency[6] (Figure 2.2).

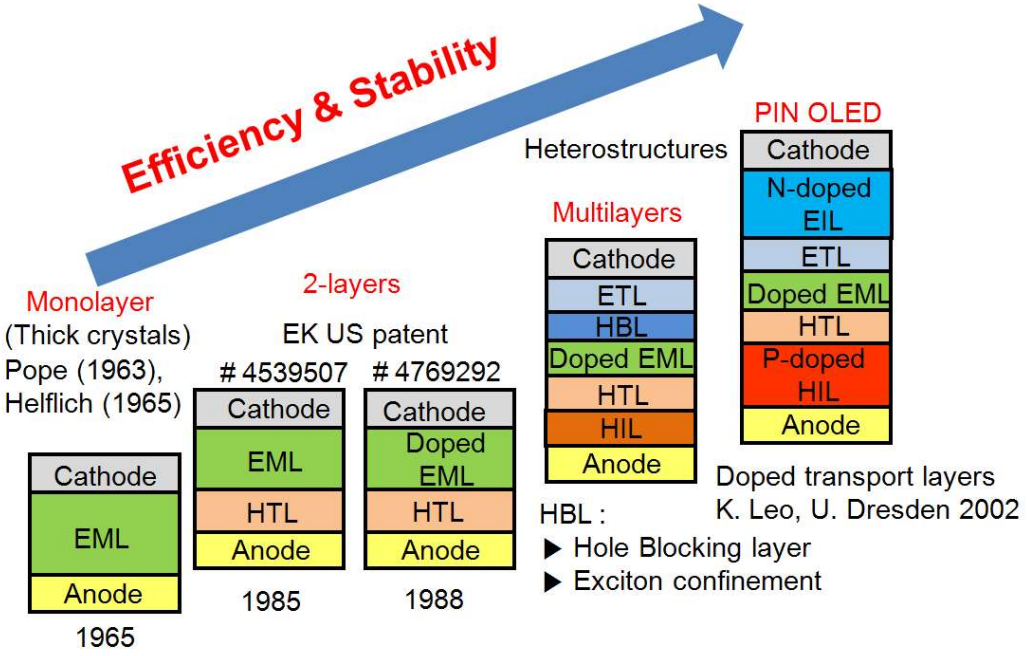


**Figure 2.2** Evolution of OLED architecture over the years to improve device efficiency and stability[7]

A typical OLED stack (Figure 2.3), consists of the following components:

**Substrate**: The substrate supports the OLED device and depending on the application the OLED is used for, it can vary from rigid glass for OLED modules or even plastic for flexible or wearable electronics.

**Anode**: The transparent conducting oxide deposited on the substrate acts as an anode, transporting holes through the OLED when a bias is applied.

**Organic layers**: The organic layers in an OLED refer to the charge selective and emitting layers.

- **Hole transport layer:** The hole transport layer functions to transport holes (antithesis of electrons) from the anode to the emitter layer. Depending on the energy level, it can also function as an electron blocker.

- **Emitting layer:** The holes and electrons recombine in this layer to generate photons.

- **Electron transport layer:** The electron transport layer facilitates the flow of electrons from the cathode to the emitting layer for radiative recombination.

**Cathode**: Electrons are injected into the device through the cathode when a voltage is applied across the OLED.

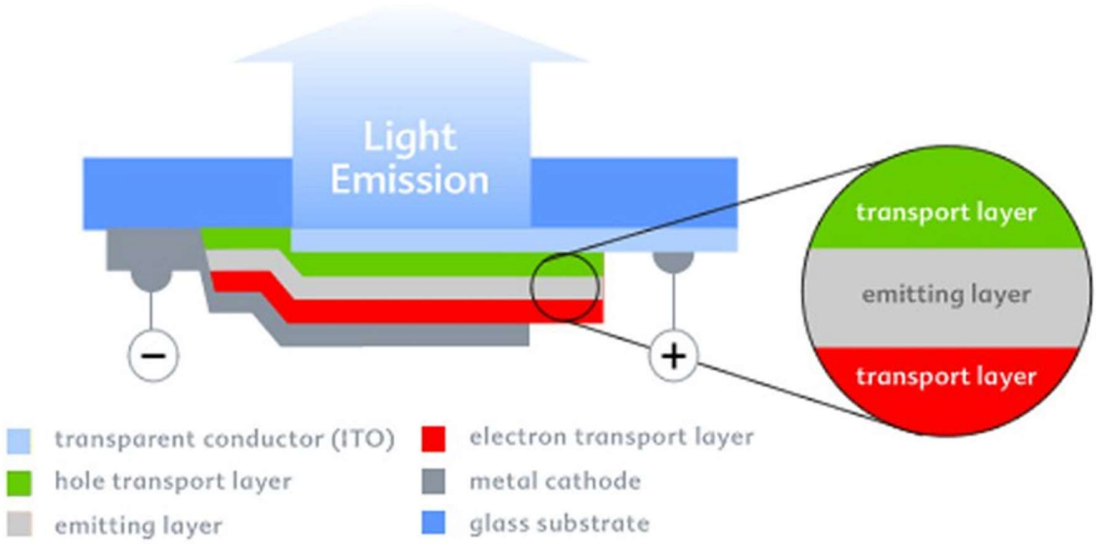


**Figure 2.3** OLED device architecture[8]

### 2.1.2 Working principle

When an external bias is applied across the OLED, electrons and holes are injected into the device from the cathode and anode respectively. The holes would then enter the highest occupied molecular orbital (HOMO) of a high mobility semiconductor material (hole transporting layer), followed by the electron blocking layer, which restricts the leakage of electrons (opposite carrier) from the emitter layer by utilizing a large energy barrier in the lowest unoccupied molecular orbital (LUMO). Finally, the holes would form excitons with electrons in the emissive layer, and decay radiatively to emit photons. The injection and transport processes for electrons adopt the same principles as that of holes, with the exception of migration through the LUMO levels of the corresponding electron transporting and hole blocking layers, to reach the emissive layer. While the various layers present in the device serve to enhance OLED efficiency, the possibility of combining different functions into a single layer, may deem some layers redundant.[6]

In short, the light production process in OLEDs (Figure 2.4) can be summarized into four main steps.[9]

- Injection of electrons and holes at the electrodes
- Transport of charge carriers through the corresponding transporting and blocking layers
- Formation of excitons in the emitting layer
- Light emission through radiative decay of excitons

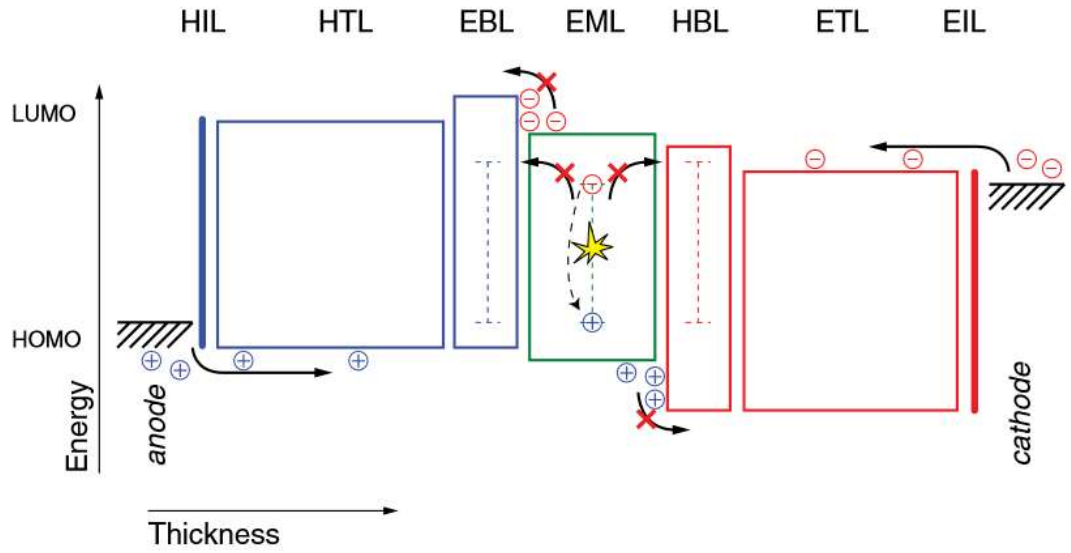


**Figure 2.4** Schematic of electroluminescence process occurring in an OLED device[6]

The emission wavelength of the OLED device is directly related to the energy difference between the HOMO and LUMO levels of the emitting material, also referred to as the band gap of the material. Consequently, emission colour tuning can be made possible by substitution of emitter material. Brightness or intensity of emitted light, on the other hand, can be manipulated by varying the amount of electrical current supplied.[10]

### 2.1.3 Performance metrics for OLEDs

Efficiency is a crucial aspect which needs to be considered, not just to account for device energy consumption, but also for its lifetime. Three main parameters used in the assessment of OLED performance are current efficiency (cd $A^{-1}$), luminous efficiency (lm $W^{-1}$), and external quantum efficiency.[6, 11] In brief, while the latter provides a ratio of photons emitted to injected charge carriers, the other two efficiencies are photometric quantities, having a strong correlation to the human eye's spectral sensitivity (Figure 2.5).

The current efficiency can be obtained by applying the following formula; where $L_0$ and $J_{meas}$ represent the luminance and the measured current density flowing through the device, respectively.

$$\eta_C = \frac{L_0}{J_{meas}} \left[cd\ A^{-1}\right]$$

The luminous efficiency on the other hand, is a point measurement which takes into consideration the driving voltage and current density, which can be described using the formula;

$$\eta_{LE} = \eta_C \frac{f_D \pi}{V_{meas}} \left[lm\ W^{-1}\right]$$

with $f_D$ defined as

$$f_D = \frac{1}{\pi I_0} \int_0^{\frac{\pi}{2}} \int_{-\pi}^{+\pi} I\ (\theta, \phi) \sin\theta\ d\phi\ d\theta$$

where $f_D$ represents the angular distribution of the emitted light intensity defined in terms of the azimuthal ($\theta$) and polar angles ($\phi$) whereas $I_0$ represents the light intensity. All calculated values are to be taken from the forward direction measurements.

Last but not least, the external quantum efficiency is represented using the following:

$$\eta_{ext} = \eta_C \frac{f_D \pi e}{K_r E_{ph}} \left[\frac{\%}{100}\right]$$

with the luminous efficacy of radiation represented by $K_r$ is obtained by

$$K_r = \frac{\int_{380nm}^{780nm} \phi_r\ (\lambda)\ V(\lambda)\ d\lambda}{\int_0^{\infty} \phi_r(\lambda)\ d\lambda} \left[lm\ W^{-1}\right]$$

where $E_{ph}$, $\phi_r(\lambda)$ and $V(\lambda)$ refer to the average energy of the emitted photon, radiant flux and weighing function with consideration of human eye spectral sensitivity. In other words, $K_r$ can be simply defined as the number of lumens a given spectrum can produce per watt. However, it is important to note that the accuracy of the integrated efficiency values only holds true if the measurement considers the angular $f_D$ distribution. As such, it is crucial that an integrating sphere or goniometer be included into the experimental set up for precise angular considerations.

For simplicity, the external quantum efficiency is often presented as follows:

$$\eta_{ext} = \eta_r \phi_f \, x \, \eta_{out} = \eta_{int} \, \eta_{out}$$

where $\eta_r$, $\phi_f$ , $x$ and $\eta_{out}$ refer to the probability of electron and hole recombination, fluorescence quantum efficiency, probability of radiative decay occurrence and fraction of photons leaving the device, respectively. The product of $\eta_r$, $\phi_f$ and $x$ gives rise to the internal quantum efficiency ($\eta_{int}$) of the device.

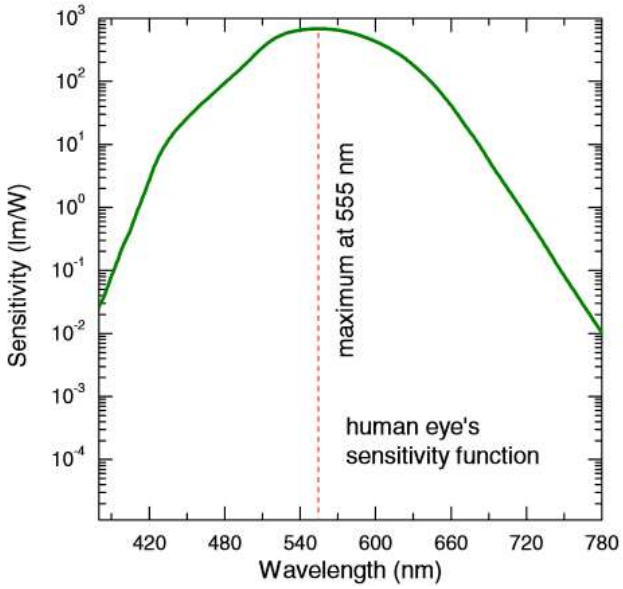


**Figure 2.5** Human eye response function as a function of wavelength[11]

### 2.1.4 Disadvantages of OLEDs

Despite the promise of revolutionizing the illumination industry with potentially large energy savings, the high costs associated with use of expensive precursors and need for epitaxial film matching has been a challenge. This creates opportunities for the development of innovative illuminating technologies which not only offer high efficiencies, but concomitantly, at low cost.

## 2.2 Metal Halide Perovskites for Light Emission

### 2.2.1 Three-dimensional metal halide perovskites

While MHPs adopt the same crystal structure as their classic oxide-based counterpart with an $ABX_3$ formula, the former consists of a monovalent A-site cation surrounded by four corner-sharing $BX_6$ metal halide octahedra (Figure 2.6), where A = $CH(NH_2)_2^+$, $CH_3NH_2^+$ or $Cs^+$, B = $Pb^{2+}$, $Sn^{2+}$, $Cu^{2+}$ or $Ge^{2+}$ and X = $Cl^-$, $Br^-$ or $I^-$.[12]

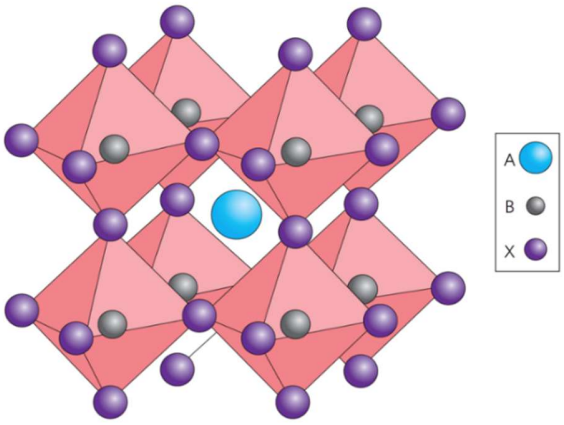


**Figure 2.6** Crystal structure of a typical oxide perovskite[13]

The ideality of the MHP structure is defined using two parameters namely the Goldschmidt tolerance factor ($t$) and octahedral factor ($\mu$) which are defined as follows:

$$t = \frac{r_A + r_X}{\sqrt{2}(r_A + r_X)}$$

$$\mu = \frac{r_B}{r_X}$$

Based on the tolerance and octahedral factors above, stable structures are found to fall within the range of $0.80 < t < 0.90$ and $0.40 < \mu < 0.90$.[13-14] Deviations in values beyond the range result in excessive distortion of the crystal structure leading to destruction of the connected 3D metal halide network.[14] High cubic symmetry yields optimum electronic properties owing to the high degree of ionic bonding. However, in most cases, MHPs do not take on the ideal structure but instead form distorted variants. The deviation from the ideal tolerance range due to resultant tensile and compressive stresses in the crystal gives rise to distortion and tilting[15] of metal halide octahedras consequently affecting material properties such as electronic, magnetic and dielectric characteristics, which are critical in determining the applications of MHPs.

Research into lead-free MHPs have driven efforts towards substitution of the B-site cation. However, structural stability and optoelectronic properties are strongly correlated with the presence of lead, as evidenced by the less than satisfactory performance of lead-free MHPs to date.[16-17] On the other hand, introduction of trace amounts of dopants such as tin, bismuth and strontium, have been shown to be successful in imparting unique properties to this class of materials[18] with little effect on μ (Figure 2.7).

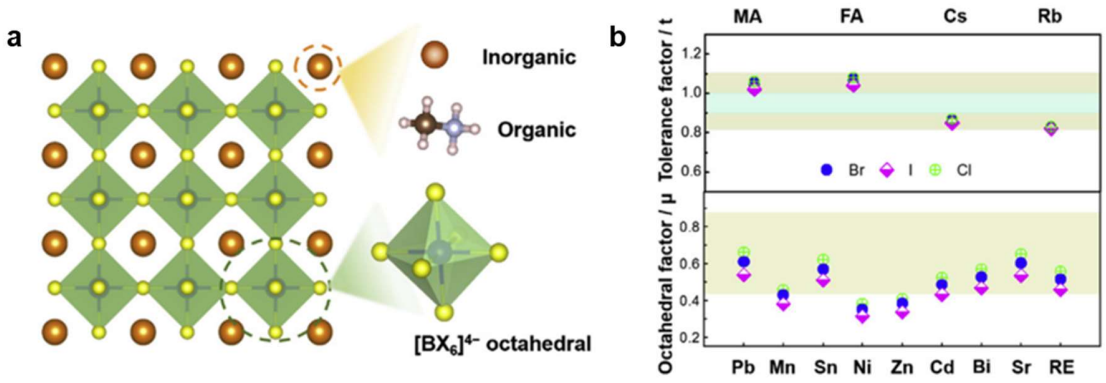


**Figure 2.7** (a) Planar view (001) of metal halide perovskite. (b) Tolerance and octahedral factor variation on substitution of A-site and B-site cation respectively for chloride-, bromide- and iodide-based perovskites[18]

The unique range of properties offered by MHPs in association with its structural symmetry[19] include ultra-low defect densities, high absorption coefficients of $10^4 – 10^5$ $cm^{-1}$ within the visible region,[12, 20-21] low exciton binding energy,[22] excellent charge carrier mobilities[23] and long-range balanced charge transport lengths.[24] The superb characteristics coupled with low-cost manufacturing associated with earth abundant precursors and solution-based processing, appeals it to a wide range of optoelectronic applications beyond photovoltaics. These and other optoelectronic properties of MHPs can be modulated simply through elemental doping of A-, B- or X-site in the crystal lattice (Figure 2.8).

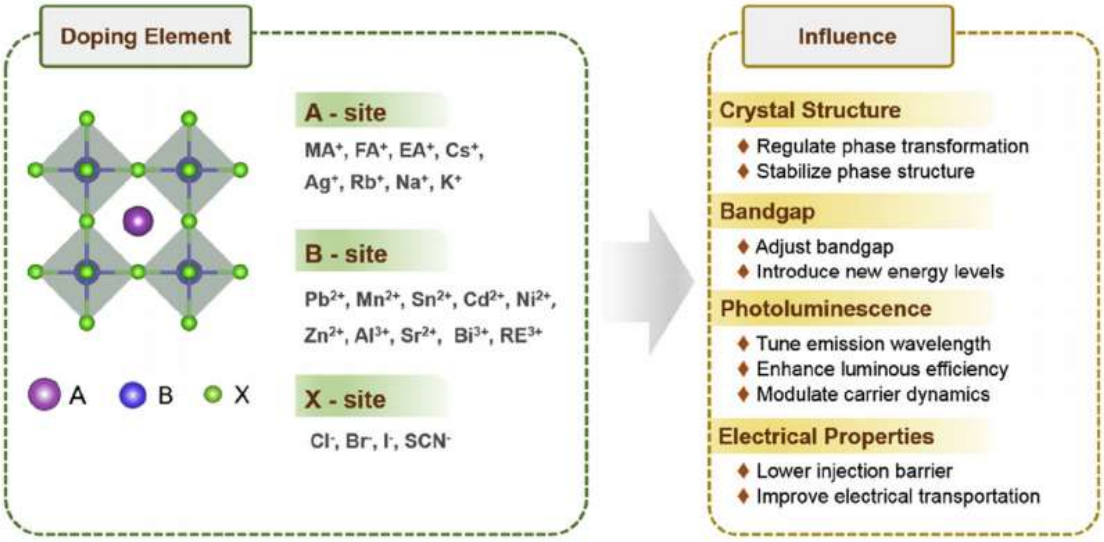


**Figure 2.8** Possible doping elements for the A-, B- and X-sites of the perovskite structure and their influence on material properties[18]

Although PeLEDs have shown unprecedented growth in efficiencies since the early reports of their photoluminescence,[25-26] the efficiency of PeLEDs based on pristine MHPs thin films are low. This is despite the various modifications made to the processing technique to enable smooth and compact films of high electronic quality[27-28] to be achieved. The underlying cause for the low efficiency of these PeLEDs stems from the very characteristic which presents MHPs as an efficient light harvester; its low exciton binding energy. Low exciton binding energy facilitates efficient charge carrier extraction from light harvesting layer due to the rapid exciton dissociation to free charge carriers[29-30] on photon absorption. However, in the case of PeLEDs, instead, high exciton binding energy is desired to promote rapid radiative recombination of the charge carriers on injection into the emitting layer. Thus, high localized charge carrier density is required to compensate for the low exciton binding energy in order to achieve high radiative recombination. To overcome this, exciton confinement is proposed[29] and achieved via two approaches : (a) geometric confinement and (b) intrinsic confinement (Figure 2.9).

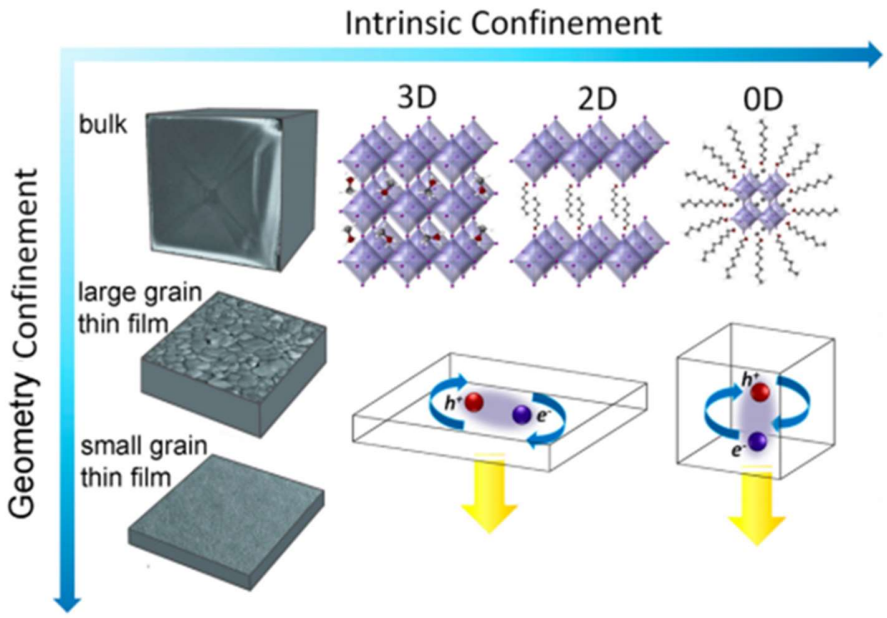


**Figure 2.9** Proposed routes for increasing exciton confinement to promote radiative recombination[29].

This provided the catalyst for research into small grain and nanoparticle emitters due to the spatial and electronic confinement of charge carriers afforded. Examples of literature adopting this principle include embedding of emitter within a polymer matrix,[31-32] introduction of additive for in-situ nanograin formation[33-34] and use of nanoparticles as emitting material.[35-37] Despite the enhancement seen for thin film-based MHPs with the adoption of geometric confinement principle, the PeLED efficiency still lags behind those of their quantum confined counterparts. This suggests that the electronic confinement offered by the change in emitter dimensionality offers a more effective approach towards achieving efficient radiative recombination in PeLEDs.

### 2.2.2 Lower dimensional metal halide perovskites

Unlike 3D MHPs, the 2D analogues with a formula of $L_2A_{n-1}B_nX_{3n+1}$ (where L is an organic spacer molecule, n is a positive integer and n = 1 refers to the pure 2D MHP) adopt a layered structure due to the inability of the bulky organic spacer molecule to fit into the cubic corner-sharing metal halide octahedra network. Collapse of this network results in

the formation of <001> or <110> cuts of the 3D structure[38] (Figure 2.10). Held together by van der Waals forces, these layered analogues are structured similarly to quantum wells with the inorganic layers forming the wells whereas the organic spacer molecules, function as barriers. The difference in the dielectric constants of the organic and inorganic layers within the lattice results in the high exciton binding energies characteristic of 2D MHPs, giving rise to their high PLQYs.[39] Although the quantum well-like structure[40] offers high exciton binding energies which are ideal for light emission applications,[41-43] the poor connectivity of the metal halide network results in extremely poor charge transport properties of these 2D MHPs. To combat this while still retaining the high radiative recombination efficacy offered by dimensional confinement, amalgamation of the 2D and 3D MHPs is proposed, where depending on the degree of intercalation of the 2D cation into the 3D metal halide network, a myriad of layered compounds with varying binding energies and band gaps can be obtained. With dimensionalities falling somewhere in-between the 2D and 3D systems, these compounds are often referred to as mixed-dimensional MHPs. This creates new opportunities for the inclusion of larger and more complex molecules such as conjugated molecules enabling π–π stacking,[40] dyes (e.g., thiophenes[44]), or even chromophores, to better tune optoelectronic properties of the otherwise restrictive 2D and 3D archetype MHPs for a wide range of applications.

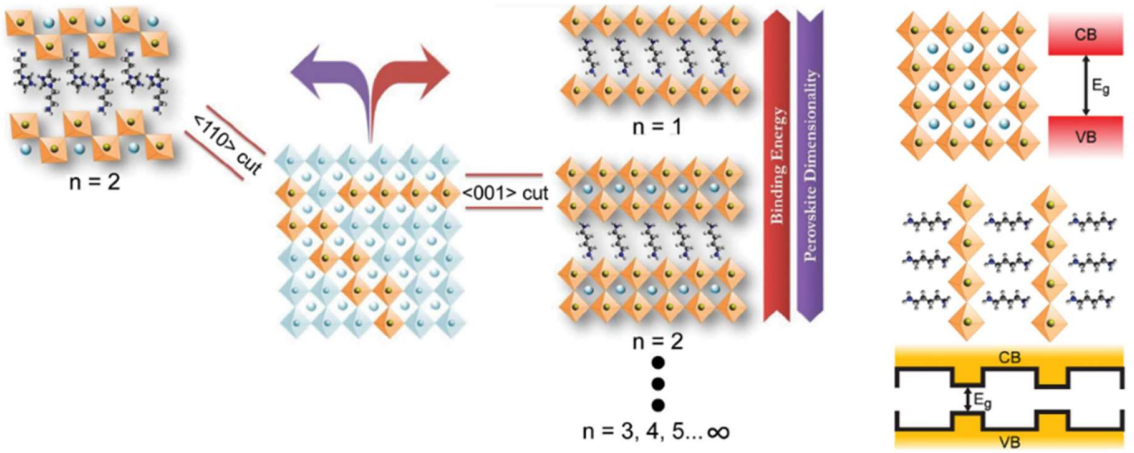


**Figure 2.10** Schematic of mixed-dimensional perovskites where incorporation of organic spacer molecules results in the destruction of the 3D metal-halide network and the formation of characteristic 2D layered structure[38]

### 2.2.3 Colour tunability

MHPs are extremely flexible; not only can the morphology be modified easily through processing to yield grains or particles of varying shapes and sizes, the emission wavelength too can be tailored via composition engineering. Having been shown to be a successful approach to yield improved band gap and phase stability for photovoltaics, compositional engineering through A-site or X-site ion substitution enables a wide spectrum of colours to be realized. Coupled with the narrow emission line-width[45] afforded by MHPs which translates to high colour purity, it is hardly surprising MHPs are an emerging class of materials for lighting and display applications.

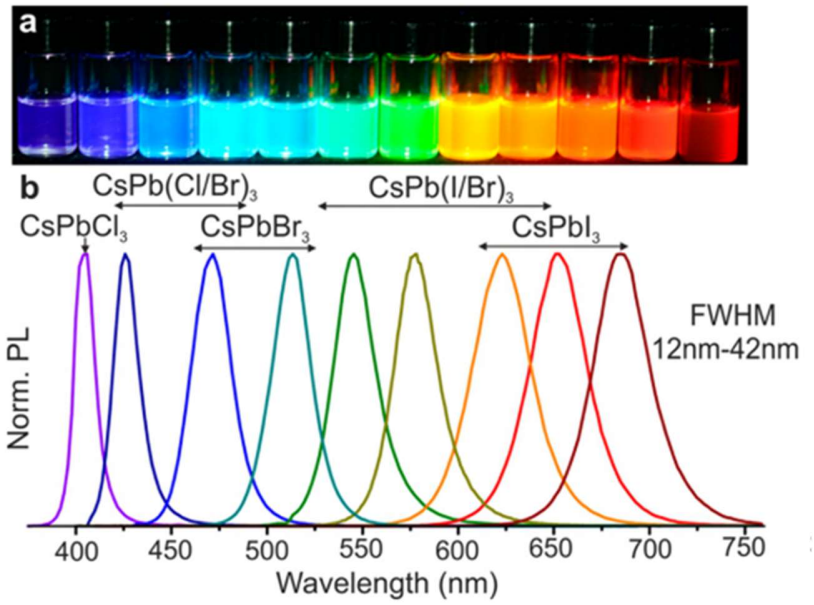


**Figure 2.11** Tuning of PL emission through halide-mixing[46]

X-site colour tuning for MHPs is typically carried out by (a) employing different halide sources or through a process called (b) anion exchange. Similar in concept to the mixed-dimensional MHPs, where varying degree of 2D cation incorporation into the 3D matrix results in mixed-dimensional systems, the mixing of the various halide sources yield MHPs with an intermediate emission relative to that of their pure halide counterparts. Anion exchange on the other hand, involves the substitution of the prevailing halide in the system with another.[37, 47] This process is generally viable for all halide combinations except for the Cl- and I- pair,[38] where the lattice mismatch and stark disparity in ionic radii between the two anions results in ineffective exchange process. While both approaches enable emission spanning the entire visible spectrum to be obtained, the tendency for halide segregation or leeching[48] to ensue, particularly at high driving voltages, necessitates mitigating actions to eliminate issues pertaining to spectral stability, such as through the use of a polymer-emitter blend.[48-49] A-site substitution too enables colour tuning to be carried out, but due to the smaller degree of tuning afforded through this method, X-site colour tuning is often preferred.

## 2.3 Perovskite-based Light Emitting Diodes (PeLEDs)

As compared to mature display technologies such as OLEDs and quantum dot LEDs (QLEDs), research into PeLEDs is still in its infancy. However, despite this, PeLEDs have charted an unprecedented rise in efficiency, achieving peak external quantum efficiency (EQE) values exceeding 20%[38, 50] within a short span of five years where OLEDs and QLEDs which have taken decades of research to do so (Figure 2.12).

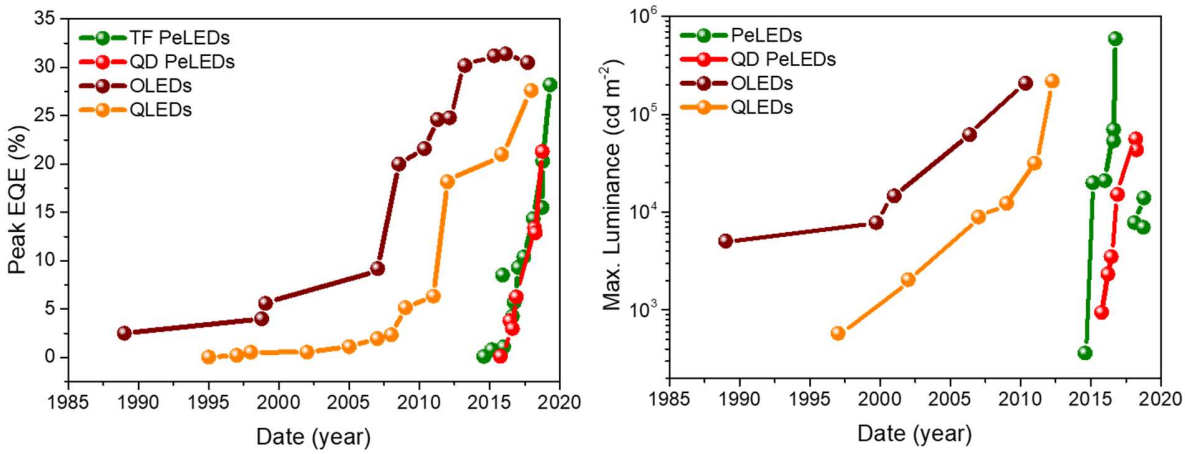


**Figure 2.12** Evolution of (left) EQE and (right) luminance of PeLEDs over the years as compared to OLEDs and quantum dot LEDs (QLEDs)[50]

### 2.3.1 Device architecture

The most commonly adopted architecture for PeLED is that of a triple-layered device which consists of an MHP emitter sandwiched between the electron and hole transporting layers. The PeLED device architecture draws inspiration from OLEDs, albeit the absence of electron and hole blocking layers due to the dual function of the charge-selective transport materials.[6] Figure 2.13 illustrates the schematic of a typical PeLED device architecture.

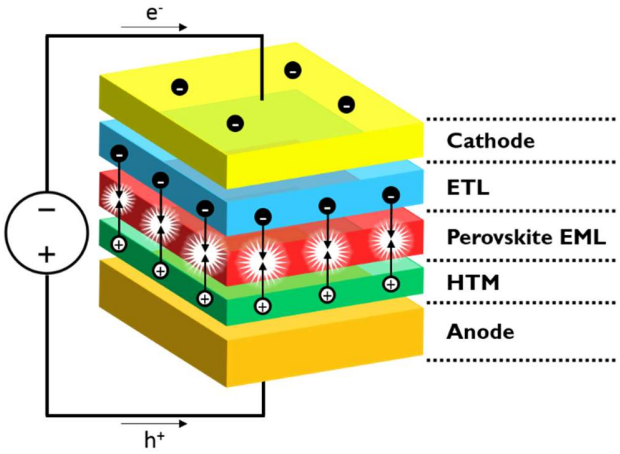


**Figure 2.13** Schematic of a PeLED device architecture

Numerous attempts have been made to enhance device performance through (a) improvements to quality of emitter via solvent engineering processing or perovskite-polymer blend,[31, 51] (b) tailoring the interfacial charge transport layers[52-53] to facilitate balanced charge carrier injection and (c) promoting radiative recombination for light generation through efficient confinement of charge carriers,[27, 34, 54-55] giving rise to peak EQEs of 6.2%[56], and 20.3%[57] and 20.1%[49] for blue-, green- and red-emitting thin film PeLEDs respectively.

### 2.3.2 Optical and electrical losses in PeLEDs

Akin to the working mechanism in OLEDs, photon generation in PeLEDs occur on radiative recombination of electron and hole in the emitter layer. As such, PeLED efficiency is affected by several factors such as fluorescence efficiency, the probability of radiative recombination for light emission and the efficiency of light extraction from the device.[11] Theoretically, improvement to any of these factors will yield enhancement to device performance. However, limitations to radiative recombination processes and light out coupling are the main suppressors[9, 30, 58] of PeLED efficiency. Radiative recombination process can be improved by allaying non-radiative recombination which can occur within the emitter as well as the interfaces. Electrical losses (Figure 2.14) in the emitter arise due

to Auger and trap assisted (defects) non-radiative recombination whereas at the interfaces, surface defect states act as charge carrier quenching sites resulting in loss of charge carrier injection efficiency and manifests in the form of higher operating voltages and current densities. The mismatch in injection efficiency into the emitter from the charge selective contacts result in carrier accumulation at the emitting layer interfaces, lowering device efficiency at high voltage and luminance.[59] As such, effective engineering of the interfacial layers is crucial to promote both efficient charge carrier transport into the emitter[24, 60] and effective light extraction from the device. Non-radiative recombination losses in the emitter and interfaces on the other hand, can be allayed through additive[61] and post-deposition[62] processing. Optical losses in PeLEDs stem from the differences in refractive indexes ($\eta$) of the layers within the device. This results in the trapping of generated photons in the emitter layer (total internal reflection) instead of their effective extraction out of the device. Modifications to substrates[63] or the transparent electrode/emitter interface[58] have been reported to be effective in tackling this issue.

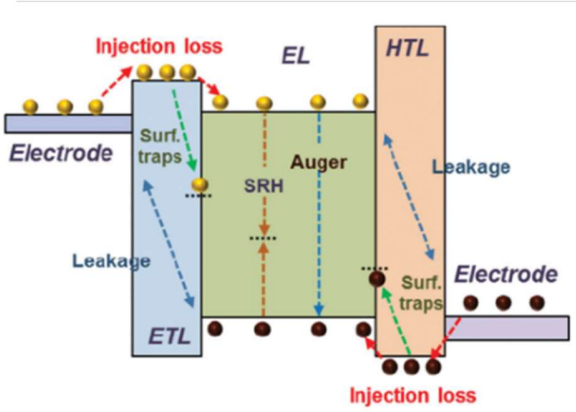


**Figure 2.14** Schematic of electrical loss mechanisms in PeLED devices[64]

## 2.4 Defects in Halide Perovskites

Despite reports of their defect tolerance,[65-66] MHPs are, in fact, not defect free. Instead, it refers to the shallow nature of defects present in these systems which do not exceedingly impact the optoelectronic properties of these materials, as evidenced by the superior properties exhibited. The reason for this lies in the location of the defects within the electronic band structure. A case in point would be the principle material, $CH_3NH_3PbI_3$,

where the high ionic character of $CH_3NH_3PbI_3$ and strong antibonding coupling between the Pb s-orbital and I p-orbital[30, 65] results in the formation of shallow defects such as interstitials ($I_i$ and $MA_i$), vacancies ($V_I$, $V_{MA}$, and $V_{Pb}$), and substitutions ($MA_{Pb}$, $Pb_{MA}$, and $MA_I$)[30] near the conduction and valence bands (Figure 2.15). Although these defects have low formation energies, their relatively inert character, enables the functional properties of the material to be preserved, unlike the mid-gap states present in other semiconductors such as CdSe and GaAs,[67] which form deep trap states and are detrimental to radiative recombination process.

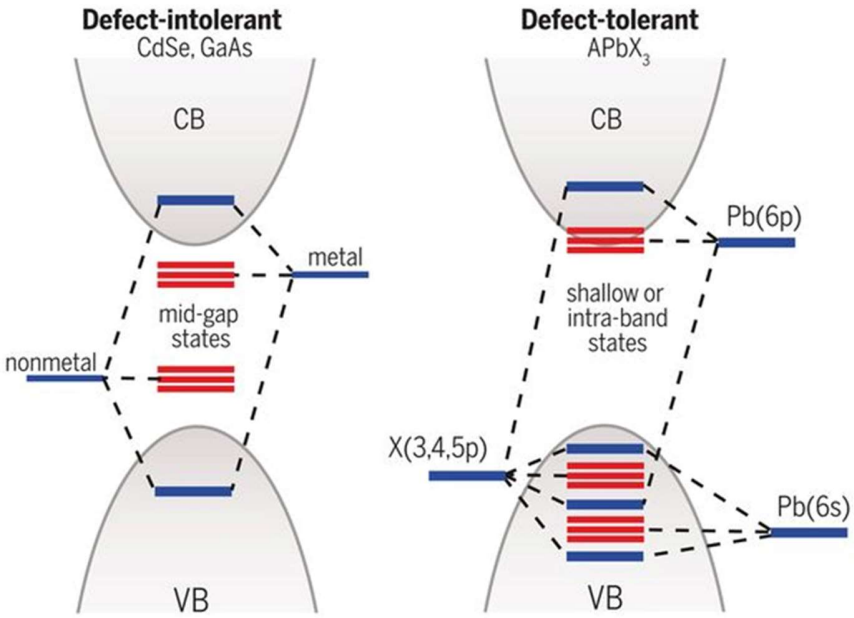


**Figure 2.15** Schematic of deep traps and shallow traps present in defect intolerant and defect tolerant systems respectively[67]

### 2.4.1 Effect of defects on PeLED characteristics

Low exciton binding energies simply refer to the ease of exciton dissociation to form free charges. This translates to the increased dependency of bimolecular radiative recombination on trap density and charge carrier density[68-70] (Figure 2.16). Trap assisted monomolecular recombination prevail at low carrier density regime owing to the defect filling process, whereas radiative recombination dominates at higher carrier density

regimes due to band filling.[69] This is consistent with the trend of increased photoluminescence quantum yield values of pristine MHPs at higher excitation intensities, where the presence of charge carriers is significantly higher than the defect density. However, the low current densities flowing through the PeLED during device operation[33, 71] is insufficient to completely fill these defects. As such, the poor efficiencies noted for these devices stem from the domination of defect filling process. To address the issue of low radiative recombination, defects can be alleviated or the charge carrier density within the emitter during device operation be modulated to facilitate effective bimolecular recombination.

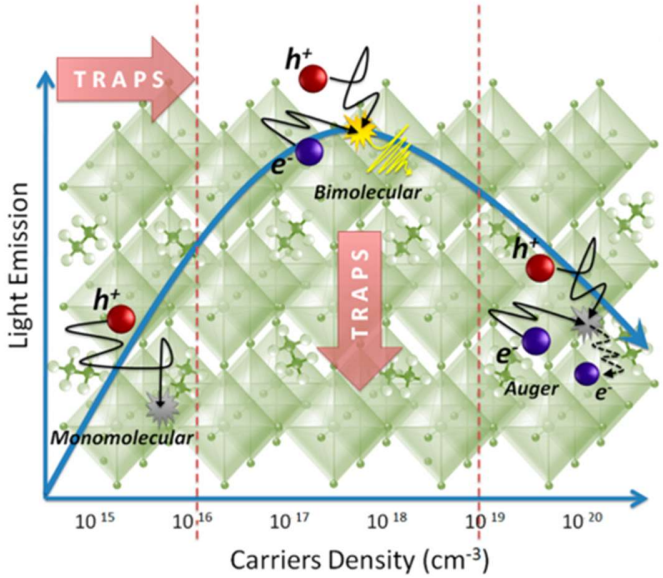


**Figure 2.16** Schematic of the electron-hole recombination processes occurring within MHPs at different carrier density regimes[29]

### 2.4.2 Influence of defects on stability of MHPs and PeLEDs

Despite their defect tolerant nature, the presence of shallow defects such as vacancies render MHPs susceptible to degradation due to the increase in tendency to bind with extrinsic molecules, such as moisture, for charge neutralization.[30] The water molecules can easily penetrate the perovskite structure and form intermediate monohydrate and dihydrate perovskite. The hydrogen bonds between water molecules and organic cations weakens the

bond between the latter and the lead halide octahedra, enabling rapid deprotonation of organic cation and facilitating effective degradation by external factors such as heat and electric field. Water protonates bromide, resulting in the formation of volatile hydrobromic acid (HBr) and lead bromide as decomposition byproducts.[72] The propensity for degradation is further exacerbated with the higher density of dangling bonds at the grain boundaries, facilitating ion loss. The degradation process is accelerated in the presence of light, with optical properties of $CH_3NH_3PbBr_3$ shown to decline under light illumination due to bromide ion activation[73-74] whereas thermal degradation initiates from the grain boundaries due to ion migration from the MHP lattice.[75] The extrinsic instability of MHPs is worsened in PeLEDs due to the interaction with the adjacent layers particularly under bias application. While the surface vacancies act as sites for non-radiative recombination, the high electric fields under which the active layer is subjected to during operation, spurs the ion migration process in the emitter. Driven to the charge selective contacts, the halide reacts with the metal cathode to form an insulating layer.[76] The vulnerability of MHPs to degradation due to environmental effects and ionic migration does not only influence its intrinsic stability, but also in PeLEDs due to the electrically driven interfacial reactions.

## 2.5 Managing Defects in MHPs

Despite its defect tolerant nature, the influence on intrinsic stability of MHPs and the corresponding PeLED is anything but. This has propelled the employment of various strategies to passivate them such as through non-stoichiometric precursor ratio to suppress formation of luminescence quenching lead atoms,[34, 77] additive incorporation; for grain size modulation[33, 54] and surface passivation as well as post deposition treatment for remedial of interfacial defects.[78-79] However, defect management for improved radiative recombination process need not be confined only to alleviating defects. Non-radiative losses can also be mitigated through the energy cascade concept where an engineered energetic emitter landscape facilitates rapid charge funneling process while simultaneously suppressing non-radiative recombination.

### 2.5.1 Passivation of defects

Despite the equimolar ratio of AX and $BX_2$ in the prepared precursor solutions, the stoichiometry of the final film often deviates from the expected. This results in the presence of $Pb^0$ and/or under coordination of lead, both of which are detrimental to device performance due to their luminescence quenching effect. Efforts to overcome this non-stoichiometry of elements include incorporation of excess precursors in the MHP solution,[34, 77] or even in the anti-solvent[17] used for the solvent engineering process. In either case, corresponding increase in B: X ratio towards the correct stoichiometry and photoluminescence intensity, are testament to the effectiveness of this approach. The surface treatment process is typically carried out using a Lewis base passivator. By leveraging on the knowledge that lead present in $CH_3NH_3PbBr_3$ is a lone electron pair acceptor, Lewis acid-base interaction is proposed to rectify this (lead) under-coordination[80]. Some examples of Lewis bases with electron donating abilities include amine,[81-82] carboxyl,[83-84] and phosphine oxide[36, 62] derivatives. Alternatively, ionic passivators such as alkyl ammonium halides, offering possibility of both cation and anion passivation, have also been utilized.

### 2.5.2 Energy cascade for mitigation of non-radiative recombination losses

Amalgamation of 2D and 3D MHPs have been proposed to achieve a balance between high radiative recombination efficiency afforded by the former, and good charge transport properties by the latter. While indeed the dimensional-mixing process enables the advantages of both systems to be reaped, the introduction of a 2D cation also templates the formation of an energetic emitter landscape.[85] Consisting of numerous domains of varying band gaps depending on the degree of 2D cation incorporation into the 3D metal halide network, the energetically engineered emitter acts as a conduit for charge localization by functioning similarly to quantum wells,[86-87] thus enabling effective exciton confinement.[88] On injection of charge carriers into the larger band gap domains, the charge carriers are funneled to the energetically favoured lower band gap domains in a process termed as energy cascade.[54-55, 62] The rapid charge transfer supersedes non-radiative processes in the

larger band gap domains and concentrates the charges in the smaller band gap domains. This not only leads to the mitigation of non-radiative loss but also localizes charge carriers for enhanced bimolecular recombination in the emitting lower band gap domains. Moreover, only the trap states within the smaller band gap domains need to be filled as opposed to the case in pure 3D MHPs.[54] Due to the efficacy of the energy cascade process in mixed-dimensional films, high efficiency PeLEDs can be achieved even at low current densities.

## 2.6 Challenges

With the high colour purity and tunability offered by MHPs, it is not difficult to comprehend the attractiveness of this class of materials for light emission applications. However, the low binding energies present a challenge for effective radiative recombination. Furthermore, low photoluminescence quantum yield (PLQY) persists at low charge carrier densities due to domination of trap filling monomolecular recombination process with bimolecular recombination process proceeding only at higher current densities.

To overcome the issue relating to low exciton binding energy and inefficient radiative recombination at low current densities, the following approaches are proposed:

- Enhance exciton confinement
- Alleviate defects (traps)
- Suppress non-radiative recombination process

Exciton confinement can be achieved through geometric confinement and/or intrinsic confinement. Employing geometric confinement entails reducing grain or particle size to spatially constrain the charge carriers. However, doing so would lead to an increase in grain boundary density of grains which is undesirable due to the consequence towards non-radiative recombination. Processing techniques enabling both grain size modulation and passivation would thus be required to allow the advantage of spatial confinement to be reaped. While passivation has been shown to be a successful route for remedial of defects,

the choice of passivator is crucial to ensure that device performance does not suffer due to increased series resistance. Furthermore, depending on the type of passivator employed, other variations to emitter properties such as energy band level realignment and conductivity, which will affect the effectiveness of charge carrier recombination, may emerge. Meanwhile, defect alleviation is not the only approach to mitigate defects in the emitter. Monomolecular recombination can also be suppressed by engineering an energetic landscape consisting of multi-dimensional MHP domains. The energetically favoured charge funneling process concentrates the carriers into the smallest band gap domains, promoting bimolecular recombination. However, despite the effectiveness of this process in managing the defects, no clear guideline has been proposed on the type of 2D cation which would enable the templating of efficient energy cascade process.

# References

1. Bender, V. C.; Marchesan, T. B.; Alonso, J. M., Solid-State Lighting: A Concise Review of the State of the Art on LED and OLED Modeling. *IEEE Industrial Electronics Magazine* **2015,** *9* (2), 6-16.

2. Lighting, P. Intro to OLED Technology. https://www.premierltg.com/intro-to-oled-technology/ (accessed 13 August 2019).

3. newegg LG C8 65" OLED 4K HDR Dolby Atmos Smart TV with AI ThinQ OLED65C8PUA. https://www.newegg.com/p/N82E16889007642 (accessed 13 August 2019).

4. Microtech, I. Ultra-thin flexible OLED screen can flutter in the wind like a flag. https://www.itmicrotech.com/ultra-thin-flexible-oled-screen-can-flutter-in-the-wind-like-a-flag/ (accessed 13 August 2019).

5. Newsletter, O. D. LG Display showcases OLED light panels at IFA 2016 in Berlin. http://www.osadirect.com/news/article/1774/lg-display-showcases-oled-light-panels-at-ifa-2016-in-berlin/ (accessed 13 August 2019).

6. Reineke, S.; Thomschke, M.; Lüssem, B.; Leo, K., White organic light-emitting diodes: Status and perspective. *Reviews of Modern Physics* **2013,** *85* (3), 1245-1293.

7. Kwon, R. P. a. J. H., High Efficiency Red Phosphorescent Organic Light-Emitting Diodes with Simples Structure. In *Organic Light Emitting Diode - Material, Process and Devices*, Ko, S. H., Ed. InTech Open: 2011.

8. Research, L. Novaled Develops World's Most Power-Efficient Fluorescent White PIN OLEDs. https://www.led-professional.com/technology/light-generation/novaled-develops-worlds-most-power-efficient-fluorescent-white-pin-oleds (accessed 13 August 2019).

9. Brütting, W.; Frischeisen, J.; Schmidt, T. D.; Scholz, B. J.; Mayr, C., Device efficiency of organic light-emitting diodes: Progress by improved light outcoupling. *physica status solidi (a)* **2013,** *210* (1), 44-65.

10. Thejo Kalyani, N.; Dhoble, S. J., Organic light emitting diodes: Energy saving lighting technology—A review. *Renewable and Sustainable Energy Reviews* **2012,** *16* (5), 2696-2723.

11. Geffroy, B.; le Roy, P.; Prat, C., Organic light-emitting diode (OLED) technology: materials, devices and display technologies. *Polymer International* **2006,** *55* (6), 572-582.

12. Boix, P. P.; Nonomura, K.; Mathews, N.; Mhaisalkar, S. G., Current progress and future perspectives for organic/inorganic perovskite solar cells. *Materials Today* **2014,** *17* (1), 16-23.

13. Green, M. A.; Ho-Baillie, A.; Snaith, H. J., The emergence of perovskite solar cells. *Nat Photon* **2014,** *8* (7), 506-514.

14. Li, C.; Lu, X.; Ding, W.; Feng, L.; Gao, Y.; Guo, Z., Formability of ABX3 (X = F, Cl, Br, I) halide perovskites. *Acta Crystallographica Section B* **2008,** *64* (6), 702-707.

15. Chen, Q.; De Marco, N.; Yang, Y.; Song, T.-B.; Chen, C.-C.; Zhao, H.; Hong, Z.; Zhou, H.; Yang, Y., Under the spotlight: The organic–inorganic hybrid halide perovskite for optoelectronic applications. *Nano Today* **2015,** *10* (3), 355-396.

16. Kumar, M. H.; Dharani, S.; Leong, W. L.; Boix, P. P.; Prabhakar, R. R.; Baikie, T.; Shi, C.; Ding, H.; Ramesh, R.; Asta, M.; Graetzel, M.; Mhaisalkar, S. G.; Mathews, N., Lead-Free Halide Perovskite Solar Cells with High Photocurrents Realized Through Vacancy Modulation. *Advanced Materials* **2014,** *26* (41), 7122-7127.

17. Harikesh, P. C.; Mulmudi, H. K.; Ghosh, B.; Goh, T. W.; Teng, Y. T.; Thirumal, K.; Lockrey, M.; Weber, K.; Koh, T. M.; Li, S.; Mhaisalkar, S.; Mathews, N., Rb as an Alternative Cation for Templating Inorganic Lead-Free Perovskites for Solution Processed Photovoltaics. *Chemistry of Materials* **2016,** *28* (20), 7496-7504.

18. Xu, L.; Yuan, S.; Zeng, H.; Song, J., A comprehensive review of doping in perovskite nanocrystals/quantum dots: evolution of structure, electronics, optics, and light-emitting diodes. *Materials Today Nano* **2019,** *6*, 100036.

19. Yin, W.-J.; Shi, T.; Yan, Y., Unique Properties of Halide Perovskites as Possible Origins of the Superior Solar Cell Performance. *Advanced Materials* **2014,** *26* (27), 4653-4658.

20. Kim, H.-S.; Im, S. H.; Park, N.-G., Organolead Halide Perovskite: New Horizons in Solar Cell Research. *The Journal of Physical Chemistry C* **2014,** *118* (11), 5615-5625.

21. Singh, S. P.; Nagarjuna, P., Organometal halide perovskites as useful materials in sensitized solar cells. *Dalton transactions* **2014,** *43* (14), 5247-51.

22. Wehrenfennig, C.; Eperon, G. E.; Johnston, M. B.; Snaith, H. J.; Herz, L. M., High Charge Carrier Mobilities and Lifetimes in Organolead Trihalide Perovskites. *Advanced Materials* **2014,** *26* (10), 1584-1589.

23. Ponseca, C. S.; Savenije, T. J.; Abdellah, M.; Zheng, K.; Yartsev, A.; Pascher, T.; Harlang, T.; Chabera, P.; Pullerits, T.; Stepanov, A.; Wolf, J.-P.; Sundström, V., Organometal Halide Perovskite Solar Cell Materials Rationalized: Ultrafast Charge Generation, High and Microsecond-Long Balanced Mobilities, and Slow Recombination. *Journal of the American Chemical Society* **2014,** *136* (14), 5189-5192.

24. Xing, G.; Mathews, N.; Sun, S.; Lim, S. S.; Lam, Y. M.; Grätzel, M.; Mhaisalkar, S.; Sum, T. C., Long-Range Balanced Electron- and Hole-Transport Lengths in Organic-Inorganic CH3NH3PbI3. *Science* **2013,** *342* (6156), 344-347.

25. Tan, Z.-K.; Moghaddam, R. S.; Lai, M. L.; Docampo, P.; Higler, R.; Deschler, F.; Price, M.; Sadhanala, A.; Pazos, L. M.; Credgington, D.; Hanusch, F.; Bein, T.; Snaith, H. J.; Friend, R. H., Bright light-emitting diodes based on organometal halide perovskite. *Nat Nano* **2014,** *9* (9), 687-692.

26. Deschler, F.; Price, M.; Pathak, S.; Klintberg, L. E.; Jarausch, D.-D.; Higler, R.; Hüttner, S.; Leijtens, T.; Stranks, S. D.; Snaith, H. J.; Atatüre, M.; Phillips, R. T.; Friend, R. H., High Photoluminescence Efficiency and Optically Pumped Lasing in Solution-Processed Mixed Halide Perovskite Semiconductors. *The Journal of Physical Chemistry Letters* **2014,** *5* (8), 1421-1426.

27. Ng, Y. F.; Jamaludin, N. F.; Yantara, N.; Li, M.; Irukuvarjula, V. K. R.; Demir, H. V.; Sum, T. C.; Mhaisalkar, S.; Mathews, N., Rapid Crystallization of All-Inorganic CsPbBr3 Perovskite for High-Brightness Light-Emitting Diodes. *ACS Omega* **2017,** *2* (6), 2757-2764.

28. Yu, J. C.; Kim, D. W.; Kim, D. B.; Jung, E. D.; Park, J. H.; Lee, A.-Y.; Lee, B. R.; Di Nuzzo, D.; Friend, R. H.; Song, M. H., Improving the Stability and Performance of Perovskite Light-Emitting Diodes by Thermal Annealing Treatment. *Advanced Materials* **2016,** *28* (32), 6906-6913.

29. Colella, S.; Mazzeo, M.; Rizzo, A.; Gigli, G.; Listorti, A., The Bright Side of Perovskites. *The Journal of Physical Chemistry Letters* **2016,** *7* (21), 4322-4334.

30. Lee, S.; Kim, D. B.; Yu, J. C.; Jang, C. H.; Park, J. H.; Lee, B. R.; Song, M. H., Versatile Defect Passivation Methods for Metal Halide Perovskite Materials and their Application to Light-Emitting Devices. *Advanced Materials* **2019,** *31* (20), 1805244.

31. Li, G.; Tan, Z.-K.; Di, D.; Lai, M. L.; Jiang, L.; Lim, J. H.-W.; Friend, R. H.; Greenham, N. C., Efficient Light-Emitting Diodes Based on Nanocrystalline Perovskite in a Dielectric Polymer Matrix. *Nano Letters* **2015,** *15* (4), 2640-2644.

32. Bade, S. G. R.; Shan, X.; Hoang, P. T.; Li, J.; Geske, T.; Cai, L.; Pei, Q.; Wang, C.; Yu, Z., Stretchable Light-Emitting Diodes with Organometal-Halide-Perovskite–Polymer Composite Emitters. *Advanced Materials* **2017,** *29* (23), 1607053.

33. Kulkarni, S. A.; Muduli, S.; Xing, G.; Yantara, N.; Li, M.; Chen, S.; Sum, T. C.; Mathews, N.; White, T. J.; Mhaisalkar, S. G., Modulating Excitonic Recombination Effects through One-Step Synthesis of Perovskite Nanoparticles for Light-Emitting Diodes. *ChemSusChem* **2017,** *10* (19), 3818-3824.

34. Cho, H.; Jeong, S.-H.; Park, M.-H.; Kim, Y.-H.; Wolf, C.; Lee, C.-L.; Heo, J. H.; Sadhanala, A.; Myoung, N.; Yoo, S.; Im, S. H.; Friend, R. H.; Lee, T.-W., Overcoming the electroluminescence efficiency limitations of perovskite light-emitting diodes. *Science* **2015,** *350* (6265), 1222-1225.

35. Veldhuis, S. A.; Ng, Y. F.; Ahmad, R.; Bruno, A.; Jamaludin, N. F.; Damodaran, B.; Mathews, N.; Mhaisalkar, S. G., Crown Ethers Enable Room-Temperature Synthesis of CsPbBr3 Quantum Dots for Light-Emitting Diodes. *ACS Energy Letters* **2018,** *3* (3), 526-531.

36. Brown, A. A. M.; Hooper, T. J. N.; Veldhuis, S. A.; Chin, X. Y.; Bruno, A.; Vashishtha, P.; Tey, J. N.; Jiang, L.; Damodaran, B.; Pu, S. H.; Mhaisalkar, S. G.; Mathews, N., Self-assembly of a robust hydrogen-bonded octylphosphonate network on cesium lead bromide perovskite nanocrystals for light-emitting diodes. *Nanoscale* **2019,** *11* (25), 12370-12380.

37. Chiba, T.; Hayashi, Y.; Ebe, H.; Hoshi, K.; Sato, J.; Sato, S.; Pu, Y.-J.; Ohisa, S.; Kido, J., Anion-exchange red perovskite quantum dots with ammonium iodine salts for highly efficient light-emitting devices. *Nature Photonics* **2018,** *12* (11), 681-687.

38. Veldhuis, S. A.; Boix, P. P.; Yantara, N.; Li, M.; Sum, T. C.; Mathews, N.; Mhaisalkar, S. G., Perovskite Materials for Light-Emitting Diodes and Lasers. *Advanced Materials* **2016,** *28* (32), 6804-6834.

39. Cao, D. H.; Stoumpos, C. C.; Farha, O. K.; Hupp, J. T.; Kanatzidis, M. G., 2D Homologous Perovskites as Light-Absorbing Materials for Solar Cell Applications. *Journal of the American Chemical Society* **2015,** *137* (24), 7843-7850.

40. Gauthron, K.; Lauret, J. S.; Doyennette, L.; Lanty, G.; Al Choueiry, A.; Zhang, S. J.; Brehier, A.; Largeau, L.; Mauguin, O.; Bloch, J.; Deleporte, E., Optical spectroscopy of two-dimensional layered (C6H5C2H4-NH3)2-PbI4 perovskite. *Opt. Express* **2010,** *18* (6), 5912-5919.

41. Yangui, A.; Garrot, D.; Lauret, J. S.; Lusson, A.; Bouchez, G.; Deleporte, E.; Pillet, S.; Bendeif, E. E.; Castro, M.; Triki, S.; Abid, Y.; Boukheddaden, K., Optical Investigation of Broadband White-Light Emission in Self-Assembled Organic–Inorganic Perovskite (C6H11NH3)2PbBr4. *The Journal of Physical Chemistry C* **2015,** *119* (41), 23638-23647.

42. Dohner, E. R.; Hoke, E. T.; Karunadasa, H. I., Self-Assembly of Broadband White-Light Emitters. *Journal of the American Chemical Society* **2014,** *136* (5), 1718-1721.

43. Dohner, E. R.; Jaffe, A.; Bradshaw, L. R.; Karunadasa, H. I., Intrinsic White-Light Emission from Layered Hybrid Perovskites. *Journal of the American Chemical Society* **2014,** *136* (38), 13154-13157.

44. Mitzi, D. B.; Chondroudis, K.; Kagan, C. R., Design, Structure, and Optical Properties of Organic−Inorganic Perovskites Containing an Oligothiophene Chromophore. *Inorganic Chemistry* **1999,** *38* (26), 6246-6256.

45. Kim, Y.-H.; Cho, H.; Lee, T.-W., Metal halide perovskite light emitters. *Proceedings of the National Academy of Sciences* **2016,** *113* (42), 11694-11702.

46. Protesescu, L.; Yakunin, S.; Bodnarchuk, M. I.; Krieg, F.; Caputo, R.; Hendon, C. H.; Yang, R. X.; Walsh, A.; Kovalenko, M. V., Nanocrystals of Cesium Lead Halide Perovskites (CsPbX3, X = Cl, Br, and I): Novel Optoelectronic Materials Showing Bright Emission with Wide Color Gamut. *Nano Letters* **2015,** *15* (6), 3692-3696.

47. Akkerman, Q. A.; D'Innocenzo, V.; Accornero, S.; Scarpellini, A.; Petrozza, A.; Prato, M.; Manna, L., Tuning the Optical Properties of Cesium Lead Halide Perovskite

Nanocrystals by Anion Exchange Reactions. *Journal of the American Chemical Society* **2015,** *137* (32), 10276-10281.

48. Klug, M. T.; Osherov, A.; Haghighirad, A. A.; Stranks, S. D.; Brown, P. R.; Bai, S.; Wang, J. T. W.; Dang, X.; Bulović, V.; Snaith, H. J.; Belcher, A. M., Tailoring metal halide perovskites through metal substitution: influence on photovoltaic and material properties. *Energy & Environmental Science* **2017,** *10* (1), 236-246.

49. Zhao, B.; Bai, S.; Kim, V.; Lamboll, R.; Shivanna, R.; Auras, F.; Richter, J. M.; Yang, L.; Dai, L.; Alsari, M.; She, X.-J.; Liang, L.; Zhang, J.; Lilliu, S.; Gao, P.; Snaith, H. J.; Wang, J.; Greenham, N. C.; Friend, R. H.; Di, D., High-efficiency perovskite–polymer bulk heterostructure light-emitting diodes. *Nature Photonics* **2018,** *12* (12), 783-789.

50. Chin, X. Y.; Perumal, A.; Bruno, A.; Yantara, N.; Veldhuis, S. A.; Martínez-Sarti, L.; Chandran, B.; Chirvony, V.; Lo, A. S.-Z.; So, J.; Soci, C.; Grätzel, M.; Bolink, H. J.; Mathews, N.; Mhaisalkar, S. G., Self-assembled hierarchical nanostructured perovskites enable highly efficient LEDs via an energy cascade. *Energy & Environmental Science* **2018,** *11* (7), 1770-1778.

51. Bade, S. G. R.; Li, J.; Shan, X.; Ling, Y.; Tian, Y.; Dilbeck, T.; Besara, T.; Geske, T.; Gao, H.; Ma, B.; Hanson, K.; Siegrist, T.; Xu, C.; Yu, Z., Fully Printed Halide Perovskite Light-Emitting Diodes with Silver Nanowire Electrodes. *ACS Nano* **2016,** *10* (2), 1795-1801.

52. Wang, J.; Wang, N.; Jin, Y.; Si, J.; Tan, Z.-K.; Du, H.; Cheng, L.; Dai, X.; Bai, S.; He, H.; Ye, Z.; Lai, M. L.; Friend, R. H.; Huang, W., Interfacial Control Toward Efficient and Low-Voltage Perovskite Light-Emitting Diodes. *Advanced Materials* **2015,** *27* (14), 2311-2316.

53. Ling, Y.; Yuan, Z.; Tian, Y.; Wang, X.; Wang, J. C.; Xin, Y.; Hanson, K.; Ma, B.; Gao, H., Bright Light-Emitting Diodes Based on Organometal Halide Perovskite Nanoplatelets. *Advanced Materials* **2016,** *28* (2), 305-311.

54. Ng, Y. F.; Kulkarni, S. A.; Parida, S.; Jamaludin, N. F.; Yantara, N.; Bruno, A.; Soci, C.; Mhaisalkar, S.; Mathews, N., Highly efficient Cs-based perovskite light-emitting diodes enabled by energy funnelling. *Chemical Communications* **2017,** *53* (88), 12004-12007.

55. Yantara, N.; Bruno, A.; Iqbal, A.; Jamaludin, N. F.; Soci, C.; Mhaisalkar, S.; Mathews, N., Designing Efficient Energy Funneling Kinetics in Ruddlesden–Popper Perovskites for High-Performance Light-Emitting Diodes. *Advanced Materials* **2018,** *30* (33), 1800818.

56. Vashishtha, P.; Ng, M.; Shivarudraiah, S. B.; Halpert, J. E., High Efficiency Blue and Green Light-Emitting Diodes Using Ruddlesden–Popper Inorganic Mixed Halide Perovskites with Butylammonium Interlayers. *Chemistry of Materials* **2019,** *31* (1), 83-89.

57. Lin, K.; Xing, J.; Quan, L. N.; de Arquer, F. P. G.; Gong, X.; Lu, J.; Xie, L.; Zhao, W.; Zhang, D.; Yan, C.; Li, W.; Liu, X.; Lu, Y.; Kirman, J.; Sargent, E. H.; Xiong, Q.; Wei, Z., Perovskite light-emitting diodes with external quantum efficiency exceeding 20 per cent. *Nature* **2018,** *562* (7726), 245-248.

58. Shen, Y.; Cheng, L.-P.; Li, Y.-Q.; Li, W.; Chen, J.-D.; Lee, S.-T.; Tang, J.-X., High-Efficiency Perovskite Light-Emitting Diodes with Synergetic Outcoupling Enhancement. *Advanced Materials* **2019,** *31* (24), 1901517.

59. Dong, Q.; Fang, Y.; Shao, Y.; Mulligan, P.; Qiu, J.; Cao, L.; Huang, J., Electron-hole diffusion lengths >175 μm in solution-grown CH3NH3PbI3 single crystals. *Science* **2015,** *347* (6225), 967-970.

60. Stranks, S. D.; Eperon, G. E.; Grancini, G.; Menelaou, C.; Alcocer, M. J. P.; Leijtens, T.; Herz, L. M.; Petrozza, A.; Snaith, H. J., Electron-Hole Diffusion Lengths Exceeding 1 Micrometer in an Organometal Trihalide Perovskite Absorber. *Science* **2013,** *342* (6156), 341-344.

61. Ban, M.; Zou, Y.; Rivett, J. P. H.; Yang, Y.; Thomas, T. H.; Tan, Y.; Song, T.; Gao, X.; Credgington, D.; Deschler, F.; Sirringhaus, H.; Sun, B., Solution-processed perovskite light emitting diodes with efficiency exceeding 15% through additive-controlled nanostructure tailoring. *Nature Communications* **2018,** *9* (1), 3892.

62. Yang, X.; Zhang, X.; Deng, J.; Chu, Z.; Jiang, Q.; Meng, J.; Wang, P.; Zhang, L.; Yin, Z.; You, J., Efficient green light-emitting diodes based on quasi-two-dimensional composition and phase engineered perovskite with surface passivation. *Nature Communications* **2018,** *9* (1), 570.

63. Zhang, Q.; Tavakoli, M. M.; Gu, L.; Zhang, D.; Tang, L.; Gao, Y.; Guo, J.; Lin, Y.; Leung, S.-F.; Poddar, S.; Fu, Y.; Fan, Z., Efficient metal halide perovskite light-emitting

diodes with significantly improved light extraction on nanophotonic substrates. *Nature Communications* **2019,** *10* (1), 727.

64. Veldhuis, S. A.; Boix, P. P.; Yantara, N.; Li, M.; Sum, T. C.; Mathews, N.; Mhaisalkar, S. G., Perovskite Materials for Light-Emitting Diodes and Lasers. *Advanced Materials* **2016**, n/a-n/a.

65. Steirer, K. X.; Schulz, P.; Teeter, G.; Stevanovic, V.; Yang, M.; Zhu, K.; Berry, J. J., Defect Tolerance in Methylammonium Lead Triiodide Perovskite. *ACS Energy Letters* **2016,** *1* (2), 360-366.

66. Kang, J.; Wang, L.-W., High Defect Tolerance in Lead Halide Perovskite CsPbBr3. *The Journal of Physical Chemistry Letters* **2017,** *8* (2), 489-493.

67. Kovalenko, M. V.; Protesescu, L.; Bodnarchuk, M. I., Properties and potential optoelectronic applications of lead halide perovskite nanocrystals. *Science* **2017,** *358* (6364), 745.

68. Miyata, A.; Mitioglu, A.; Plochocka, P.; Portugall, O.; Wang, J. T.-W.; Stranks, S. D.; Snaith, H. J.; Nicholas, R. J., Direct measurement of the exciton binding energy and effective masses for charge carriers in organic–inorganic tri-halide perovskites. *Nature Physics* **2015,** *11*, 582.

69. Stranks, S. D.; Burlakov, V. M.; Leijtens, T.; Ball, J. M.; Goriely, A.; Snaith, H. J., Recombination Kinetics in Organic-Inorganic Perovskites: Excitons, Free Charge, and Subgap States. *Physical Review Applied* **2014,** *2* (3), 034007.

70. Xing, G.; Wu, B.; Wu, X.; Li, M.; Du, B.; Wei, Q.; Guo, J.; Yeow, E. K. L.; Sum, T. C.; Huang, W., Transcending the slow bimolecular recombination in lead-halide perovskites for electroluminescence. *Nature Communications* **2017,** *8*, 14558.

71. Wu, X.; Trinh, M. T.; Niesner, D.; Zhu, H.; Norman, Z.; Owen, J. S.; Yaffe, O.; Kudisch, B. J.; Zhu, X. Y., Trap States in Lead Iodide Perovskites. *Journal of the American Chemical Society* **2015,** *137* (5), 2089-2096.

72. Boyd, C. C.; Cheacharoen, R.; Leijtens, T.; McGehee, M. D., Understanding Degradation Mechanisms and Improving Stability of Perovskite Photovoltaics. *Chemical Reviews* **2019,** *119* (5), 3418-3451.

73. Wen, X.; Sheng, R.; Ho-Baillie, A. W. Y.; Benda, A.; Woo, S.; Ma, Q.; Huang, S.; Green, M. A., Morphology and Carrier Extraction Study of Organic–Inorganic Metal

Halide Perovskite by One- and Two-Photon Fluorescence Microscopy. *The Journal of Physical Chemistry Letters* **2014,** *5* (21), 3849-3853.

74. Yuan, H.; Debroye, E.; Janssen, K.; Naiki, H.; Steuwe, C.; Lu, G.; Moris, M.; Orgiu, E.; Uji-i, H.; De Schryver, F.; Samorì, P.; Hofkens, J.; Roeffaers, M., Degradation of Methylammonium Lead Iodide Perovskite Structures through Light and Electron Beam Driven Ion Migration. *The Journal of Physical Chemistry Letters* **2016,** *7* (3), 561-566.

75. Park, C.; Ko, H.; Sin, D. H.; Song, K. C.; Cho, K., Organometal Halide Perovskite Solar Cells with Improved Thermal Stability via Grain Boundary Passivation Using a Molecular Additive. *Advanced Functional Materials* **2017,** *27* (42), 1703546.

76. Back, H.; Kim, G.; Kim, J.; Kong, J.; Kim, T. K.; Kang, H.; Kim, H.; Lee, J.; Lee, S.; Lee, K., Achieving long-term stable perovskite solar cells via ion neutralization. *Energy & Environmental Science* **2016,** *9* (4), 1258-1263.

77. Yantara, N.; Bhaumik, S.; Yan, F.; Sabba, D.; Dewi, H. A.; Mathews, N.; Boix, P. P.; Demir, H. V.; Mhaisalkar, S., Inorganic Halide Perovskites for Efficient Light-Emitting Diodes. *The Journal of Physical Chemistry Letters* **2015,** *6* (21), 4360-4364.

78. Naphade, R.; Zhao, B.; Richter, J. M.; Booker, E.; Krishnamurthy, S.; Friend, R. H.; Sadhanala, A.; Ogale, S., High Quality Hybrid Perovskite Semiconductor Thin Films with Remarkably Enhanced Luminescence and Defect Suppression via Quaternary Alkyl Ammonium Salt Based Treatment. *Advanced Materials Interfaces* **2017,** *4* (19), 1700562-n/a.

79. Chih, Y.-K.; Wang, J.-C.; Yang, R.-T.; Liu, C.-C.; Chang, Y.-C.; Fu, Y.-S.; Lai, W.-C.; Chen, P.; Wen, T.-C.; Huang, Y.-C.; Tsao, C.-S.; Guo, T.-F., NiOx Electrode Interlayer and CH3NH2/CH3NH3PbBr3 Interface Treatment to Markedly Advance Hybrid Perovskite-Based Light-Emitting Diodes. *Advanced Materials* **2016**, n/a-n/a.

80. Sharenko, A.; Toney, M. F., Relationships between Lead Halide Perovskite Thin-Film Fabrication, Morphology, and Performance in Solar Cells. *Journal of the American Chemical Society* **2016,** *138* (2), 463-470.

81. Lee, S.; Park, J. H.; Lee, B. R.; Jung, E. D.; Yu, J. C.; Di Nuzzo, D.; Friend, R. H.; Song, M. H., Amine-Based Passivating Materials for Enhanced Optical Properties and Performance of Organic–Inorganic Perovskites in Light-Emitting Diodes. *The Journal of Physical Chemistry Letters* **2017,** *8* (8), 1784-1792.

82. Lee, S.; Park, J. H.; Nam, Y. S.; Lee, B. R.; Zhao, B.; Di Nuzzo, D.; Jung, E. D.; Jeon, H.; Kim, J.-Y.; Jeong, H. Y.; Friend, R. H.; Song, M. H., Growth of Nanosized Single Crystals for Efficient Perovskite Light-Emitting Diodes. *ACS Nano* **2018,** *12* (4), 3417-3423.

83. Zhang, T.; Xie, L.; Chen, L.; Guo, N.; Li, G.; Tian, Z.; Mao, B.; Zhao, Y., In Situ Fabrication of Highly Luminescent Bifunctional Amino Acid Crosslinked 2D/3D NH3C4H9COO(CH3NH3PbBr3)n Perovskite Films. *Advanced Functional Materials* **2017,** *27* (1), 1603568.

84. Wang, N.; Cheng, L.; Si, J.; Liang, X.; Jin, Y.; Wang, J.; Huang, W., Morphology control of perovskite light-emitting diodes by using amino acid self-assembled monolayers. *Applied Physics Letters* **2016,** *108* (14), 141102.

85. Quan, L. N.; Zhao, Y.; García de Arquer, F. P.; Sabatini, R.; Walters, G.; Voznyy, O.; Comin, R.; Li, Y.; Fan, J. Z.; Tan, H.; Pan, J.; Yuan, M.; Bakr, O. M.; Lu, Z.; Kim, D. H.; Sargent, E. H., Tailoring the Energy Landscape in Quasi-2D Halide Perovskites Enables Efficient Green-Light Emission. *Nano Letters* **2017,** *17* (6), 3701-3709.

86. Silver, S.; Dai, Q.; Li, H.; Brédas, J.-L.; Kahn, A., Quantum Well Energetics of an n = 2 Ruddlesden–Popper Phase Perovskite. *Advanced Energy Materials* **2019,** *9* (25), 1901005.

87. Yu, M.; Yi, C.; Wang, N.; Zhang, L.; Zou, R.; Tong, Y.; Chen, H.; Cao, Y.; He, Y.; Wang, Y.; Xu, M.; Liu, Y.; Jin, Y.; Huang, W.; Wang, J., Control of Barrier Width in Perovskite Multiple Quantum Wells for High Performance Green Light–Emitting Diodes. *Advanced Optical Materials* **2019,** *7* (3), 1801575.

88. Wang, N.; Cheng, L.; Ge, R.; Zhang, S.; Miao, Y.; Zou, W.; Yi, C.; Sun, Y.; Cao, Y.; Yang, R.; Wei, Y.; Guo, Q.; Ke, Y.; Yu, M.; Jin, Y.; Liu, Y.; Ding, Q.; Di, D.; Yang, L.; Xing, G.; Tian, H.; Jin, C.; Gao, F.; Friend, R. H.; Wang, J.; Huang, W., Perovskite light-emitting diodes based on solution-processed self-organized multiple quantum wells. *Nat Photon* **2016,** *10* (11), 699-704.

# Chapter 3

# Experimental Methodology

*This section covers the processing of metal halide perovskites for defect passivation and the engineering of an energetically landscaped emitter, the fabrication of perovskite-based light emitting devices as well as the characterization techniques involved in the study of these materials for efficient light emission.*

## 3.1 Material Synthesis

### 3.1.1 Molecular design of two-dimensional perovskite cation for energy cascade

Synthesis procedures for 1-(2-Ammonioethyl)-1H-imidazol-3-ium dibromide and 2-Phenethylammonium bromide

General procedure for preparation of 1-(2-Ammonioethyl)-1H-imidazol-3-ium dibromide and 2-Phenethylammonium bromide is similar to that of other ammonium bromide salts. To a round bottom flask containing ethanol and the requisite amine cooled to 0°C, a stoichiometric amount of concentrated hydrobromic acid is added. After stirring the solution for 1 hour, all volatile solvents are removed using a rotary evaporator. The solids obtained are then washed copiously with diethyl ether and dried under vacuum at 50°C overnight. The resultant 1-(2-Ammonioethyl)-1H-imidazol-3-ium dibromide (ImEABr) and 2-Phenethylammonium bromide (PEABr) are isolated as white solids (1.52g; 84% yield and 1.13g; 85% yield respectively).

Synthesis procedure for 1-(2-Ammonioethyl)pyridin-1-ium (1) dibromide

A flamed-dried two-neck round bottom flask is filled with pyridine (1.05 equivalent), bromoethylammonium bromide (1.00 equivalent), a magnetic stirring bar, and anhydrous acetonitrile (dried with $CaH_2$ prior to distillation). The resulting mixture is then heated with stirring and left to reflux for 3-4 days. Progress of the reaction is monitored through 1H NMR spectroscopy and allowed to cool to room temperature on completion of reaction. The precipitate which forms during reaction is then isolated by filtration and thoroughly washed with diethyl ether prior to vacuum drying to obtain the desired beige coloured solid product (1.52g, 85% yield).

## 3.2 Film Fabrication

### 3.2.1 Passivation of surface defects through post-deposition treatment

The films characterized in this study are prepared as follows; $CH_3NH_3PbBr_3$ solution is prepared with a 1:1.05 molar ratio of $PbBr_2$ (TCI) and $CH_3NH_3Br$ (Dyesol) in a co-solvent of DMF and DMSO (3:1) to form a solution of 1 M concentration. The reference film is spin coated at 5000 rpm for 12 s with toluene dripped 4 s from the start of the spin coating process. Thereafter, the films are annealed at 100 °C for 30 min. The tetra ethyl ammonium bromide (TEABr) solution (10, 15 and 20 mg $mL^{-1}$ in IPA) is allowed to settle on the film for 15 s before spin-coating at 4000 rpm for 30 s. The films are then re-annealed at 100 °C for 10 min.

### 3.2.2 Additive engineering for suppression of grain size modulated defects

Preparation of $CH_3NH_3PbBr_3$ solution and reference film for this study are carried out as mentioned in Section 3.2.1 above, with exception for the annealing step. Instead of annealing, the as-prepared films are dried under vacuum for 30 min. The small molecule additive is incorporated into the emitter layer by first dissolving Bathophenanthroline (BPhen) (Aldrich, 97%) in toluene prior to use as the anti-solvent during the spin coating process. BPhen concentrations ranging from 0-0.750 mg $mL^{-1}$ in toluene are utilized throughout the experiment.

### 3.2.3 Molecular design of two-dimensional perovskite cation for energy cascade

Depending on the choice of 2D cation, mixture of $PbBr_2$, $CH(NH_2)_2Br$ and either $C_6H_5C_2H_4NH_2Br$ (PEABr), $C_5H_5NC_2H_4NH_2Br$ (PyrEABr) or $C_3H_5N_2C_2H_4NH_2Br$ (ImEABr) are prepared in a co-solvent of DMF and DMSO (3:1) to form a solution of 0.25 M concentration with respect to $PbBr_2$. The 2D cation is added in excess of the 3D cation while maintaining the 3D cation concentration in all precursor solutions. The films are then prepared similarly to the reference in Section 3.2.1.

### 3.2.4 Tailoring the distribution and spread of m domains for stable blue emission

Depending on the choice of A-site cation, mixtures of $PbBr_2$, ABr (A: $CH(NH_2)_2^+$, $CH_3NH_3^+$, $Cs^+$), and $C_6H_5(CH_2)_4NH_3Br$ are prepared in a co-solvent of DMF and DMSO (64:36). To make <m> = 2 solutions with excess $C_6H_5(CH_2)_4NH_3Br$, 0.11 M $PbBr_2$ is mixed with 0.05 M ABr and 0.165 M $C_6H_5(CH_2)_4NH_3Br$ in which the PBA/Pb and PBA/Cs ratios are equivalent to 1.5 and 3.3 respectively. While keeping the $PbBr_2$ concentration fixed at 0.11 M, the ratio of ABr and $C_6H_5(CH_2)_4NH_3Br$ is adjusted accordingly. Films are spin coated from various precursor solutions at 5000 rpm for 12 s and allowed to dry at room temperature. When fast nucleation is required, the spin coating with anti-solvent is done as described in Section 3.2.1.

## 3.3 Device Fabrication

The PeLED devices are fabricated on indium-doped tin oxide (ITO, 7 Ω $sq^{-1}$) coated glass substrates. The substrates are first cleaned sequentially using decon soap, deionized water and ethanol before being dried and ozone treated for 15 mins. PEDOT: PSS (Clevios P VP Al 4083) is subsequently spin coated at 4000 rpm for 60 s and annealed at 130 °C for 15 min to remove excess moisture. The MHP films are deposited as detailed in Section 3.2, before the deposition of the electron transporting layer (ETL) and cathode. 2, 4, 6-Tris[3-(diphenylphosphinyl)phenyl]-1,3,5-triazine (PO-T2T) (Lumtec, >99%) (45 nm), lithium fluoride (LiF) (0.8 nm) and aluminium (Al) (100 nm) are thermally evaporated to form the ETM and cathode respectively. Evaporation is carried out under high vacuum (< 1 x $10^{-6}$ Torr) and encapsulated prior to testing. The measured device area is 8 $mm^2$.

## 3.4 Physical Characterization Techniques

### 3.4.1 Field emission scanning electron microscopy (FESEM)

Working Principle

The electron source produces a beam which the anode accelerates towards the sample surface, for imaging. The lenses function to focus the beam onto the sample surface[1] (Figure 3.1). Interaction of electron with the sample results in the generation of secondary electrons, backscatter electrons and x-rays[2] (Figure 3.2). The respective detector collects the signal and converts them into an image.

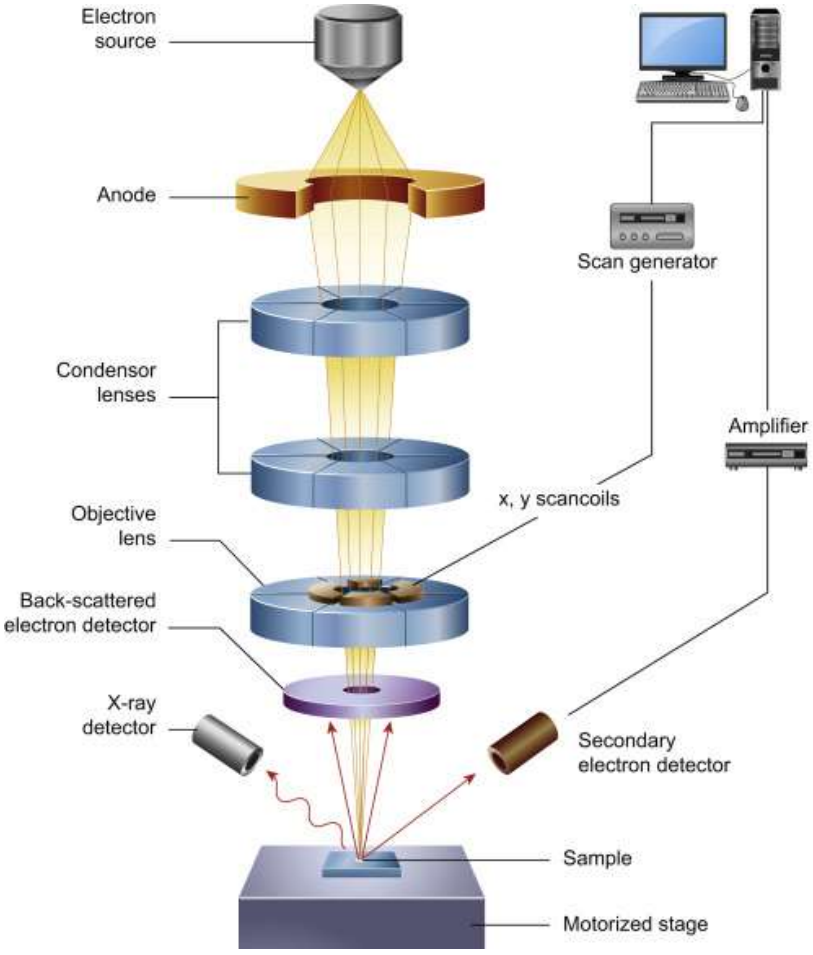


**Figure 3.1** Components of Field Emission Scanning Electron Microscope[3]

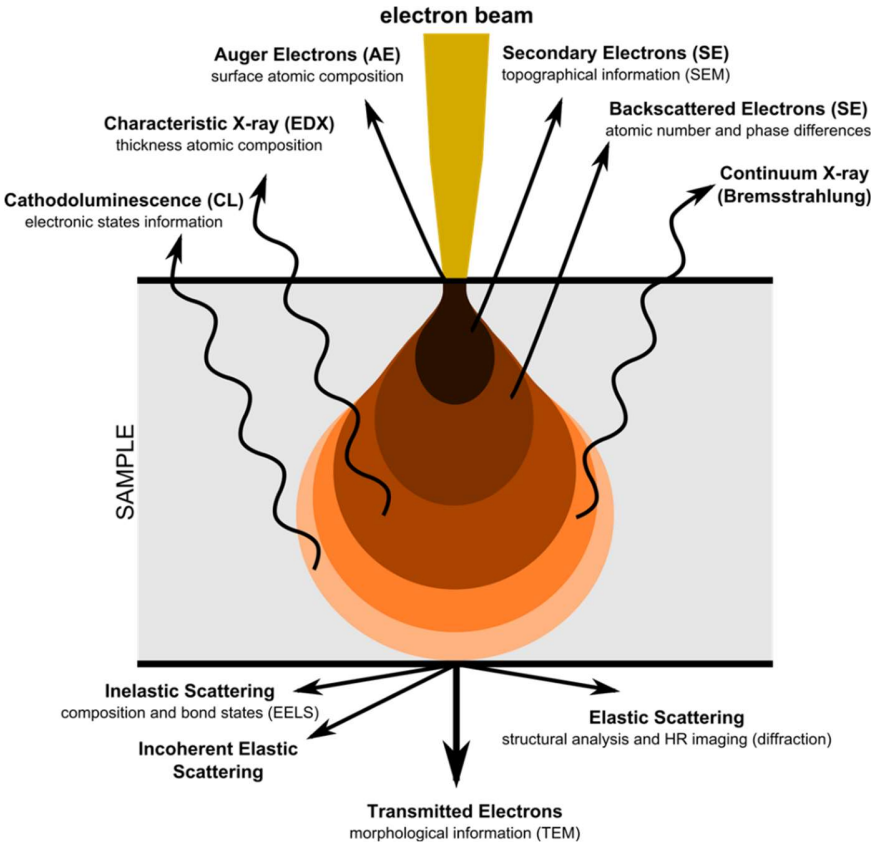


**Figure 3.2** Types of signal obtained from electron-sample interaction[2]

Equipment Description

Top and cross-sectional images of all MHP films are characterized using a field emission scanning electron microscope (JEOL 7600F) with an electron source. Prior to imaging all samples are sputtered with a thin layer of platinum to improve conductivity and minimize the sample charging effect.

### 3.4.2 X-ray diffraction (XRD)

Working Principle

This spectroscopic technique is based on the diffraction of x-rays. Diffraction occurs due to the scattering of electromagnetic waves in a periodic array with long-range order, resulting in constructive interference at specific angles, thus creating a diffraction pattern.[4] X-ray is used as its wavelength is of the same order as interatomic distances which enables

crystal information such as the atoms and their arrangement, to be probed. In the absence of long-range order such as in the case of amorphous materials, no diffraction pattern will be observed.

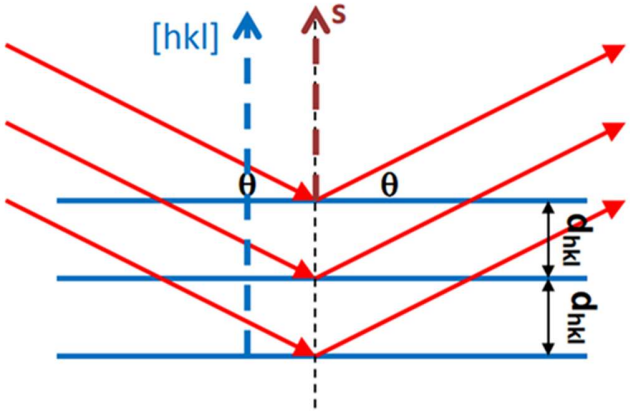


**Figure 3.3** Schematic of X-ray interaction with crystal planes to produce diffraction pattern[4]

- In order to obtain an x-ray diffraction pattern of a material, Bragg's law, $\lambda = 2\, d_{hkl} \sin\theta$ , must be fulfilled, where $\lambda$, $d_{hkl}$ and $\theta$ refer to the wavelength of the x-ray source, interplanar distance and incident angle (the angle at which the incident x-ray beam hits the atomic plane) (Figure 3.3).
- For parallel planes of atoms separated by a distance $d_{hkl}$ between them, diffraction pattern is obtained on satisfying Bragg's law. Since $\lambda$ (wavelength of x-ray source) is fixed, diffraction peaks corresponding to a family of planes will appear at specific $2\theta$ angles.
- The diffraction vector *s* is always normal to the sample's surface (Figure 3.4).

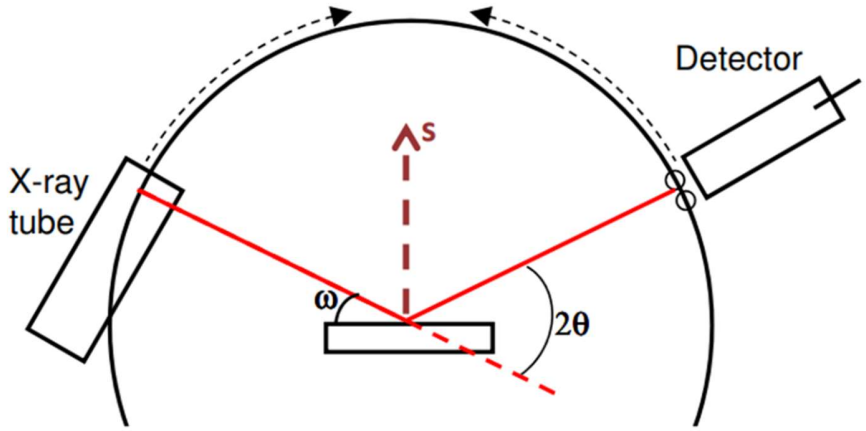


**Figure 3.4** Bragg-Brentano geometry of diffractometer[4]

- The incident angle, ω, refers to the angle formed between the incident X-ray beam and sample surface.
- The diffraction angle, 2θ, is defined as the angle between the incident X-ray beam and the detector. The diffraction angle is always double of the incident angle.
- The resultant pattern consists of peaks which correspond to the diffraction angles (Figure 3.5).

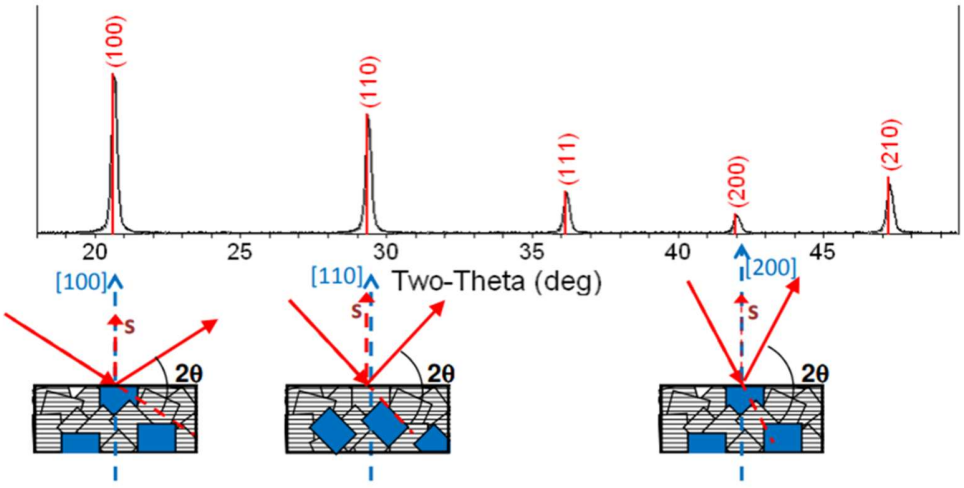


**Figure 3.5** An example of XRD pattern obtained from a polycrystalline powder sample[4]

**Assumption**: A large sample is typically needed for this characterization to ensure the presence of statistically relevant number of crystallites in each set of planes to contribute towards the diffraction pattern.

Equipment Description

All phase and composition analysis of the prepared films are characterized using an X-ray diffractometer (Bruker D8 ADVANCE) with Cu Kα radiation (λ = 1.5418 Å) as the X-ray source and 0D LynxEYE™ as the detector. XRD spectra of the MHP films are recorded for the scan range 2θ = 5-60° with a grazing angle of 1.5°, scan step of 0.02° and dwell time of 1 s.

### 3.4.3 Ultraviolet-visible (UV-Vis) spectroscopy

Working Principle

The UV-Vis-NIR spectrophotometer measures the absorption and transmittance of electromagnetic waves spanning the UV-Vis-NIR range through the sample. The beam of light from the light source passes through the diffraction grating and slit which separates the light into its component wavelengths. The monochromatic light which emerges from the slit is then split into two equal intensities – one passing through the reference and the other, the sample, following which the change in intensities of the two light beams are detected by the detector.[5] (Figure 3.6)

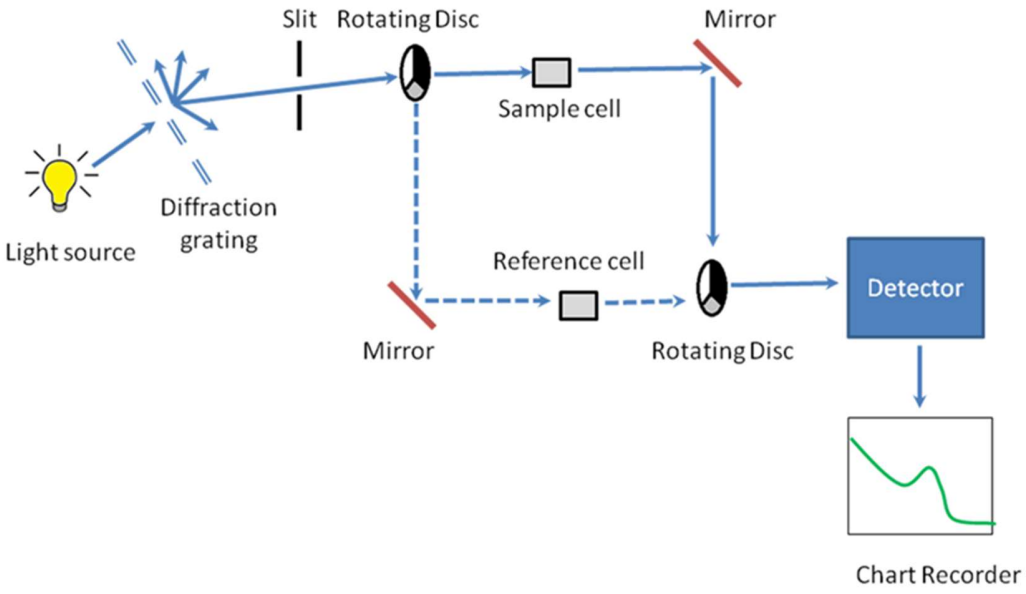


**Figure 3.6** Components of UV-Vis spectrophotometer[6]

The light intensity which passes through the reference is assigned as $I_0$ while the intensity of light passing through the sample is defined as I. If the sample is non-absorbing, $I_0 = I$. However, if it does, the difference in intensity between I and $I_0$ can be plotted as function of wavelength[6] (Figure 3.7).

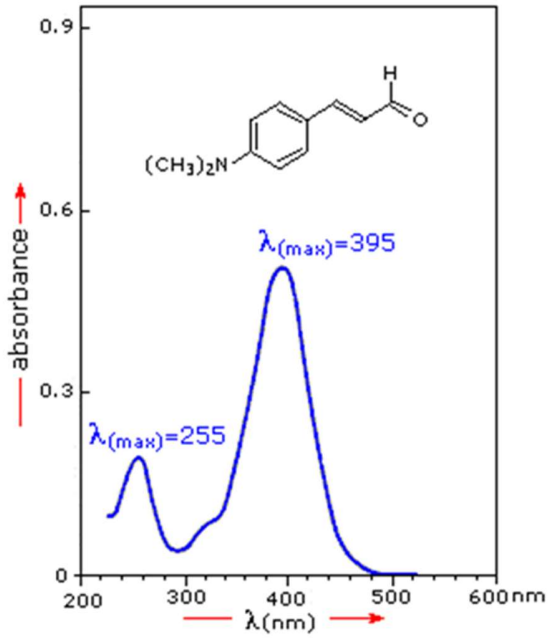


**Figure 3.7** An example of a typical absorbance spectrum[5]

The absorption of the sample can be presented in the form of transmittance (T) or absorbance (A), where the absence of absorption leads to T and A values of 1 and 0.

$$T = \frac{I}{I_0}$$

$$A = \log \frac{I_0}{I}$$

As absorbance is proportional to the molar concentration of a sample (ε), molar absorptivity is used to compare the absorption of different compounds.

$$\varepsilon = \text{Alc}$$

where A, l and c are the absorbance, sample concentration (moles $L^{-1}$) and length of light path (cm) respectively.

Equipment Description

UV-VIS-NIR spectrophotometer (Shimadzu UV-3600) was used to obtain the absorption spectra of thin films with an integrating sphere attachment (ISR-3100).

### 3.4.4 Nuclear Magnetic Resonance (NMR) spectroscopy

Working Principle

An analytical chemistry technique, nuclear magnetic resonance spectroscopy enables the determination of a sample's content, purity and molecular structure such as in a case of a mixture of known compounds. It functions based on the principle of energy transfer when an elemental nucleus, excited to a higher energy state on application of external magnetic field, returns to base energy level and emits energy equivalent to the difference between the excited and base energy states[7] (Figure 3.8). The signal obtained from this energy transfer is then processed to yield an NMR spectrum for the nucleus.

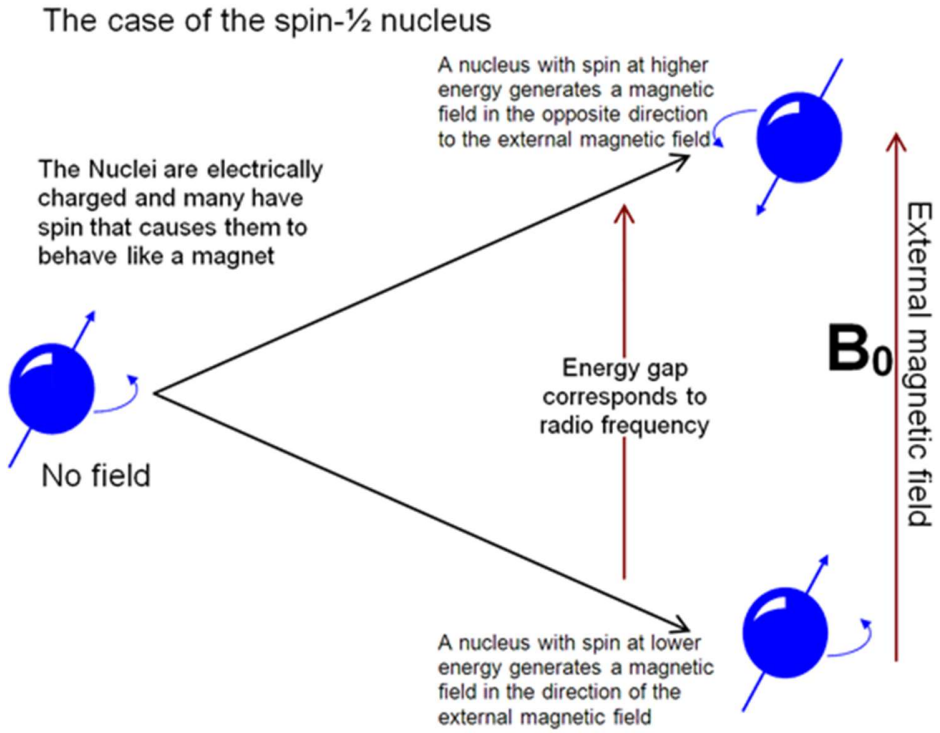


**Figure 3.8** Effect on nucleus on application of external magnetic field[7]

The resonant frequency corresponding to the energy change is dependent on the effective magnetic field at the nucleus, which in turn, is influenced by electron shielding as a result of the chemical environment. Hence, from the NMR spectrum, it is possible to gain insights into the chemical environment of the nuclei. Other factors affecting the resonant frequency include electronegativity of the nucleus, ring currents and bond strains. The effective magnetic field acting on the nucleus is also dependent on the orientation of the surrounding nuclei. This effect, referred to as spin-spin coupling, results in the splitting of the nucleus signal into two or more lines. The number of splitting corresponds to the number of chemically bonded nuclei within the surroundings of the nucleus of interest[7] (Figure 3.9).

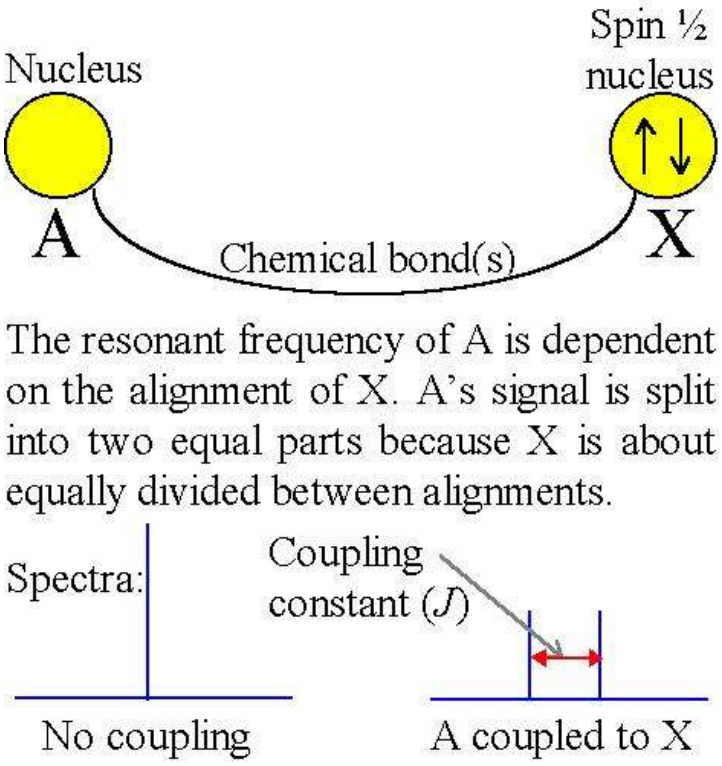


**Figure 3.9** Spin coupling effect on interacting with other nuclei in the vicinity of nucleus of interest[7]

Equipment Description

1H and 13C(1H) NMR spectra of organic compounds are generally recorded in DMSO-d6 solution using a Bruker Avance 400 spectrometer. Chemical shift values (ppm) are referenced against residual protic solvent peaks.

### 3.4.5 Photoluminescence (PL) spectroscopy

Working Principle

Photoluminescence is a process whereby atoms or molecules, excited to a higher energy state due to absorption of electromagnetic radiation, emit photons during de-excitation[8] (Figure 3.10). As photoluminescence, a result of radiative recombination, is often used as a measure of radiative and non-radiative recombination processes occurring in fluorescent systems.[9] The quality of a luminescent system can thus be measured by means of its photoluminescence.[10]

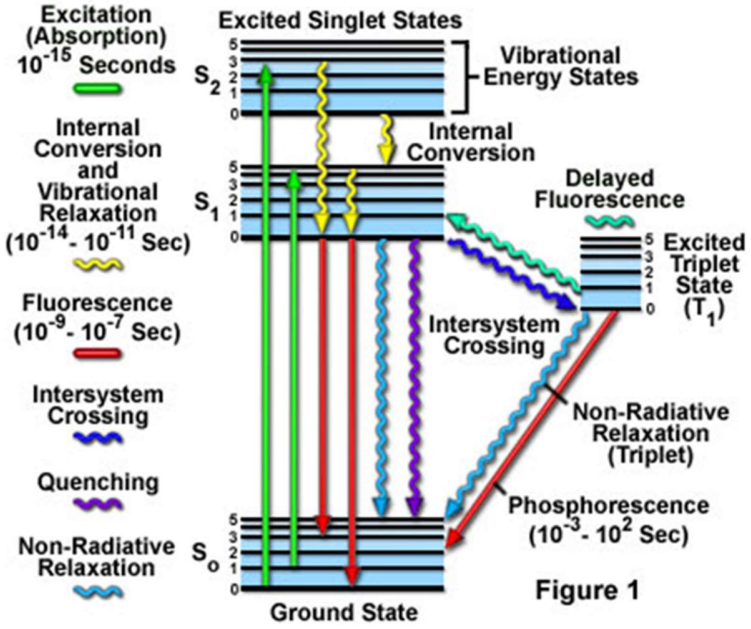


**Figure 3.10** Jablonski energy diagram showcasing the various electron transition on light absorption[8]

In a photoluminescence measurement set up (Figure 3.11), monochromatically selected wavelength from the Xenon lamp is used to excite the sample following which the photoluminescence is captured by the emission's monochromator.[11] The intensity of the excitation and emission spectra can be controlled by the grating slits and integration time although the former is not preferred due to the resultant decrease in spectral resolution.

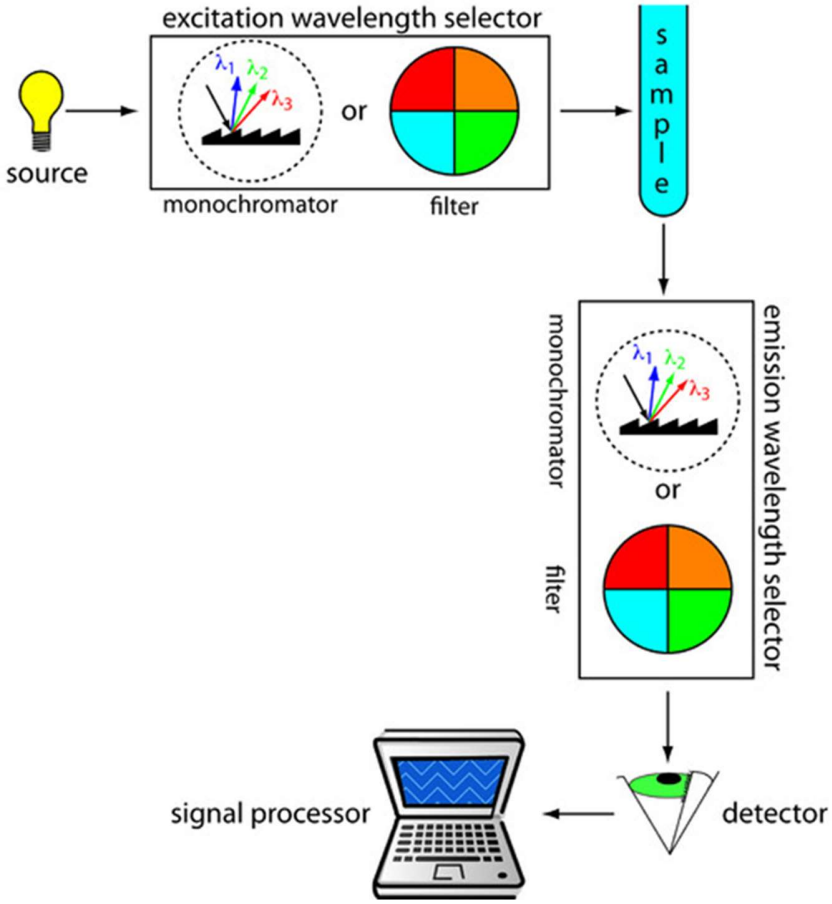


**Figure 3.11** Components in a photoluminescence spectrometer[10]

Equipment Description

The photoluminescence (PL) spectra of films were measured using a Horiba Fluoromax-4 with excitation wavelength, slit width and integration time of 350/400 nm, 1 nm and 0.1 s, respectively. For the excitation spectra measurement, the wavelength set corresponds to the peak emission of the sample (540 nm). The intensities of the films are corrected against the absorbance at the same excitation wavelength (405 nm).

### 3.4.6 Transient PL spectroscopy

Working Principle

Transient photoluminescence spectroscopy enables the investigation of minority carrier lifetimes in emissive semiconductors. The spectral and temporal evolution of the sample's

emission on illumination can be measured using this technique, in particular the decay of electron-hole pairs to lower energy states as a function of time which yields the lifetimes corresponding to specific transition energies. A streak camera[12] (Figure 3.12) is used to capture the decay times of the emitted light due to the higher time-based resolution it provides as compared to a conventional analyzer. This is especially important is cases where the decay is extremely fast and the intensity of emitted light is weak.

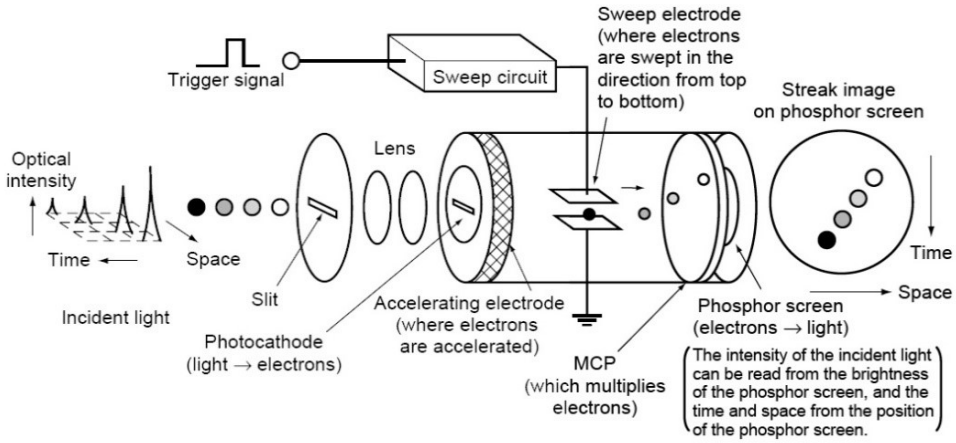


**Figure 3.12** Components in a streak camera[12]

During the measurement, the sample is excited with picosecond or femtosecond laser pulses and the optical response is then collected by the microscope which is directly connected to the streak camera optics[13] (Figure 3.13). The information is then processed and a graph showcasing the decay dynamics, shown.

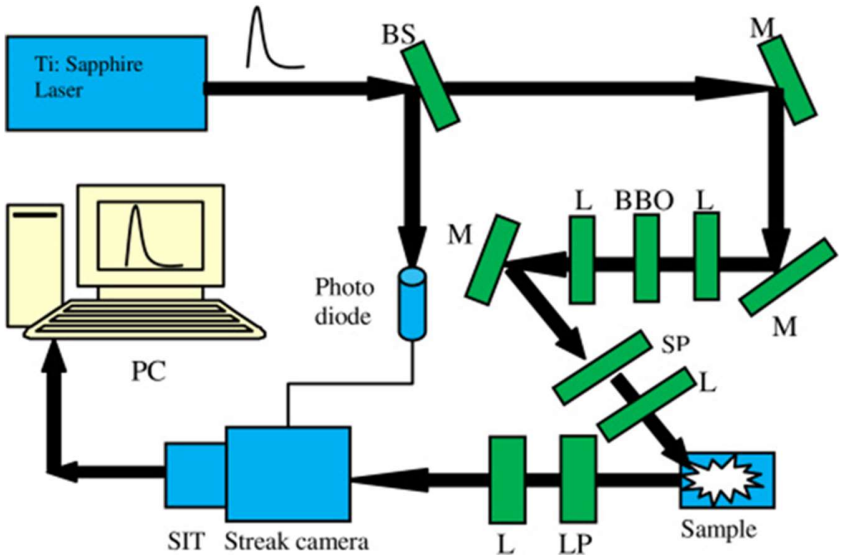


**Figure 3.13** Schematic diagram of the experimental set up for TRPL spectroscopy[13]

Equipment Description

All time-resolved photoluminescence measurements were conducted using a Picoquant PicoHarp 300 time-correlated single photon counting (TCSPC) system coupled to a micro-PL setup with Nikon microscope objective (20x magnification, NA = 0.3). A ps-pulsed laser diode ($\lambda = 405$ nm, f = 40 MHz) (Picoquant P-C-405B) was used to excite the sample. The output signal is then fiber coupled to Acton SP-2300i monochromator (300 mm focal length) for spectral selection of the emission light at 540 nm with slit width of 15 nm. Another optical fiber connected to the output of the monochromator is used to couple spectral separated output light to an avalanche diode that is synchronized with the excitation laser via the TCSPC electronic. Overall, the FWHM of the system instrument respond function is expected to be at 50 ps.

### 3.4.7 Transient Absorption (TA) spectroscopy

Working Principle

In transient absorption spectroscopy, a pump pulse is used to excite the sample and induces changes such as transmittance/absorbance which is detected through a probe pulse. The laser beam is split using a beam splitter to form the pump and probe beams which reach

the sample surface with a time difference controlled by the variable delay[14] (Figure 3.14). After propagating through the sample, only the probe beam, which provides information about the sample, is analyzed. The recovery time scales of the sample's absorbance/transmittance can be obtained through variation of the probe pulse delays. Information pertaining to the relaxation optical gain and index on sample excitation is useful for assessing the potential of luminescent materials for photonic applications.[15]

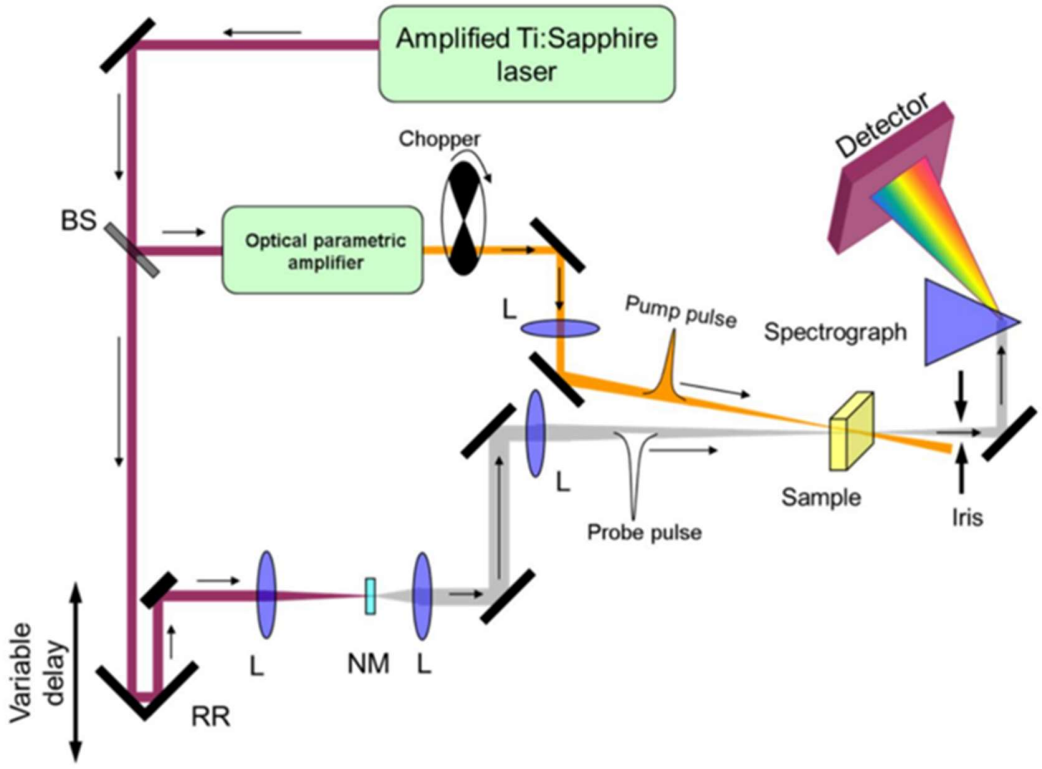


**Figure 3.14** Schematic of a transient absorption measurement set up[14]

Equipment Description

The transient absorption measurement was carried out using a Helios spectrometer (UltrafastSystems, LLC). The pump pulse was generated from a 1 KHz regenerative amplifier [Coherent Legend (150 fs, 1 KHz, 800 nm)] and doubled via second harmonic generation (SHG) by a BBO crystal to obtain 400 nm laser pulses. The regenerative amplifier was seeded by a mode-locked Ti-sapphire oscillator (Coherent Vitesse, 80 MHz). The white light continuum probe beam (in the range from 410 to 750 nm) was generated by focusing a small portion (~10 μJ) of the fundamental 800 nm laser pulses into a 2 mm

sapphire crystal, before filtering out the residual by using a 750 nm short-pass filter. Both pump and probe beam were focused onto the sample with 1/e2 spot diameter of ~510 μm and ~200 μm, respectively.

### 3.4.8 PL Quantum Yield (PLQY)

Working Principle

The photoluminescence quantum yield set up is similar to photoluminescence spectroscopy where the information pertaining to the radiative recombination process occurring in the emissive materials is probed. However, with this method, it is possible to quantify the photoluminescence (fluorescence) efficiency of the material of interest, as per the formula:

$$\text{PLQY} = \frac{\text{Number of photons emitted}}{\text{Number of photons absorbed}}$$

The measurement is typically done in an integrating sphere where the laser beam enters through the entrance port, excites the sample resulting in photon generation. The photons exit the integrating sphere through the exit port to the optics of the spectrometer[16] (Figure 3.15).

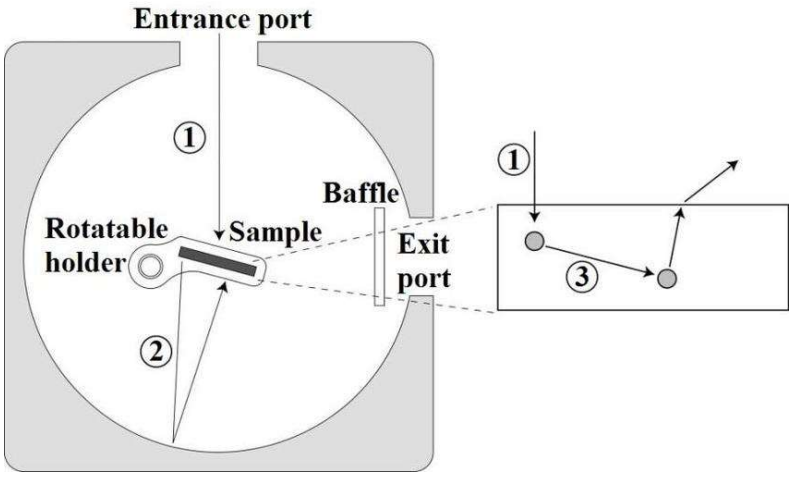


**Figure 3.15** Schematic of photon collection during PLQY measurement[16]

Equipment Description

The absolute PLQY is measured using a calibrated integrating sphere under the 400 nm fs laser excitation.

## 3.5 Electrical Characterization Technique

Working Principle

On applying a bias across the PeLED device which is placed on top of the integrating sphere, the light emitted due to the radiative recombination of the charges enters the integrating sphere before being channeled to the spectrometer through fiber optics. The current-voltage readings and corresponding luminance values are recorded in the measurement software and computed to give the efficiency values of the device[17] (Figure 3.16).

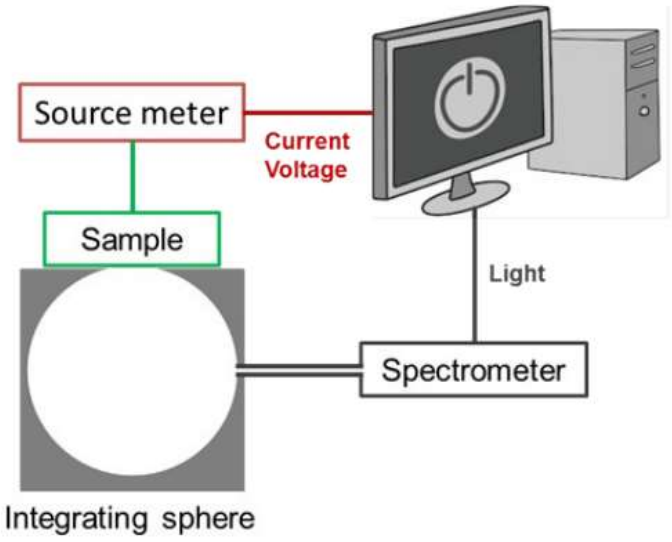


**Figure 3.16** Schematic of PeLED electrical measurement set up[17]

Equipment Description

A Keithley 2612B is used to obtain the LED device characteristics. The emission from the sample is collected by an integrating sphere (OceanOptics FOIS-1) coupled to a calibrated spectrophotometer (OceanOptics QEPro). An OceanOptics HL-3 Plus vis-NIR light source, calibrated using a procedure and documentation patterned after the ISO 17025, IEC Guide 115 and JCGM100:2008 (GUM) protocols, is used to calibrate the absolute irradiance

measurement of the spectrometer. Only forward emission from the LED devices are captured due to their placement outside the integrating sphere.

## References

1. Jordan, J. How does scanning electron microscopy work? https://www.jeremyjordan.me/scanning-electron-microscopy/.

2. Electron microscope. https://en.wikipedia.org/wiki/Electron_microscope.

3. Inkson, B. J., 2 - Scanning electron microscopy (SEM) and transmission electron microscopy (TEM) for materials characterization. In *Materials Characterization Using Nondestructive Evaluation (NDE) Methods*, Hübschen, G.; Altpeter, I.; Tschuncky, R.; Herrmann, H.-G., Eds. Woodhead Publishing: 2016; pp 17-43.

4. Speakman, S. A. Basics of X-ray Powder Diffraction. http://prism.mit.edu/xray/Basics%20of%20X-Ray%20Powder%20Diffraction.pdf.

5. Barron, P. M. V. R. A. R. Using UV-Vis for the Detection and Characterization of Silicon Quantum Dots. https://chem.libretexts.org/Bookshelves/Analytical_Chemistry/Book%3A_Physical_Methods_in_Chemistry_and_Nano_Science_(Barron)/08%3A_Structure_at_the_Nano_Scale/8.5%3A_Using_UV-Vis_for_the_detection_and_characterization_of_silicon_quantum_dots.

6. University, M. S. UV-Visible Spectroscopy. https://www2.chemistry.msu.edu/faculty/reusch/VirtTxtJml/Spectrpy/UV-Vis/uvspec.htm.

7. Lab, N. What is NMR. http://chem.ch.huji.ac.il/nmr/whatisnmr/whatisnmr.html.

8. Davidson, I. D. J. M. W. Jablonski Energy Diagram. https://www.olympus-lifescience.com/en/microscope-resource/primer/java/jablonski/jabintro/.

9. Ghoshal, K. Photoluminescence Spectroscopy. http://ocw.utm.my/file.php/351/ocw-chapter-6.pdf.

10. Harvey, D. Photoluminescence Spectroscopy. https://chem.libretexts.org/Bookshelves/Analytical_Chemistry/Book%3A_Analytical_Chemistry_2.0_(Harvey)/10_Spectroscopic_Methods/10.6%3A_Photoluminescence_Spectroscopy.

11. Barron, P. M. V. R. A. R. Photoluminescence, Phosphorescence and Fluorescence Spectroscopy. https://chem.libretexts.org/Bookshelves/Analytical_Chemistry/Book%3A_Physical_Meth

ods_in_Chemistry_and_Nano_Science_(Barron)/04%3A_Chemical_Speciation/04.5%3A_Photoluminescence%2C_Phosphorescence%2C_and_Fluorescence_Spectroscopy.

12. Analysis, C. f. A. P. P., Time-Resolved Photoluminescence.

13. Islam, S. Z.; Gayen, T.; Das, B. B.; Shi, L.; Seredych, M.; Moussawi, A.; Bandosz, T. J.; Alfano, R., Time-resolved photoluminescence of Zn(OH)2 and its composites with graphite oxides. *Opt. Lett.* **2013,** *38* (13), 2227-2229.

14. Till, N. Ultrafast Spectroscopic Methods: Fundamental Principles and Applications in Photocatalysis. http://chemlabs.princeton.edu/macmillan/wp-content/uploads/sites/6/NT-Ultrafast-Spectroscopy-min.pdf.

15. Analysis, C. f. A. P. P. Pump-Probe Spectroscopy. http://www.cappa.ie/advanced-research/techniques/pump-probe-spectroscopy/.

16. Wilson, L. R.; Richards, B. S., Measurement method for photoluminescent quantum yields of fluorescent organic dyes in polymethyl methacrylate for luminescent solar concentrators. *Appl. Opt.* **2009,** *48* (2), 212-220.

17. Chin, X. Y.; Perumal, A.; Bruno, A.; Yantara, N.; Veldhuis, S. A.; Martínez-Sarti, L.; Chandran, B.; Chirvony, V.; Lo, A. S.-Z.; So, J.; Soci, C.; Grätzel, M.; Bolink, H. J.; Mathews, N.; Mhaisalkar, S. G., Self-assembled hierarchical nanostructured perovskites enable highly efficient LEDs via an energy cascade. *Energy & Environmental Science* **2018,** *11* (7), 1770-1778.

# Chapter 4

# Passivation of surface defects through post-deposition treatment

*In this chapter, processing-influenced defects leading to the non-stoichiometric ratio of Pb: Br, is addressed through a post-deposition treatment process during which tetra ethyl ammonium bromide (TEABr) is introduced. The ionic nature of the passivator species chosen enables both the positively and negatively charged vacancies to be remedied during the treatment process. Surface analysis reveals surface Br: Pb ratio approaching 3.0 on increasing TEABr concentration, confirming the effectiveness of the treatment process. The device characteristics too improved with TEABr concentration up to 15 mg $mL^{-1}$ beyond which efficiency drops and threshold voltage increases. This is explained by the greater proportion of less conducting lower dimensional secondary phase formed in the film which hinders charge injection and effective radiative recombination during device operation, despite the higher PLQY accorded.*

---

* Nur Fadilah Jamaludin, Natalia Yantara, Yan Fong Ng, Mingjie Li, Teck Wee Goh, Krishnamoorthy Thirumal, Tze Chien Sum, Nripan Mathews, Cesare Soci, and Subodh Mhaisalkar, Grain Size Modulation and Interfacial Engineering of $CH_3NH_3PbBr_3$ Emitter Films through Incorporation of Tetraethylammonium Bromide. *ChemPhysChem* **2018**, 19, 1075 – 1080. DOI: 10.1002/cphc.201701380.

## 4.1 Introduction

Despite boasting cheap solution-based processing, the tendency for defect formation with this technique necessitates studies focusing on passivation of these electrical shunt pathways.[1-3] This is further exacerbated by the tendency for degradation or phase segregation[4] during post-deposition annealing. Not only does it result in changes to surface properties, but more importantly, lead to under-coordination of surface lead atoms to the detriment of device performance.[5] Other than acting as sites for non-radiative recombination, under-coordination of surface elements also expedites film degradation due to the increased susceptibility to the adsorption of other species for charge neutralization.[6] Moreover, thermally-induced grain growth may also introduce defect states within the system owing to the formation of unconnected grains.[7] Poor device performance arising from charge trapping at interfaces[8] have fueled investigation into non-radiative loss reductions, which include incorporation of excess precursor material in the perovskite solution,[9] solvent engineering processes[10] and even through layering of passivating materials to inhibit moisture and oxygen permeation.[6, 11] However, these methods have only shown limited success. The introduction of excess precursor material resulted in higher hysteresis due to the increased effect of ionic migration under device operation[12-13] whereas too thick a passivator layer can have adverse effect on device performance arising from reduced carrier injection efficacy.[14-15]

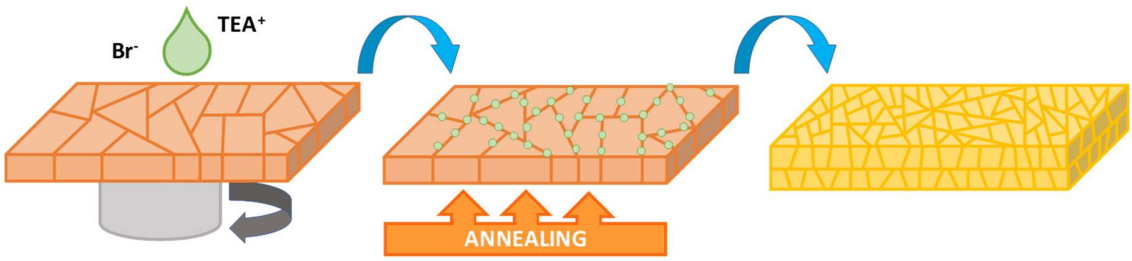


**Figure 4.1** Schematic of the post-deposition treatment process of $MAPbBr_3$ with TEABr

In this chapter, surface defects arising from the non-stoichiometric ratio of Pb: Br is addressed through a post-deposition treatment process during which tetra ethyl ammonium bromide (TEABr), a branched alkyl ammonium ionic species is introduced (Figure 4.1). The rational for employing an ammonium-based ionic passivator such as TEABr is its ability to remedy both positively and negatively charged vacancies. In this study, methyl ammonium lead bromide ($MAPbBr_3$) films are first prepared using a widely reported solvent engineering technique to achieve smooth and compact thin films. While the reference sample is left untreated, the other films were subjected to an additional post-deposition step where varying concentrations of TEABr in IPA (10, 15 and 20 mg $mL^{-1}$), are spin coated onto the films and annealed. The results and discussion will be presented in the subsequent section.

## 4.2 Results and Discussion

### 4.2.1 Crystal structure and phase analysis

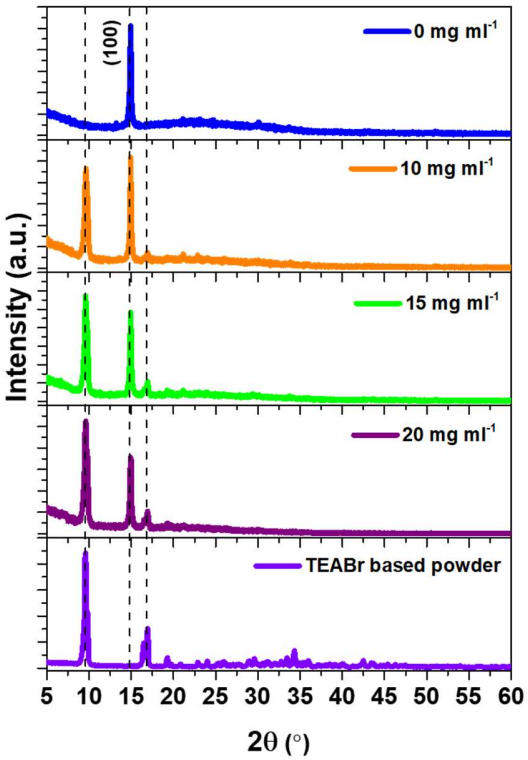


**Figure 4.2** XRD patterns of the reference and TEABr-treated films

The XRD patterns of the reference (0 mg $mL^{-1}$) and TEABr-treated films as well as that of the powder obtained from drying an equimolar solution of TEABr and $PbBr_2$ are taken to affirm the effect of TEABr treatment on film composition and crystallinity (Figure 4.2). While the XRD patterns of all films show characteristic peaks of $CH_3NH_3PbBr_3$ with preferred orientation in the (100) plane, treatment of films with various TEABr concentrations gives rise to the presence of additional peaks at 2θ values of 9.62° and 16.92°, corresponding to reflections from the TEABr-based compound. This suggests the co-existence of two separate phases in the resulting film; in line with reports of lower dimensional MHPs forming on introduction of bulkier cation groups.[16-17] The increasing ratio of peak intensities with TEABr concentration between peak positions 9.62° and 14.94° translates to the increasing proportion of this secondary phase in the film. Incorporation of TEABr into the film during the post-deposition treatment is further attested on comparing

the nuclear magnetic resonance (NMR) spectra of the reference and 10 mg $mL^{-1}$ TEABr-treated films (Figure 4.3). From the NMR spectra, it is evident that additional resonances corresponding to TEABr (marked in red and shown in insets), are present for the 10 mg $mL^{-1}$ TEABr-treated film.

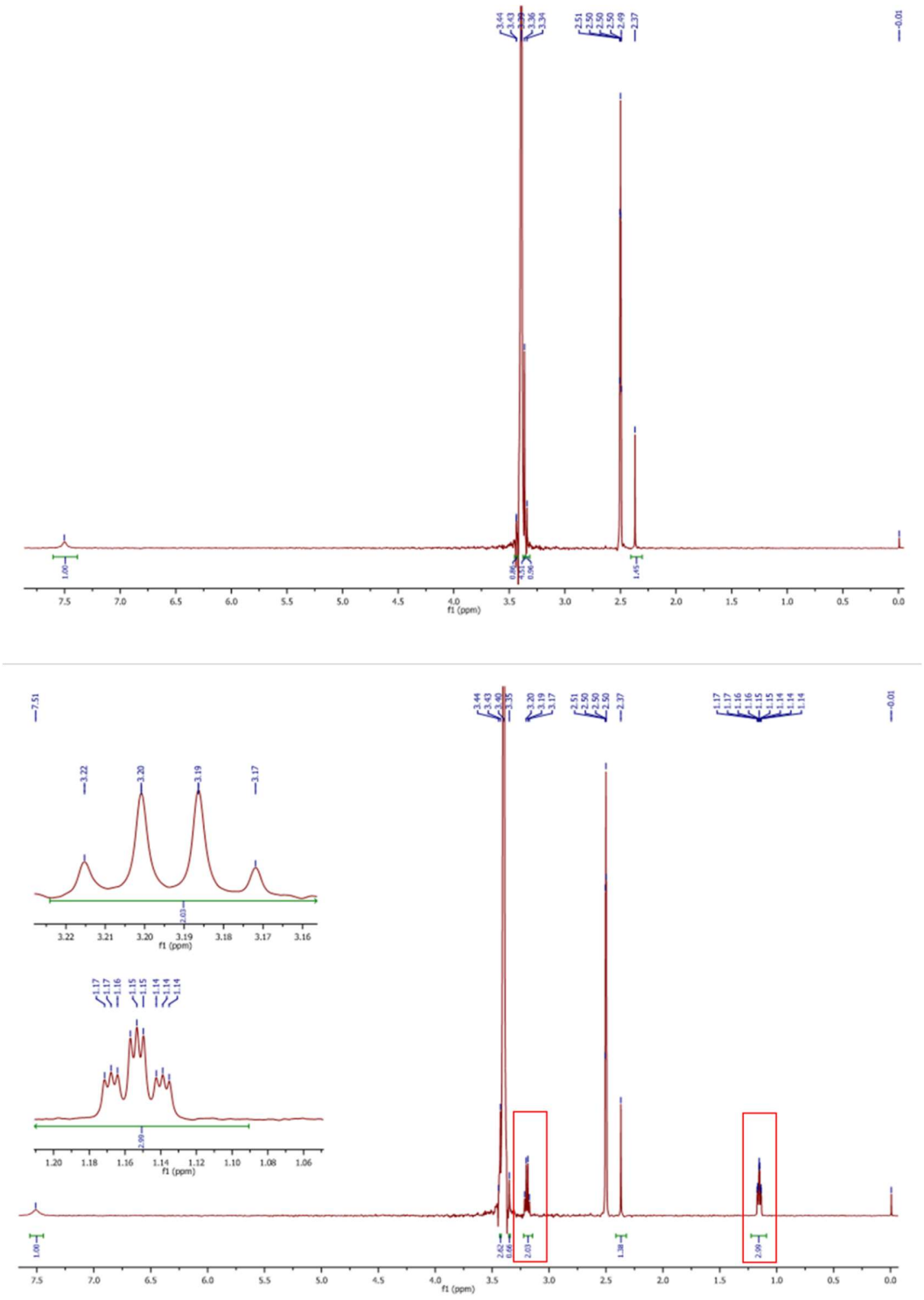

**Figure 4.3** NMR spectra of reference (top) and 10mg $ml^{-1}$ TEABr-treated (bottom) films. Characteristic peaks corresponding to TEABr are indicated in red in the bottom figure.

### 4.2.2 Photophysical properties

Photophysical characterization involves investigation of material interaction with light. It provides a means for probing the influence of TEABr treatment on defect states alleviation in the films. In this section, the various photophysical techniques used concurrently to verify TEABr's passivating effects, will be showcased.

Decrease in absorbance and presence of additional excitonic peak at 325 nm with increasing TEABr concentration (Figure 4.4 (a)) can be accrued to the formation of a lower dimensional phase in the resulting film. This is in good agreement with the XRD phase analysis, where introduction of a bulky cation species such as the tetra ethyl ammonium cation, into the 3D MHP framework result in peaks at lower 2θ values, consistent with the presence of a secondary phase. The normalized PL spectra (Figure 4.4 (a)), reveals no change in peak emission position (538 nm) despite increasing TEABr concentration, implying the non-emissive nature of the lower dimensional phase. This is further confirmed through excitation spectra measurements (Figure 4.4 (b)), where no increase in PL intensity is noted within the absorption range of the secondary phase. The single peak emission noted for all films eliminates energy funneling[18] as a possible mechanism for the notable PL enhancement whereas the PL full width at half maximum (FWHM) too remains at ~ 24 nm, unaffected by the TEABr concentration.

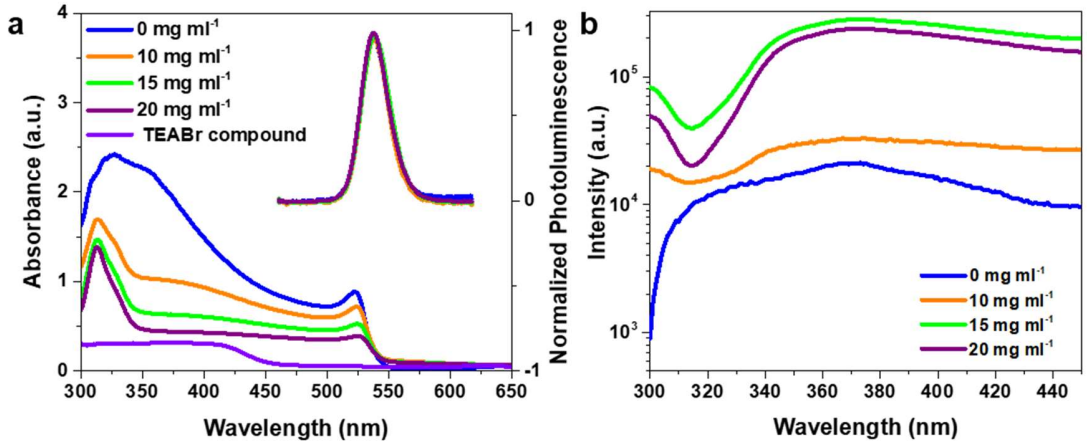


**Figure 4.4** (a) Absorbance, normalized PL and (b) excitation spectra of reference and TEABr treated films

Computation of PL quantum yield (PLQY) values is possible by considering the absorbance-corrected fluorimetric determination of the films (Table 4.1). It is clearly seen that increasing the TEABr concentration results in increased fluorescence with 20 mg $mL^{-1}$ showcasing more than ten-fold enhancement in PLQY value as compared to the reference.

**Table 4.1** PLQY values of reference and TEABr treated films

| Sample | λ (nm) | FWHM (nm) | PLQY (%) |
|---|---|---|---|
| 0 mg $mL^{-1}$ | 538 | 24 ± 1 | 1.2 ± 0.1 |
| 10 mg $mL^{-1}$ | 538 | 24 ± 1 | 6.6 ± 0.2 |
| 15 mg $mL^{-1}$ | 538 | 24 ± 1 | 11.5 ± 0.3 |
| 20 mg $mL^{-1}$ | 538 | 24 ± 1 | 12.6 ± 0.3 |

The systematic improvement to fluorescence is due to surface defect passivation on treating the films with TEABr solution. X-ray photoelectron spectroscopy (XPS) is then carried out to determine the surface elemental stoichiometry for the reference and 20 mg $mL^{-1}$ TEABr-treated films (Figure 4.5), corresponding to the extremities of the measured PLQY values.

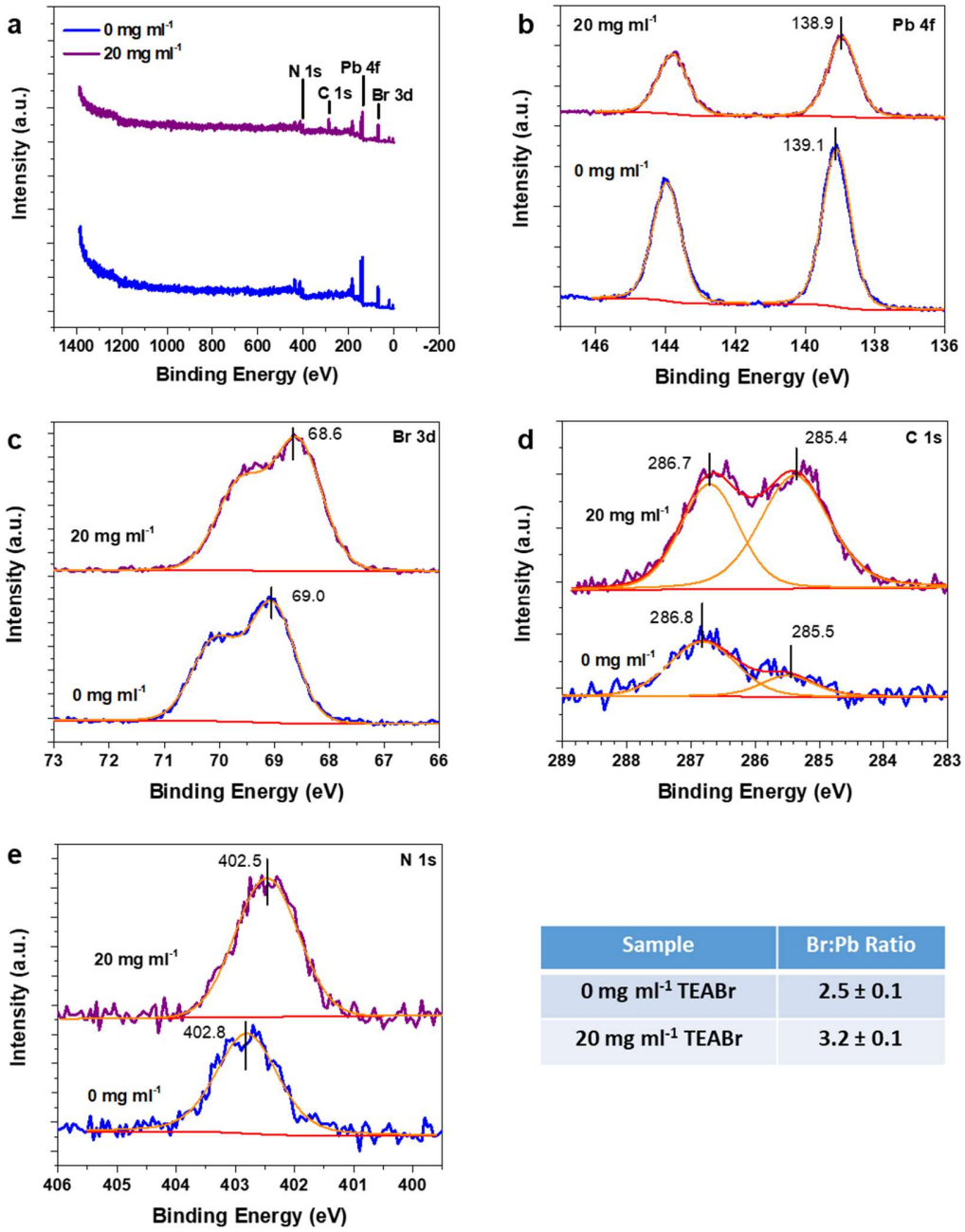


| Sample | Br:Pb Ratio |
|---|---|
| 0 mg ml$^{-1}$ TEABr | 2.5 ± 0.1 |
| 20 mg ml$^{-1}$ TEABr | 3.2 ± 0.1 |

**Figure 4.5** (a) XPS spectra for reference and 20 mg ml$^{-1}$, and the analysis at (b) Pb 4f, (c) Br 3d, (d) C 1s, and (e) N 1s positions.

It is found that the atomic ratio of Br: Pb on the surface of the un-passivated film is 2.5, whereas on treating the film with TEABr, the stoichiometry improves. This suggests that

the TEABr treatment allows surface Br vacancies to be filled and Pb atoms to be more coordinated, thus demonstrating its beneficial effect in remedying surface defects.

Typically, in the presence of a lower dimensional phase, a blue shift in the absorbance spectrum is expected. Though negligible change in absorbance is observed on TEABr treatment, Elliot fitting of the spectra and photoelectron spectroscopy in air (PESA) is done to ascertain influence of TEABr treatment on the band gap as well as the conduction and valence band levels.

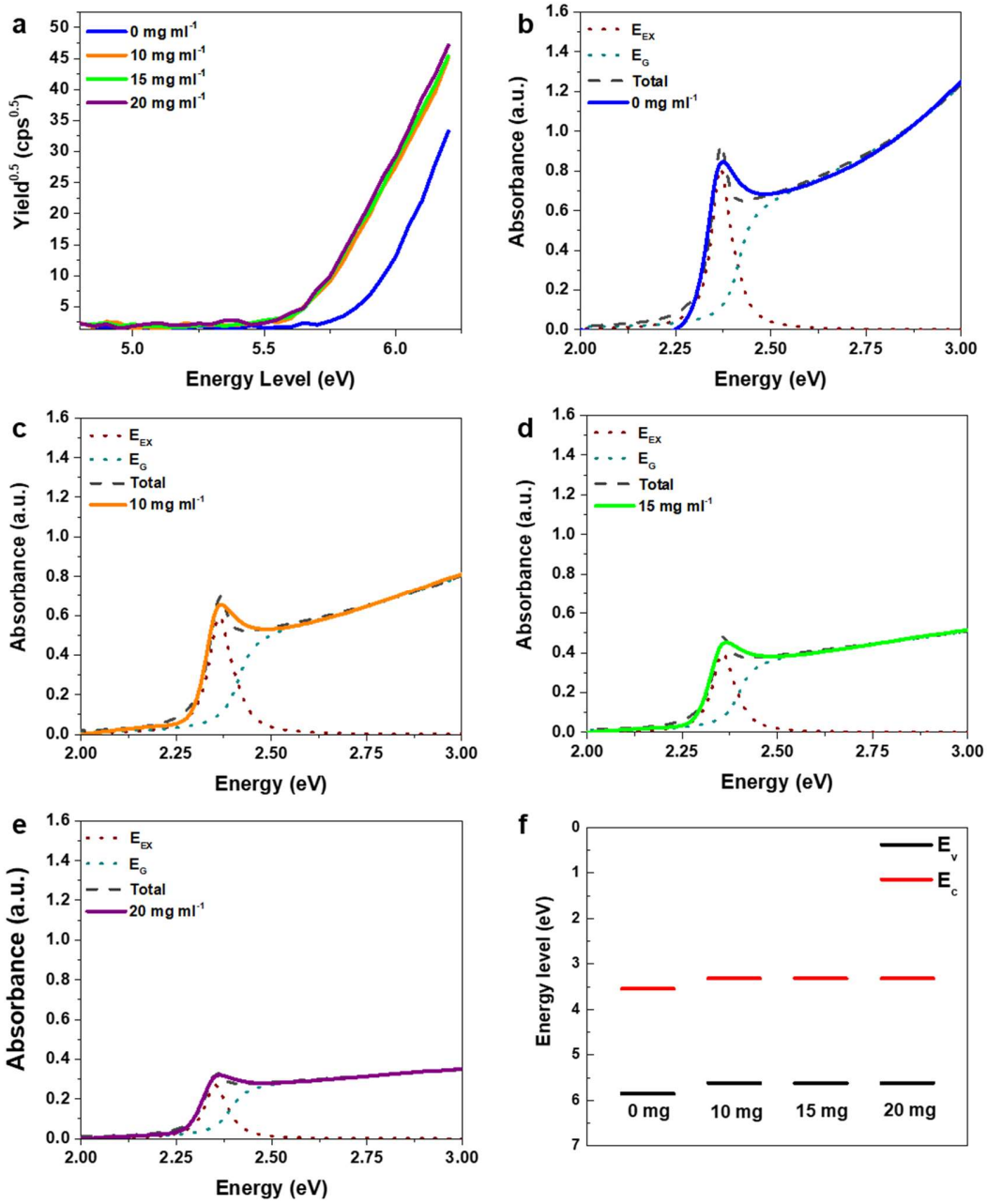


**Figure 4.6** Valence band and band gap determination for (a) reference, (b) 10, (c) 15 and (d) 20 mg mL$^{-1}$ TEABr treated films. (f) Schematic of the conduction and valence band energy levels.

The valence and conduction energy band levels with respect to vacuum are measured using photoelectron spectroscopy in air (PESA) along with the band gap values, estimated from

the absorbance spectra (Figure 4.6). In this case, Tauc plot is not employed in the band gap determination, rather, the Elliot model for optical absorption by exciton is used to deconvolute the excitonic feature present near the absorption edge to provide a more accurate representation of the optical band gap.[19] The change in band energy alignment is also supported by the binding energy shift of Br 3d peak towards lower binding energy (from 69.0±0.1 eV to 68.6±0.1 eV) on treating the film with 20 mg $ml^{-1}$ of TEABr. However, effect on the electronic band gap is negligible despite the notable shifts in energy levels as the valence band maximum is mainly contributed by the Br 4p state rather than the Br 3d state (Figure 4.5).[20] From the band diagram (Figure 4.6), the valence band is found to shift towards vacuum with the incorporation of TEABr, regardless of the concentration used. This implies a reduction in energy barrier between the hole transport material and the MHP, enabling better matching of energy levels at the interface thereby allowing for more effective charge injection into the emitter.

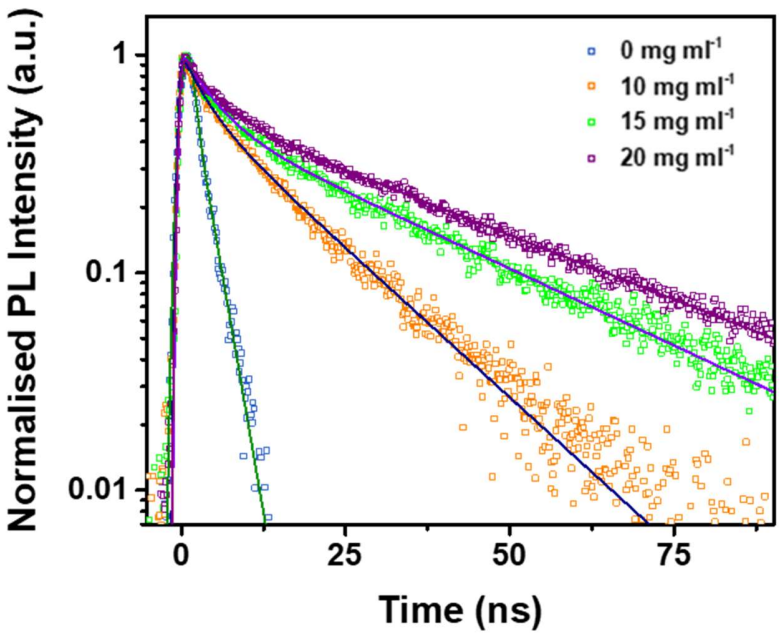


**Figure 4.7** Transient PL decay for reference and TEABr treated films

**Table 4.2** Summary of transient PL decay lifetime for reference and TEABr treated films

| Sample | λ (nm) | $\tau_{PL}$ (ns) | $\tau_{rad}$ (ns) | $\tau_{non\text{-}rad}$ (ns) |
|---|---|---|---|---|
| 0 mg $mL^{-1}$ | 538 | 2.1 ± 0.1 | 175 ± 1 | 2.1 ± 0.1 |
| 10 mg $mL^{-1}$ | 538 | 10.7 ± 0.1 | 162 ± 2 | 11.5 ± 0.2 |
| 15 mg $mL^{-1}$ | 538 | 17.4 ± 0.1 | 151 ± 3 | 19.7 ± 0.3 |
| 20 mg $mL^{-1}$ | 538 | 22.4 ± 0.1 | 178 ± 3 | 25.6 ± 0.3 |

The effect of TEABr concentration is also probed through PL decay measurements (Figure 4.7 and Table 4.2). The PL decay curves are fitted with a bi-exponential decay function to derive the amplitude weighted average lifetimes ($\tau_{PL}$). The fast and slow decay constants are attributed to the recombination of excitons in the defect-rich regions (e.g. near grain surfaces) and the defect-poor regions (e.g. inside the grains), respectively. The average PL lifetime of the reference film is found to be $\tau_{PL} \sim 2.1$ ns whereas the TEABr-treated samples give progressively longer lifetimes with the 20 mg $mL^{-1}$ TEABr-treated sample yielding $\tau_{PL} \sim 22.4$ ns, concurring with expectation of longer $\tau_{PL}$ on reduction of defect density. Based on the correlation between the PLQY and PL decay lifetimes,[21] $\tau_{rad}$ and $\tau_{non\text{-}rad}$ are calculated. It is noted that $\tau_{rad}$ decreases from 175 ns in the reference to 151 ns in the 15 mg $mL^{-1}$ TEABr-treated sample. The $\tau_{non\text{-}rad}$, on the other hand, shows systematic increase (i.e. decrease of non-radiative recombination rates) with TEABr concentration which is consistent with the passivation of surface defects. The XPS data provides further evidence of TEABr passivating nature as seen by the improvement to the Pb: Br surface stoichiometry.

### 4.2.3 Morphological analysis

Morphological assessment of the films was carried out to ascertain if topological change accompanied the change in the film properties.

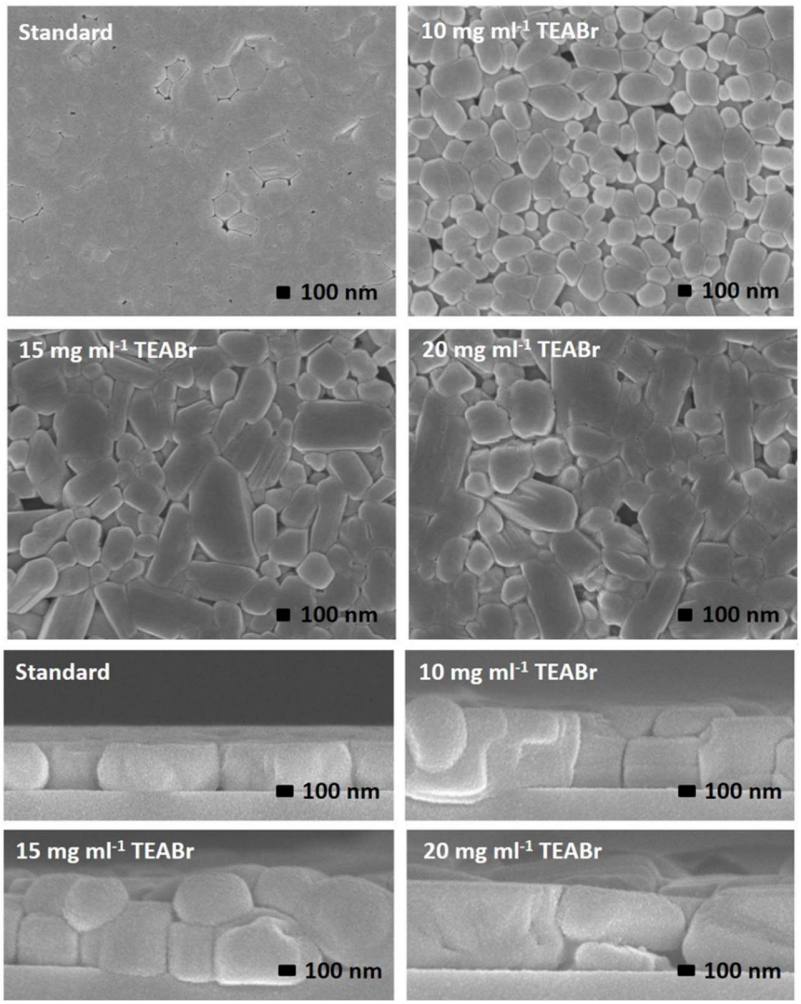


**Figure 4.8** Top and cross-sectional view of the reference and TEABr treated samples

While the reference film shows a smooth surface consisting of fused grains, with TEABr treatment however, the films become progressively rougher noted by the appearance of more defined grains (Figure 4.8). As compared to the columnar grains in the single layered reference film, all TEABr-treated films form a bilayer stack consisting of small, globular grains. It is postulated that the smaller grains for the TEABr-treated films, evident in the cross-section images, contribute significantly towards the higher PLQY values. This is in strong agreement with published reports where spatial confinement facilitates radiative recombination of charges in MHP.[21-22]

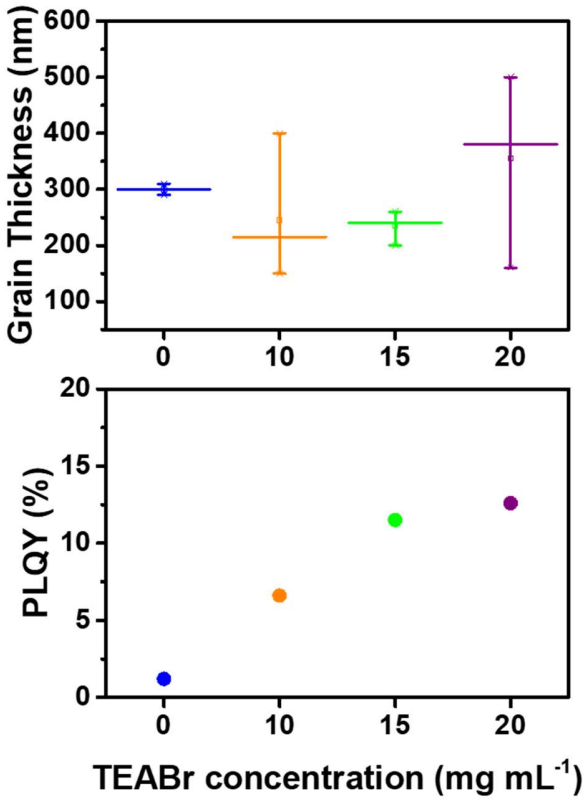


**Figure 4.9** Grain thickness and PLQY as a function of TEABr concentration

It needs to be noted that in this case, the grain's thickness, rather than its width, is used as a basis for comparison due to the vertical manner of charge injection during device operation. From the comparison of grain thickness and PLQY values against TEABr concentration (Figure 4.9), it is interesting to note that although grain thickness increases for concentration beyond 15 mg $mL^{-1}$, PLQY did not suffer. This is explained by the higher proportion of lower dimensional phase formed in the film offering a confined low dimensional quantum well structure,[23] facilitating the radiative recombination process. It is surmised that the grain size effect dominates at lower concentrations of TEABr but the lower dimensional phase effect (quantum well structure) plays a more critical role in carrier confinement at higher TEABr concentrations. However, the increase in proportion of secondary phase may result in reduced film conductivity despite the higher PLQY value achieved, and in turn affect device performance.

### 4.2.4 Phase distribution analysis

The samples are also analyzed using backscattered electron imaging to determine the phase distribution in the films.

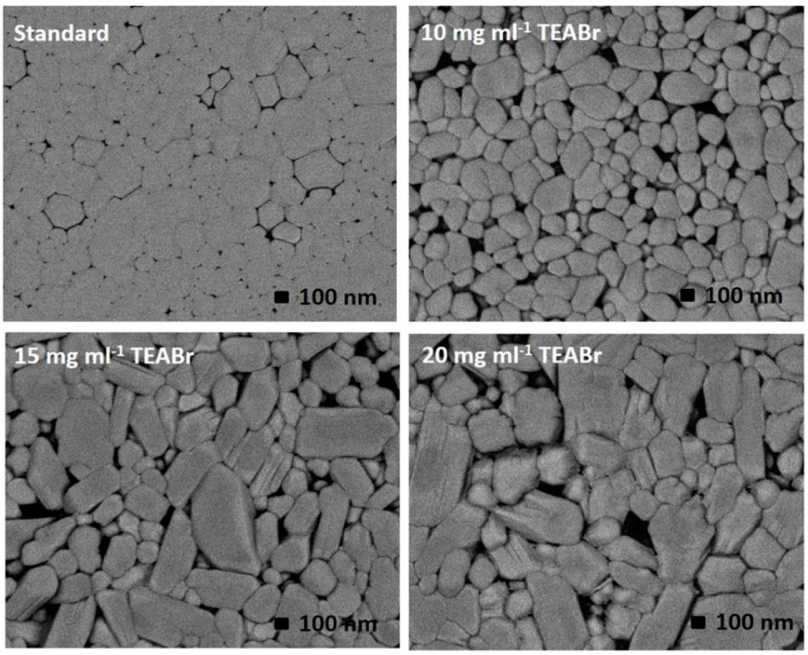


**Figure 4.10** Backscattered electron image of the reference and TEABr treated films

However, no distinct differences in contrast is observed for the samples (Figure 4.10), plausibly due to the minimal difference in elemental content of the two phases. It is hypothesized that the post-deposition treatment with TEABr passivates both the surface vacancies and grain boundary defects present in the film.[24] The annealing step which is carried out subsequently, provides the driving force for diffusion of the ions into the deeper layers resulting in the formation of a bi-layered mixed-dimensional MHP phase as seen by the XRD pattern. It is also intriguing to note that in comparison to the reference, the TEABr-treated films see a 50% increase in thickness independent of TEABr concentration. This volume expansion is attributed to the incorporation of bulky tetra ethyl ammonium ions into the 3D framework.

### 4.2.5 Eliminating solvent effect on film properties

To affirm that the overall enhancement to the optoelectronic properties of the TEABr-treated films arise solely from TEABr incorporation, topographical assessment of the untreated and isopropanol (IPA) treated films is done (Figure 4.11), where no change in morphology was observed on treating the reference film surface with IPA.

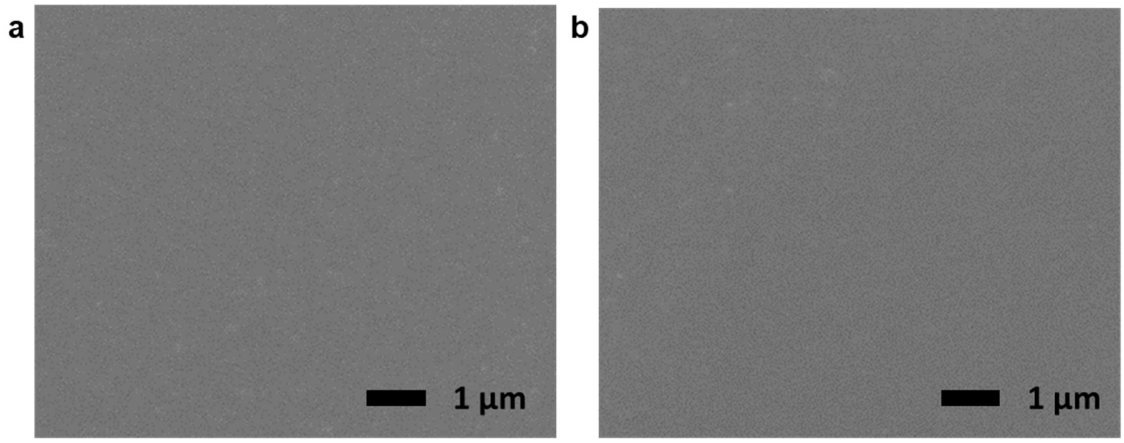


**Figure 4.11** Surface morphology of films (a) untreated and (b) IPA-treated films

### 4.2.6 Correlating film properties with PeLED performance

PeLED performance is directly correlated with the emitter's PLQY, providing the impetus in the search for highly luminescent species. However, PeLED efficiency is also affected by efficiency of charge injection into the emitter. In view of the increasing proportion of poorly conducting low dimensional phase in the TEABr treated film, it is crucial that the electrical properties of the films be investigated to assess its suitability as an efficient emitter in the operating device.

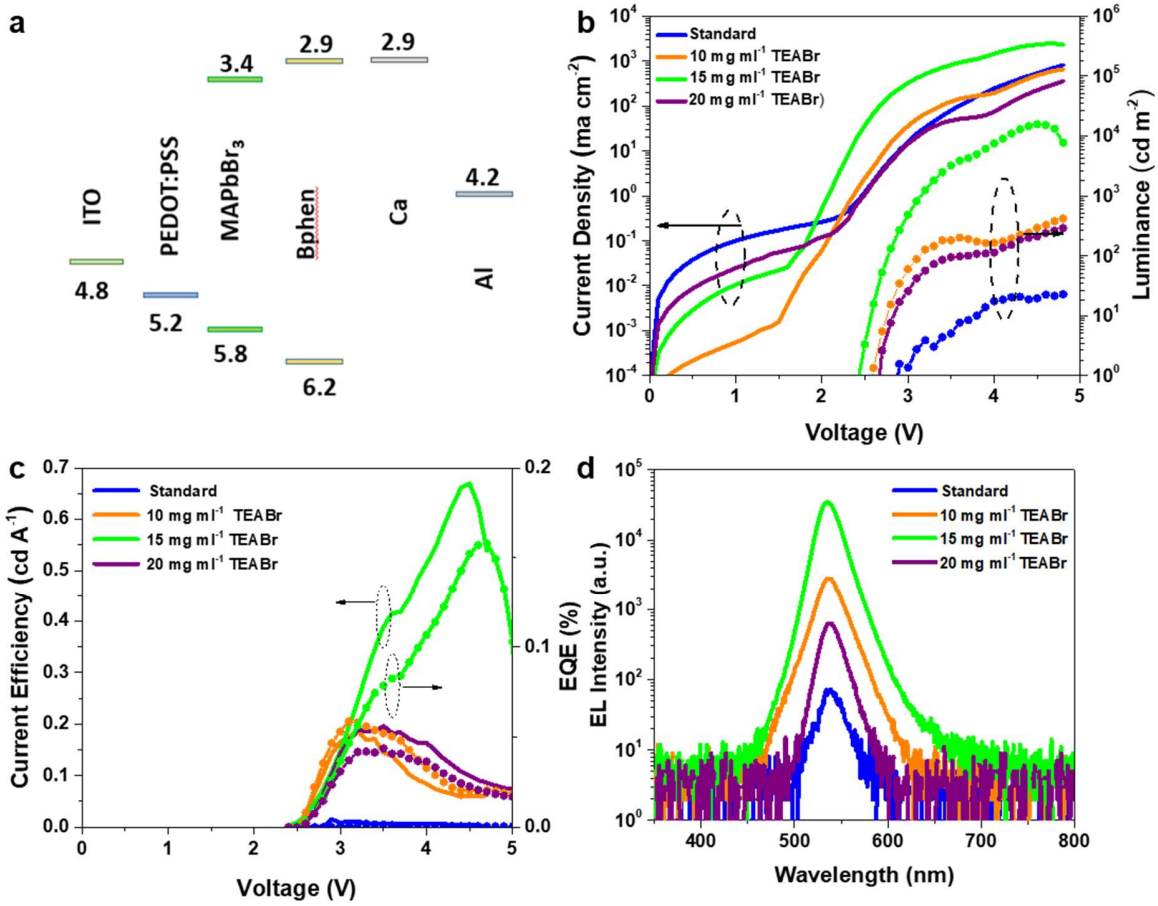


**Figure 4.12** (a) Architecture of fabricated device. (b) Current density and luminance against voltage, (c) current efficiency and external quantum efficiency against voltage and (d) electroluminescence spectra of the reference and TEABr treated films

Progressive increase in maximum luminance with TEABr concentration is seen from a mere 20 cd $m^{-2}$ in the reference $MAPbBr_3$ device to a maximum value of 11,000 cd $m^{-2}$ for the 15 mg $mL^{-1}$ device (Figure 4.12 (b)). Beyond this concentration, device performance starts to deteriorate. Lower threshold voltage is also observed, from 3 V in the reference device to 2.4 V in the 15 mg $mL^{-1}$ TEABr-treated device. The higher efficiencies seen coincides with increased luminance levels (Figure 4.12 (c)). The most efficient device is achieved with 15 mg $mL^{-1}$ TEABr treatment, reaching a current efficiency and EQE of 0.68 cd $A^{-1}$ and 0.16 % respectively, which is approximately a hundred-fold improvement as compared to the reference device (0.0018 %). The enhancement in device performance is

attributed to three phenomena: (a) increased radiative recombination through spatial charge confinement, (b) reduction in surface defect density and (c) lowering of interfacial energetic barrier due to improved energy level matching, thereby allowing for more efficient carrier injection into the emitter layer. The lower current turn-on noted also attests to the improved injection offered with TEABr treatment. However, although the energy band levels of the TEABr-treated films are similar, at higher concentration of 20 mg $mL^{-1}$ TEABr, the threshold voltage increases. This stems from the higher resistance arising from the excessive amount of lower dimensional phase present in the film, limiting charge conduction across the perovskite emitter, thus leading to poorer device efficiency. Despite the increasing proportion of lower dimensional phase with higher concentrations of TEABr, the EL spectra shows no shift in peak position which indicates that emitting domain remains unchanged (Figure 4.12 (d)).

### 4.2.7 Eliminating influence of film thickness on PeLED performance

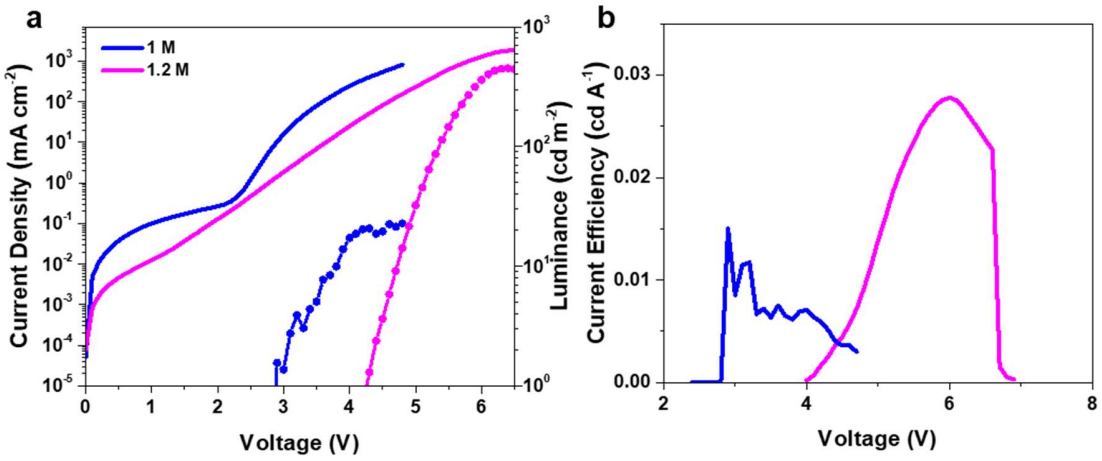


**Figure 4.13** (a) Current density and luminance against voltage and (b) current efficiency against voltage for 1 M (reference) and 1.2 M films

To rule out the influence of emitter thickness on the improvement in device performance, PeLEDs with emitter layer thickness comparable to that of the TEABr-treated films is fabricated by increasing the concentration of the solution to 1.2 M. Despite the slight improvement in luminance and current efficiency observable with the thicker device

(Figure 4.13), the overall performance still lags behind that of the TEABr-treated devices. This provides strong evidence that TEABr treatment is the main contributor towards the overall enhancement in device performance.

## 4.3 Conclusion

In conclusion, it has been shown that through an inexpensive and facile post-deposition treatment process using TEABr, the performance of resultant PeLED devices can be greatly improved. The mixed-dimensional MHP formed on TEABr treatment, evident by the presence of peaks at lower 2θ values, indicates that the secondary phase plays a role in the enhancement of overall device performance. While the absence of emission in the excitation spectra corresponding to the absorption edge at 325 nm eliminates energy funneling as the mechanism for improved device performance, it does not discount the plausibility that grain size modulation is crucial for optimum intercalation of the two phases. Not only did the TEABr treatment resolve the issue of non-stoichiometric ratio of surface elements, the simultaneous improvement in morphology and tailoring of the energy band levels at the charge selective interfaces have also allowed for more efficient injection and radiative recombination of charge carriers, as supported by the substantial enhancement in both film optical properties as well as device performance. This provide strong evidence that contributions from these factors lead to enhanced photoluminescence and electroluminescence despite absence of energy funneling. This crucial discovery is not only testament to the need for stringent defect management in MHP film deposition but may very well present a new opportunity for further research into mixed-dimensional systems as effective emitters for PeLEDs.

# References

1. Abate, A.; Saliba, M.; Hollman, D. J.; Stranks, S. D.; Wojciechowski, K.; Avolio, R.; Grancini, G.; Petrozza, A.; Snaith, H. J., Supramolecular Halogen Bond Passivation of Organic–Inorganic Halide Perovskite Solar Cells. *Nano Letters* **2014,** *14* (6), 3247-3254.

2. Shao, Y.; Xiao, Z.; Bi, C.; Yuan, Y.; Huang, J., Origin and elimination of photocurrent hysteresis by fullerene passivation in CH3NH3PbI3 planar heterojunction solar cells. *Nature Communications* **2014,** *5*, 5784.

3. Wang, B.; Wong, K. Y.; Yang, S.; Chen, T., Crystallinity and defect state engineering in organo-lead halide perovskite for high-efficiency solar cells. *Journal of Materials Chemistry A* **2016,** *4* (10), 3806-3812.

4. Xie, H.; Liu, X.; Lyu, L.; Niu, D.; Wang, Q.; Huang, J.; Gao, Y., Effects of Precursor Ratios and Annealing on Electronic Structure and Surface Composition of CH3NH3PbI3 Perovskite Films. *The Journal of Physical Chemistry C* **2016,** *120* (1), 215-220.

5. Noel, N. K.; Abate, A.; Stranks, S. D.; Parrott, E. S.; Burlakov, V. M.; Goriely, A.; Snaith, H. J., Enhanced Photoluminescence and Solar Cell Performance via Lewis Base Passivation of Organic–Inorganic Lead Halide Perovskites. *ACS Nano* **2014,** *8* (10), 9815-9821.

6. Yang, S.; Wang, Y.; Liu, P.; Cheng, Y.-B.; Zhao, H. J.; Yang, H. G., Functionalization of perovskite thin films with moisture-tolerant molecules. *Nature Energy* **2016,** *1*, 15016.

7. Cohen, B.-E.; Etgar, L., Parameters that control and influence the organo-metal halide perovskite crystallization and morphology. *Frontiers of Optoelectronics* **2016,** *9* (1), 44-52.

8. Tachikawa, T.; Karimata, I.; Kobori, Y., Surface Charge Trapping in Organolead Halide Perovskites Explored by Single-Particle Photoluminescence Imaging. *The Journal of Physical Chemistry Letters* **2015,** *6* (16), 3195-3201.

9. Cho, H.; Jeong, S.-H.; Park, M.-H.; Kim, Y.-H.; Wolf, C.; Lee, C.-L.; Heo, J. H.; Sadhanala, A.; Myoung, N.; Yoo, S.; Im, S. H.; Friend, R. H.; Lee, T.-W., Overcoming the electroluminescence efficiency limitations of perovskite light-emitting diodes. *Science* **2015,** *350* (6265), 1222-1225.

10. Harikesh, P. C.; Mulmudi, H. K.; Ghosh, B.; Goh, T. W.; Teng, Y. T.; Thirumal, K.; Lockrey, M.; Weber, K.; Koh, T. M.; Li, S.; Mhaisalkar, S.; Mathews, N., Rb as an Alternative Cation for Templating Inorganic Lead-Free Perovskites for Solution Processed Photovoltaics. *Chemistry of Materials* **2016,** *28* (20), 7496-7504.

11. Chaudhary, B.; Kulkarni, A.; Jena, A. K.; Ikegami, M.; Udagawa, Y.; Kunugita, H.; Ema, K.; Miyasaka, T., Poly(4-Vinylpyridine)-Based Interfacial Passivation to Enhance Voltage and Moisture Stability of Lead Halide Perovskite Solar Cells. *ChemSusChem* **2017,** *10* (11), 2473-2479.

12. Meloni, S.; Moehl, T.; Tress, W.; Franckevičius, M.; Saliba, M.; Lee, Y. H.; Gao, P.; Nazeeruddin, M. K.; Zakeeruddin, S. M.; Rothlisberger, U.; Graetzel, M., Ionic polarization-induced current–voltage hysteresis in CH3NH3PbX3 perovskite solar cells. **2016,** *7*, 10334.

13. Cheng, Y.; Li, H.-W.; Qing, J.; Yang, Q.-D.; Guan, Z.; Liu, C.; Cheung, S. H.; So, S. K.; Lee, C.-S.; Tsang, S.-W., The detrimental effect of excess mobile ions in planar CH3NH3PbI3 perovskite solar cells. *Journal of Materials Chemistry A* **2016,** *4* (33), 12748-12755.

14. Li, G.; Tan, Z.-K.; Di, D.; Lai, M. L.; Jiang, L.; Lim, J. H.-W.; Friend, R. H.; Greenham, N. C., Efficient Light-Emitting Diodes Based on Nanocrystalline Perovskite in a Dielectric Polymer Matrix. *Nano Letters* **2015,** *15* (4), 2640-2644.

15. Lee, S.; Park, J. H.; Lee, B. R.; Jung, E. D.; Yu, J. C.; Di Nuzzo, D.; Friend, R. H.; Song, M. H., Amine-Based Passivating Materials for Enhanced Optical Properties and Performance of Organic–Inorganic Perovskites in Light-Emitting Diodes. *The Journal of Physical Chemistry Letters* **2017,** *8* (8), 1784-1792.

16. Cao, D. H.; Stoumpos, C. C.; Farha, O. K.; Hupp, J. T.; Kanatzidis, M. G., 2D Homologous Perovskites as Light-Absorbing Materials for Solar Cell Applications. *Journal of the American Chemical Society* **2015,** *137* (24), 7843-7850.

17. Smith, I. C.; Hoke, E. T.; Solis-Ibarra, D.; McGehee, M. D.; Karunadasa, H. I., A Layered Hybrid Perovskite Solar-Cell Absorber with Enhanced Moisture Stability. *Angewandte Chemie International Edition* **2014,** *53* (42), 11232-11235.

18. Ng, Y. F.; Kulkarni, S. A.; Parida, S.; Jamaludin, N. F.; Yantara, N.; Bruno, A.; Soci, C.; Mhaisalkar, S.; Mathews, N., Highly efficient Cs-based perovskite light-emitting

diodes enabled by energy funnelling. *Chemical Communications* **2017,** *53* (88), 12004-12007.

19. Elliott, R. J., Intensity of Optical Absorption by Excitons. *Physical Review* **1957,** *108* (6), 1384-1389.

20. Endres, J.; Egger, D. A.; Kulbak, M.; Kerner, R. A.; Zhao, L.; Silver, S. H.; Hodes, G.; Rand, B. P.; Cahen, D.; Kronik, L.; Kahn, A., Valence and Conduction Band Densities of States of Metal Halide Perovskites: A Combined Experimental–Theoretical Study. *The Journal of Physical Chemistry Letters* **2016,** *7* (14), 2722-2729.

21. Ng, Y. F.; Jamaludin, N. F.; Yantara, N.; Li, M.; Irukuvarjula, V. K. R.; Demir, H. V.; Sum, T. C.; Mhaisalkar, S.; Mathews, N., Rapid Crystallization of All-Inorganic CsPbBr3 Perovskite for High-Brightness Light-Emitting Diodes. *ACS Omega* **2017,** *2* (6), 2757-2764.

22. Park, M.-H.; Jeong, S.-H.; Seo, H.-K.; Wolf, C.; Kim, Y.-H.; Kim, H.; Byun, J.; Sung Kim, J.; Cho, H.; Lee, T.-W., *Unravelling Additive-based Nanocrystal Pinning for High Efficiency Organic-Inorganic Halide Perovskite Light-Emitting Diodes*. 2017; Vol. 42.

23. Misra, R. K.; Cohen, B.-E.; Iagher, L.; Etgar, L., Low-Dimensional Organic–Inorganic Halide Perovskite: Structure, Properties, and Applications. *ChemSusChem* **2017,** *10* (19), 3712-3721.

24. Zhao, T.; Chueh, C.-C.; Chen, Q.; Rajagopal, A.; Jen, A. K. Y., Defect Passivation of Organic–Inorganic Hybrid Perovskites by Diammonium Iodide toward High-Performance Photovoltaic Devices. *ACS Energy Letters* **2016,** *1* (4), 757-763.

# Chapter 5

# Additive engineering for suppression of grain size modulated defects

*Geometric confinement involves imposition of spatial constraints to facilitate bimolecular recombination process. However, the simultaneous increase in grain boundary density necessitates effective passivation at the grain boundaries for the full advantage of spatial confinement to be realized. In this chapter, it is shown that by incorporating BPhen into the emitter layer via the anti-solvent process, higher photoluminescence, luminance and efficiency are attained due to the formation of smaller grains which enhances radiative recombination. This is possible due to the passivating nature of Bphen which enables small grains to be formed without detriment to MHP film properties. The controllable alteration of the MHP's energy bands via simple variation of BPhen concentration in the anti-solvent too allows for efficient injection of charge carriers into the emitter as seen by the reduction in threshold voltage. The champion device is made with 0.500 mg $mL^{-1}$ of BPhen, resulting in a ten-fold increase in luminance and fifteen-fold improvement in current efficiency and EQE compared to the reference.*

---

* Nur Fadilah Jamaludin, Natalia Yantara, Yan Fong Ng, Annalisa Bruno, Bevita K. Chandran, Xin Yu Chin, Krishnamoorthy Thirumal, Nripan Mathews, Cesare Soci and Subodh Mhaisalkar, Perovskite templating via a bathophenanthroline additive for efficient light-emitting devices. J. Mater. Chem. C, 2018, 6, 2295 –2302. DOI: 10.1039/C7TC05643E.

## 5.1 Introduction

Offering a wide array of excellent optoelectronic properties such as direct band gap, high extinction coefficient and low defect density,[1-3] MHPs have shown tremendous success as light absorbers in recent years. The similar properties required for both light-harvesting and -emitting applications indicate MHPs' potential beyond the field of photovoltaics.[4] This, coupled with early reports of narrow PL emission band[5-6] observed in MHPs, has driven research into employment of these materials in PeLEDs.[4, 7] The expeditious rise in PeLED performance can be ascribed to MHPs' compatibility with OLED device architecture[8-10] which facilitates the technological transfer. In addition, the low material and processing cost of MHPs[2, 11-12] further fortify efforts to realize a cheap and viable alternative to current OLEDs. Recent improvements in PeLED device performance have been dominated by process-engineered grain size modulation techniques to improve film morphology, such as nanocrystal pinning,[13] and use of polymer composites,[14-15] all in a bid to increase radiative recombination through spatial confinement of injected charges. However, to leverage on the benefits of spatial confinement, the grain size needs to be reduced, translating to an increase in grain boundary density. Typically, increase in grain boundary density is undesired as grain boundaries act as sites for non-radiative recombination (i.e defects and traps). Thus, to fully harness the advantages offered by small grains for efficient photon generation, a method to form small passivated grains needs to be developed. Here, it is shown that by incorporating Bphen into the MHP emitter during the anti-solvent process, small grains can be formed in-situ during solution processing.

## 5.2 Results and Discussion

The films used in this study are prepared using the widely reported solvent engineering process, which allows for the facile fabrication of smooth and compact MHP films. By tuning the BPhen concentration in the anti-solvent from 0 to 0.750 mg $mL^{-1}$, notable enhancement to the films' optoelectronic properties and device performance were observed.

### 5.2.1 Phase and crystal structure analysis

To ascertain the films' phase purity on BPhen incorporation, compositional evaluation using XRD is carried out.

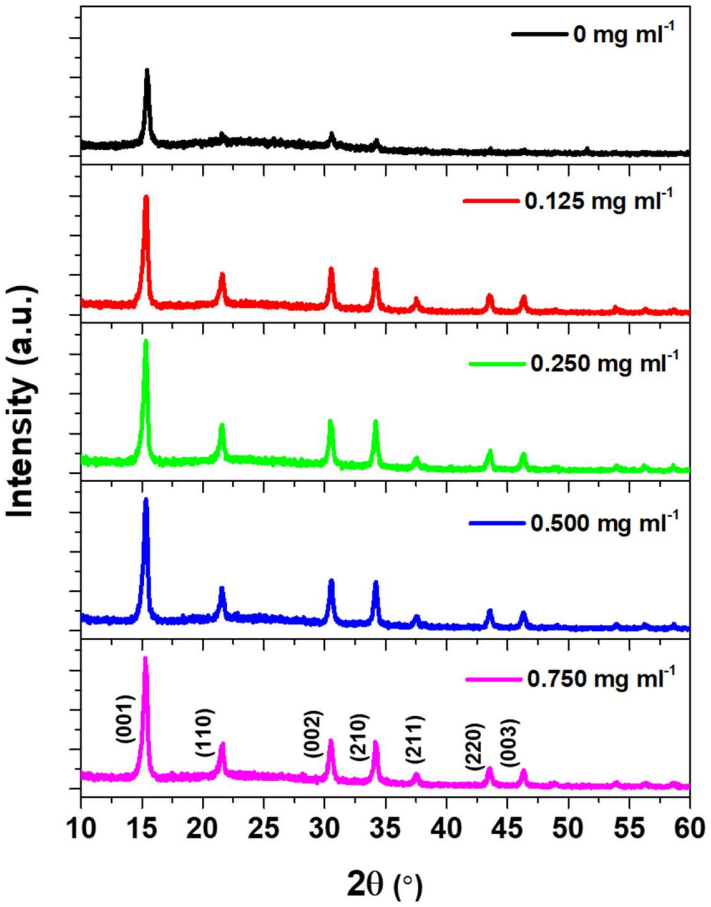


**Figure 5.1** XRD pattern of films prepared with varying amounts of Bphen in the anti-solvent

Figure 5.1 shows the XRD patterns of $CH_3NH_3PbBr_3$ films prepared with varying BPhen concentration. Analysis of the patterns revealed characteristic reflections of $CH_3NH_3PbBr_3$ cubic (*Pm3m*) phase,[16-18] with no extra peaks to imply the presence of secondary phases. Intriguingly, inclusion of BPhen results in more crystalline films (as inferred from the sharpening of XRD peaks), consisting of crystallites with reduced tendency for preferred orientation (indicated by the presence of additional XRD peaks corresponding to

orientations other than the (001) plane). Negligible change in lattice parameters is also observed, concurring with the report by Cho et al., where inclusion of a small molecule additive induced no change to MHP crystal structure[13].

BPhen incorporation in MHP via the templating process is further affirmed by Fourier transform infrared spectroscopy (FTIR), where the inclusion of the Bphen molecule into the perovskite is detectable at around ~ 1570 $cm^{-1}$ as denoted by the dashed vertical line (Figure 5.2).

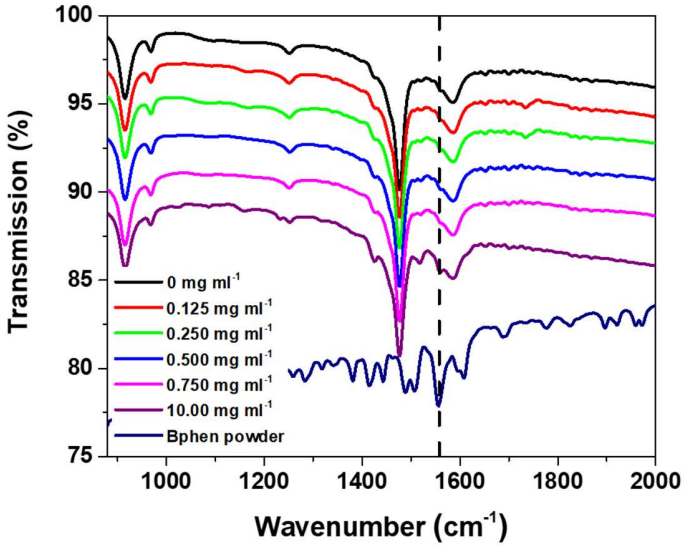


**Figure 5.2** FTIR spectra of reference and BPhen-incorporated films

### 5.2.2 Photophysical properties

Based on the premise that a highly photoluminescent material is well-suited for light emission applications,[4] various spectroscopic techniques are employed to probe the influence of BPhen concentration on PL characteristics.

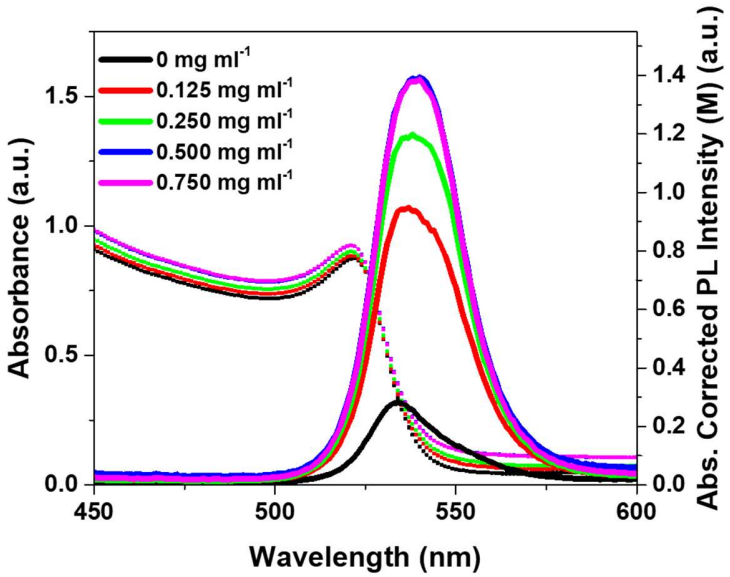


**Figure 5.3** Absorbance and PL spectra of reference and BPhen-incorporated films

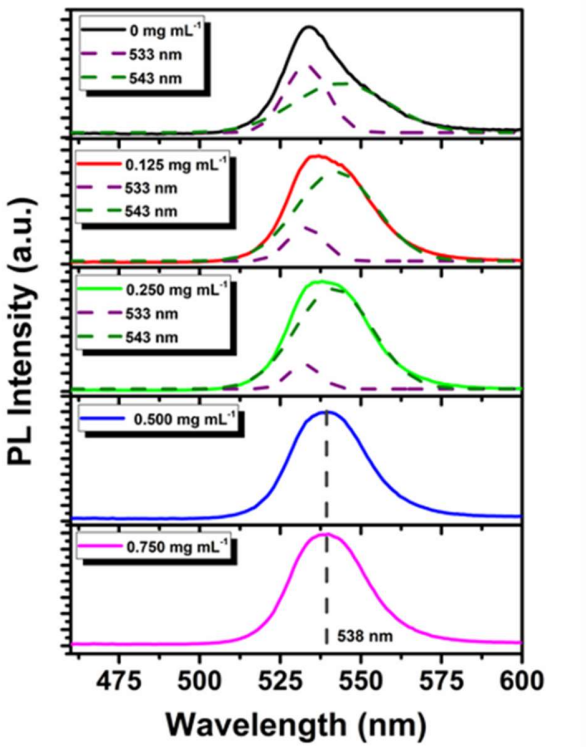


**Figure 5.4** PL peak fitting of reference and BPhen-incorporated films

The absorbance-corrected PL emission spectra (Figure 5.3) is presented to account for re-absorption of emitted photons at the excitation wavelength (400 nm). While double emission peaks are noted for the PL spectra of the reference and BPhen-incorporated films up to 0.250 mg $mL^{-1}$ (Figure 5.4) due to either the co-existence of ordered and disordered domains[19] or to inner filtering effect,[20-21] films prepared with higher BPhen concentrations showed only single PL peak emission. This can be explained by the formation of increasingly ordered domains for the 0.500 and 0.750 mg $mL^{-1}$ Bphen-incorporated films.

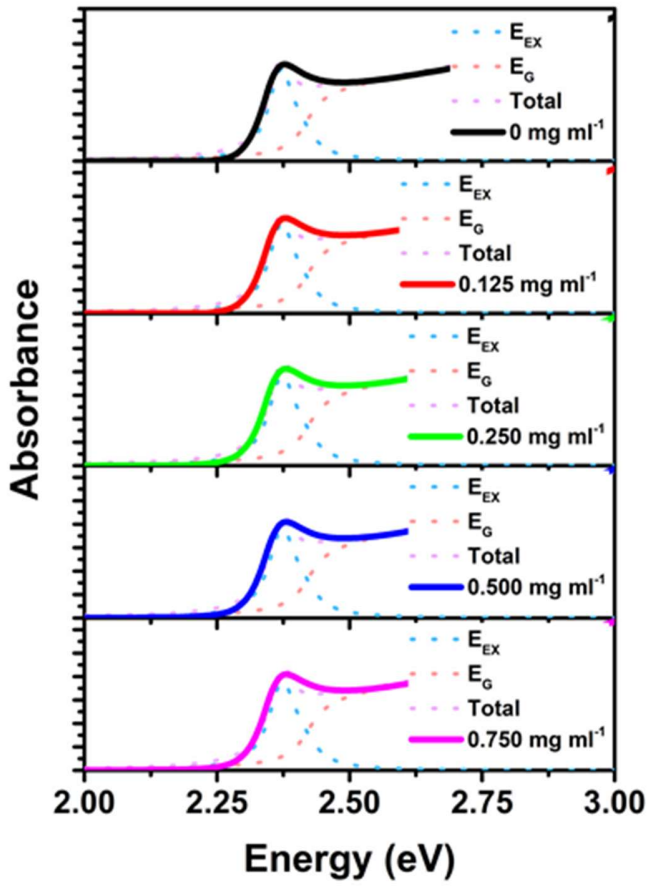


**Figure 5.5** Elliot fitting of reference and BPhen-incorporated films to derive band gap and exciton binding energy values

The optical band gap (~2.40 eV) and exciton binding energy (~50 meV) of the films extracted with Elliot's fitting (Figure 5.5 and Table 5.1)[22-23] as well as the corresponding

PL peak energy (~2.3 eV) is found to be nearly unaffected by BPhen incorporation. Remarkably, the PL intensity increases substantially with increasing BPhen concentration up to 0.500 mg $mL^{-1}$, beyond which the intensity saturates, implying a strong correlation between BPhen concentration and radiative recombination yield.

**Table 5.1** Exciton binding energy and optical band gap energy of reference and BPhen-incorporated films obtained by Elliot's fitting of the absorbance spectra

| Bphen concentration (mg $mL^{-1}$) | Exciton Binding Energy ($E_{EX}$) (meV) | Band Gap ($E_G$) (eV) | Valence band maximum (eV) |
|---|---|---|---|
| 0 | 48 ± 2 | 2.45 ± 0.02 | 5.75 ± 0.05 |
| 0.125 | 49 ± 2 | 2.48 ± 0.03 | 5.47 ± 0.04 |
| 0.250 | 50 ± 3 | 2.49 ± 0.03 | 5.43 ± 0.03 |
| 0.500 | 50 ± 3 | 2.50 ± 0.05 | 5.39 ± 0.03 |
| 0.750 | 49 ± 2 | 2.52 ± 0.05 | 5.35 ± 0.05 |

The energy band alignments of the films are obtained from photoelectron spectroscopy in air (PESA) and ultraviolet-visible (UV-Vis) absorption measurements.

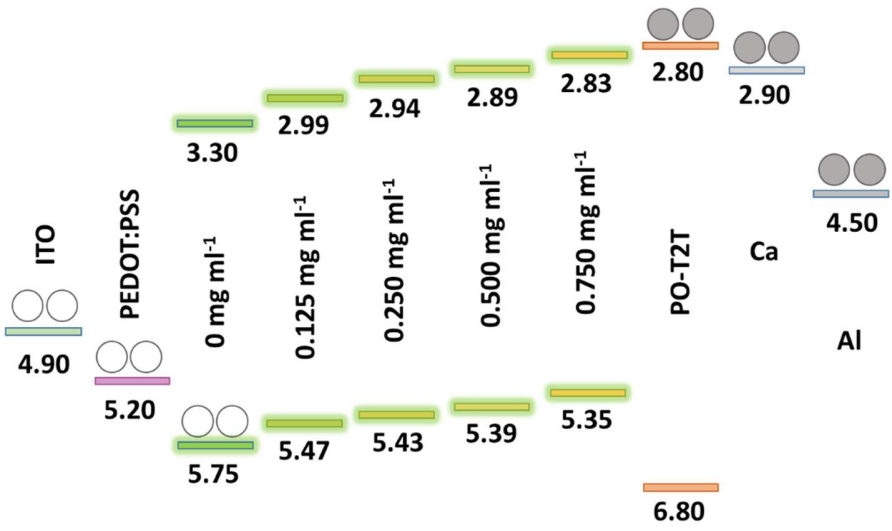


**Figure 5.6** Schematic diagram on the change in emitter valence and conduction band levels of reference and BPhen-incorporated films

The upward shift of the energy levels with higher BPhen concentration (Figure 5.6) suggests that its addition during processing offers interfacial band engineering which can be imputed to the stoichiometric modification[24] or accommodation of the BPhen molecule in the microstructure. This consequently reduces the hole injection barrier through better matching at the HTM/MHP interface without introducing any additional energy barrier at the electron transporting layer (ETL)/MHP interface. The reduction in energetic offset between the conduction band of the MHP and the lowest unoccupied molecular orbital (LUMO) of the ETL is expected to improve electron transfer and reduce energy loss, while the larger offset between the valence band of the perovskite and the highest occupied molecular orbital (HOMO) of the ETL increases the hole blocking capabilities of this interface.

Effect of BPhen addition is also probed through time-resolved PL (TRPL) decay measurements to assess the influence on PL radiative lifetimes.

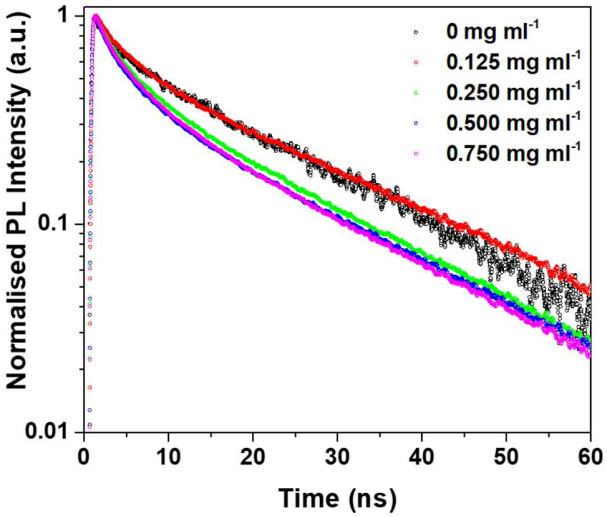


**Figure 5.7** PL decay lifetimes of reference and BPhen-incorporated films

Figure 5.7 shows the TRPL decays for the reference and BPhen incorporated films. The decay curves are fitted with a bi-exponential decay function to extract the fast and slow time constants related to the non-radiative and radiative recombination processes occurring

in the films. It is found that the weighted average lifetime decreases with increasing BPhen concentration (Table 5.2). This can be attributed to either an increase in defect states or decrease in film grain size, where enhanced radiative recombination rate is triggered due to the spatial confinement offered by the latter.[25] It is postulated that grain size reduction is a more plausible explanation for the shortened TRPL decay lifetime owing to the negligible change in non-radiative decay times and amplitude as well as the improvement in PL intensities noted with BPhen incorporation (Figure 5.3).

**Table 5.2** Summary of the PL decay lifetimes of reference and BPhen-incorporated films

| Sample | $A_1$ | $T_1$ (ns) | $A_2$ | $T_2$ (ns) | $T_{ave}$ (ns) |
|---|---|---|---|---|---|
| **0 mg ml$^{-1}$** | 0.33 ± 0.01 | 3.09 ± 0.03 | 0.67 ± 0.01 | 23.98 ± 0.08 | **17.09 ± 0.07** |
| **0.125 mg ml$^{-1}$** | 0.42 ± 0.01 | 4.04 ± 0.01 | 0.58 ± 0.01 | 27.27 ± 0.05 | **17.51 ± 0.06** |
| **0.250 mg ml$^{-1}$** | 0.48 ± 0.01 | 3.18 ± 0.01 | 0.52 ± 0.01 | 19.80 ± 0.03 | **11.82 ± 0.06** |
| **0.500 mg ml$^{-1}$** | 0.52 ± 0.01 | 2.89 ± 0.01 | 0.48 ± 0.01 | 19.76 ± 0.04 | **10.99 ± 0.06** |
| **0.750 mg ml$^{-1}$** | 0.51 ± 0.01 | 3.06 ± 0.01 | 0.49 ± 0.01 | 18.95 ± 0.03 | **10.84 ± 0.06** |

### 5.2.3 Morphological analysis of Bphen-incorporated films

Topological assessment of the films is carried out to verify the hypothesis of grain size modulation on BPhen incorporation.

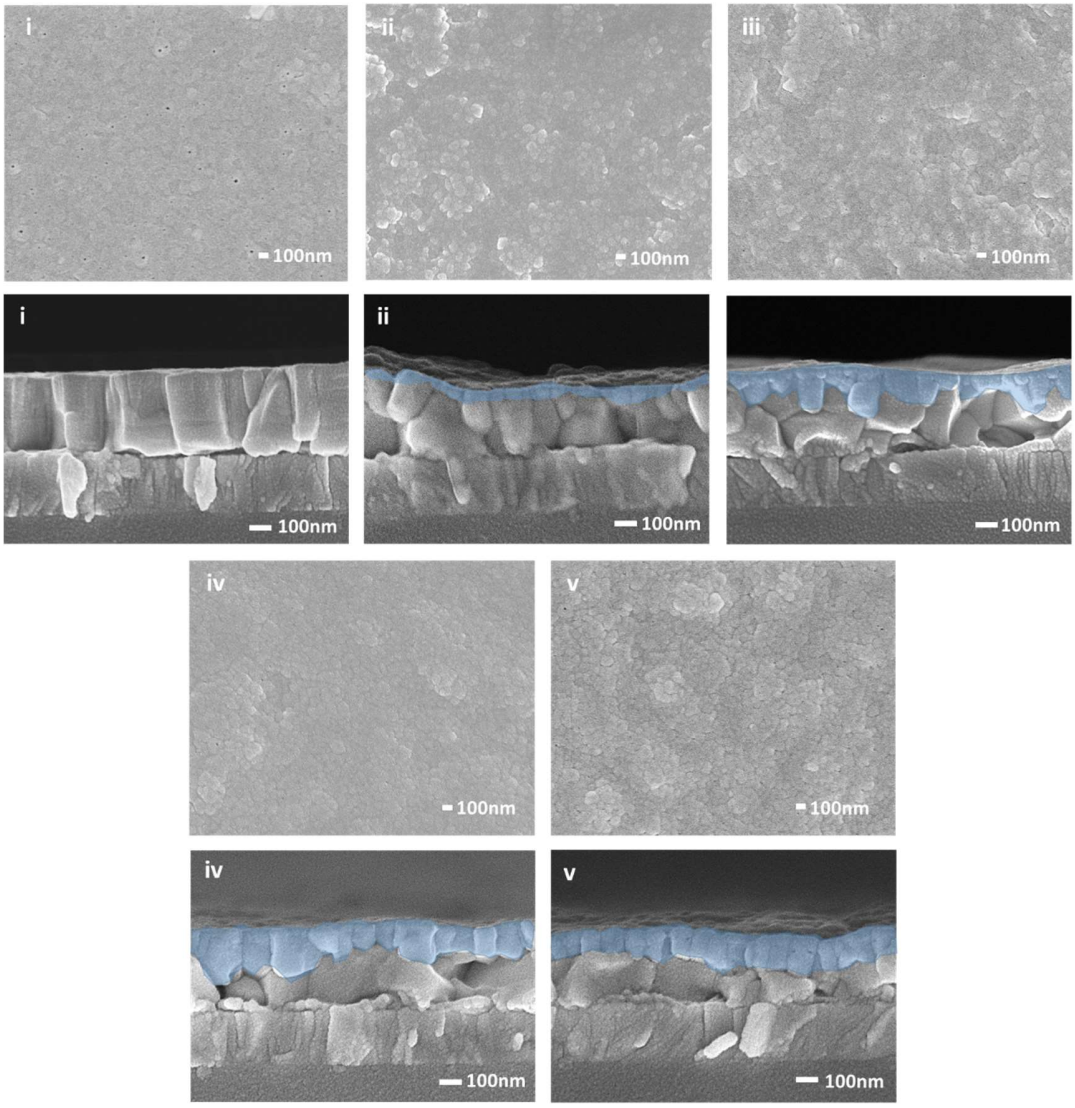


**Figure 5.8** Top and cross-sectional image of reference and BPhen-incorporated films

Although thickness (ca. 400 nm) and surface coverage remain unaffected with increasing BPhen concentration (Figure 5.8), the grain boundaries become progressively more conspicuous. From the cross-sectional images of the films, noticeable change from columnar to polycrystalline grain structures is observed with increasing BPhen concentration, although larger surface roughness is also detected (Figure 5.9). While the reference film consists of a single layer of large columnar grains (> 200 nm in size), it is curious to note that the BPhen-incorporated films exhibit a bimodal grain size distribution, with the bottom layer consisting of larger grains (> 200 nm) and the overlayer comprising

of smaller grains (< 100 nm). The smaller grains in the overlayer can be ascribed to the pinning effect of the small molecule additive[13], while the formation of a double layer implies that the pinning effect only occurs at the top surface during the solvent engineering process. Since the smaller grains are known to enhance radiative recombination through stronger spatial charge confinement,[25] we ascribe the higher PL emission reported in Figure 5.3 to the presence of the overlayer in BPhen-incorporated films.

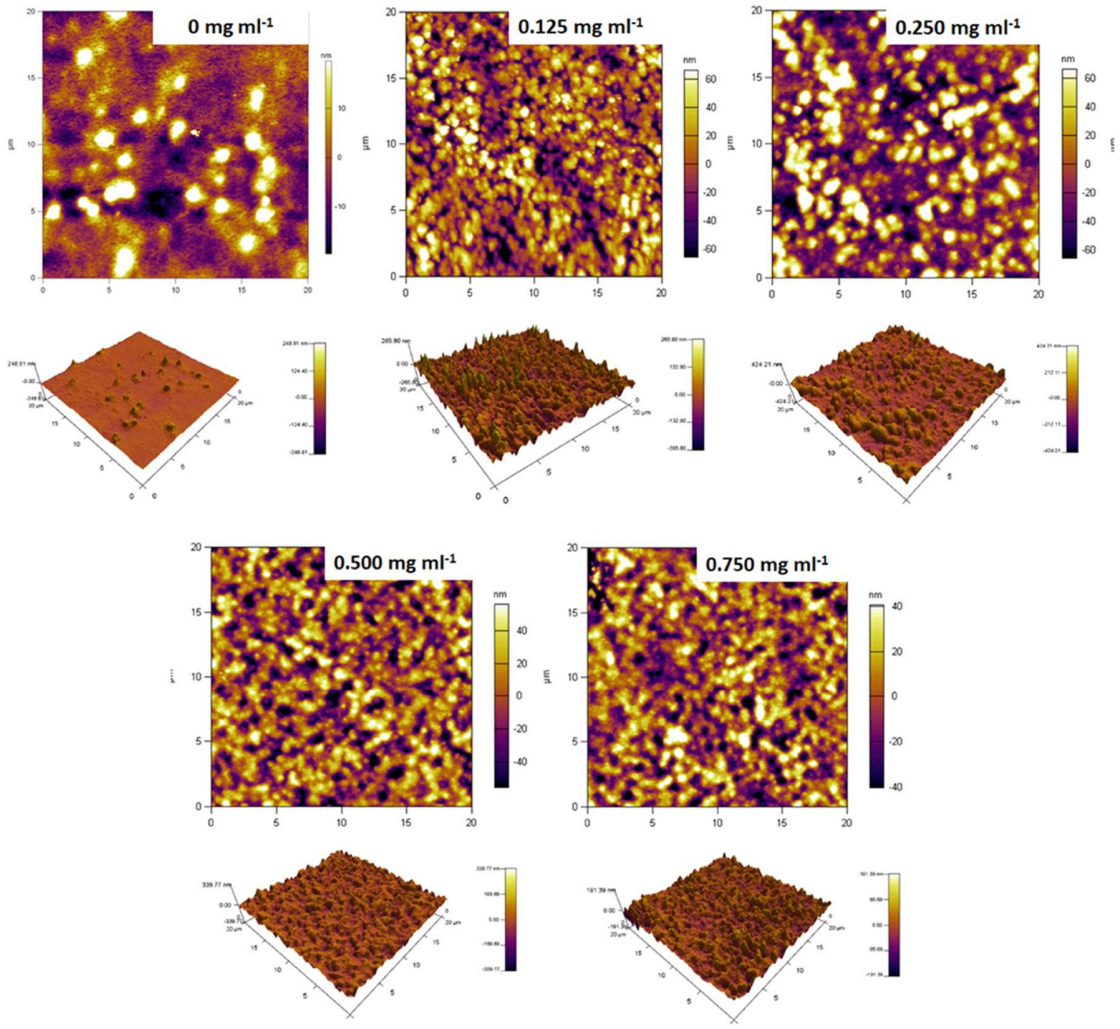


**Figure 5.9** Surface roughness analysis of reference and BPhen-incorporated films

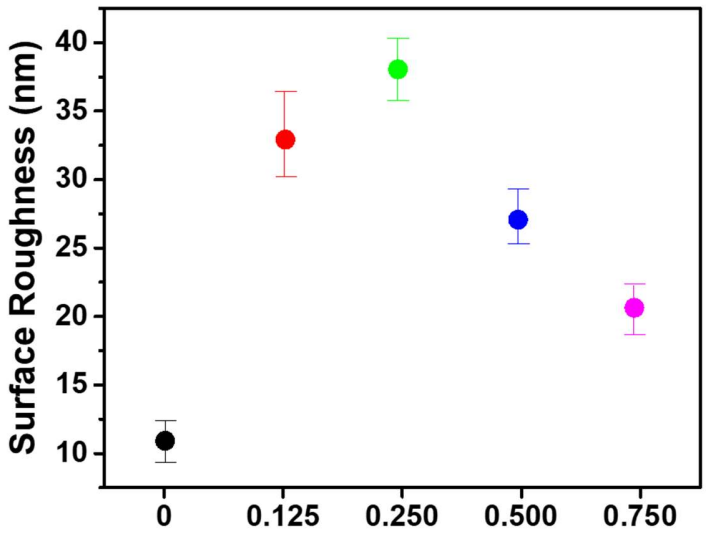


**Figure 5.10** Graph of surface roughness as a function of Bphen concentration

BPhen-incorporated PeLEDs are subsequently fabricated to correlate film morphology and optoelectronic properties with device performance.

### 5.2.4 Electrical characterization of additive incorporated films

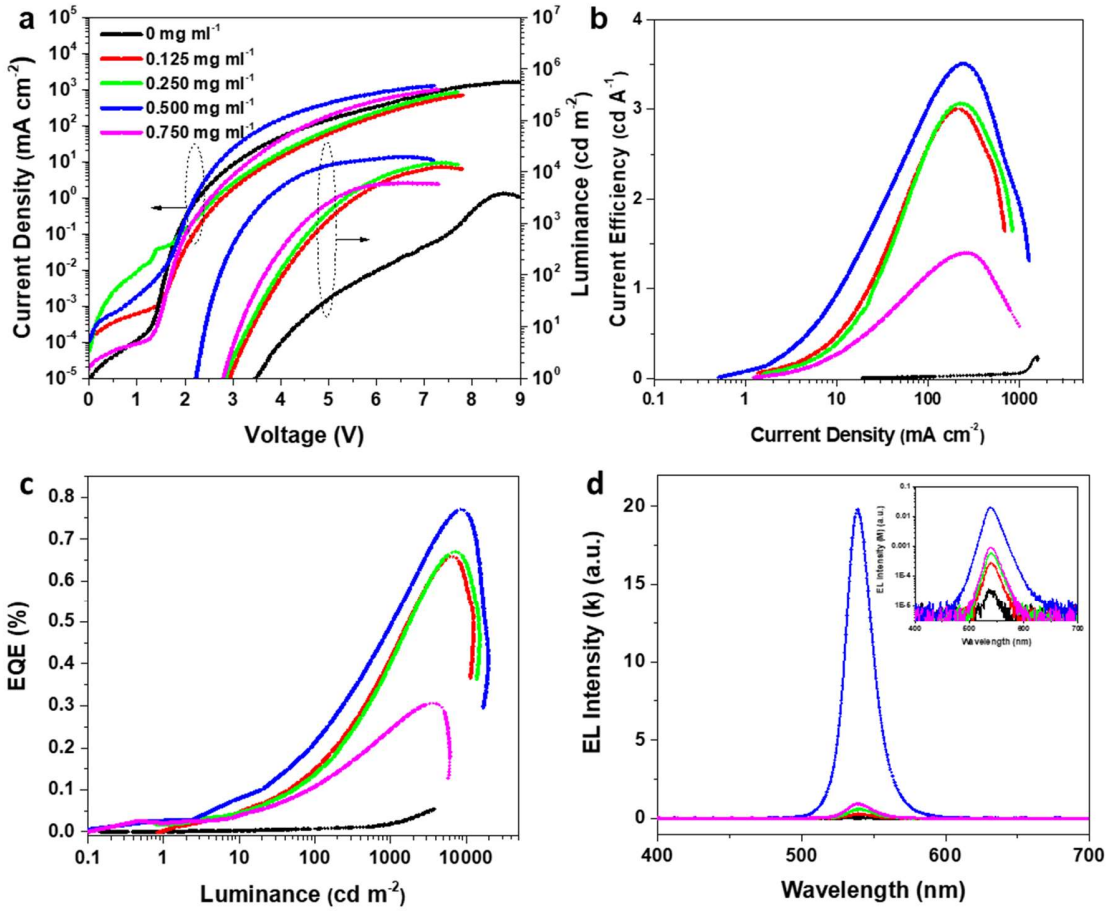


**Figure 5.11** (a) Current density and luminance against voltage, (b) current efficiency against current density and (c) EQE against luminance curves. (d) EL spectra of devices prepared from reference and BPhen-incorporated films

Clearly, addition of BPhen into the emitter layer improves device performance across all measured parameters (Figure 5.11). The reference device gives a peak luminance of 2,000 cd $m^{-2}$ at 8.5 V – inferior to the BPhen-incorporated devices, which exhibit substantially higher luminance (> 10,000 cd $m^{-2}$) at much lower voltages. The threshold voltage, indicative of carrier injection efficiency,[26] is reduced to the range of 2.3-2.8 V, a notable improvement from the reference (>3.5 V). Current efficiencies and EQE (Figure 5.11 (b)-(c)) are also well above those of the reference device, consistent with the higher luminance

attained for comparable current densities. The champion device is obtained with a BPhen concentration of 0.500 mg $mL^{-1}$, yielding maximum luminance, current efficiency and EQE of 19,627 cd $m^{-2}$, 3.7 cd $A^{-1}$ and 0.78 %, respectively. This is equivalent to a ten-fold increase in luminance and fifteen-fold improvement in current efficiency and EQE as compared to the reference device. The remarkable enhancement across all performance metrics obtained through a simple incorporation of BPhen implies significant losses in the reference device, assigned predominantly to optical and electrical losses.[27] Smaller grains achieved through BPhen incorporation in PeLEDs afford effective radiative recombination of charges due to enhanced spatial confinement.[13] This is consistent with the rapid PL decay and high photoluminescence intensity measured in BPhen-incorporated films[13-14, 28-29]. The reduction in threshold voltage to values as low as the band gap of the emitter implies that the energy barrier at the HTM/perovskite interface is effectively eliminated, due to the re-alignment of energy band levels, facilitating hole injection into the MHP. Although the energy levels show continuous shift with higher BPhen concentration (> 0.500 mg $mL^{-1}$), the decline in device performance can be explained by the need for optimum positioning of the energy levels to facilitate simultaneous carrier injection and confinement. Correspondingly, the higher current efficiency stems from the more effective radiative recombination in BPhen-incorporated devices, giving rise to higher luminance for similar current densities. Moreover, the lone pair of electrons on the $sp^2$-hybridized orbital of N in the pyridine molecules of BPhen is able to bind with under-coordinated Pb atoms,[30] thus passivating possible trap states. The extremely narrow full width at half maximum (ca. 20-22 nm) indicates high colour purity emission (Figure 5.12 (d)).

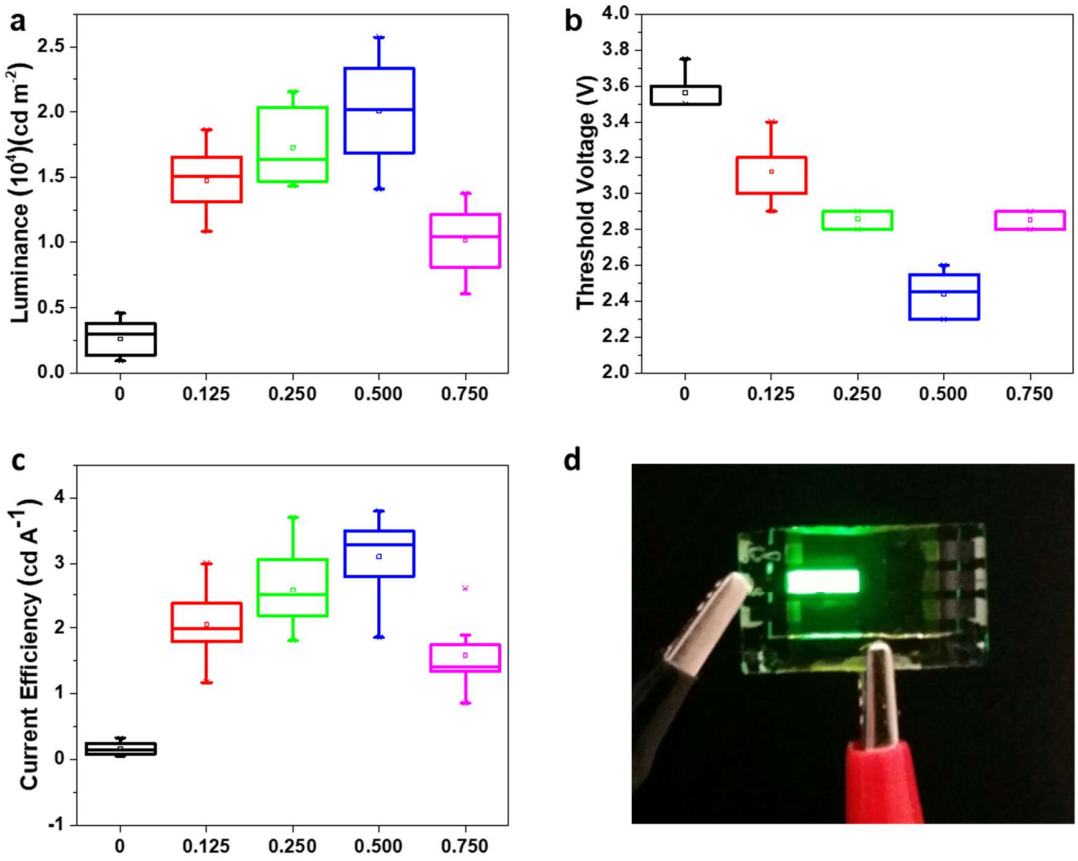


**Figure 5.12** Statistical representation of the performance metric of 50 devices

Statistical distribution of the device performance is as shown in Figure 5.12.

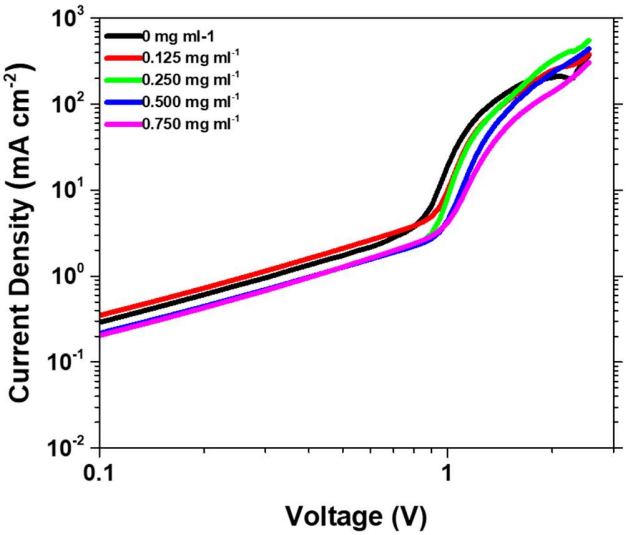


**Figure 5.13** Current density against voltage of hole-only devices of reference and BPhen-incorporated films

The drop in current efficiency on addition of 0.750 mg $mL^{-1}$ of BPhen, on the other hand, is due to the decrease in carrier mobility arising from increased impurity scattering[31] at high BPhen concentration, as deduced from the lower current density measured in hole-only devices (Figure 5.13).

### 5.2.5 Effect of type of additive used

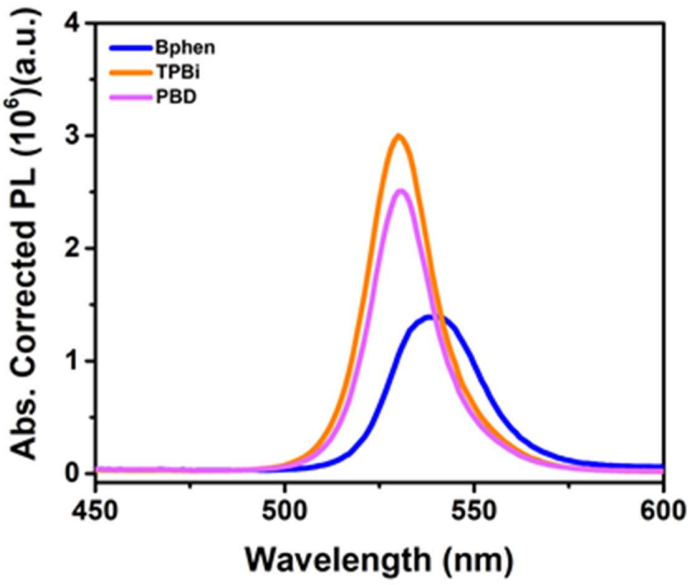


**Figure 5.14** Comparison of PL emission spectra of films incorporated with different molecules

Two other small organic molecules, namely 1,3,5-tris(1-phenyl-1Hbenzimidazol-2-yl)benzene (TPBi) and 2-(4-biphenyl)-5-(4-tert-butylphenyl)-1,3,4-oxadiazole (PBD), are also investigated as potential BPhen substitutes due to their deep HOMO levels offering potentially similar hole-blocking capabilities. Although TPBi, PBD and BPhen-incorporated films yield higher PL emission (Figure 5.14), in the respective order, no direct correlation between the PL enhancement and device performance is found (Figure 5.15). Secondly, the size of the organic molecules used will likely determine the extent of incorporation in the MHP framework.

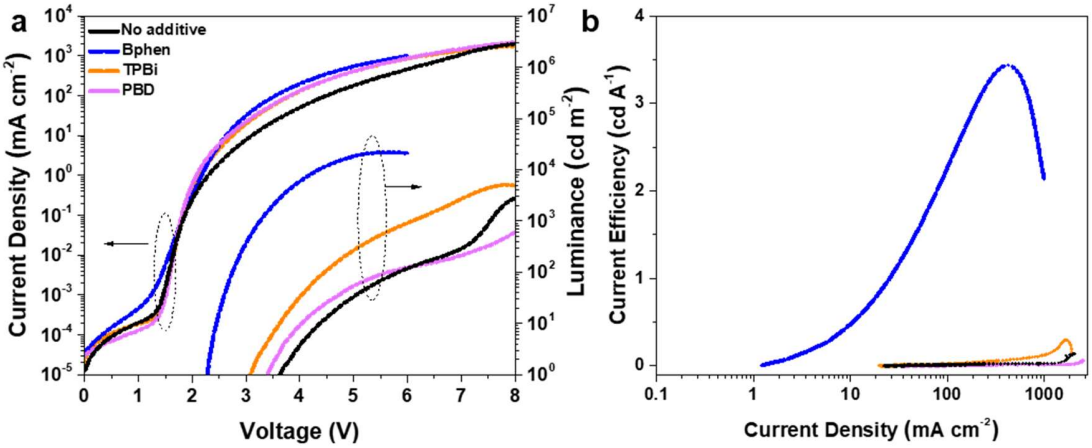


**Figure 5.15** (a) Current density and luminance against voltage as well as (b) current efficiency against current density of Bphen, TPBi and PBD incorporated devices

Rather, BPhen-incorporated devices yield the best performance, whereas TPBi and PBD-incorporated devices showed similar efficiency to the reference device. This suggests that the specific choice of small molecules used as additive plays a crucial role in alleviating the electrical and optical losses of PeLEDs. A few reasons are posited. Firstly, the electron mobility is highest for BPhen (5.2 x $10^{-4}$ $cm^2$ $V^{-1}$ $s^{-1}$), followed by TPBi (3.3 x $10^{-5}$ $cm^2$ $V^{-1}$ $s^{-1}$) and PBD (2 x $10^{-5}$ $cm^2$ $V^{-1}$ $s^{-1}$), which could have influenced the electron charge dynamics in the perovskite emitter and thus explaining the shift in threshold voltage[32-34].

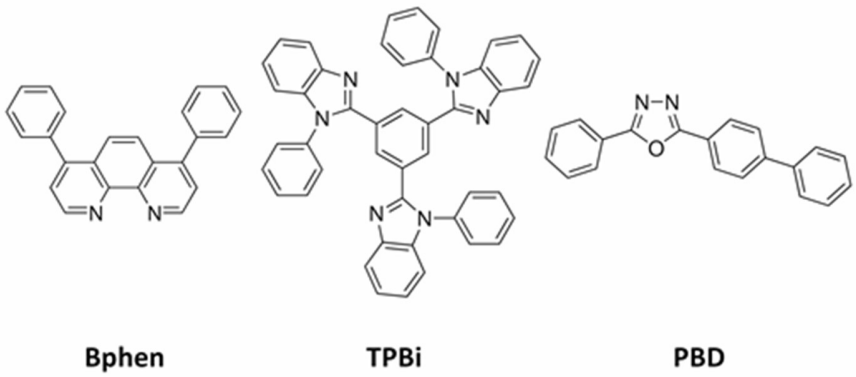


**Figure 5.16** Molecular structures of Bphen, TPBi and PBD

Based on their molecular structure (Figure 5.16) TPBi and PBD, which are larger than BPhen, can distort the MHP structure and introduce lattice defects.

### 5.2.6 Effect of electron transporting material selection on PeLED performance

One of the key parameters governing PeLED performance is charge injection efficiency. Balanced charge transport into the emitter is desired to allow for efficient radiative recombination. However, this is often affected by the interfacial charge selective layers. Here, alternative electron transport materials to PO-T2T are investigated to further improve device performance. The alternative electron transport materials are chosen based on their energetic compatibility with Ca and the emitter (Figure 5.17). Ideally, minimal energy mismatch at the interface is preferred to avoid charge accumulation at the interfaces and facilitate efficient transfer into the emitter.

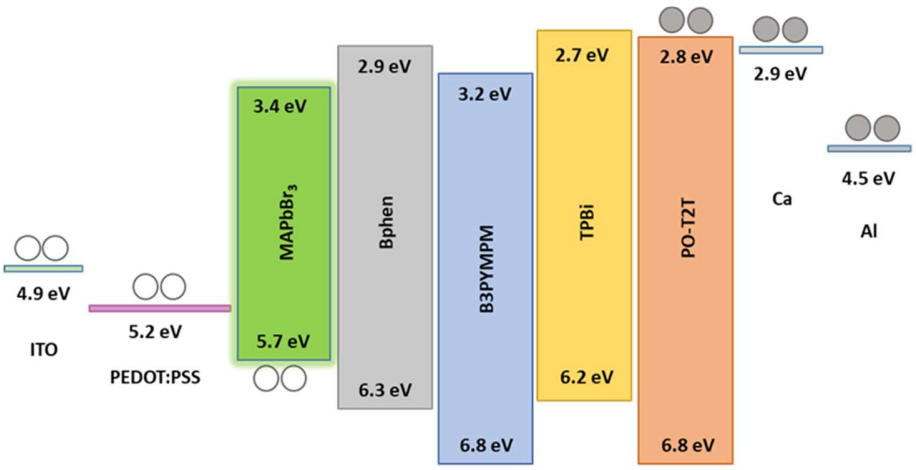


**Figure 5.17** Energy diagram of Bphen incorporated emitter and the various alternative electron transporting material used

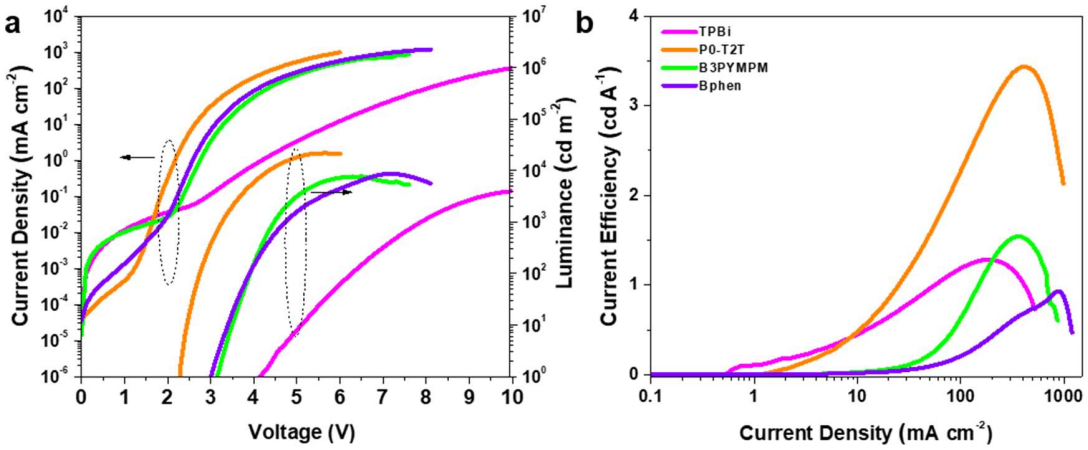


**Figure 5.18** PeLED performance on substitution on electron transporting material. (a) Current density and luminance against voltage as well as (b) current efficiency against current density for 0.500 mg $ml^{-1}$ Bphen.

Based on the device characteristics, employing PO-T2T as the electron transporting material yields the best performance (Figure 5.18). Not only is the luminance obtained, the highest, the threshold voltage and the difference between the current turn on and the threshold voltage, are also the lowest. This implies that the energetic barrier for injection is the least of the four ETLs. The efficiency of the device employing alternative ETLs are also significantly lower, despite the similar band edge energy levels seen for Bphen, TPBi and PO-T2T. Another plausible reason for the higher efficiency noted for PO-T2T device may be the electron mobility in the material. Referring to Table 5.3, it is seen that PO-T2T has an extremely high electron mobility value, i.e two orders of magnitude higher than TPBi and B3PYMPM. This may be a contributive factor in the higher efficiency noted, although the influence of molecular structure (with regards to ETL/MHP interaction) should not be discounted.

**Table 5.3** Summary of electron mobility values for the various electron transporting materials used

| Electron Transporting Material | Electron Mobility ($cm^2 V^{-1} s^{-1}$) |
|---|---|
| Bphen | $5.2 \times 10^{-4}$ |
| B3PYMPM | $1.5 \times 10^{-5}$ |
| TPBi | $3.3 \times 10^{-5}$ |
| PO-T2T | $3.0 \times 10^{-3}$ |

## 5.3 Conclusion

In conclusion, it has been shown that incorporation of BPhen via a solvent engineering process leads to improved device performance due to the synergistic effect of smaller grains that improve the yield of radiative recombination and lower electron/hole injection at the ETL/HTM-MHP interfaces respectively. This is possible due to the passivating nature of Bphen which enables small grains to be formed without detriment to film properties. The controllable alteration of the MHP's energy bands via simple variation of the BPhen concentration in the anti-solvent too allows for efficient injection of charge carriers into the emitter as seen by the reduction in threshold voltages. Our best device is fabricated using 0.500 mg $mL^{-1}$ of BPhen, resulting in a ten-fold increase in luminance and fifteen-fold improvement in current efficiency and EQE compared to the reference device. Excessive BPhen (> 0.500 mg $mL^{-1}$), however, resulted in a decline of device performance, which is attributed to the reduction of charge carrier mobility at high additive concentration. Although substitution of the small molecule inclusion (BPhen) with PBD and TPBi brings about improvement to PL intensity, the minimal effect seen in device efficiency indicates that the choice of additive molecule requires careful selection so that the optoelectronic characteristics have a positive influence on device performance. Charge injection balance is also an important consideration in the journey towards efficient devices. As such, the choice of charge transport material to ensure minimal barrier to carrier injection is crucial and factors such as energy band levels and charge mobilities should not be discounted.

# References

1. Boix, P. P.; Nonomura, K.; Mathews, N.; Mhaisalkar, S. G., Current progress and future perspectives for organic/inorganic perovskite solar cells. *Materials Today* **2014,** *17* (1), 16-23.

2. Kim, H.-S.; Im, S. H.; Park, N.-G., Organolead Halide Perovskite: New Horizons in Solar Cell Research. *The Journal of Physical Chemistry C* **2014,** *118* (11), 5615-5625.

3. Singh, S. P.; Nagarjuna, P., Organometal halide perovskites as useful materials in sensitized solar cells. *Dalton Transactions* **2014,** *43* (14), 5247-5251.

4. Veldhuis, S. A.; Boix, P. P.; Yantara, N.; Li, M.; Sum, T. C.; Mathews, N.; Mhaisalkar, S. G., Perovskite Materials for Light-Emitting Diodes and Lasers. *Advanced Materials* **2016,** *28* (32), 6804-6834.

5. Tan, Z.-K.; Moghaddam, R. S.; Lai, M. L.; Docampo, P.; Higler, R.; Deschler, F.; Price, M.; Sadhanala, A.; Pazos, L. M.; Credgington, D.; Hanusch, F.; Bein, T.; Snaith, H. J.; Friend, R. H., Bright light-emitting diodes based on organometal halide perovskite. *Nat Nano* **2014,** *9* (9), 687-692.

6. Yantara, N.; Bhaumik, S.; Yan, F.; Sabba, D.; Dewi, H. A.; Mathews, N.; Boix, P. P.; Demir, H. V.; Mhaisalkar, S., Inorganic Halide Perovskites for Efficient Light-Emitting Diodes. *The Journal of Physical Chemistry Letters* **2015,** *6* (21), 4360-4364.

7. Kim, Y.-H.; Cho, H.; Lee, T.-W., Metal halide perovskite light emitters. *Proceedings of the National Academy of Sciences* **2016,** *113* (42), 11694-11702.

8. Correa Baena, J. P.; Steier, L.; Tress, W.; Saliba, M.; Neutzner, S.; Matsui, T.; Giordano, F.; Jacobsson, T. J.; Srimath Kandada, A. R.; Zakeeruddin, S. M.; Petrozza, A.; Abate, A.; Nazeeruddin, M. K.; Gratzel, M.; Hagfeldt, A., Highly efficient planar perovskite solar cells through band alignment engineering. *Energy & Environmental Science* **2015,** *8* (10), 2928-2934.

9. Yang, S.; Fu, W.; Zhang, Z.; Chen, H.; Li, C.-Z., Recent advances in perovskite solar cells: efficiency, stability and lead-free perovskite. *Journal of Materials Chemistry A* **2017**.

10. Zhou, Z.; Pang, S.; Liu, Z.; Xu, H.; Cui, G., Interface engineering for high-performance perovskite hybrid solar cells. *Journal of Materials Chemistry A* **2015,** *3* (38), 19205-19217.

11. Jung, H. S.; Park, N.-G., Perovskite Solar Cells: From Materials to Devices. *Small* **2015,** *11* (1), 10-25.

12. Green, M. A.; Ho-Baillie, A.; Snaith, H. J., The emergence of perovskite solar cells. *Nat Photon* **2014,** *8* (7), 506-514.

13. Cho, H.; Jeong, S.-H.; Park, M.-H.; Kim, Y.-H.; Wolf, C.; Lee, C.-L.; Heo, J. H.; Sadhanala, A.; Myoung, N.; Yoo, S.; Im, S. H.; Friend, R. H.; Lee, T.-W., Overcoming the electroluminescence efficiency limitations of perovskite light-emitting diodes. *Science* **2015,** *350* (6265), 1222-1225.

14. Ling, Y.; Tian, Y.; Wang, X.; Wang, J. C.; Knox, J. M.; Perez-Orive, F.; Du, Y.; Tan, L.; Hanson, K.; Ma, B.; Gao, H., Enhanced Optical and Electrical Properties of Polymer-Assisted All-Inorganic Perovskites for Light-Emitting Diodes. *Advanced Materials* **2016,** *28* (40), 8983-8989.

15. Yu, J. C.; Lee, A.-Y.; Kim, D. B.; Jung, E. D.; Kim, D. W.; Song, M. H., Enhancing the Performance and Stability of Perovskite Nanocrystal Light-Emitting Diodes with a Polymer Matrix. *Advanced Materials Technologies* **2017**, 1700003-n/a.

16. Chih, Y.-K.; Wang, J.-C.; Yang, R.-T.; Liu, C.-C.; Chang, Y.-C.; Fu, Y.-S.; Lai, W.-C.; Chen, P.; Wen, T.-C.; Huang, Y.-C.; Tsao, C.-S.; Guo, T.-F., NiOx Electrode Interlayer and CH3NH2/CH3NH3PbBr3 Interface Treatment to Markedly Advance Hybrid Perovskite-Based Light-Emitting Diodes. *Advanced Materials* **2016**, n/a-n/a.

17. Chen, Q.; De Marco, N.; Yang, Y.; Song, T.-B.; Chen, C.-C.; Zhao, H.; Hong, Z.; Zhou, H.; Yang, Y., Under the spotlight: The organic–inorganic hybrid halide perovskite for optoelectronic applications. *Nano Today* **2015,** *10* (3), 355-396.

18. Peng, W.; Wang, L.; Murali, B.; Ho, K.-T.; Bera, A.; Cho, N.; Kang, C.-F.; Burlakov, V. M.; Pan, J.; Sinatra, L.; Ma, C.; Xu, W.; Shi, D.; Alarousu, E.; Goriely, A.; He, J.-H.; Mohammed, O. F.; Wu, T.; Bakr, O. M., Solution-Grown Monocrystalline Hybrid Perovskite Films for Hole-Transporter-Free Solar Cells. *Advanced Materials* **2016,** *28* (17), 3383-3390.

19. Dar, M. I.; Jacopin, G.; Meloni, S.; Mattoni, A.; Arora, N.; Boziki, A.; Zakeeruddin, S. M.; Rothlisberger, U.; Grätzel, M., Origin of unusual bandgap shift and dual emission in organic-inorganic lead halide perovskites. *Science Advances* **2016,** *2* (10).

20. Shao, Y.; Xiao, Z.; Bi, C.; Yuan, Y.; Huang, J., Origin and elimination of photocurrent hysteresis by fullerene passivation in CH3NH3PbI3 planar heterojunction solar cells. *Nature Communications* **2014,** *5*, 5784.

21. Jang, D. M.; Park, K.; Kim, D. H.; Park, J.; Shojaei, F.; Kang, H. S.; Ahn, J.-P.; Lee, J. W.; Song, J. K., Reversible Halide Exchange Reaction of Organometal Trihalide Perovskite Colloidal Nanocrystals for Full-Range Band Gap Tuning. *Nano Letters* **2015,** *15* (8), 5191-5199.

22. Kumar, A.; Kumawat, N. K.; Maheshwari, P.; Kabra, D. In *Role of halide anion on exciton binding energy and disorder in hybrid perovskite semiconductors*, 2015 IEEE 42nd Photovoltaic Specialist Conference (PVSC), 14-19 June 2015; 2015; pp 1-4.

23. Elliott, R. J., Intensity of Optical Absorption by Excitons. *Physical Review* **1957,** *108* (6), 1384-1389.

24. Emara, J.; Schnier, T.; Pourdavoud, N.; Riedl, T.; Meerholz, K.; Olthof, S., Impact of Film Stoichiometry on the Ionization Energy and Electronic Structure of CH3NH3PbI3 Perovskites. *Advanced Materials* **2016,** *28* (3), 553-559.

25. Ng, Y. F.; Jamaludin, N. F.; Yantara, N.; Li, M.; Irukuvarjula, V. K. R.; Demir, H. V.; Sum, T. C.; Mhaisalkar, S.; Mathews, N., Rapid Crystallization of All-Inorganic CsPbBr3 Perovskite for High-Brightness Light-Emitting Diodes. *ACS Omega* **2017,** *2* (6), 2757-2764.

26. Wang, J.; Wang, N.; Jin, Y.; Si, J.; Tan, Z.-K.; Du, H.; Cheng, L.; Dai, X.; Bai, S.; He, H.; Ye, Z.; Lai, M. L.; Friend, R. H.; Huang, W., Interfacial Control Toward Efficient and Low-Voltage Perovskite Light-Emitting Diodes. *Advanced Materials* **2015,** *27* (14), 2311-2316.

27. Meerheim, R.; Furno, M.; Lenk, S.; Lüssem, B.; Leo, K., Quantification of energy loss mechanisms in organic light-emitting diodes. *Applied Physics Letters* **2010,** *97* (25), 253305-253305-3.

28. Lim, S. S.; Chong, W. K.; Solanki, A.; Dewi, H. A.; Mhaisalkar, S.; Mathews, N.; Sum, T. C., Modulating carrier dynamics through perovskite film engineering. *Physical Chemistry Chemical Physics* **2016,** *18* (39), 27119-27123.

29. Saba, M.; Cadelano, M.; Marongiu, D.; Chen, F.; Sarritzu, V.; Sestu, N.; Figus, C.; Aresti, M.; Piras, R.; Geddo Lehmann, A.; Cannas, C.; Musinu, A.; Quochi, F.; Mura, A.;

Bongiovanni, G., Correlated electron–hole plasma in organometal perovskites. **2014,** *5*, 5049.

30. Noel, N. K.; Abate, A.; Stranks, S. D.; Parrott, E. S.; Burlakov, V. M.; Goriely, A.; Snaith, H. J., Enhanced Photoluminescence and Solar Cell Performance via Lewis Base Passivation of Organic–Inorganic Lead Halide Perovskites. *ACS Nano* **2014,** *8* (10), 9815-9821.

31. Hilsum, C., Simple empirical relationship between mobility and carrier concentration. *Electronics Letters* **1974,** *10* (13), 259-260.

32. Jou, J.-H.; Kumar, S.; Agrawal, A.; Li, T.-H.; Sahoo, S., Approaches for fabricating high efficiency organic light emitting diodes. *Journal of Materials Chemistry C* **2015,** *3* (13), 2974-3002.

33. Kawabe, Y.; Abe, J., Electron mobility measurement using exciplex-type organic light-emitting diodes. *Applied Physics Letters* **2002,** *81* (3), 493-495.

34. Kulkarni, A. P.; Tonzola, C. J.; Babel, A.; Jenekhe, S. A., Electron Transport Materials for Organic Light-Emitting Diodes. *Chemistry of Materials* **2004,** *16* (23), 4556-4573.

# Chapter 6

# Molecular design of two-dimensional perovskite cation for energy cascade

*PL improvement with defect passivation is testament to its importance in improving film optoelectronic properties and subsequent device performance. Alternatively, enhancement to radiative recombination can also be attained through defect mitigation such as in the case of the energy cascade phenomenon. By varying the amount of 2D cation incorporation into the 3D network, multiple band gap domains acting as mini quantum wells, are formed in the emitter, providing electronic confinement to the charge carriers resulting in an increased rate of radiative recombination in the smallest band gap domains due to the high localized charge carrier density. In this chapter, three 2D aromatic cations $PEA^+$, $PyrEA^+$ and $ImEA^+$ are investigated to understand the influence of aromatic core on efficacy of the energy cascade phenomenon. Despite the potential for improved charge transport with bi-cationic $PyrEA^+$ and $ImEA^+$, their corresponding 2D3D films show a higher degree of distortion as evidenced by the XRD analysis. The PL excitation spectra, provide further evidence of 2D3D PEA efficiency for charge carrier funneling. The implication of inefficient energy cascade process in 2D3D PyrEA and 2D3D ImEA is the increased susceptibility towards non-radiative losses due to the outcompeting of the former process by the latter.*

---

*This chapter is a manuscript in progress.

## 6.1 Introduction

Despite the remarkable properties exhibited, the inherent limitations of 3D MHP in terms of low exciton binding energy, moisture instability and propensity for light degradation, hamper the development of high efficiency devices.[1-3] This has driven research towards the use of 2D MHPs, which are layered analogues of 3D MHPs with thicknesses of a single or several lead halide octahedral layers. Not only do they exhibit superior ambient stability, their potential for high PLQY values arising from high exciton binding energies identify them as attractive candidates for optoelectronic applications.[4] It is thus unsurprising that much effort has been directed into the field of mixed-dimensional MHP research to fully harness the broad ranging advantages offered by amalgamating both the 2D and 3D systems. Improved performance of mixed-dimensional MHP for light emission have been driven by the process termed as energy cascade.[5] This involves the rapid energy transfer from domains of high band gaps to those of low band gaps, enabling efficient light emission in the latter. The presence of multiple domains of varying band gaps in the emitter, arising from the varying degree of 3D cation incorporation results in the formation of an energetic landscape where carriers injected into high band gap domains funnel to the energetically favoured, lower band gap domains.[6-8] Outcompeting of non-radiative recombination process in the high band gap by the energy cascade, coupled with effective radiative recombination facilitated by high carrier density in the lowest band gap domains, explains the lower power thresholds required for efficient light emission.[8-9]

Despite the numerous reports on mixed-dimensional MHPs for various optoelectronic applications, knowledge on the type of templating cation required for fabrication of efficient LED devices remains elusive. Typically, the presence of an impurity results in the formation of defects arising from lattice mismatch during crystallization. As such, careful selection of the type of impurity, 2D cation in this case, to be introduced into the 3D matrix is necessary. Two design criteria identified for the design of suitable 2D cation are the need for (i) an aromatic core to facilitate charge transport between the two inorganic layers due to π–π stacking which enables localized electron density[10-11] and (ii) ammonium-functionalization of the organic cation to ensure efficient binding to the lead halide

octahedra.[1, 12-13] Here, three aromatic cations, namely phenyl ethyl ammonium ($PEA^+$), pyridinium ethyl ammonium ($PyrEA^{2+}$) and imidazolium ethyl ammonium ($ImEA^{2+}$) are investigated to understand influence of aromatic molecular design on templating an energetic landscape in the emitter for the energy cascade process.

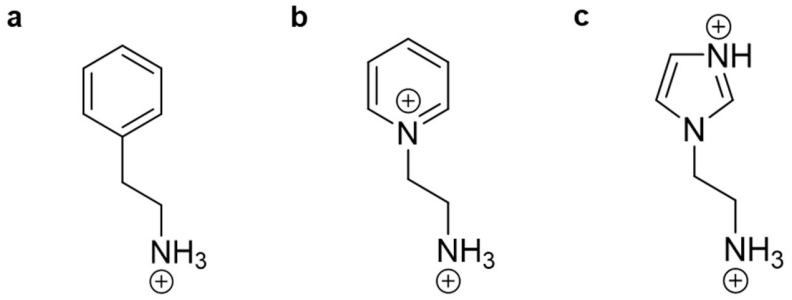


**Figure 6.1** Molecular structure of (a) $PEA^+$, (b) $PyrEA^{2+}$ and (c) $ImEA^{2+}$ cations

## 6.2 Results and Discussion

Single crystals of pure $(PEA)_2PbBr_4$, $(PyrEA)PbBr_4$ and $(ImEA)PbBr_4$ are grown to allow insights into the properties of the pure 2D materials.

### 6.2.1 Crystal structure and phase analysis of pure 2D perovskite single crystals

The crystal structure of the pure 2D perovskites of $(PEA)_2PbBr_4$, $(PyrEA)PbBr_4$ and $(ImEA)PbBr_4$ are obtained through single crystal XRD analysis.

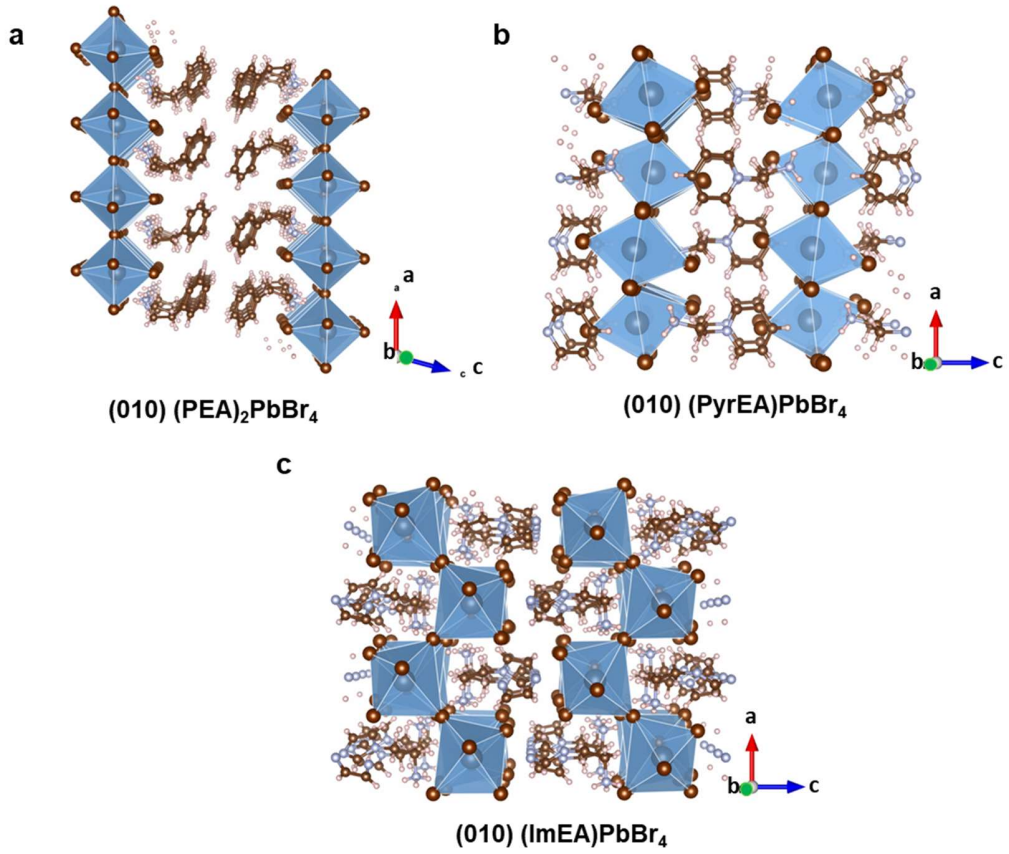


**Figure 6.2** Crystal structure of pure (a) $(PEA)_2PbBr_4$, (b) $(PyrEA)PbBr_4$ and (c) $(ImEA)PbBr_4$

From the single crystal XRD analysis, it is found that although the molecular binding in crystal lattices of $(PEA)_2PbBr_4$ and $(PyrEA)PbBr_4$ differ, where the organic ligand forms a bilayer, sandwiched between lead halide octahedra in the former and only a monolayer in the latter owing to the bi-cationic nature of the PyrEA, both yield the ordered <001> structure. On the other hand, the binding of ImEA monolayer to the two inorganic layers in the corresponding 2D structure results in a <110> arrangement. The difference in structure between $(PEA)_2PbBr_4$, $(PyrEA)PbBr_4$ and $(ImEA)PbBr_4$, where a layered stack in attained in the former two and corrugated in the latter, arises due to the accommodation of the increased degree of distortion in the lattice. The crystal distortion can be expressed in two ways; (a) localized structural distortion (intraoctahedra) and (b) octahedral tilting arising from deviation from ideal octahedral symmetry and metal-halide-metal angle from 180°, respectively. The octahedral distortion can be described quantitatively through the

following equations:

Octahedral distortion parameter[14] ($\Delta d$)

$$\Delta d = \left(\frac{1}{6}\right)\sum\left[\frac{d_n - d}{d}\right]^2$$

Quadratic elongation of the metal-halide bond[15] ($\lambda_{oct}$)

$$\lambda_{oct} = \frac{1}{6}\sum_{i=1}^{6}(d_i/d_0)^2$$

Bond angle variance of the halide-metal-halide angle[15] ($\sigma_{oct}^2$)

$$\sigma_{oct}^2 = \frac{1}{11}\sum_{i=1}^{12}(\alpha_i - 90)^2$$

The $\Delta d$, $\lambda_{oct}$ and $\sigma_{oct}^2$ of pure $(PEA)_2PbBr_4$, (PyrEA)$PbBr_4$ and (ImEA)$PbBr_4$ are presented below.

**Table 6.1** Summary of $\Delta d$, $\lambda_{oct}$ and $\sigma_{oct}^2$ of pure 2D $(PEA)_2PbBr_4$, (PyrEA)$PbBr_4$ and (ImEA)$PbBr_4$ obtained from single crystal analysis

| Compound | *Octahedra Distortion* | | |
|---|---|---|---|
| | **$\Delta d$ (x$10^{-4}$)** | **$\lambda_{oct}$** | **$\sigma_{oct}^2$** |
| (ImEA)$PbBr_4$ | 22.93 | 1.0177 | 53.67 |
| (PyrEA)$PbBr_4$ | 19.59 | 1.0131 | 36.41 |
| $(PEA)_2PbBr_4$ | 10.89 | 1.0056 | 15.70 |

Ideally, to achieve a crystal structure with a low octahedral distortion, the following criteria need to be realized; (a) a low $\Delta d$ value, (b) $\lambda_{oct}$ value which approaches 1 and (c) a low $\sigma_{oct}^2$. Based on the criteria set and Table 6.1, it can be deduced that $(PEA)_2PbBr_4$ gives the lowest degree of distortion followed by (PyrEA)$PbBr_4$ and (ImEA)$PbBr_4$.

As processing is known to be critical in influencing the optoelectronic properties of MHP films, basic characterization of pure 2D $(PEA)_2PbBr_4$, (PyrEA)$PbBr_4$ and (ImEA)$PbBr_4$ thin films are done prior to their introduction as templating cation in a mixed-dimensional system.

### 6.2.2 Crystal structure and phase analysis of pure 2D perovskite thin films

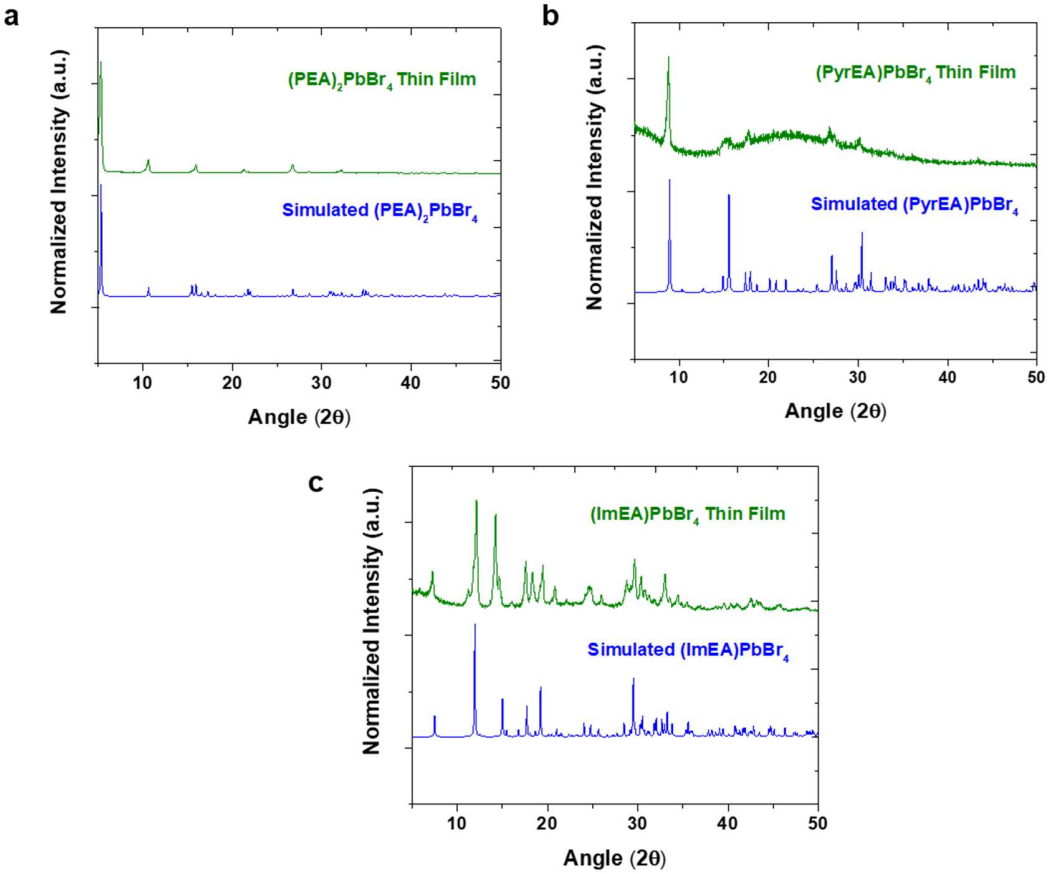


**Figure 6.3** Simulated and thin film XRD patterns of pure 2D (a) $(PEA)_2PbBr_4$, (b) (PyrEA)$PbBr_4$ and (c) (ImEA)$PbBr_4$

On comparing the simulated patterns and XRD data obtained from thin films of $(PEA)_2PbBr_4$, (PyrEA)$PbBr_4$ and (ImEA)$PbBr_4$ (Figure 6.3 (a)-(c)), it can be deduced that the fabricated films are phase pure with characteristics peaks corresponding to the respective 2D MHP present in the films.

### 6.2.3 Photophysical characteristics of pure 2D perovskite thin films

The 2D cations are added in excess of the 3D precursors while retaining the concentration of the latter throughout. Various spectroscopic measurements are then carried out to probe the photophysical properties of the 2D3D thin films on 2D cation incorporation.

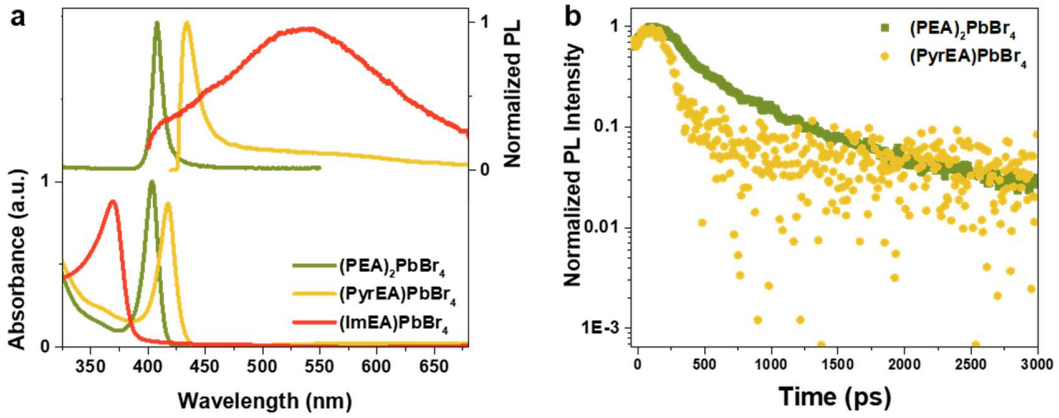


**Figure 6.4** (a) Absorbance and steady state photoluminescence of pure $(PEA)_2PbBr_4$ thin films as well as $(PyrEA)PbBr_4$ and $(ImEA)PbBr_4$ single crystals. (b) Transient photoluminescence decay of $(PEA)_2PbBr_4$ and $(PyrEA)PbBr_4$ films.

While $(PEA)_2PbBr_4$ emits strongly at ~ 410 nm, for $(PyrEA)PbBr_4$ and $(ImEA)PbBr_4$ thin films, the former emits weakly while the latter does not, with the PL spectra shown (of $(PyrEA)PbBr_4$ and $(ImEA)PbBr_4$ are obtained through excitation of the corresponding single crystals (Figure 6.4 (a)). Unlike $(PEA)_2PbBr_4$ and $(PyrEA)PbBr_4$ which exhibit narrow line-widths, $(ImEA)PbBr_4$ shows a broad emission centering about 550 nm which likely stems from charge self-trapping phenomenon[16-17]. The PL broadening is also ascribed to the increased structural distortion of the material[18], manifesting in low photoluminescence despite the high exciton binding energies up to hundreds of meV reported for 2D systems[19]. This is further attested by the transient photoluminescence decay of the 2D thin films (Figure 6.4 b), where $(PEA)_2PbBr_4$ and $(PyrEA)PbBr_4$ exhibited bi-exponential lifetimes of 473 and 143 ps respectively whereas the poor photoluminescence characteristic and rapid quenching of $(ImEA)PbBr_4$ resulted in absence of measurable decay.

### 6.2.4 Crystal structure and phase analysis of mixed-dimensional perovskites

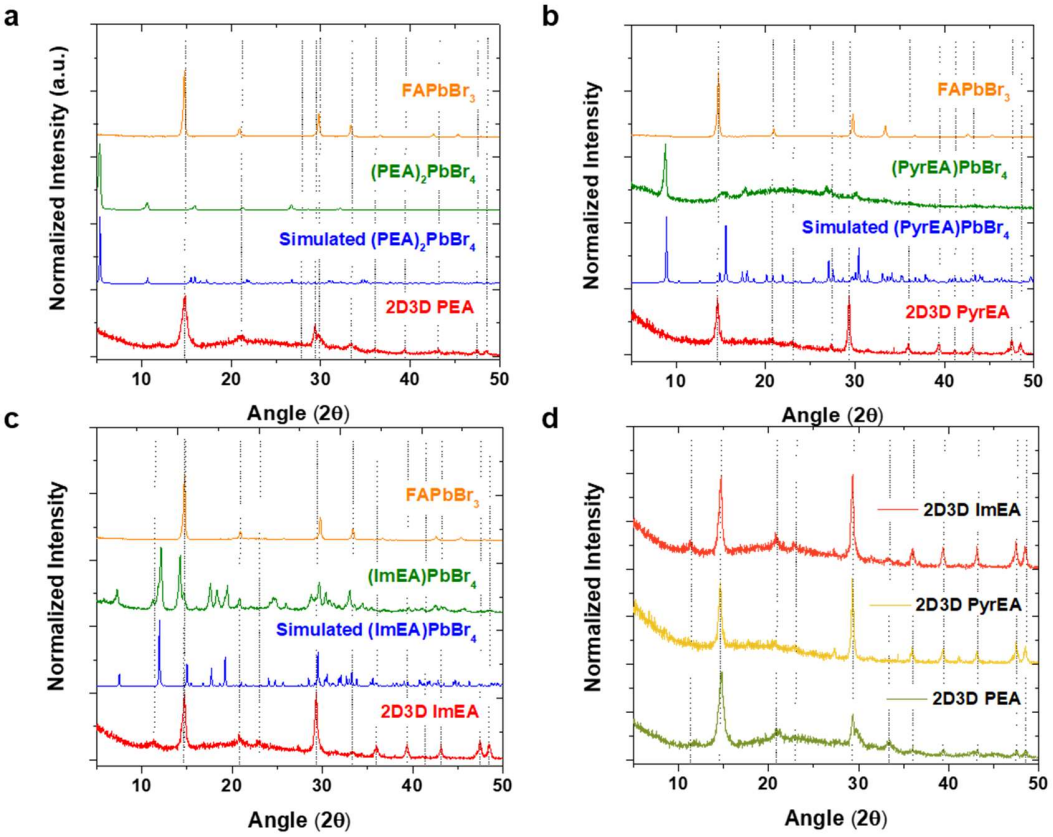


**Figure 6.5** XRD patterns of 2D3D (a) PEA, (b) PyrEA and (c) ImEA as compared to pure 3D FA and their respective 2D perovskites as well as (d) relative to each other.

From the comparison of the XRD patterns (Figure 6.5 (a)-(c)), it is confirmed that phase segregation did not occur as noted by the absence of characteristic 2D MHP peak at low 2θ angles (below 10°). Instead, peaks corresponding to the 3D MHP dominate the pattern. Generally, across the three 2D3D MHP films, several observations can be made; (a) decrease in reflection intensities, attributed to decreased crystallinity, (b) presence of new peaks at higher 2θ angles beyond 29°, relative to the 3D, arise possibly due to increased strain or symmetry change and (c) peak splitting at high 2θ angles, in particular for 2D3D ImEA, which suggests increased degree of distortion. Furthermore, the similarity of the three 2D3D MHP patterns despite the incorporation of different 2D templating cations (Figure 6.5 d), provide further validation of the absence of phase segregation.

### 6.2.5 Photophysical characteristics of mixed-dimensional perovskites

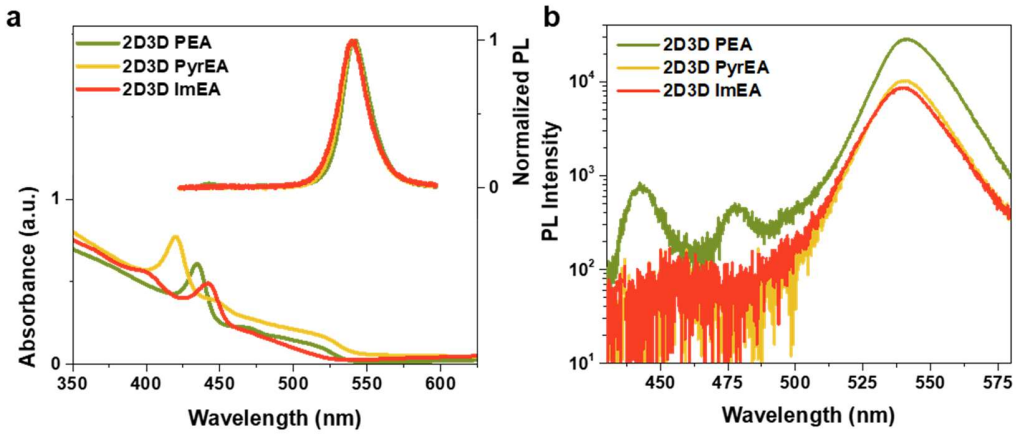


**Figure 6.6** (a) Absorbance and normalized photoluminescence spectra and (b) static photoluminescence spectra in logarithmic scale for 2D3D PEA, PyrEA and ImEA

The absence of excitonic absorbance peaks around 405 nm, 417 nm and 370 nm for the 2D3D PEA, PyrEA and ImEA films respectively (Figure 6.6 (a)), corroborate with the XRD data which indicates the absence of pure 2D domains. Despite the lack of pure 2D excitonic absorbance peak, the dual peaks observed (Figure 6.6 (a)) at 435 and 465 nm for 2D3D PEA, 420 and 445 nm for 2D3D PyrEA as well as 400 and 440 nm for 2D3D ImEA suggest the formation of lower dimensional domains on introduction of the respective 2D cations. This is in line with the concept of energy cascade where the different domains, corresponding to varying band gaps promote the funneling of charge carriers into the smallest band gap domains resulting in a high concentration of charge carriers within a localized region, thereby facilitating effective radiative bimolecular recombination. The formation of different phases in the 2D3D perovskites films could also provide explanation for the emergence of additional peaks in the higher 2θ angle regions of the XRD patterns (Figure 6.5). The absorption edge of the three films are also found to be similar, falling within expectation of the pure 3D domains. On excitation of the 2D3D films with a 400 nm laser, all three films exhibited primary emissions centered about 540 nm (Figure 6.6 a), which corresponds to the emission from the 3D domains. Although (ImEA)$PbBr_4$ exhibits broad emission which spans the 3D emission range, the primary emission is assigned to the 3D MHP instead of (ImEA)$PbBr_4$ owing to the significantly narrow line-width of the

emission, matching that of the former. Secondary emission peaks are expected in the region below 500 nm due to the corresponding excitonic absorbance features of the three 2D3D MHP films. For clarity, the PL spectra is presented in logarithmic scale to enable facile visualization of the secondary emissions. While two additional emission features are detectable for 2D3D PEA – assigned to the lower dimensional phases present in the film, only a slight peak is observed for 2D3D ImEA and PyrEA, possibly due to the weakly-emitting nature of these domains (Figure 6.6 (b)). The PLQY of the three films are subsequently measured. Defined as the ratio of emitted photons to absorbed photons, the PLQY provides a quantitative measure of photoluminescence efficiency, corrected for absorption at the excitation wavelength. 2D3D PEA is revealed to have the highest PLQY of 35%, while 2D3D PyrEA and 2D3D ImEA showed significantly lower values, exhibiting PLQYs of 18% and 15% respectively. The trend in the PLQY values for these multi-dimensional systems are likely due to three reasons; (a) the prevalence of defects, particularly in the high band gap phases, (b) the efficacy of charge carrier funneling between the high band gap and low band gap phases and (c) the efficiency of radiative bimolecular recombination occurring in the lower band gap domains. The higher degree of defect density in the higher band gap domains would nullify the advantage rendered by the energy cascade process; where the high defect density impedes the charge transfer process. This in turn, suppresses (b), the efficiency of the charge carrier transfer process. With less charge carriers effectively transferred across the different domains to the emitting smallest band gap domains, the lower eventual concentration of charge carriers in the emitting domains curbs (c). The charge funneling process occurring in the three 2D3D films is probed through PL excitation spectra, where the peak emission is fixed at 540 nm and the intensity of emission at varying excitation wavelengths is detected. From the PL excitation spectra (Figure 6.7), features corresponding to wavelengths in the vicinity of the 2D3D secondary emissions are evident as indicated in green. The change in PL intensity on excitation at the secondary emission wavelength is significantly greater for 2D3D PEA than that observed for 2D3D PyrEA and 2D3D ImEA. This implies the significantly greater influence of the lower dimensional domains in enhancing the primary emission for 2D3D PEA as compared to 2D3D PyrEA and 2D3D ImEA. Moreover, in the case of 2D3D PyrEA and ImEA, additional features that do not correspond to any of the secondary emission

peaks are also present. This may be due to their weakly emitting nature, as noted by the smaller change in photoluminescence intensity (Figure 6.7) when the films are excited at these wavelengths (indicated in pink), which also provide evidence of the greater funneling efficiency in 2D3D PEA[7].

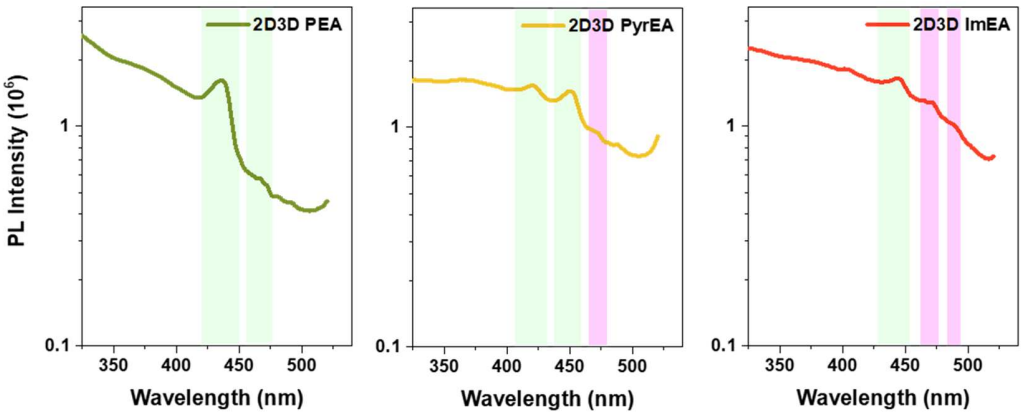


**Figure 6.7** Photoluminescence excitation spectra of 2D3D PEA, PyrEA and ImEA

Transient photoluminescence spectroscopy is also carried out for the three 2D3D films, at the primary emission wavelength of 540 nm. The decay lifetimes are fitted with a bi-exponential decay function where the fast and slow decays correspond to rapid non-radiative recombination process (trap filling) and slow radiative recombination process (photon generation) (Figure 6.8) following light illumination on the samples. Decay lifetimes of 32.1 ns, 27.7 ns and 19.3 ns are noted for the 2D3D PEA, PyrEA and ImEA films respectively.

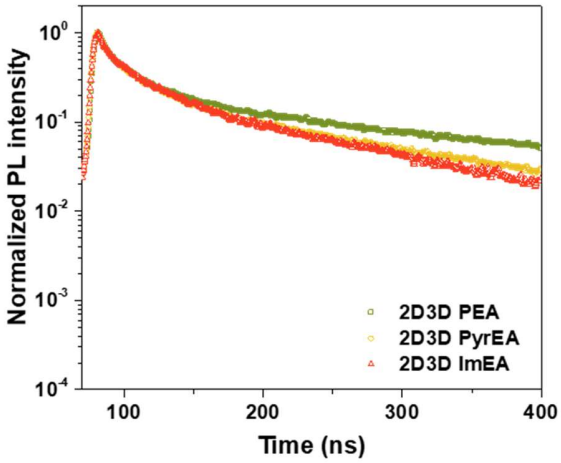


**Figure 6.8** Transient photoluminescence decay lifetimes ($\lambda_{exc}$ = 405 nm) of 2D3D PEA, PyrEA and ImEA

A common technique to assess defects in luminescent materials is by probing the PL intensity with varying pump fluence.[20] Typically, high PL intensity at low fluence is desired, which is indicative of effective radiative recombination on light irradiation. On comparing the PL intensity of the three 2D3D films at 540 nm across different pump fluence (Figure 6.9), it is found that 2D3D PEA yields the highest photoluminescence intensity regardless of the pump fluence. This is consistent with enhanced charge funneling efficiency noted in 2D3D PEA as compared to 2D3D PyrEA and ImEA. The efficient charge transfer process in 2D3D PEA facilitates high localized charge carrier concentration in the emitting domains, which promotes bimolecular recombination and hence explaining the higher photoluminescence intensities observed across the pump fluence range.

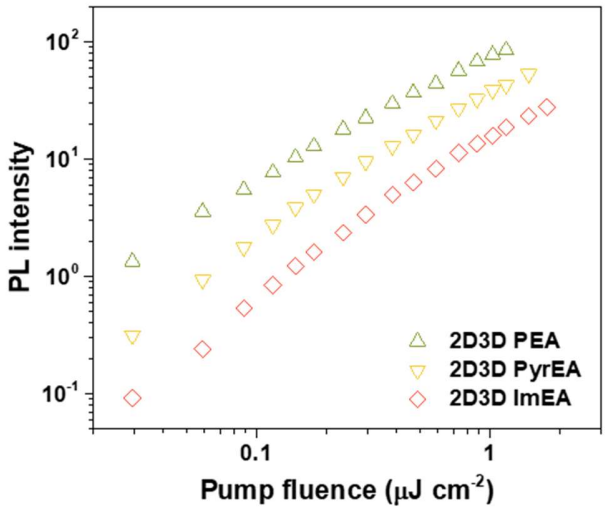


**Figure 6.9** Photoluminescence intensity as a function of pump fluence of 2D3D PEA, PyrEA and ImEA

In order to correlate the film properties with the eventual device performance, PeLEDs based on the three 2D3D perovskites films are fabricated.

### 6.2.6 Electrical characteristics of mixed-dimensional perovskites

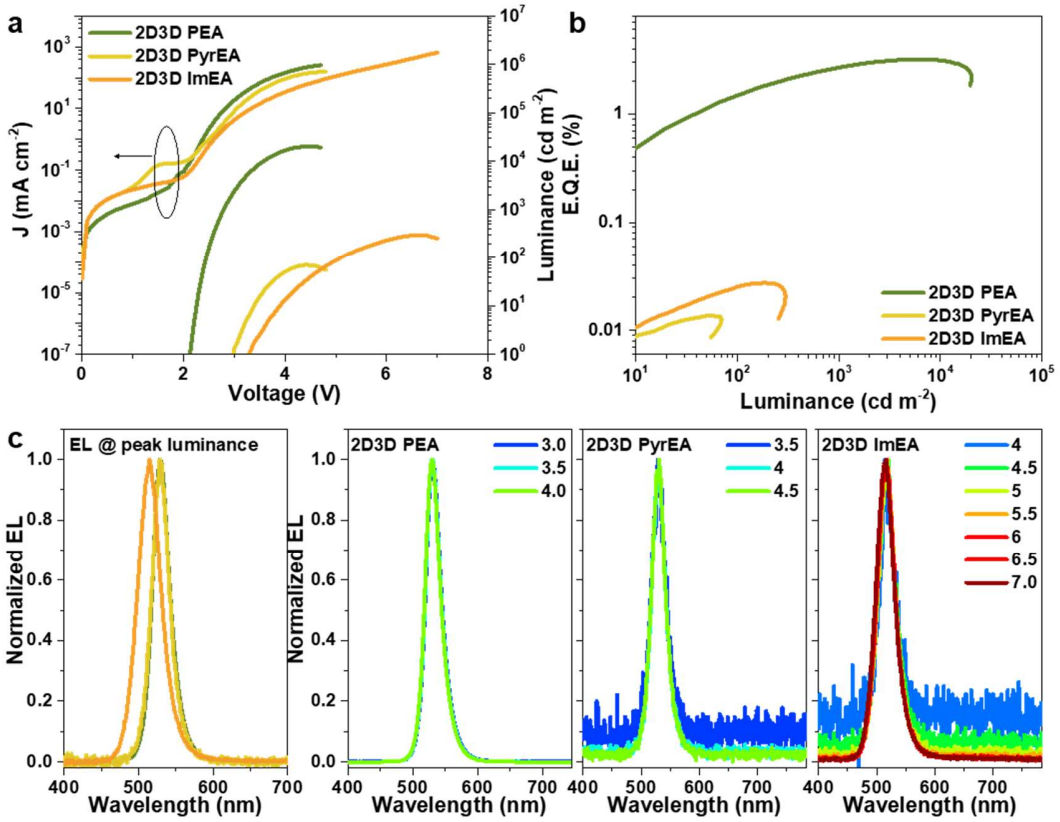


**Figure 6.10** (a) Current density and luminance against voltage curves, (b) EQE against luminance, (c) normalized EL spectra at peak luminance, (d) normalized EL spectra at various voltage application for 2D3D PEA, 2D3D PyrEA and 2D3D ImEA.

Based on the device characteristics, 2D3D PEA yields the best performance (Figure 6.10). The threshold voltage ($V_{th}$), luminance ($L_{max}$) and external quantum efficiency (EQE), are significantly higher than those obtained for 2D3D PyrEA and 2D3D ImEA. The low $V_{th}$ of 2D3D PEA, indicative of series resistance in the device, implies low charge carrier injection barrier and effective radiative recombination, supported by the low current density required for high luminance (Figure 6.10 (a)). The steep increase in luminance on device turn on, on the other hand, indicates rapid radiative recombination process occurring during device operation as explained by the efficient charge carrier funneling process into the emitting domains in the active layer. Despite the low current density, the rapid charge

carrier transfer from the high band gap to the emitting low band gap domains (coupled with low defect density in the former) ensures that losses due to non-radiative recombination at the high band gap domains are minimized. In doing so, only non-radiative recombination pathways in the emitting domain needs to be managed[9], and as the proportion of these losses is significantly lower relative to the overall defect density, radiative recombination is maximized in the emitting domains. This is turn manifests in the form of extremely high luminance of about 20, 380 cd $m^{-2}$ at low current density and voltage. In comparison, the 2D3D PyrEA and 2D3D ImEA devices require higher operating voltage and current density values. The high $V_{th}$ suggests the possible existence of injection barrier into the active layer, often characterized by the emergence of a shoulder in the current density against voltage curve. For 2D3D PyrEA, presence of said barrier is clear, as seen in the vicinity of 2 V. The larger offset between current turn on and device turn on for the latter two devices provide direct evidence of the lower charge carrier funneling efficiency as compared to 2D3D PEA. The high current density suggests that charge carrier funneling into the emitting phase is impeded, likely outcompeted by the non-radiative recombination processes. Thus, to compensate for the lower charge carrier localization in the smallest band gap phase, more charge carriers need to be supplied externally, translating to higher operating current densities. However, as compared to 2D3D PEA and 2D3D PyrEA, 2D3D ImEA requires current density of an order higher to achieve peak luminance. This could be due to the greater non-radiative recombination loss which typically afflict defective systems. Interestingly however, 2D3D PyrEA achieved the lowest EQE despite the higher PLQY value achieved relative to 2D3D ImEA (Figure 6.10 (b)). It is expected that highly luminescent materials will yield highly efficient devices, provided that all other device parameters such as injection, radiative recombination and outcoupling efficiency are well managed. However, the difference in performance of 2D3D PyrEA and 2D3D ImEA appears to also suggest the contribution of other factors in determining device performance. The EL peak at $L_{max}$ (Figure 6.10 (c)) shows that while 2D3D PEA and 2D3D PyrEA showed emission consistent with the PL, 2D3D ImEA EL blue shifts. This could be due to either (a) insufficient emitting band gap domains or (b) change in emitting domain composition. The former is eliminated as the cause for difference between the PL and EL of 2D3D ImEA as the EL remains spectrally stable with applied voltage. In the case where

phenomenon (a) persists, the EL spectra would reflect two peaks; one from the smallest band gap domain and the other, from the next smallest band gap domain[7]. The reason for this is that the excessive charge carriers which are unable to recombine radiatively in the smallest band gap domain spills over to the next energetically available domain. The dual EL emission will prevail throughout the measurement with the EL contribution from the latter domain increasing with voltage due to the influx of charge carriers. On the other hand, (b) substrate influenced crystallization could be possible. For this study, all photophysical characterizations were carried out for 2D3D MHP films prepared on quartz substrates. However, for the device, the 2D3D MHP films were instead deposited on PEDOT: PSS coated ITO substrates. The difference in substrate surface energy can potentially be the reason for compositional variation and in turn device performance.

### 6.2.7 Morphological analysis of mixed-dimensional perovskites

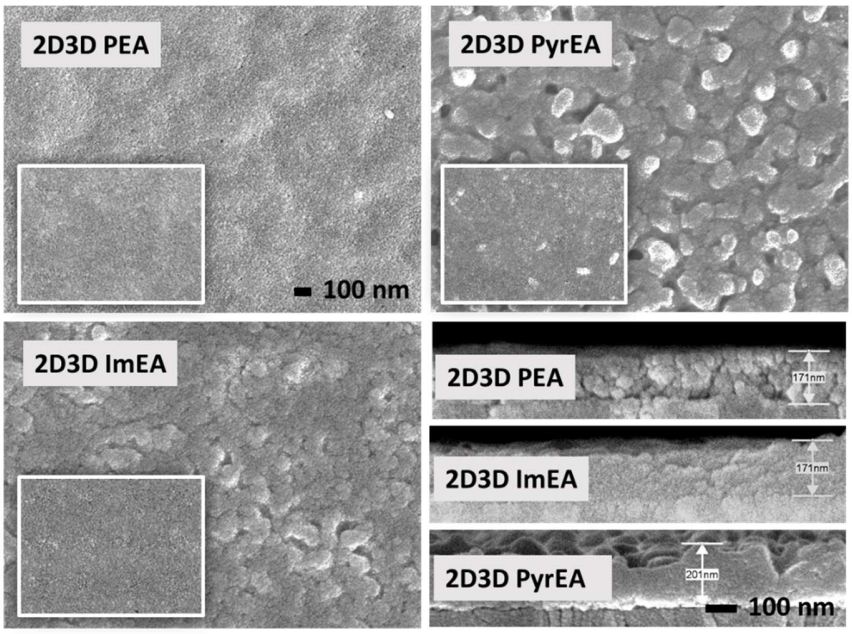


**Figure 6.11** Top and cross-sectional SEM images of 2D3D PEA, PyrEA and ImEA spin coated on PEDOT: PSS coated ITO, with inset showcasing top view of samples prepared on glass.

On comparing the film formation of all three 2D3D MHP films prepared on glass (inset), it is apparent that the films are generally smooth and uniform. However, the films which

are prepared on PEDOT: PSS coated ITO are remarkably different. While the morphology of 2D3D PEA on glass and PEDOT: PSS coated ITO looks similar, the same does not hold true for 2D3D PyrEA and ImEA. Rather, the films are rougher with distinct grooves demarcating the individual large grains in the films. The 2D3D PyrEA has an undulating texture as confirmed by the cross-sectional image. 2D3D ImEA on the other hand, though shows larger grains on the PEDOT: PSS coated ITO substrate, still yields a relatively smooth film. The difference in morphology of the films deposited on different substrates suggests the possibility of substrate-influenced crystallization which potentially gives rise to the difference in resultant EL spectra.

## 6.3 Conclusion

This chapter intends to establish a guideline for the design of suitable 2D cation to template the formation of an energetic landscape to promote an efficient energy cascade process. It is shown that depending on the molecular structure of the 2D cation, either <001> or <110> type of 2D MHPs will form. While the three 2D cations are similar in terms of aromaticity, only 2D PEA thin film is emissive with PyrEA and ImEA showing distinct emission on excitation of the corresponding 2D crystal. On incorporation of the 2D cations into the 3D framework, 2D3D PEA exhibits the highest PLQY and longest decay lifetimes of the three films studied. This is ascribed to the lowest degree of defects and highest charge funneling efficiency as evidenced by the high PL intensities independent of pump fluence. The effect of efficient charge carrier funneling process manifests in the form of high device performance of 2D3D PEA. From the study carried out, it is proposed that high PL of the 2D film is crucial for templating of an efficient energy cascade landscape. As the charge transfer process in the energetically engineered emitter landscape initiates at the high band gap domains, a 2D cation with high PL in thin film form will ensure that high quality (low defect density) high band gap domains will form on incorporation of the 2D cation into the 3D framework. This promotes efficient charge transfer across the various band gap domains as this process will not be impeded by non-radiative recombination process (defect filling) at the high band gap domains as evidenced by the results obtained from the 2D3D films. From this study, it is shown that mixed-dimensional MHP offers a route for attaining

high efficiency devices. However, prudent selection of 2D cation which enables effective mini quantum wells to form without detriment to charge funneling kinetics, is critical in the pursuit of efficiency.

# References

1. Lee, S.; Kim, D. B.; Yu, J. C.; Jang, C. H.; Park, J. H.; Lee, B. R.; Song, M. H., Versatile Defect Passivation Methods for Metal Halide Perovskite Materials and their Application to Light-Emitting Devices. *Advanced Materials* **2019,** *31* (20), 1805244.

2. Colella, S.; Mazzeo, M.; Rizzo, A.; Gigli, G.; Listorti, A., The Bright Side of Perovskites. *The Journal of Physical Chemistry Letters* **2016,** *7* (21), 4322-4334.

3. Zhao, T.; Chueh, C.-C.; Chen, Q.; Rajagopal, A.; Jen, A. K. Y., Defect Passivation of Organic–Inorganic Hybrid Perovskites by Diammonium Iodide toward High-Performance Photovoltaic Devices. *ACS Energy Letters* **2016,** *1* (4), 757-763.

4. Veldhuis, S. A.; Boix, P. P.; Yantara, N.; Li, M.; Sum, T. C.; Mathews, N.; Mhaisalkar, S. G., Perovskite Materials for Light-Emitting Diodes and Lasers. *Advanced Materials* **2016**, n/a-n/a.

5. Chin, X. Y.; Perumal, A.; Bruno, A.; Yantara, N.; Veldhuis, S. A.; Martínez-Sarti, L.; Chandran, B.; Chirvony, V.; Lo, A. S.-Z.; So, J.; Soci, C.; Grätzel, M.; Bolink, H. J.; Mathews, N.; Mhaisalkar, S. G., Self-assembled hierarchical nanostructured perovskites enable highly efficient LEDs via an energy cascade. *Energy & Environmental Science* **2018,** *11* (7), 1770-1778.

6. Quan, L. N.; Zhao, Y.; García de Arquer, F. P.; Sabatini, R.; Walters, G.; Voznyy, O.; Comin, R.; Li, Y.; Fan, J. Z.; Tan, H.; Pan, J.; Yuan, M.; Bakr, O. M.; Lu, Z.; Kim, D. H.; Sargent, E. H., Tailoring the Energy Landscape in Quasi-2D Halide Perovskites Enables Efficient Green-Light Emission. *Nano Letters* **2017,** *17* (6), 3701-3709.

7. Yantara, N.; Bruno, A.; Iqbal, A.; Jamaludin, N. F.; Soci, C.; Mhaisalkar, S.; Mathews, N., Designing Efficient Energy Funneling Kinetics in Ruddlesden–Popper Perovskites for High-Performance Light-Emitting Diodes. *Advanced Materials* **2018,** *30* (33), 1800818.

8. Ng, Y. F.; Kulkarni, S. A.; Parida, S.; Jamaludin, N. F.; Yantara, N.; Bruno, A.; Soci, C.; Mhaisalkar, S.; Mathews, N., Highly efficient Cs-based perovskite light-emitting diodes enabled by energy funnelling. *Chemical Communications* **2017,** *53* (88), 12004-12007.

9. Yuan, M.; Quan, L. N.; Comin, R.; Walters, G.; Sabatini, R.; Voznyy, O.; Hoogland, S.; Zhao, Y.; Beauregard, E. M.; Kanjanaboos, P.; Lu, Z.; Kim, D. H.; Sargent, E. H.,

Perovskite energy funnels for efficient light-emitting diodes. *Nat Nano* **2016,** *advance online publication*.

10. Wei, F.; Jiao, B.; Dong, H.; Xu, J.; Lei, T.; Zhang, J.; Yu, Y.; Ma, L.; Wang, D.; Chen, J.; Hou, X.; Wu, Z., Bifunctional π-conjugated ligand assisted stable and efficient perovskite solar cell fabrication via interfacial stitching. *Journal of Materials Chemistry A* **2019,** *7* (27), 16533-16540.

11. Bi, D.; Li, X.; Milić, J. V.; Kubicki, D. J.; Pellet, N.; Luo, J.; LaGrange, T.; Mettraux, P.; Emsley, L.; Zakeeruddin, S. M.; Grätzel, M., Multifunctional molecular modulators for perovskite solar cells with over 20% efficiency and high operational stability. *Nature Communications* **2018,** *9* (1), 4482.

12. Noel, N. K.; Abate, A.; Stranks, S. D.; Parrott, E. S.; Burlakov, V. M.; Goriely, A.; Snaith, H. J., Enhanced Photoluminescence and Solar Cell Performance via Lewis Base Passivation of Organic–Inorganic Lead Halide Perovskites. *ACS Nano* **2014,** *8* (10), 9815-9821.

13. Chaudhary, B.; Kulkarni, A.; Jena, A. K.; Ikegami, M.; Udagawa, Y.; Kunugita, H.; Ema, K.; Miyasaka, T., Poly(4-Vinylpyridine)-Based Interfacial Passivation to Enhance Voltage and Moisture Stability of Lead Halide Perovskite Solar Cells. *ChemSusChem* **2017,** *10* (11), 2473-2479.

14. Lufaso, M. W.; Woodward, P. M., Jahn-Teller distortions, cation ordering and octahedral tilting in perovskites. *Acta Crystallographica Section B* **2004,** *60* (1), 10-20.

15. Robinson, K.; Gibbs, G. V.; Ribbe, P. H., Quadratic Elongation: A Quantitative Measure of Distortion in Coordination Polyhedra. *Science* **1971,** *172* (3983), 567.

16. Hu, T.; Smith, M. D.; Dohner, E. R.; Sher, M.-J.; Wu, X.; Trinh, M. T.; Fisher, A.; Corbett, J.; Zhu, X. Y.; Karunadasa, H. I.; Lindenberg, A. M., Mechanism for Broadband White-Light Emission from Two-Dimensional (110) Hybrid Perovskites. *The Journal of Physical Chemistry Letters* **2016,** *7* (12), 2258-2263.

17. Daniele Cortecchia, J. Y., Annalisa Bruno, Shu-Zee Alencious Lo, Gagik G. Gurzadyan, Subodh Mhaisalkar, Jean-Luc Brédas, Cesare Soci Polaron Self-localization in white-light emitting hybrid perovskites. https://arxiv.org/abs/1603.01284v2 (accessed August 8, 2019).

18. Cortecchia, D.; Neutzner, S.; Srimath Kandada, A. R.; Mosconi, E.; Meggiolaro, D.; De Angelis, F.; Soci, C.; Petrozza, A., Broadband Emission in Two-Dimensional Hybrid Perovskites: The Role of Structural Deformation. *Journal of the American Chemical Society* **2017,** *139* (1), 39-42.

19. Saparov, B.; Mitzi, D. B., Organic–Inorganic Perovskites: Structural Versatility for Functional Materials Design. *Chemical Reviews* **2016,** *116* (7), 4558-4596.

20. Fu, J.; Jamaludin, N. F.; Wu, B.; Li, M.; Solanki, A.; Ng, Y. F.; Mhaisalkar, S.; Huan, C. H. A.; Sum, T. C., Localized Traps Limited Recombination in Lead Bromide Perovskites. *Advanced Energy Materials* **2019,** *9* (12), 1803119.

# Chapter 7

# Tailoring the distribution and spread of m domains for stable blue emission

*Despite the success of energy cascade in yielding high performing green and red PeLEDs, their applicability for blue emission has been hampered due to the penchant for emission to shift to the multi-dimensional MHP domains with the lowest band gap. Although a high concentration of the 2D cation provides a means for the realization of blue emission, the low conductivity of the 2D cation limits its device performance. In this chapter, it is shown that by relying on a triptych of 2D and A-site cation concentrations, solubility limit of A-site cation, and nucleation kinetics; tailoring of MHP structural landscape to deliver a narrow distribution (m = 2-5) of MHP domains is made possible, allowing efficient blue emission to be achieved. High concentration of the 2D cation is necessary to eliminate 3D domains, whereas the role of low solubility A-site cation is to curb the formation of undesired 2D domains. The MHP structural landscape control allows record efficiencies of spectrally stable deep blue (~ 465 nm) and cyan (~ 493 nm) emissions to be achieved. The single halide system utilized in this study also circumvents issues relating to halide segregation.*

*The manuscript based on this chapter is under review at the point of thesis submission.

## 7.1 Introduction

PeLEDs present new exciting prospects for applications requiring efficient blue, green and red emitters such as displays and solid-state lighting. However, the rapid efficiency strides have been noted only for green and red emission – with the efficiency for blue-emitting PeLED still wanting. Although wide band gap MHPs are achievable by employing chloride as the halide anion, the increased tendency for formation of deep trap states translates to an increase in undesired non-radiative recombination.[1] Attempts to yield blue emission through partial substitution of bromide with chloride ions are mired in issues pertaining to low efficiency and colour instability due to reduced PLQY and electric field-induced halide segregation.[2] Therefore, it is imperative that an alternative strategy to halide mixing be devised to obtain spectrally stable PeLED spanning the cyan-deep blue region of the visible light spectrum (band gap $\geq$ 2.48 – 2.56 eV).

One possible approach to attain larger band gaps is through the intercalation of the 3D network with bulky 2D cations to form mixed-dimensional MHPs.[3] This points to the need for the emissive MHP layers to consist of an intermediate number of lead octahedral layers to satisfy both band gap and charge transport criteria. However, depositing phase pure films of intermediate dimensionality is a challenge due to (a) the progressively smaller difference in thermodynamic stability of the compounds with increasing number of layers, or (b) the propensity for pure 2D domains to form due to strong van der Waals interaction between the 2D cations which would deplete the concentration of the 2D cations in the reservoir and in turn, promote formation of heterogeneous films. The formation of multiple domains with different band gap characteristics within the same film facilitates the energy cascade effect which drives the high PLQY and device efficiencies typically seen of mixed-dimensional MHPs. Despite the advantages of the energy cascade phenomenon, it inevitably leads to efficient green emission due to the presence of 3D bromide emitters. Clearly, elimination of 3D MHP formation is critical to realize pure blue emission. While introduction of excess 2D cation is often employed to restrict formation of 3D MHP domains in the film, however the formation of less conducting, undesired 2D MHP domains usually accompanies this protocol. Here, it is shown that by introducing excess

2D cation together with a low solubility A-site cation (and therefore a fast nucleation rate), a narrow, monodispersed distribution of intermediate multi-dimensional domains centered at the desired blue emission peak can be attained. The narrow spread of these domains increases the efficacy of the energy cascade process; repressing non-radiative recombination losses at the high band gap domains thereby allowing high PLQY and device efficiency to be achieved at lower power densities. Furthermore, the use of a pure bromide system ensures that not only is phase segregation mitigated, deep trap-induced losses are also curbed with the elimination of chloride as a conduit for blue emission. In utilizing this strategy, highly efficient, spectrally stable blue PeLEDs spanning the entire blue region ranging from 437 to 495 nm with EQEs of 2.34%, 4.34%, and 4.8% at EL peak wavelengths of 465, 486, and 493 nm respectively, are achieved. The broader impact of this concept is also demonstrated through the use of alternative 2D cations.

## 7.2 Results and Discussion

Formation of mixed-dimensional MHP film results in energy transfer between the domains which enable the fabrication of high efficiency PeLEDs[4-5]. However, energy cascade from high band gap domains to low band gap domains also reveal the need to eliminate formation of 3D domains to achieve emissive, colour-pure, blue-emitting MHPs. To eliminate the formation of 3D domains, tailoring the precursors with excess 2D cation is necessary. However, the inevitable formation of large population of 2D domains[6] which hinders charge transport of the film, needs to be duly addressed.[7] Therefore, a strategy to eliminate the formation of 2D and 3D domains is necessary to obtain blue-emitting mixed-dimensional MHP films.

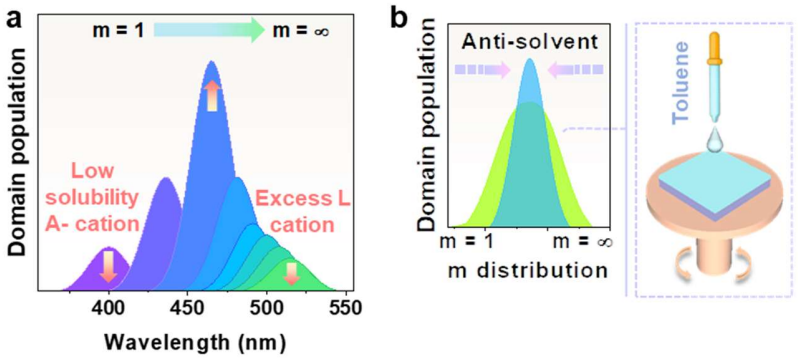


**Figure 7.1** (a) Variation in distribution of intermediate mixed-dimensional MHP domains on introduction of low solubility A-site cation and excess of organic spacer molecule and (b) the schematic of the anti-solvent treatment process, enabling narrow intermediate mixed-dimensional MHP distribution to be attained.

To tackle the formation of 2D domains, A-site cations with low solubility are proposed to boost the incorporation of A-site cations to form intermediate mixed-dimensional MHP domains. Three types of A-site cations with different bulk solubilities are compared, i.e. formamidinium ($FA^+$), methyl ammonium ($MA^+$), and cesium ($Cs^+$). Bulk solubility of these cations in a mixed DMF-DMSO co-solvent are found to be 10 M, 5 M, and 0.05 M respectively.

### 7.2.1 Proposed growth mechanism of intermediate mixed-dimensional perovskite domains

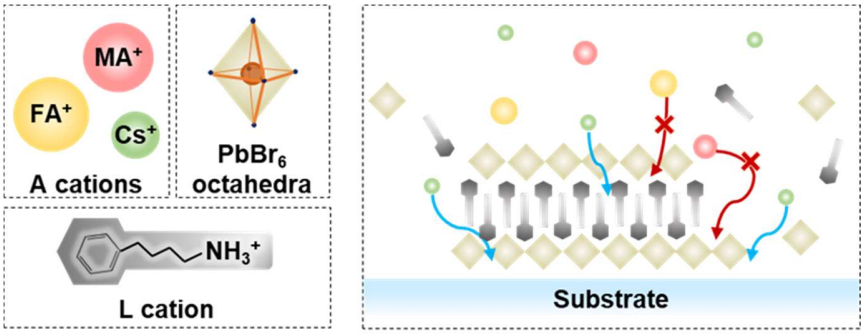


**Figure 7.2** Schematic of film growth process on introduction of A-site cations of varying bulk solubility

It is proposed that the formation of high band gap domains is kinetically favoured during the initial stages of film growth due to strong van der Waals interaction between the 2D cations.[6, 8] As the film growth process progresses, the A-site cation gets incorporated into the 4-phenyl-1-butylammonium ($C_6H_5(CH_2)_4NH_3^+$ or $PBA^+$) bilayer and precipitates to form lower band gap domains[9] (Figure 7.2). The high solubility and large size of the $FA^+$ cation promotes phase separation in the system as they do not readily get incorporated during the growth of high band gap domains. On the other hand, the small size and low solubility of $Cs^+$ cation allows it to be easily incorporated into the high band gap domains to form intermediate mixed-dimensional MHP domains with a narrower distribution.

### 7.2.2 Crystal structure and phase analysis of mixed-dimensional MHP films

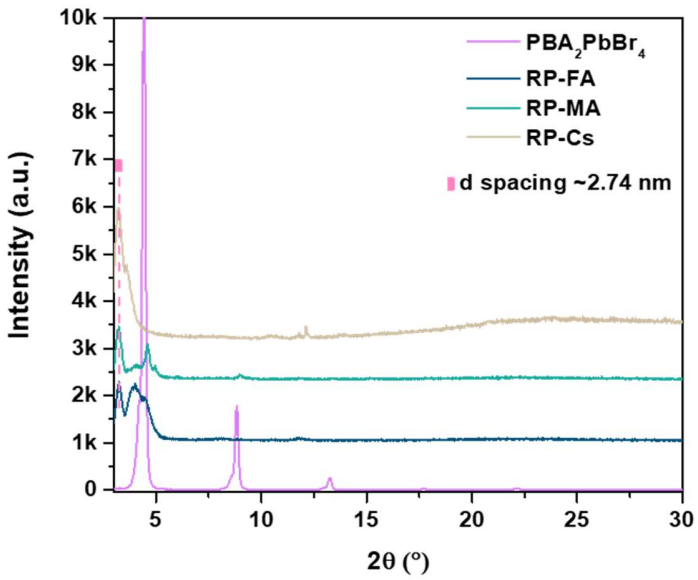


**Figure 7.3** XRD patterns of pure $PBA_2PbBr_4$, RP-FA, RP-MA and RP-Cs.

The capability of $PBA^+$ cation to form 2D RP MHP is confirmed from XRD analysis (Figure 7.3) where the (001) planes are found to have an interlayer spacing (d-spacing) of ~ 2 nm. Difficulty in obtaining pure intermediate mixed-dimensional MHP phases from both homogeneous[10] and heterogeneous[11-12] nucleation methods are known and therefore for simplicity, <m> will be used to represent the stoichiometric precursor ratio while m denotes the actual number of $PbBr_6$ layers of the system. Regardless of the choice of A-site cation, XRD analysis of the films deposited from <m> = 2 solutions indicate the formation of mixed-dimensional MHP with an average d-spacing of ~2.74 nm. As the width of the $[PbBr_6]^{4-}$ octahedra is approximately 0.59 nm, formation of multi-band gap domains consisting of various m values within the film is deduced, regardless of the choice of A-site cation since the theoretical d-spacing does not match with experimental d-spacing of mixed-dimensional MHP, assuming that m is a positive integer value.

### 7.2.3 Photophysical characteristics of mixed-dimensional perovskite films

The influence of nucleation rate on the distribution of m domains is investigated by preparing RP-FA, RP-MA and RP-Cs films via spin coating processes with and without the use of anti-solvent.

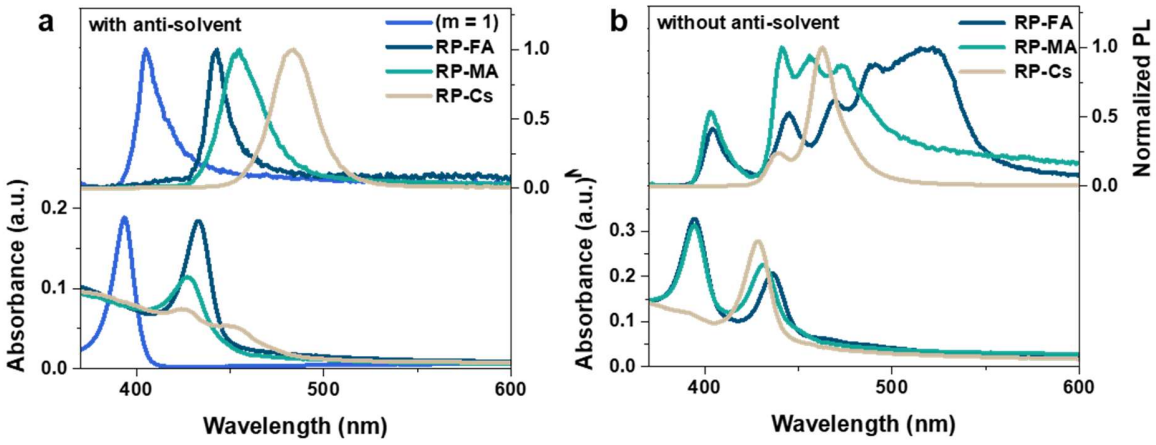


**Figure 7.4** Absorbance and PL of RP-FA, RP-MA and RP-Cs films which are prepared (a) with and (b) without the anti-solvent process

Distinct excitonic absorbance feature at 393 nm with a photoluminescence (PL) peak at 405 nm is observed for the m = 1 film (Figure 7.4 (a)). On the other hand, the low solubility A-site cation ($Cs^+$) is expected to limit the formation of m =1 and promote intermediate m domain formation due to their higher tendency to nucleate. For <m> = 2 films which are prepared via the anti-solvent process, only single excitonic absorbance features at 433 nm and 428 nm are observed for the RP-FA and RP-MA respectively, while two excitonic absorbance peaks are detected at 426 nm and 453 nm for RP-Cs (Figure 7.4 (b)). Understanding that the band gap generally increases exponentially with ($1/m^2$),[13] the excitonic absorbance features at 433 nm, 428 nm, and 426 nm are tentatively assigned to the signature of m = 2 domains for RP-FA, RP-MA and RP-Cs respectively. The red shift of the absorbance excitonic feature on employing bigger-sized cation (Cs < MA < FA) is due to the increment of B – X – B bond angle which modulates the band gap of the material itself.[14] The additional excitonic absorbance peak at 453 nm for RP-Cs, is assigned to m =

3 indicating that the formation of higher m domain is not observed for RP-FA and RP-MA. Red shifting of the PL peak is observed with smaller cation size in which PL peak at 442 nm, 454 nm, and 484 nm are observed for RP-FA, RP-MA, and RP-Cs respectively in contrast to the absorbance data. Asymmetric PL shape with a shoulder at longer wavelength region is evident in both the RP-FA and RP-MA where the FWHM values are 16 nm and 27 nm respectively, whereas a more symmetrical PL is obtained for the RP-Cs, with FWHM of 27 nm. The discrepancy between the absorbance and PL spectra across the three systems is accrued to the higher sensitivity of the PL measurement in detecting trace populations of high-m domains; a result of the energy funneling mechanism[4-5]. In case of RP-FA and RP-MA, although the majority of the domains are m = 2 as observed by the absorbance spectra, presence of trace amounts of higher-m domains in the film could explain the PL tail at longer wavelengths. On the other hand, a higher fraction of intermediate m domains in RP-Cs provides an explanation for the dual excitonic absorbance peak and red-shifted PL despite the reduction of B – X – B angle.

The effect of employing low solubility A-site cation to form intermediate m domain is clearly noted on comparing anti-solvent treated samples. Employing high solubility $FA^+$ resulted in a wide distribution of m domains as seen in the PL spectra of RP-FA film where multiple peaks ranging from 405 to 525 nm corresponding to m = 1 and m values approaching ∞ are observed. Multiple PL peaks with narrow peak distribution ranging from 405 to 474 nm, tentatively assigned to m = 1 and m = 4, are produced when less soluble $MA^+$ cation (relative to $FA^+$) is utilized. Further narrowing of PL peak distribution ranging from 438 to 463 nm is obtained for RP-Cs film when $Cs^+$, the cation with the smallest bulk solubility, is employed. These observations can be explained by the energetically favoured formation of m = 1 during the early nucleation stage which reduces the 2D cation reservoir, facilitating the formation of m =1 and domains of higher m (including ∞) in the case of cations with high bulk solubility, such as $FA^+$. The highly soluble $FA^+$ is slowly incorporated into the low m domain, resulting in higher m domains and therefore a larger PL peak distribution. For the low solubility $Cs^+$, the situation is reversed and rapid incorporation of Cs results in RP-Cs films with intermediate domains. In addition to composition, variations to the nucleation and growth kinetics during film preparation also

influences the distribution of m-domains in mixed-dimensional MHP. Deposition methods, involving fast and slow super saturation processes, are also investigated by employing the anti-solvent assisted and conventional spin coating procedures.

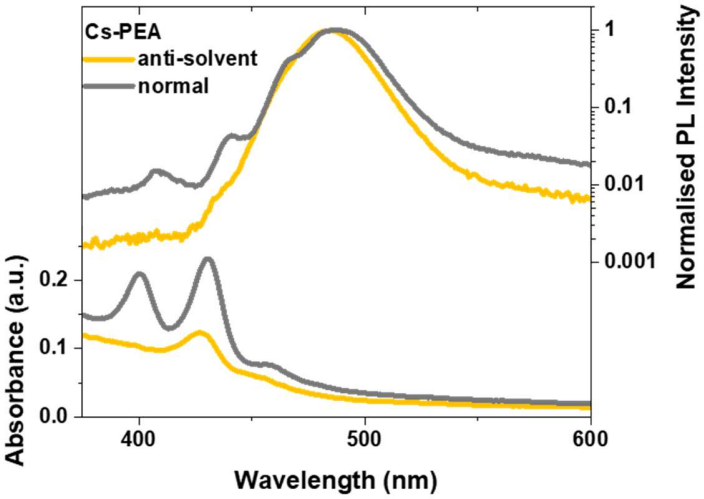


**Figure 7.5** Absorbance and PL spectra of RP-Cs (PEABr) prepared with and without anti-solvent process

Employing the anti-solvent technique to induce fast supersaturation state results in a smaller PL FWHM due to narrower m distribution across all systems regardless of the choice of A-site and L cations (Figure 7.4-7.5). This is in line with the LaMer burst model[9, 15], where a high rate of nucleation within a short period of time followed by slow rate of growth over a longer growth period promotes the formation of more monodisperse colloids and vice versa. Hence, aside from employing the compositional engineering strategy, anti-solvent is shown to be a crucial processing step to achieve a narrower mixed-dimensional MHP domain distribution regardless of A-site cation and 2D cation size. The m domain distributions and signature of high band gap to low band gap domain charge carrier transfer is further investigated using transient absorption spectroscopy.

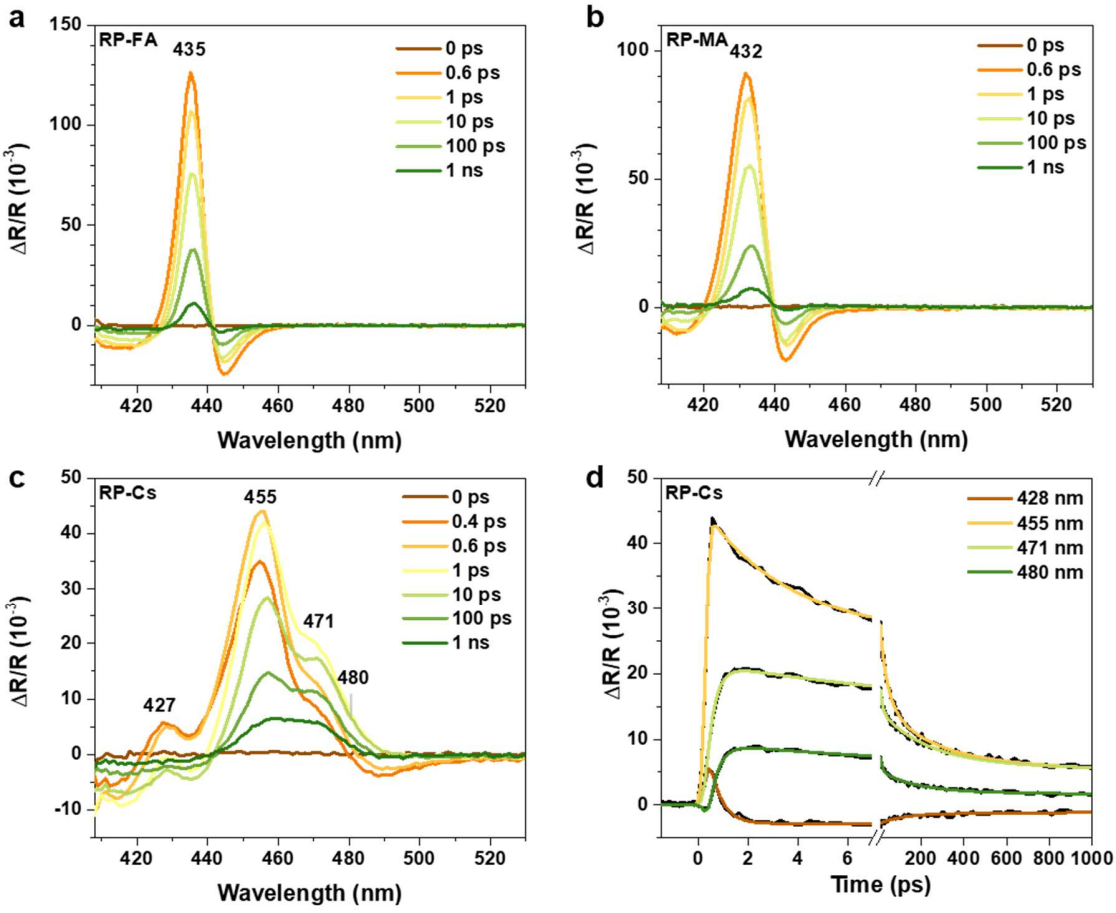


**Figure 7.6** Transient absorption spectra of (a) RP-FA, (b) RP-MA and (c) RP-Cs. (d) The kinetics of photo-bleaching in RP-Cs.

Presence of photo-bleaching signatures around 435 nm and 432 nm for RP-FA and RP-MA films respectively (Figure 7.6 (a)-(b)), indicate carrier filling upon excitation above band gap at m = 2. Multiple photo-bleaching peaks are observed for RP-Cs at 427 nm, 455 nm, 471 nm, and 480 nm (Figure 7.6 (c)), tentatively assigned to the signatures of m = 2 – 5. This is in agreement with the absorbance and PL spectra where features of higher intermediate m domains are observed for the RP-Cs. The kinetics of photo-bleaching in the RP-Cs are illustrated in Figure 7.6 (d). Instant buildup of excited states is observed on photo-bleaching at 427 nm followed by a fast decay. A progressively slower photo-bleaching rise time and a slower photo-bleaching decay are observed with increasing photo-bleaching wavelength. This provides strong evidence of the charge carrier transfer

process and accumulation of excited states in low band gap domains (photo-bleaching at 480 nm).

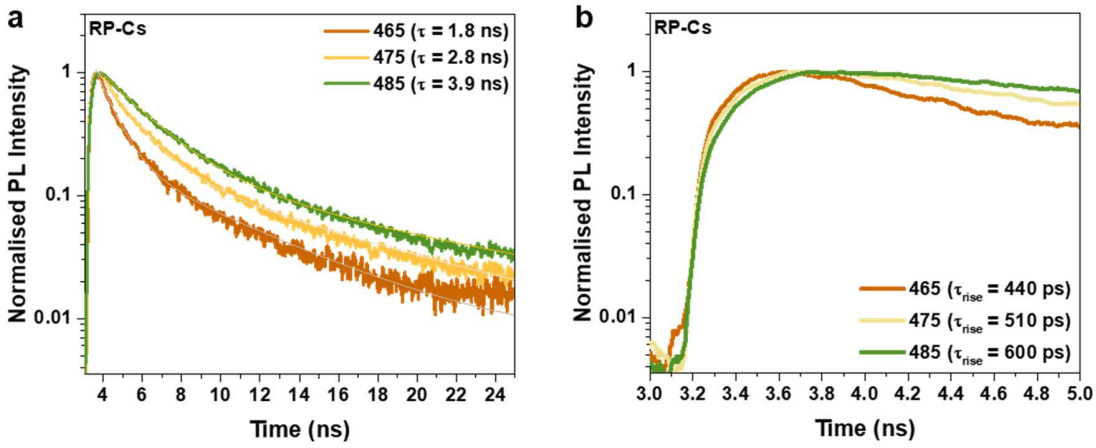


**Figure 7.7** Transient photoluminescence decay of RP-Cs. (a) PL decay profile of RP-Cs and (b) rise time comparison at probed wavelengths of 465 nm, 475 nm and 485 nm.

Charge carrier transfer and accumulation signatures are also apparent from the transient PL spectra; where on increasing the probed wavelength, the PL decay becomes progressively longer whereas the rise time becomes progressively slower (Figure 7.7). As fast charge carrier funneling is observed, complete elimination of 3D domain is an important criterion to obtained pure blue EL devices.

### 7.2.4 Influence of A-site cation substitution on morphology

Topological studies are also carried out to assess the influence of cation substitution on film morphology and roughness.

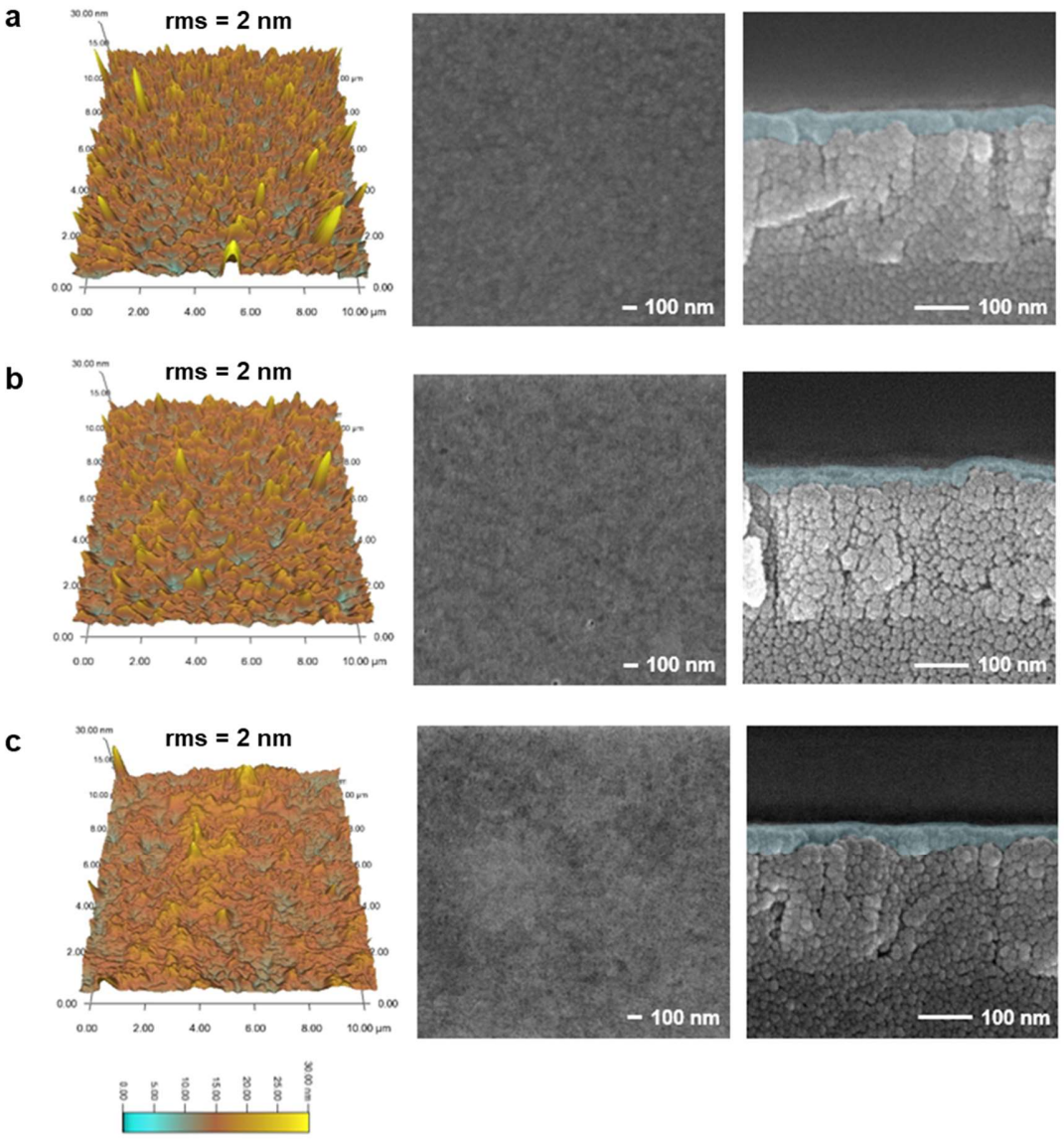


**Figure 7.8** Topological mapping of (a) RP-FA, (b) RP-MA and (c) RP-Cs for roughness analysis (left column), surface morphology (middle column) and thickness verification (right column).

A-site cation variation does not appear to affect the roughness (~ 2 nm) and thickness of the resulting RP-FA, RP-MA and RP-Cs films (~ 30 nm) (Figure 7.8).

### 7.2.5 Electrical characterization of RP PeLEDs based on different A-site cations

The suitability of intermediate m domains formed from low solubility A-site cation for blue light emission is put to the test by fabricating PeLEDs.

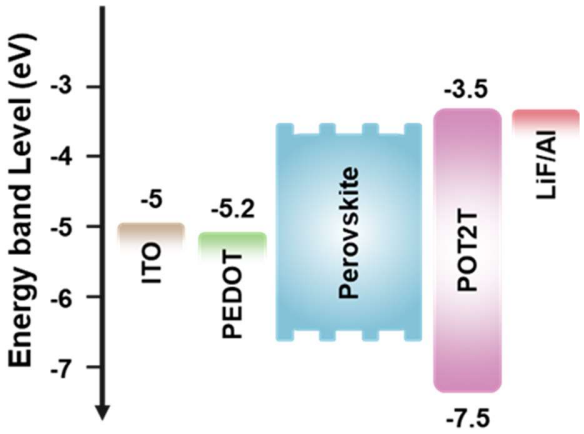


**Figure 7.9** Energy band alignments of the various layers in a PeLED device

The choice of hole transporting layer (HTL: Poly(3,4-ethylenedioxythiophene )polystyrene sulfonate / Pedot:PSS) and electron transporting layer (ETL : (1,3,5-triazine-2,4,6-triyl)tris(benzene-3,1- diyl))tris(diphenylphosphine oxide / POT2T) are standardized for easy comparison (Figure 7.9).

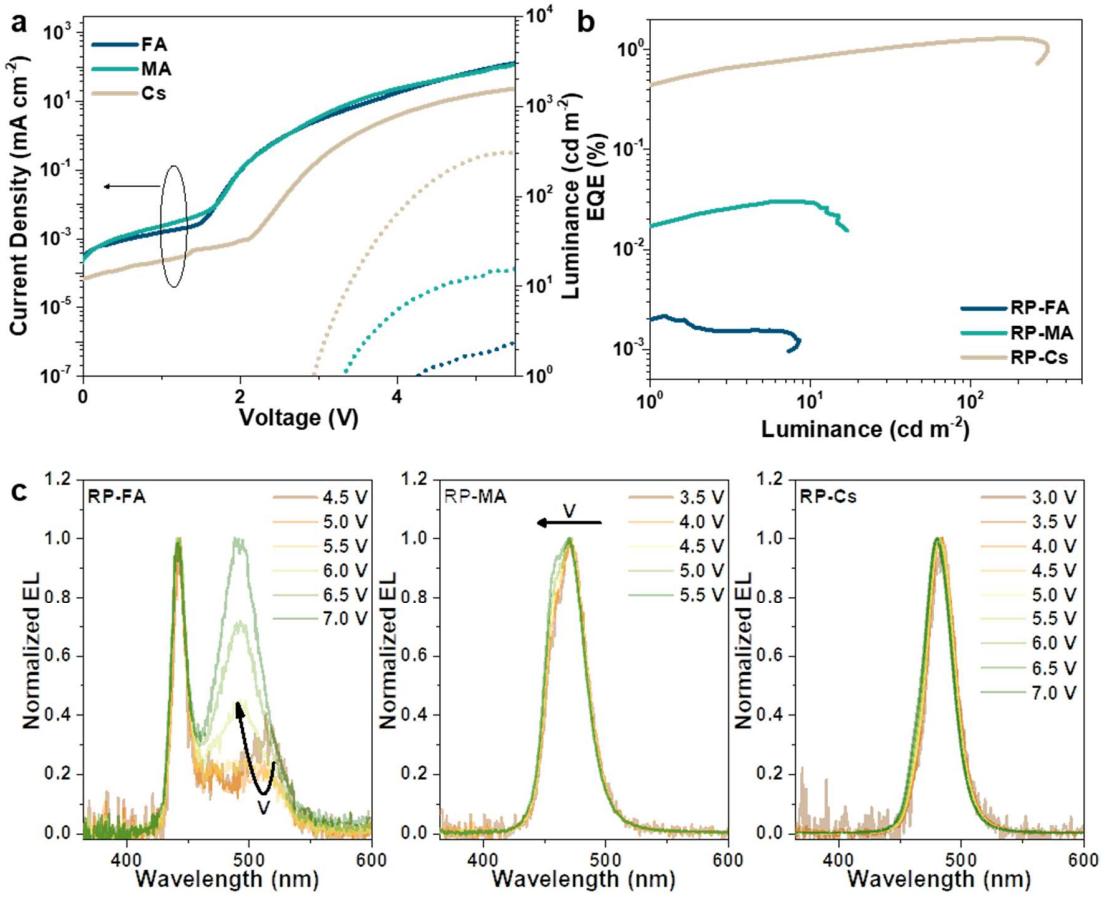


**Figure 7.10** (a) Current density-luminance against voltage curves, (b) EQE against luminance and (c) electroluminescence spectra taken at various voltages for RP-FA, RP-MA and RP-Cs.

Due to the lowest proportion of poor conductivity m = 1 domains, RP-Cs shows the lowest turn on voltages ($V_{th}$ ~2.9V), signifying the best charge injection of the three systems (Figure 7.10 (a)). The $V_{th}$ increases to 3.3 V and 4.2 V for RP-MA and RP-FA respectively, supporting the hypothesis that the increased proportion of low m domains is facilitated by employing more soluble A-site cations. The energy cascading process can be modulated by varying the ratio of high band gap to low band gap domains, where efficient charge carrier transfer results in a boost to the EQE. On the other hand, a larger proportion of high band gap to low band gap domains results in inefficient energy cascade to the low band gap domains which manifests in the form of multiple emission peaks with low EQEs[16].

Multiple EL peaks (Figure 7.10 (c)) are observed for both RP-FA and RP-MA systems due to the larger proportion of high band gap to low band gap domains, which is in agreement with the PL data. On increasing bias application, the EL spectra blue shifts, signifying incomplete charge transfer to the lowest band gap domains due to the low concentration.[16] The blue shifting of EL is prominent in both RP-FA and RP-MA system where the EL peak at longer wavelength start to shift with increasing bias application from 4.5 V and 5 V respectively, due to the smaller proportion of low band gap domain concentration in the system. Spectrally stable devices can be achieved with the RP-Cs system as narrower m distribution offers an ideal high band gap to low band gap domains ratio in the system which guarantees high efficiency.[16]

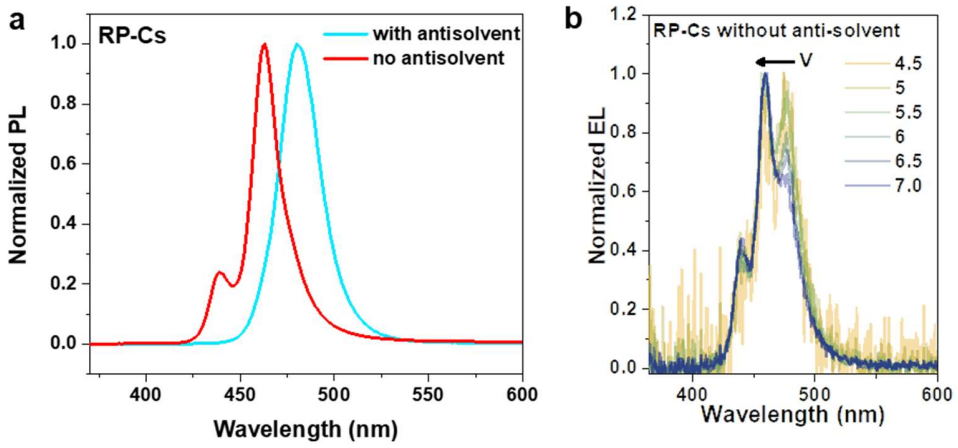


**Figure 7.11** Normalized (a) PL spectra of RP-Cs prepared with and without anti-solvent process and (b) EL spectra for RP-Cs prepared without anti-solvent process

The importance of the anti-solvent process for formation of narrow intermediate m domain distribution is evidenced by the PL and EL spectra (Figure 7.11). During device operation, the EL spectra of RP-Cs devices made with conventional spin coating methods shifts towards the blue region with increasing bias application, unlike RP-Cs prepared with the anti-solvent process. This signifies the sub-optimal ratio of the high band gap to low band gap domains in the former which arises due the slow nucleation process afforded by the conventional spin coating process. These findings are well-aligned with the EQE trend (Figure 7.10 (b)) where devices with optimum high band gap to low band gap domains

ratio produce high EQE (i.e. RP-Cs system ~ 1.29%) whereas an inadequate high band gap to low band gap domains ratio results in low EQE (i.e. RP-FA system ~0.002%).

On confirming that employing low solubility $Cs^+$ cation promotes formation of intermediate m domains from optical and electrical characterization, further refinement of the PBA and Cs concentration is done to tune the emission colour within the blue region.

### 7.2.6 Influence of A-site, B-site and L-cations ratios on RP film properties

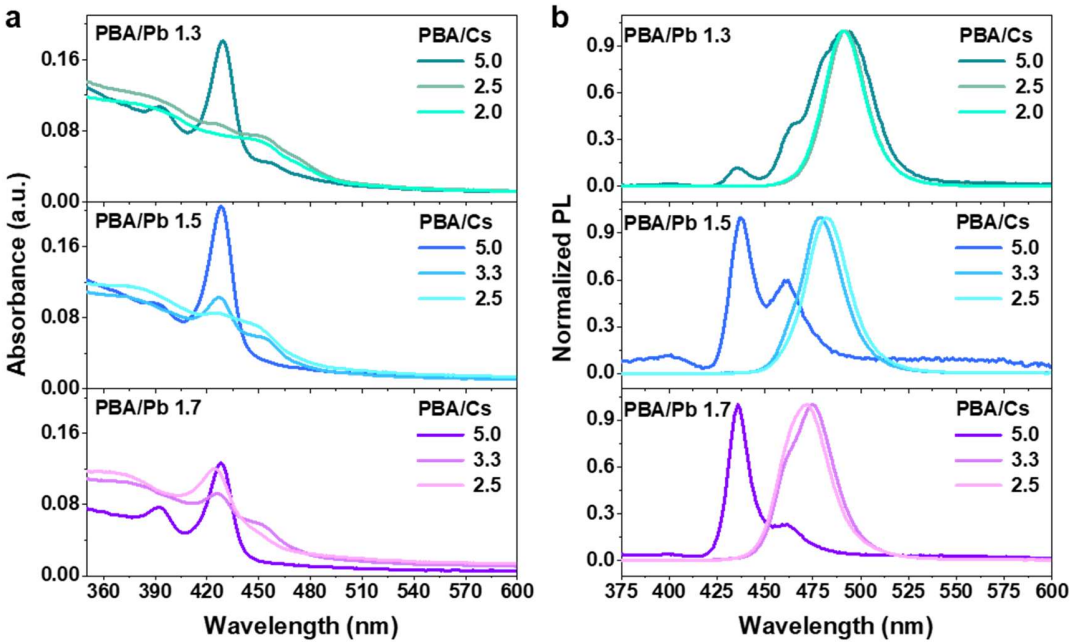


**Figure 7.12** (a) Absorbance and (b) normalized PL spectra on varying PBA/Pb and PBA/Cs ratios in the precursor solution.

Despite the use of <m> = 2 solution where PBA/Pb and PBA/Cs ratios are set at 1.5 and 3.3, the emission comes primarily from m = 4 – 5, with the EL peaking at 486 nm. It is proposed that both PBA/Pb and PBA/Cs ratios play significant roles in controlling the proportion of intermediate m domains in the film. For deep blue emission (~460 nm), narrow spread of lower intermediate m domains (m = 3 – 4) can be achieved by increasing PBA/Pb ratio precursors slightly. Meanwhile, although lowering Cs content enables the tuning of PL emission, sufficient $Cs^+$ supply is needed to maintain high PL intensity as low

band gap domain concentration grows with Cs incorporation into low m domains. This prediction is in good agreement with the observed systematic blue shift of the PL peak and absorbance onset when PBA/Pb ratio is increased up to 1.7; due to the preferred formation of lower intermediate m domains (Figure 7.12). Increasing the PBA/Cs ratio to 5.0 on the other hand, results in a lower proportion of low band gap domains as compared to the high band gap domains, which manifests in the form of multiple PL peaks regardless of the PBA/Pb ratio. Lowering the PBA/Cs ratio on the other hand, slightly red shifts the PL and enhances the PL intensity of film regardless of PBA/Pb ratio due to the more efficient energy cascade process with higher concentration of low band gap domains. The corresponding positions of the PL on the CIE chart are shown in Figure 7.13.

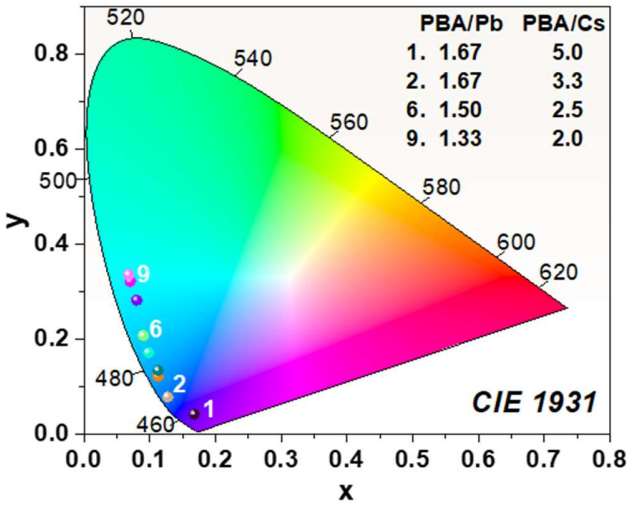


**Figure 7.13** The corresponding positions of the PL with varying PBA/Pb and PBA/Cs on the CIE chart

Devices are subsequently fabricated to assess the device performance of RP-Cs prepared from varying ratios of PBA/Pb and PBA/Cs. The corresponding cation ratios (PBA/Pb and PBA/Cs) for compositions 1, 2, 6 and 9 in the devices, are as indicated in Figure 7.13.

### 7.2.7 Electrical characterization of RP-Cs-based PeLEDs with varying precursor stoichiometry

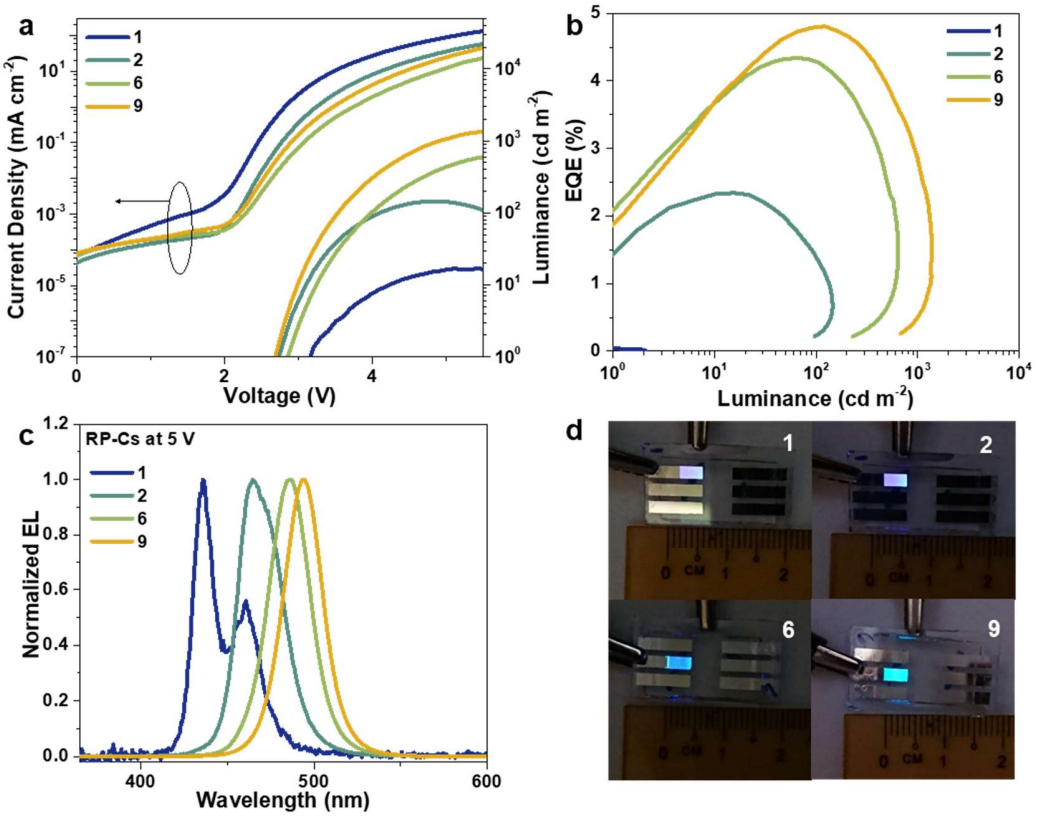


**Figure 7.14** (a) Current density – luminance against voltage curves, (b) EQE as a function of luminance curves, (c) normalized EL spectra and (d) photos of device under operation for PBA/Pb (PBA/Cs) ratios of 1.67 (5.0), 1.67 (3.3), 1.50 (2.5) and 1.33 (2.0) respectively.

Indeed, by tuning both the PBA/Pb ratio and PBA/Cs ratio, PeLED with EL emission ranging from violet (~437 nm) to cyan (~495 nm) can be fabricated. In general, $V_{th}$ and maximum luminance ($L_{max}$) varies with EL wavelength with higher $V_{th}$ and lower $L_{max}$ seen for blue shifted EL devices (Figure 7.14 (a)). This can be explained by the fact that blue shifted devices contain higher concentration of low m domains which is generally less conducting as charge transport is perturbed by insulating organic layers. Overall, maximum EQEs of 2.34%, 4.34%, and 4.8% can be achieved with EL peak at 465 nm, 486 nm, and 493 nm respectively (Figure 7.14 (b)-(c)). Uniform EL emission is observed from the

working PeLED (Figure 7.14 (c)-(d)).

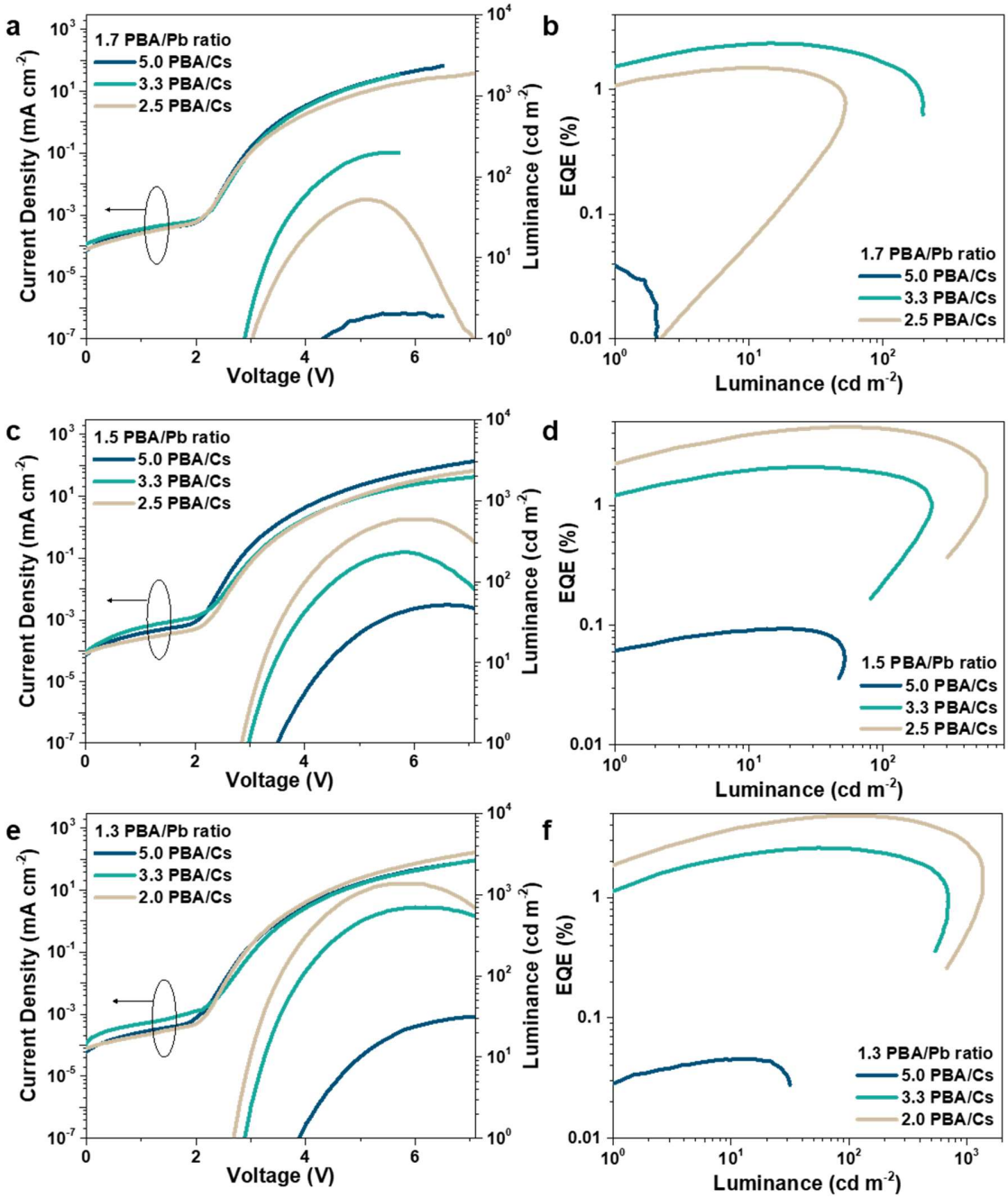


**Figure 7.15** Current density – luminance against voltage for PBA/Pb ratios of (a) 1.7, (c) 1.5 and (e) 1.3. EQE as a function of luminance for PBA/Pb ratios of (b) 1.7, (d) 1.5 and (f) 1.3.

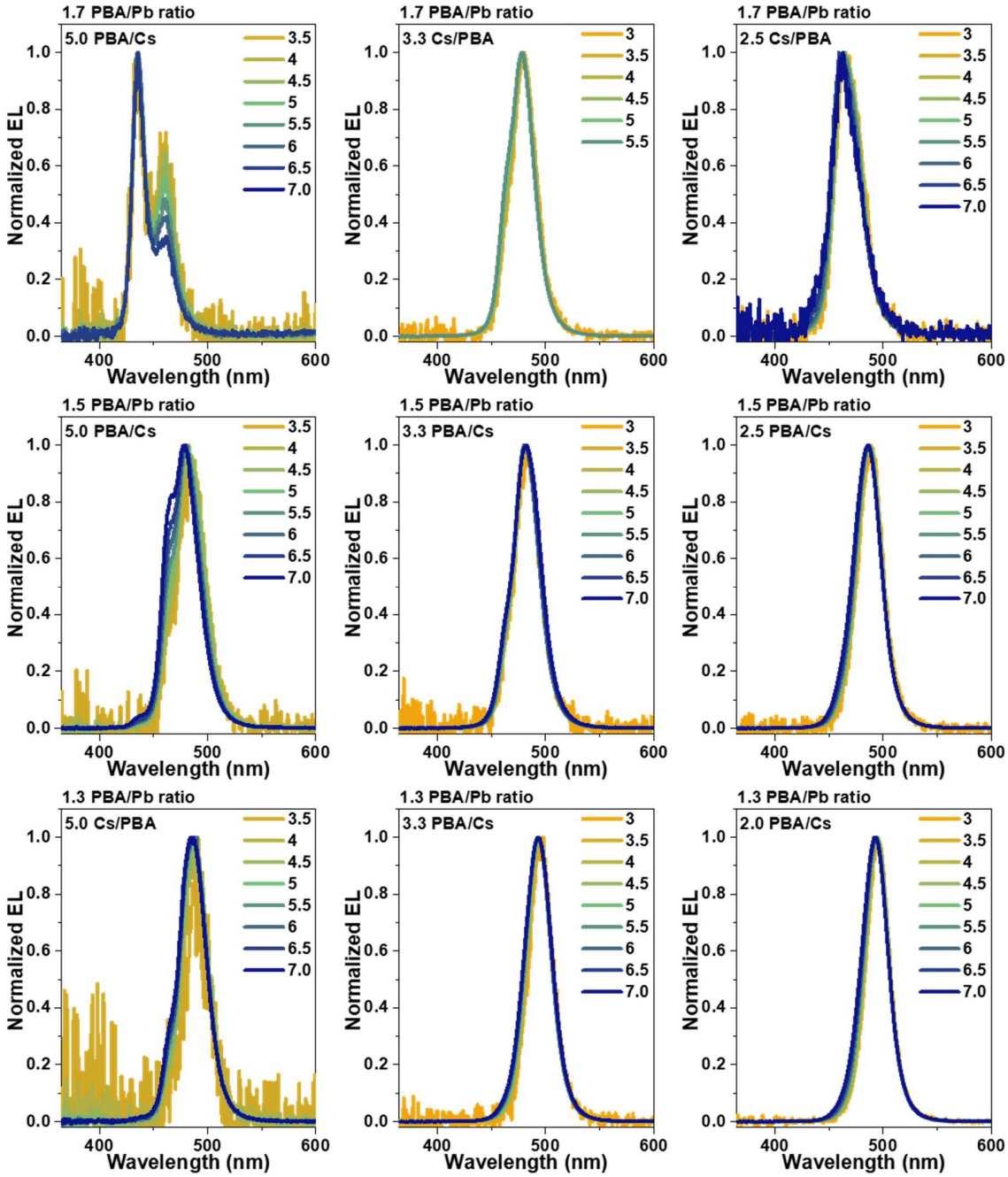


**Figure 7.16** EL stability of various PBA/Pb and PBA/Cs ratios at different voltages

High $V_{th}$, low efficiency, and blue shifting of EL with increasing bias application are obtained for devices with PBA/Cs ratio of 5.0 due to the large proportion of high band gap to low band gap domains in the film (Figure 7.15 and 7.16). On lowering PBA/Cs ratio to

3.3 and below, the higher low band gap domain concentration realizes spectrally stable EL despite high bias application (Figure 7.16). Higher EQEs are achieved with lower PBA/Cs ratio regardless of PBA/Pb ratio (Figure 7.15).

### 7.2.8 Device and film stability

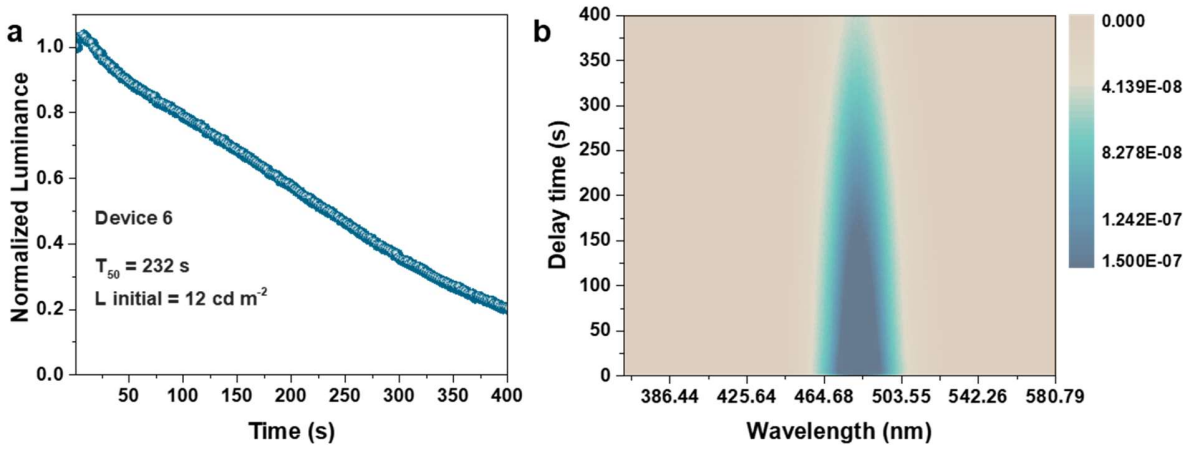


**Figure 7.17** (a) Normalized luminance as a function of time and (b) the spectral stability of device 6, corresponding to PBA/Pb and PBA/Cs ratios of 1.50 and 2.5 respectively

The device also shows spectral stability throughout the lifetime measurement which is set at an initial luminance of 12 cd $m^{-2}$ and is shown to have a decay time ($T_{50}$) of 232 s (Figure 7.17). It is postulated that the short device lifetime stems from the instability of the emitter with the interfacial layers. To validate the hypothesis, RP-Cs film prepared with PBA/Pb and PBA/Cs ratios of 1.50 and 2.5 is subjected to continuous illumination.

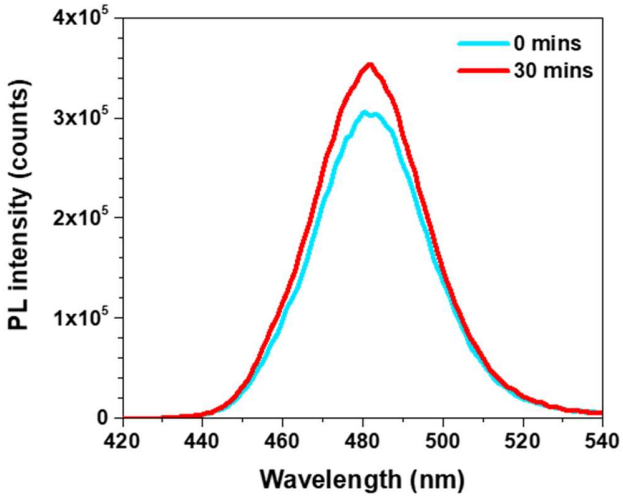


**Figure 7.18** Film stability on exposure to continuous light illumination for 30 min

On exposure to constant illumination for 30 min, although the PL intensity increases slightly, the PL spectra remains unchanged (Figure 7.18) suggesting that the device efficiency and stability are limited by the interfacial issues rather than material instability.

**Table 7.1 Comparison of fabricated device performance with state-of-the-art blue PeLEDs**

| Type of halides | Emitter | EL (nm) | $V_{th}$ (V) | $L_{max}$ ($Cd.m^{-2}$) | EQE (%) | Ref |
|---|---|---|---|---|---|---|
| Bromide | 2-phenoxyethylamonnium bromide : $CH_3NH_3Br$ : $PbBr_2$ | 480, 494, 508<br>462 | ~3.5<br>~6.2 | 19.25<br>1.26 | 1.1<br>0.06 | 1 |
| | Ethylammonium bromide : $CH_3NH_3Br$ : $PbBr_2$ | 473 | 2.4 | 200 | 3 | 2 |
| | Phenethylammonium bromide : $PbBr_2$ | 410 | 2.5 | | 0.04 | 3 |
| | Phenylethylammonium bromide : isopropylammonium bromide : CsBr : $CH_3NH_3Br$ : $PbBr_2$ | 490 | ~5.4 | 2480 | 1.5 | 4 |
| | Butylammonium bromide : $CH_3NH_3Br$ : $PbBr_2$ | ~440, 460, 475 | ~5 | 1 | 5.4 x $10^{-3}$ | 5 |
| | Phenylethylammonium bromide : CsBr : RbBr : $PbBr_2$ | 475<br>466 | ~3.8<br>~3.8 | 100.6<br>28.9 | 1.35<br>0.15 | 6 |
| | $CH_3NH_3PbBr_3$ nanocrystals | 456 | ~5.6 | 2 | 2.4 x $10^{-3}$ | 7 |
| Bromide – chloride | Butylammonium bromide : CsBr : $PbCl_2$ | 487 | 4.5 | 3340 | 6.2 | 8 |
| | Phenylethylammonium bromide : CsX(Br,Cl) : $PbBr_2$ | 480 | 3.2 | 3780 | 5.7 | 9 |
| | $CsPbX(Br,Cl)_3$ nanocrystals | 463 | 2.9 | 318 | 1.2 | 10 |
| | $CsPbX(Br,Cl)_3$ nanocrystals | 452 | 5.1 | 742 | 0.07 | 11 |
| | $Cs(Pb,Mn)X(Br,Cl)_3$ nanocrystals | 466 | ~4.2 | 245 | 2.12 | 12 |
| | $CH_3NH_3PbX(Br,Cl)_3$ nanocrystals | 445 | ~7.8 | 2673 | 1.38 | 13 |
| | $CH_3NH_3PbX(Br,Cl)_3$ nanocrystals | 490 | 3 | 35 | 1.9 | 14 |
| Bromide | **Our work** | **436,461<br>465<br>486<br>493** | **3.2<br>2.8<br>2.9<br>2.7** | **16.7<br>144.9<br>643.8<br>1371** | **0.042<br>2.34<br>4.34<br>4.8** | |

To date, this is the highest reported EQE for pure bromide-based blue-emitting RP PeLEDs in the field (Table 7.1) with high efficiency and spectral stability maintained across the blue region (i.e. deep blue to cyan).

## 7.3 Conclusion

Although mixed-dimensional MHPs have yielded excellent results in high performance green and red PeLEDs; their applicability for blue emission has been hampered due to the tendency for energy cascade phenomenon to shift emission to the multi-dimensional MHP domains with the lowest band gap. High concentrations of the large 2D cation forming low dimensional $L_2A_{m-1}B_mX_{3m+1}$ MHP provide an opportunity for realization of blue emission, however the low conductivity of the 2D cation limits the high luminescence desired. Relying on a triptych of 2D and A-site cation concentrations, solubility limit of A-site cation, and nucleation kinetics; a methodology enabling the tailoring of structural landscape to deliver a narrow distribution (m = 2-5) of MHP domains allows efficient blue emission to be achieved. High concentrations of the 2D cation have been shown to be necessary to eliminate 3D domains, whereas the low solubility A-site cation curbs the formation of undesired 2D domains. This is further compounded by the absence of 2D and 3D emissions in the EL and PL spectra, and the efficacy of charge carrier transfer; evidenced by the increasing rise and decay times at longer wavelengths, which confirms the suppression of non-radiative losses at low m domains. Control over MHP structural landscape allows record efficiencies of 2.34 and 4.8% corresponding to spectrally stable deep blue (~ 465 nm) and cyan (~ 493 nm) emissions to be achieved. The single halide system utilized in this study also circumvents issues relating to halide segregation. This strategy is readily applicable to other material systems and would lead to significant advancements in blue emissions and offer new avenues for tunability across the CIE colour spectrum.

# References

1. Kim, J.; Chung, C.-H.; Hong, K.-H., Understanding of the formation of shallow level defects from the intrinsic defects of lead tri-halide perovskites. *Physical Chemistry Chemical Physics* **2016,** *18* (39), 27143-27147.

2. Kumawat, N. K.; Liu, X.-K.; Kabra, D.; Gao, F., Blue perovskite light-emitting diodes: progress, challenges and future directions. *Nanoscale* **2019,** *11* (5), 2109-2120.

3. Manser, J. S.; Christians, J. A.; Kamat, P. V., Intriguing Optoelectronic Properties of Metal Halide Perovskites. *Chemical Reviews* **2016,** *116* (21), 12956-13008.

4. Quan, L. N.; Zhao, Y.; García de Arquer, F. P.; Sabatini, R.; Walters, G.; Voznyy, O.; Comin, R.; Li, Y.; Fan, J. Z.; Tan, H.; Pan, J.; Yuan, M.; Bakr, O. M.; Lu, Z.; Kim, D. H.; Sargent, E. H., Tailoring the Energy Landscape in Quasi-2D Halide Perovskites Enables Efficient Green-Light Emission. *Nano Letters* **2017,** *17* (6), 3701-3709.

5. Yuan, M.; Quan, L. N.; Comin, R.; Walters, G.; Sabatini, R.; Voznyy, O.; Hoogland, S.; Zhao, Y.; Beauregard, E. M.; Kanjanaboos, P.; Lu, Z.; Kim, D. H.; Sargent, E. H., Perovskite energy funnels for efficient light-emitting diodes. *Nat Nano* **2016,** *advance online publication*.

6. Zhou, N.; Shen, Y.; Li, L.; Tan, S.; Liu, N.; Zheng, G.; Chen, Q.; Zhou, H., Exploration of Crystallization Kinetics in Quasi Two-Dimensional Perovskite and High Performance Solar Cells. *Journal of the American Chemical Society* **2018,** *140* (1), 459-465.

7. Cao, D. H.; Stoumpos, C. C.; Farha, O. K.; Hupp, J. T.; Kanatzidis, M. G., 2D Homologous Perovskites as Light-Absorbing Materials for Solar Cell Applications. *Journal of the American Chemical Society* **2015,** *137* (24), 7843-7850.

8. Xing, J.; Zhao, Y.; Askerka, M.; Quan, L. N.; Gong, X.; Zhao, W.; Zhao, J.; Tan, H.; Long, G.; Gao, L.; Yang, Z.; Voznyy, O.; Tang, J.; Lu, Z.-H.; Xiong, Q.; Sargent, E. H., Color-stable highly luminescent sky-blue perovskite light-emitting diodes. *Nature Communications* **2018,** *9* (1), 3541.

9. Liang, K.; Mitzi, D. B.; Prikas, M. T., Synthesis and Characterization of Organic−Inorganic Perovskite Thin Films Prepared Using a Versatile Two-Step Dipping Technique. *Chemistry of Materials* **1998,** *10* (1), 403-411.

10. Iain W. H., O.; Alexandra A., K.; James R., N., *General Synthesis Principles for Ruddlesden–Popper Hybrid Perovskite Halides from a Dynamic Equilibrium*. 2018.

11. Hu, Y.; Spies, L. M.; Alonso-Álvarez, D.; Mocherla, P.; Jones, H.; Hanisch, J.; Bein, T.; Barnes, P. R. F.; Docampo, P., Identifying and controlling phase purity in 2D hybrid perovskite thin films. *Journal of Materials Chemistry A* **2018,** *6* (44), 22215-22225.

12. Quintero-Bermudez, R.; Gold-Parker, A.; Proppe, A. H.; Munir, R.; Yang, Z.; Kelley, S. O.; Amassian, A.; Toney, M. F.; Sargent, E. H., Compositional and orientational control in metal halide perovskites of reduced dimensionality. *Nature Materials* **2018,** *17* (10), 900-907.

13. Stoumpos, C. C.; Cao, D. H.; Clark, D. J.; Young, J.; Rondinelli, J. M.; Jang, J. I.; Hupp, J. T.; Kanatzidis, M. G., Ruddlesden–Popper Hybrid Lead Iodide Perovskite 2D Homologous Semiconductors. *Chemistry of Materials* **2016,** *28* (8), 2852-2867.

14. Filip, M. R.; Eperon, G. E.; Snaith, H. J.; Giustino, F., Steric engineering of metal-halide perovskites with tunable optical band gaps. *Nature Communications* **2014,** *5*, 5757.

15. Chiang, C.-H.; Wu, C.-G., A Method for the Preparation of Highly Oriented MAPbI3 Crystallites for High-Efficiency Perovskite Solar Cells to Achieve an 86% Fill Factor. *ACS Nano* **2018,** *12* (10), 10355-10364.

16. Yantara, N.; Bruno, A.; Iqbal, A.; Jamaludin, N. F.; Soci, C.; Mhaisalkar, S.; Mathews, N., Designing Efficient Energy Funneling Kinetics in Ruddlesden–Popper Perovskites for High-Performance Light-Emitting Diodes. *Advanced Materials* **2018,** *30* (33), 1800818.

# Chapter 8

# Conclusion and Future Work

*This chapter presents an overall summary of the work presented in this thesis on managing non-radiative recombination in metal halide perovskites through defect passivation and implementation of the energy cascade concept to mitigate the influence of defects via an energetically engineered landscape. The importance of defect management via defect suppression or mitigation of non-radiative recombination losses through efficient charge carrier funneling, is reiterated. The future work proposed stems from the lessons drawn from the studies conducted in this thesis.*

## 8.1 Contribution and Summary of Work

MHPs have been identified as wonder materials for optoelectronic applications. This is hardly surprising owing to the unique range of properties offered by this class of materials such as low defect density, balanced long-range carrier diffusion lengths and narrow photoluminescence emission. However, despite the advantage of cheap solution-based processing, the propensity for defect formation with this technique necessitates mitigation of these non-radiative recombination sites. With the goal of achieving efficient PeLEDs in mind, this thesis presents the investigation into the alleviation of defects through material processing. It is also shown here that influence of non-radiative recombination process on light emission can be effectively managed through fine control of emitter composition and crystallization kinetics, enabling best-in-class chloride-free blue-emitting PeLEDs with maximum efficiency of 4.8% at peak emission wavelength of 493 nm, to be achieved.

The summary of the work done for this thesis is presented in the following sub-sections.

### 8.1.1 Passivation of surface defects through post-deposition treatment

The presence of defects in solution-processed MHPs is further exacerbated by the tendency for degradation or phase segregation during post-deposition annealing. The consequent under-coordination of surface lead atoms act as sites for non-radiative recombination and further expedite degradation process due to the increased susceptibility towards adsorption of other charge neutralization species. Surface defects arising from the non-stoichiometric ratio of Pb: Br is addressed through an inexpensive and facile post-deposition treatment process using branched alkyl ammonium cation species. The simultaneous grain size modulation and realignment of interfacial energy levels on incorporation of tetra ethyl ammonium bromide onto the surface of $CH_3NH_3PbBr_3$ films contributes favourably towards the enhancement in overall PeLED device characteristics, achieving $V_{th}$, luminance and EQE values of **2.4 V**, **11,000 cd m$^{-2}$** and **0.16%** respectively.

### 8.1.2 Additive engineering for suppression of grain size modulated defects

Aside from suppressing effect of non-radiative recombination in the emitter to improve the resultant device performance, improved device efficiency can also be attained through enhanced radiative recombination process. This has been shown to be successful through adoption of grain size modulation techniques such as nanocrystal pinning and the dispersion of emitting species in a polymer matrix, where light emission is augmented due to the spatial confinement of the injected charge carriers. However, to utilize spatial confinement for improved radiative recombination, the size of the emitting grain needs to be reduced. This translates to a corresponding increase in grain boundary density which is undesired as grain boundaries and surfaces present sites for non-radiative recombination (i.e defects and traps). Thus, to fully harness the advantages offered by small grains for efficient photon generation, a method to form small passivated grains need to be developed. Here, it is shown that by incorporating bathophenanthroline (Bphen) into the perovskite emitter during the anti-solvent process, small grains can be formed in-situ during solution processing, enabling improved performance corresponding to $V_{th}$, luminance and EQE values of **2.3 V**, **19,627 cd m$^{-2}$** and **0.78 %** respectively, to be achieved.

### 8.1.3 Molecular design of two-dimensional perovskite cation for energy cascade

Although 3D MHPs exhibit remarkable properties, the inherent limitations in terms of low exciton binding energy, moisture instability and propensity for light degradation, hamper the development of high efficiency devices. This has driven research towards the use of 2D MHPs, which are layered analogues of 3D MHPs due to their potential for high PLQYs arising from high exciton binding energies. Amalgamation of 2D and 3D MHPs has brought about improvement to efficiency through the process termed as “energy cascade”. This involves the rapid transfer of energy from high band gap to low band gap domains, enabling efficient light emission in the latter. Formation of multiple domains with different band gaps in the emitter, arising from the varying degree of 3D cation incorporation creates an energetic landscape where carriers injected into high band gap domains funnel to the energetically favoured, low band gap domains. Outcompeting of non-radiative

recombination process (in the high band gap domains) by the energy cascade process, coupled with effective radiative bimolecular recombination facilitated by high carrier density in the low band gap domains, explains the lower power thresholds required for efficient light emission, relative to pristine 3D MHPs. Here, three molecules with different aromatic molecules adopting phenyl (PEA), pyridinium (PyrEA) and imidazolium (ImEA) cores respectively are investigated to understand the influence of aromatic molecular design on templating an efficient energetic landscape in the emitter for the energy cascade process. It was found that the least distorted 2D3D PEA yielded the best performance with $V_{th}$, luminance and EQE values of **2.1 V**, **20 380 cd A$^{-1}$** and **3.2 %** respectively.

### 8.1.4 Tailoring the distribution and spread of m domains for stable blue emission

Rapid efficiency strides for PeLEDs seen thus far have been noted only for green and red emission, with the efficiency for blue emission still wanting. Although wide band gap MHPs are achievable by employing chloride as the halide anion, the increased tendency for deep trap states formation, translates to an increase in undesired non-radiative recombination[10]. Attempts to yield blue emission through partial substitution of bromide with chloride ions are mired in issues pertaining to low efficiency and colour instability due to reduced PLQY and electric field-induced halide segregation[11]. Therefore, it is imperative that an alternative strategy to halide mixing be devised to obtain spectrally stable PeLED spanning the cyan-deep blue region of the visible light spectrum (band gap $\geq$ 2.48 – 2.56 eV). One possible approach to attain larger band gaps is through the substitution of A-site cation with bulky spacer molecules which results in the formation of mixed-dimensional MPs[12]. The formation of multiple domains with different band gap characteristics within the same film facilitates the energy cascade process which drives the high PLQY and device efficiencies seen in mixed-dimensional MHPs. Here, it is shown that by introducing excess 2D cation together with a low solubility A-site cation (and therefore a fast nucleation rate), a narrow, monodispersed distribution of intermediate m domains centered about the desired emission peak can be attained. The narrow spread of m domains increases the efficacy of the energy cascade process; repressing non-radiative recombination losses at the low m domains thereby allowing high PLQY and device

efficiency to be achieved at lower power densities. Furthermore, the use of a pure bromide system ensures that not only is phase segregation mitigated, deep trap-induced losses are also curbed with the elimination of chloride as a conduit for blue emission. In utilizing this strategy, highly efficient, spectrally stable blue PeLEDs spanning the entire blue region ranging from 437 to 495 nm with EQEs of **2.34 %**, **4.34 %**, and **4.8 %** at EL peak wavelengths of **465**, **486**, and **493 nm** respectively, are achieved.

## 8.2 Overall Conclusion

Although 3D MHPs have shown great promise for light emission applications, PeLEDs based on the pristine materials have been hampered by low efficiency due to inefficient radiative recombination. In this thesis, it is proposed that through defect management, non-radiative losses can be effectively mitigated thereby giving rise to enhanced radiative recombination and in turn higher electroluminescence. The issue is addressed via two ways; (a) passivation of defects via processing and (b) suppressing the effect of non-radiative recombination pathways through the introduction of an energetically engineered landscape. In the former, spin coated films are treated post-deposition with a branched alkyl ammonium cation ($TEABr^{+}$) to passivate the under-coordinated Pb atoms. Surface analysis of the treated films reveals surface Br: Pb ratio approaching 3.0 on increasing TEABr concentration, confirming the effectiveness of the treatment process. Although presence of lower dimensional phase is detected in the XRD patterns of the treated films, the absence of secondary PL peaks corresponding to emitting multi-dimensional phases eliminates the energy cascade process as a cause for PL enhancement. It can thus be deduced that the passivating nature of TEABr, coupled with simultaneous grain size reduction of the treatment process, provide a more dominating influence over the PL and PLQY enhancement. The device characteristics too improved with TEABr concentration up to 15 mg $mL^{-1}$ beyond which efficiency drops and threshold voltage increases. This is explained by the greater proportion of less conducting lower dimensional secondary phase formed in the film which hinders charge injection and effective radiative recombination during device operation, despite the higher PLQY.

The low exciton binding energies of 3D MHPs can be circumvented through geometric and/or electronic confinement. Geometric confinement involves imposition of spatial constraints to facilitate bimolecular recombination process. However, the simultaneous increase in grain boundary density necessitates effective passivation at the grain boundaries for the full advantage of geometric confinement to be maximized. By incorporating BPhen into the emitter layer via the anti-solvent process, higher PL, luminance and efficiency are attained due to the formation of smaller grains which enhances radiative recombination. This is possible due to the passivating nature of Bphen which enables small grains to be formed without detriment to film properties. The controllable alteration of the MHP's energy bands via simple variation of the BPhen concentration in the anti-solvent too allows for efficient injection of charge carriers into the emitter as seen by the reduction in threshold voltages. The champion device is made with 0.500 mg $mL^{-1}$ of BPhen, resulting in a ten-fold increase in luminance and fifteen-fold improvement in current efficiency and EQE compared to the reference. Excessive BPhen (> 0.500 mg $mL^{-1}$), however, resulted in the decline of device performance, attributed to the reduction of charge carrier mobility at high additive concentrations. Although substitution of the small molecule inclusion (BPhen) with PBD and TPBi also brings about improvement to PL intensity, the negligible change in device efficiency indicates that molecule selection is critical for improved film properties to be translated into efficient PeLED devices.

PL improvement on post deposition treatment and additive engineering of emitter is testament to the importance of defect passivation to improve film optoelectronic properties and subsequent device performance. Alternatively, enhancement to radiative recombination can also be attained through defect mitigation such as in the case of the energy cascade phenomenon. The inability of bulky 2D cation to fit into the network of corner sharing metal halide octahedra results in the formation of layered MHP structure with the formula $L_2A_{m-1}PbBr_{3m+1}$, where L and A are the 2D and A-site cations respectively. By varying the amount of 2D cation incorporation into the 3D network, multiple band gap domains acting as mini quantum wells, are formed in the emitter layer, providing electronic confinement to the charge carriers. On injection of charge carriers into the high band gap domains, the charge carriers funnel sequentially to the low band gap domains. The

energetically favourable process occurs within such short time scales that non-radiative recombination process within each domain is superseded. This, in tandem with the increased rate of radiative recombination with high localized charge carrier density, enables high PLQYs to be achieved with low power intensities. Though numerous reports on energy cascade for light emission have been published, a guideline for the design of suitable 2D cation to template the formation of an energetic landscape to promote energy cascade is still lacking. Three 2D aromatic cations (PEA), (PyrEA) and (ImEA) are investigated to understand the influence of aromatic core on efficacy of the energy cascade phenomenon. Despite the potential for improved charge transport with bi-cationic PyrEA and ImEA, their corresponding 2D3D films showed higher degree of distortion as evidenced by the XRD analysis. Not only were the PL intensities across varying fluence lower than 2D3D PEA, the weak PL emission from the high band gap domains too appears to suggest either (a) the presence of insufficient low band gap domains or (b) the occurrence of inefficient radiative recombination, either of which are detrimental to the energy cascade process. The PL excitation spectra, provides further evidence of 2D3D PEA efficiency for charge carrier funneling. The implication of inefficient energy cascade process in 2D3D PyrEA and 2D3D ImEA is the increased susceptibility towards non-radiative losses due to the outcompeting of the former process by the latter. It is proposed that high PL of the 2D film is crucial for templating of an efficient energy cascade landscape. As the charge transfer process in the energetically engineered emitter landscape initiates at the high band gap domains, a 2D cation with high PL in thin film form will ensure that high quality (low defect density) high band gap domains will form on incorporation of the 2D cation into the 3D framework. This promotes efficient charge transfer across the various band gap domains as this process will not be impeded by non-radiative recombination process (defect filling) at the high band gap domains. Hence, while mixed-dimensional perovskites provide a platform for high efficiency devices to be attained, judicious selection of 2D cation is crucial to enable effective mini quantum wells to form without detriment to charge funneling kinetics.

Despite the success of energy cascade in yielding high performing green and red PeLEDs; their applicability for blue emission has been hampered due to the penchant for emission to shift to the multi-dimensional MHP domains with the lowest band gap. High

concentration of the 2D cation provide a means for the realization of blue emission however, the low conductivity of the 2D cation limits the high luminescence desired. Relying on a triptych of 2D and A-site cation concentrations, solubility limit of A-site cation, and nucleation kinetics; tailoring of the structural landscape to deliver a narrow distribution (m = 2-5) of MHP domains is made possible, allowing efficient blue emission to be achieved. High concentration of the 2D cation is necessary to eliminate 3D domains, whereas the role of low solubility A-site cation is to curb the formation of undesired 2D domains. Control over MHP structural landscape allows record efficiencies of spectrally stable deep blue (~ 465 nm) and cyan (~ 493 nm) emissions to be achieved. The single halide system utilized in this study also circumvents issues relating to halide segregation.

## 8.3 Future Work and Possible Directions

The work presented in the thesis has exemplified the importance of defect management, either through passivation; as a means for defect suppression or through the energy cascade phenomenon; where the effect of non-radiative recombination process is mitigated due to the rapid charge carrier funneling, towards improving MHP films' optoelectronic properties and the resultant devices.

### 8.3.1 Merging defect passivation with energy cascade

The thesis has been focused primarily on either passivation or charge carrier funneling to manage defects in the emitter. However, the implementation of both to address the two issues simultaneously have not yet been discussed. This offers another route for exploration as non-radiative recombination losses at the interfaces increases as the device architecture becomes more complex with the presence of more layers such as the injection and transport layers to improve device efficiency. While the energy cascade concept facilitates radiative recombination process in the smallest band gap domains through mitigation of non-radiative losses in the larger band gap domains, losses in the former are not addressed. Hence, it is not impossible that efficiency can pushed further through suppression of defects in the smallest band gap domains. This can be made possible through

post deposition treatment process with Lewis bases such as pyridine and thiophene which can preferentially bind to the Pb atoms due to their electron donating capabilities.[1-2] Figure 8.1 presents an example of mixed-dimensional MHP exhibiting enhanced device performance with post deposition treatment.[3]

Not only does the post deposition treatment process enable the passivation of surface defects, the choice of molecule can also be functionalized for enhanced moisture resistance through use of ligands and hydrophobic polymers. An example would be the use of hydrophobic ligands for increased moisture resistance[4]. In selecting suitable ligands, due consideration ought to be placed on the length of the aliphatic chain which can be impede charge transport in the device. Moreover, as shown in Chapters 4 and 5, any inclusions into the emitter will affect the interfacial energy alignment and in turn the injection of both types of charge carries through the charge selective contacts. Further optimization of the type of interfacial material used would then be required to ensure that charge carrier injection into the emitter is not compromised.

a

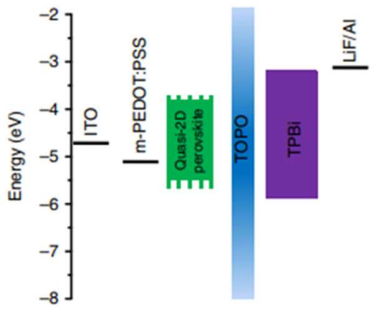


b

**Table 1 Device performance based on quasi-two-dimensional perovskites $PEA_2(FAPbBr_3)_{n-1}PbBr_4$**

| Compositions | $L_{max}$ (cd $m^{-2}$) | Current efficiency (cd $A^{-1}$) | Maximum EQE (%) |
|---|---|---|---|
| $n = 2$ | 717 | 5.98 | 1.54 |
| $n = 3$ | 6973 | 40.20 | 9.29 |
| $n = 3$ (best) | 7829 | 52.51 | 12.12 |
| $n = 4$ | 8779 | 37.61 | 8.45 |
| $n = 5$ | 3452 | 20.95 | 4.82 |
| $n = 6$ | 2281 | 16.77 | 4.00 |
| $n = 3$ and TOPO | 9120 | 62.43 | 14.36 |

c

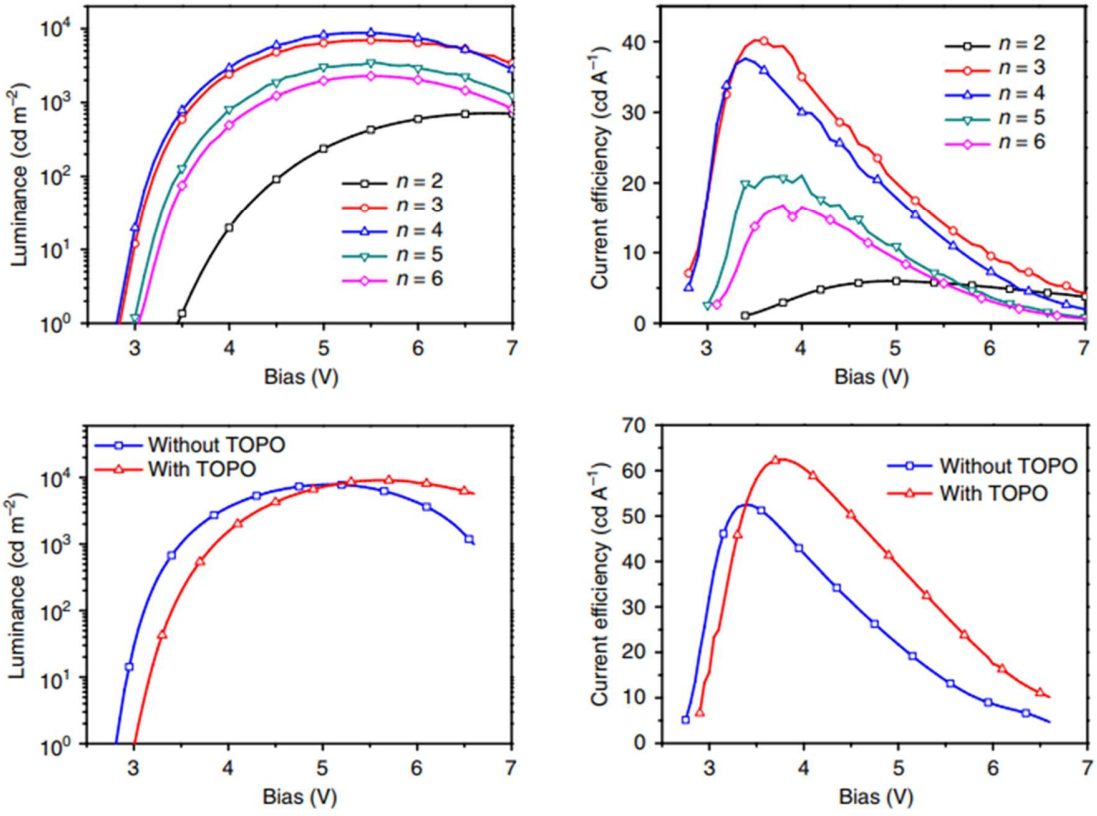


**Figure 8.1** Device performance of mixed-dimensional perovskite based on FA-PEA with post deposition treatment of trioctylphosphine oxide.[3] (a) Device architecture, (b) summary of device data and (c) luminance and current efficiency against voltage plots.

### 8.3.2 Graded emitter for high efficiency PeLEDs

From Chapters 5 and 6, it has been shown that energy level alignment at the interfaces and the energy cascade process are beneficial for charge carrier injection and radiative recombination processes, respectively. This concept can be further expanded towards the development of a graded emitter such as shown in Figure 8.2. Here, the layers closest to the charge selective interfacial layers act as confinement layers restricting recombination process to the graded region which function as multi quantum wells.[5] Although the engineered energetic landscape of the energy cascade process has been shown to be a successful method for the localization of charge carriers for increased radiative recombination, the poor control over the spatial distribution of the varied band gap domains (either laterally or vertically next to the emitting domains) suggests that modifications to processing would be necessary to drive efficiency further. As such a graded emitter is proposed; where the radiative recombination zone or the multi quantum well active region is sandwiched between two confinement layers parallel to the contacts and away from the charge transport layers. This serves three functions: (a) to electronically confine the charges within the multi-quantum well region for more efficient radiative recombination, (b) to minimize leakage of charge carriers and (b) to suppress non-radiative losses at the charge selective layers by shifting the recombination away from the interfaces. This in turn enhances the overall efficiency and stability of the device due to the effective discharge of injected charge carriers via radiative recombination, leading to less localized heating effect.

One way to ensure the formation of the graded emitter shown in Figure 8.2 is through thermal evaporation. By controlling the base pressure, evaporation rate and evaporating species during the evaporation process, the composition and band gap of the deposited films can be finely tuned and a graded emitter be achieved. The controlled manner of film growth offered by the thermal evaporation process would also offer MHP films of greater electronic quality as compared to solution processed films. The resultant lower defect density and graded emitter stack would synergistically enable high efficiency devices to be fabricated.

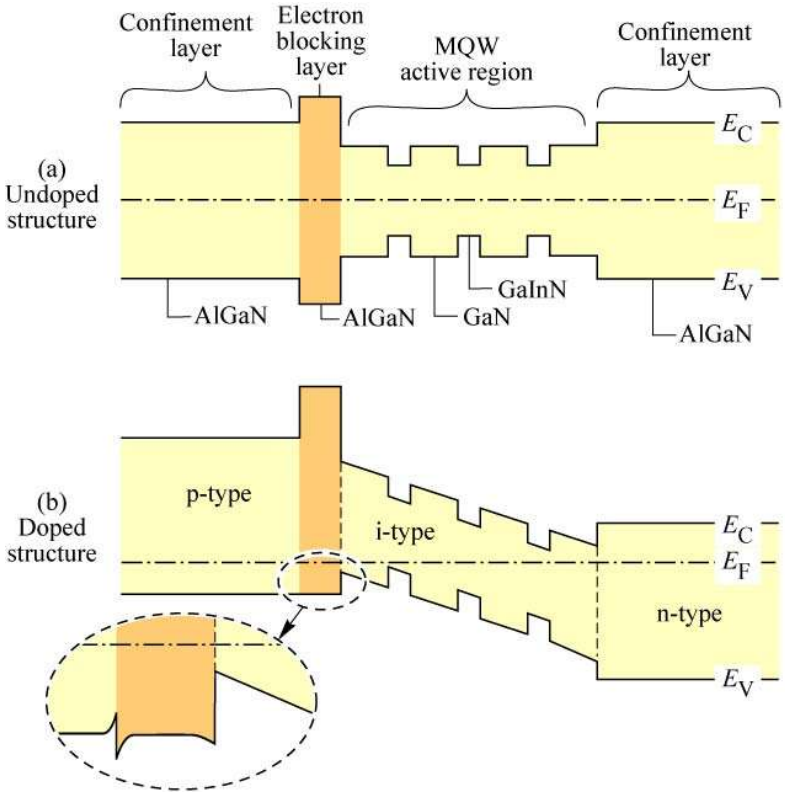


**Figure 8.2** An example of a graded emitter structure in an inorganic LED.[5]

### 8.3.3 White light emission for lighting applications

The influence of A-site and 2D cations relative solubilities on crystallization kinetics as shown in Chapter 7 provide an interesting perspective on uncovering the underlying reason for undesired multiple emissions in mixed-dimensional MHPs. Not only does it offer a more stringent degree of control over processing, but also opens up new avenues for tunability across the CIE colour spectrum. The higher colour purity of the emission allows for wider gamut of colours to be attained when incorporated with other emitters. For example, a 470 nm blue emitter enables white emission to be achieved when coupled together with ~ 570 nm emitter or alternatively, a 490 nm cyan emitter with a 600 nm orange emitter as shown on the CIE spectrum in Figure 8.3. From Chapter 7, it is shown that by simply changing the composition of PBA/Pb and PBA/Cs, emission from the blue region spanning from 465 nm to 493 nm can be achieved, suggesting that all that is needed

are complementary colour emitters. One possible candidate is $CsPbI_3$, which enables red emission to be attained through quantum confinement (nanoparticles).

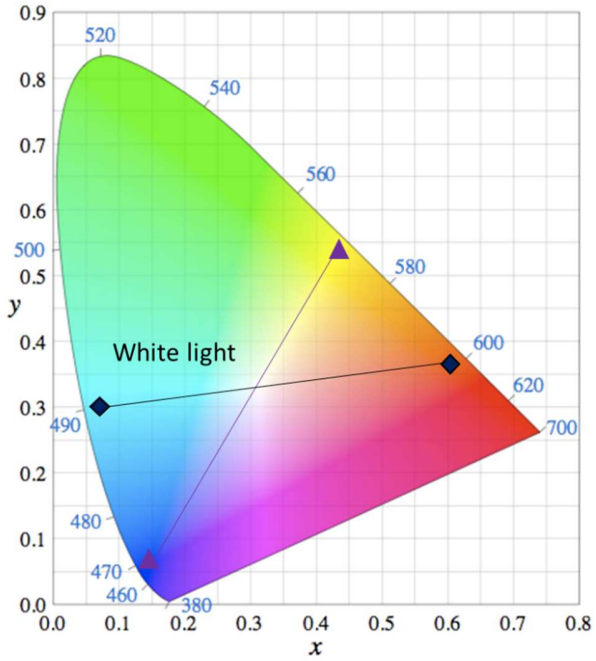


**Figure 8.3** CIE spectrum showcasing the emission combination allowing for white light emission[6]

It is proposed that by employing the blue emitter with other materials with complementary colour emission in tandem devices, white emission can be effectively achieved[6]. For example, blue emitting MHP films can be deposited on the transparent conducting substrate whereas the complementary colour emitters be placed on top, sandwiching interlayer materials 2,2'-(4,4'-(Phenylphosphoryl)bis(4,1-phenylene))bis(1-phenyl-1H -benzo[d]imidazole) (BIPO) and Poly(N,N'-bis-4-butylphenyl-N,N'-bisphenyl)benzidine (Poly-TPD) which act as electron and hole transporting materials, respectively. The presence of the interlayer facilitates charge transport between the two emitting species due to their well-matched energy levels with the MHPs. Moreover, use of insulating capping material to suppress chemical reaction between the two emitters can be avoided thus eliminating issues pertaining to charge transport.

# References

1. Chaudhary, B.; Kulkarni, A.; Jena, A. K.; Ikegami, M.; Udagawa, Y.; Kunugita, H.; Ema, K.; Miyasaka, T., Poly(4-Vinylpyridine)-Based Interfacial Passivation to Enhance Voltage and Moisture Stability of Lead Halide Perovskite Solar Cells. *ChemSusChem* **2017,** *10* (11), 2473-2479.

2. Noel, N. K.; Abate, A.; Stranks, S. D.; Parrott, E. S.; Burlakov, V. M.; Goriely, A.; Snaith, H. J., Enhanced Photoluminescence and Solar Cell Performance via Lewis Base Passivation of Organic–Inorganic Lead Halide Perovskites. *ACS Nano* **2014,** *8* (10), 9815-9821.

3. Yang, X.; Zhang, X.; Deng, J.; Chu, Z.; Jiang, Q.; Meng, J.; Wang, P.; Zhang, L.; Yin, Z.; You, J., Efficient green light-emitting diodes based on quasi-two-dimensional composition and phase engineered perovskite with surface passivation. *Nature Communications* **2018,** *9* (1), 570.

4. Yang, S.; Wang, Y.; Liu, P.; Cheng, Y.-B.; Zhao, H. J.; Yang, H. G., Functionalization of perovskite thin films with moisture-tolerant molecules. *Nature Energy* **2016,** *1*, 15016.

5. Schubert, E. F., *Light-emitting Diodes*. 1 ed.; Cambridge University Press: 2003.

6. Mao, J.; Lin, H.; Ye, F.; Qin, M.; Burkhartsmeyer, J. M.; Zhang, H.; Lu, X.; Wong, K. S.; Choy, W. C. H., All-Perovskite Emission Architecture for White Light-Emitting Diodes. *ACS Nano* **2018,** *12* (10), 10486-10492.

# List of Publications

Yan Fong Ng, Nur Fadilah Jamaludin, Natalia Yantara, Mingjie Li, Venkata Kameshwar Rao Irukuvarjula, Hilmi Volkan Demir, Tze Chien Sum, Subodh Mhaisalkar, and Nripan Mathews, Rapid Crystallization of All-Inorganic CsPbBr3 Perovskite for High Brightness Light-Emitting Diodes, *ACS Omega 2017*, 2, 2757−2764, DOI: 10.1021/acsomega.7b00360

Yan Fong Ng, Wei Jian Neo, Nur Fadilah Jamaludin, Natalia Yantara, Subodh Mhaisalkar and Nripan Mathews, Enhanced Coverage of All-Inorganic Perovskite $CsPbBr_3$ through Sequential Deposition for Green Light-Emitting Diodes, *Energy Technol. 2017*, 5, 1859–1865, DOI: 10.1002/ente.201700475

Yan Fong Ng, Sneha A. Kulkarni, Shayani Parida, Nur Fadilah Jamaludin, Natalia Yantara, Annalisa Bruno, Cesare Soci, Subodh Mhaisalkar and Nripan Mathews, Highly Efficient Cs-based perovskite light-emitting diodes enabled by energy funneling, *Chem. Commun. 2017*,53, 12004-12007, DOI: 10.1039/C7CC06615E

Nur Fadilah Jamaludin, Natalia Yantara, Yan Fong Ng, Mingjie Li, Teck Wee Goh, Krishnamoorthy Thirumal, Tze Chien Sum, Nripan Mathews, Cesare Soci and Subodh Mhaisalkar, Grain size Modulation and Interfacial Engineering of $CH_3NH_3PbBr_3$ Emitter Films through Incorporation of Tetraethylammonium Bromide, *ChemPhysChem 2018*, 19,1075 –1080, DOI:10.1002/cphc.201701380

Nur Fadilah Jamaludin, Natalia Yantara, Yan Fong Ng, Annalisa Bruno, Bevita K. Chandran, Xin Yu Chin, Krishnamoorthy Thirumal, Nripan Mathews, Cesare Soci and Subodh Mhaisalkar, Perovskite templating via a bathophenanthroline additive for efficient light-emitting devices, *J. Mater. Chem. C. 2018*, 6, 2295-2302, DOI: 10.1039/C7TC05643E

Sjoerd A. Veldhuis, Yan Fong Ng, Riyas Ahmad, Annalisa Bruno, Nur Fadilah Jamaludin, Bahulayan Damodaran, Nripan Mathews and Subodh Mhaisalkar, Crown Ethers Enable Room-Temperature Synthesis of $CsPbBr_3$ Quantum Dots for Light-Emitting Diodes, *ACS Energy Lett. 2018,* 33526-531, DOI: 10.1021/acsenergylett.7b01257

K. M. Muhammed Salim, Teck Ming Koh, Damodaran Bahulayan, P. C. Harikesh, Nur Fadilah Jamaludin, Benny Febriansyah, Annalisa Bruno, Subodh Mhaisalkar and Nripan Mathews, Extended Absorption Window and Improved Stability of Cesium-Based Triple-Cation Perovskite Solar Cells Passivated with Perfluorinated Organics, *ACS Energy Lett. 2018*, 351068-1076, DOI: 10.1021/acsenergylett.8b00328

Tao Ye, Annalisa Bruno, Guifang Han, Teck Ming Koh, Jia Li, Nur Fadilah Jamaludin, Cesare Soci, Subodh Mhaisalkar and Wei Lin Leong, Efficient and Ambient-air-stable Solar Cell with Highly Oriented 2D@3D Perovskites, *Adv. Funct. Mater. 2018*, 28, 1801654. DOI: 10.1002/adfm.201801654

Natalia Yantara, Annalisa Bruno, Azhar Iqbal, Nur Fadilah Jamaludin, Cesare Soci, Subodh Mhaisalkar, and Nripan Mathews, Designing Efficient Energy Funneling Kinetics in Ruddlesden–Popper Perovskites for High-Performance Light-Emitting Diodes, *Adv. Mater. 2018*, 30, 1800818, DOI: 10.1002/adma.201800818

Benny Febriansyah,, Teck Ming Koh, Yulia Lekina, Nur Fadilah Jamaludin, Annalisa Bruno, Rakesh Ganguly, Ze Xiang Shen, Subodh G. Mhaisalkar and Jason England, Improved Photovoltaic Efficiency and Amplified Photocurrent Generation in Mesoporous n= 1 Two-Dimensional Lead-Iodide Perovskite Solar Cells, *Chem. Mater. 2019*, 31, 890−898, DOI: 10.1021/acs.chemmater.8b04064

Xintong Guo, Teck Ming Koh, Benny Febriansyah,, Guifang Han, Saikat Bhaumik, Jia Li, Nur Fadilah Jamaludin, Biplab Ghosh, Xiaodong Chen, Subodh Mhaisalkar and Nripan Mathews, Cesium-Oleate Passivation for Stable Perovskite Photovoltaics, *ACS Appl. Mater. Interfaces 2019*, 11, 27882−27889, DOI: 10.1021/acsami.9b08026

Riyas Ahmad, Abhijith Surendran, P. C. Harikesh, Reinhard Haselsberger, Nur Fadilah Jamaludin, Rohit Abraham John, Teck Ming Koh, Annalisa Bruno, Wei Lin Leong, Nripan Mathews, Maria-Elisabeth Michel-Beyerle, and Subodh G. Mhaisalkar, Perturbation Induced Seeding and Crystallization of Hybrid Perovskites Over Surface Modified Substrates for Optoelectronic Devices, *ACS Appl. Mater. Interfaces 2019*, 11, 27727−27734, DOI: 10.1021/acsami.9b05965

Bo Wu, Haifeng Yuan, Qiang Xu, Julian A. Steele, David Giovanni, Pascal Puech, Jianhui Fu, Yan Fong Ng, Nur Fadilah Jamaludin, Ankur Solanki, Subodh Mhaisalkar, Nripan Mathews, Maarten B.J. Roeffaers, Michael Grätzel, Johan Hofkens and Tze Chien Sum, Indirect tail states formation by thermal-induced polar fluctuations in halide perovskites, *Nature Comms. 2019*, 484, DOI: 10.1038/s41467-019-08326-7

Jianhui Fu, Nur Fadilah Jamaludin, Bo Wu, Mingjie Li, Ankur Solanki, Yan Fong Ng, Subodh Mhaisalkar, Cheng Hon Alfred Huan and Tze Chien Sum, Localized Traps Limited Recombination in Lead Bromide Perovskites, *Adv. Energy Mater. 2019*, 9, 1803119, DOI: 10.1002/aenm.201803119

M. Thambidurai, Shini Foo, K. M. Muhammed Salim, P. C. Harikesh, Annalisa Bruno, Nur Fadilah Jamaludin, Stener Lie, Nripan Mathews and Cuong Dang, Improved photovoltaic performance of triple-cation mixed-halide perovskite solar cells with binary trivalent metals incorporated into the titanium dioxide electron transport layer, *J. Mater. Chem. C. 2019*, 7, 5028-5036, DOI: 10.1039/C9TC00555B

Swee Sien Lim, David Giovanni, Qiannan Zhang, Ankur Solanki, Nur Fadilah Jamaludin, Jia Wei Melvin Lim, Nripan Mathews, Subodh Mhaisalkar, Maxim S Pshenichnikov, and Tze Chien Sum, Hot Carrier Extraction in $CH_3NH_3PbI_3$ Unveiled by Pump-Push-Probe Spectroscopy, *Science Advances*, in press